Alma Mater Studiorum – Università di Bologna

DOTTORATO DI RICERCA IN

CHIMICA

Ciclo XXXIII

Settore Concorsuale: 03/B1

Settore Scientifico Disciplinare: CHIM/03

Homoleptic and Heteroleptic Metal Carbonyl Clusters and Nanoclusters

Presentata da: Beatrice Berti

Coordinatore Dottorato

Prof.ssa Domenica Tonelli

Supervisore

Prof. Stefano Zacchini

Co-supervisore

Prof.ssa Maria Carmela Iapalucci

Esame finale anno 2021

Contents

Abstract

This Thesis aims at presenting the general results achieved during my PhD, that was focused on the study and characterisation of new homoleptic and heteroleptic metal carbonyl clusters. A brief introduction to this fascinating field is reported in Chapter 1, which begins with the discovery of the first metal carbonyl compound and carries on with the synthetic procedures for the synthesis of metal carbonyl clusters (MCCs) and their physical/chemical properties.

Initially, my research was focused on the investigation of small MCCs, as reported in Chapter 2 with the study of new Fe-Au(NHC) carbonyl clusters (N-Heterocyclic Carbene, NHC). In view of the results achieved, I decided to extend the investigation to the congeners Fe-Ag(NHC) and Fe-Cu(NHC) carbonyl compounds, as described in Chapter 3. This study sheds some light on the metallophilic interactions (aurophilicity, argentophilicity and cuprophilicity) present within these compounds and demonstrates that thermal treatment represents an efficient method for the growth of the dimension of MCCs. Indeed, species of the type $[M_3Fe_3(CO)_{12}]^{3-}$ and $[M_4Fe_4(CO)_{16}]^{4-}$ (M = Ag, Au) as well as larger clusters were formed during the thermal treatment of the new Fe-M (M = Ag, Cu, Au) carbonyl compounds. These species inspired the investigation of promising reaction paths for the synthesis of Fe-M (M = Ag, Cu, Au) carbonyl compounds devoid of ancillary ligands and alloy MCCs, as reported in Chapter 4. Chapter 5 shows the interesting results obtained by extending to Co-M(NHC) species the strategy employed with Fe in Chapters 2 and 3. This first part of research allowed a better understanding of the differences and similarities between the Fe-M(NHC) and Co-M(NHC) systems (M = Cu, Ag, Au), as well as their application in homogeneous catalysis (ammonia-borane dehydrogenation).

The second part of this Thesis regards high nuclearity MCCs. In particular, Chapter 6 describes new strategies for the growth of platinum carbonyl clusters involving, for instance, the employment of bidentate phosphines, whereas Chapter 7 reports the syntheses and the thermal decomposition of new Ni-M (Pd, Pt) carbonyl clusters. All the new compounds have been characterised by a combination of different techniques, such as IR and NMR spectroscopies, ESI-MS spectrometry, electrochemical and UV-visible studies, elemental analyses, Inductively Coupled Plasma-Mass Spectrometry (ICP-MS) and single crystal X-ray diffraction (SC-XRD).

The main results obtained during my PhD have been summarised in Chapter 8, followed by the experimental section (Chapter 9) and the references.

CHAPTER 1

Introduction

1.1 A brief history of metal carbonyl clusters (MCCs)

At the end of the nineteenth century, the illuminated chemist Ludwig Mond discovered the first metal carbonyl compound, named nickel tetracarbonyl $Ni(CO)_4$ (for more details see Chapter 7).[1] His discovery introduced a new class of compounds that suddenly attracted great interest amongst scientists. During the following decades, several attempts aimed at synthesising new metal carbonyl compounds were made, but all of them faced an important limit for that time, that is the structural characterisation. Later, the improvement of the spectroscopic techniques and the development of crystallographic methods filled this gap, by allowing a more complete definition and characterisation of these new chemical species. It is proper to state that the technological progress boosted the researches, and so the identification of several new metal carbonyl compounds. Many years later the discovery of the first monometallic compound $Ni(CO)_4$, species containing more than one metal atom were discovered, and the name "metal cluster" was introduced. Indeed, in 1966 Cotton defined "cluster" as a class of compounds "*containing a finite group of metal atoms which are held together entirely, mainly, or at least to a significant extent, by bonds directly between the metal atoms even though some non-metal atoms may be associated intimately with the cluster*".[2] One of the most fascinating class of metal clusters is that stabilised by CO ligands (Molecular Metal Carbonyl Clusters, MCCs). As depicted in Figure 1.1, the nuclearities (number of metal atoms) of the structurally characterised MCCs increased along the years boosted by the technological advancement of new analytical techniques. By driving the researches along this direction, MCCs reached the nano dimension (nano cluster), joining the nano regime. Conversely, studies on metal nanoparticles pushed the researches towards ultrasmall nanoparticles (USNPs, dimension < 3 nm). At some point, these two areas of interest started to overlap: MCC size became higher while the nanoparticles ones decreased significatively (Figure 1.2). In fact, it is proper to define USNPs as polydisperse large molecular clusters, while higher nuclearity molecular clusters may be viewed as perfectly monodispersed and atomically precise metal NPs. The fascinating aspect of this crossing is the possibility to synthesise MCCs with NP dimension (Figure 1.3), well-defined number of atoms and structures, and unique chemical/physical properties.

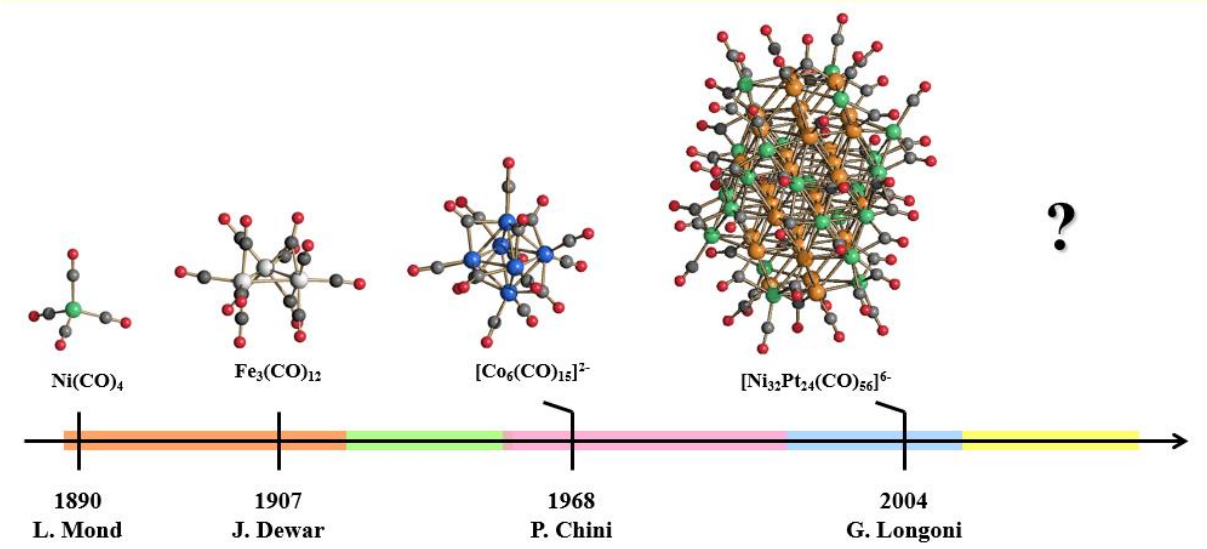

Figure 1.1 The discovery of some key compounds related to technological scientific progress. **Orange** Measure of surface tension for the estimation of the parachor, molecular refraction, temperature, pressure and volume. **Green** IR, Raman and NMR spectroscopy, conductivity and osmometric measurements. **Pink** Single crystal X-ray diffraction. **Blue** Use of CCD (charge-coupled-device) detector for X-ray diffractometer. **Yellow** New type of analytical instruments or techniques.

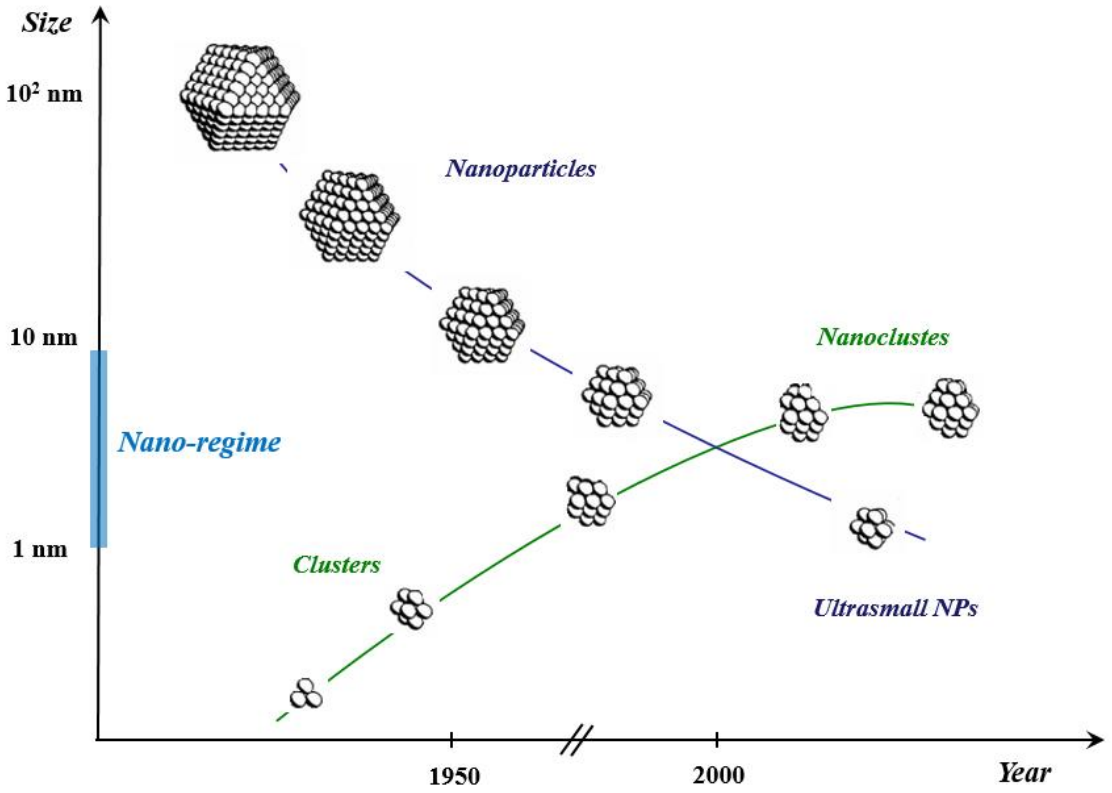

Figure 1.2 The evolution of the sizes of metal nanoparticles (blue line) and clusters (green line) with the time (qualitative picture based on literature data).

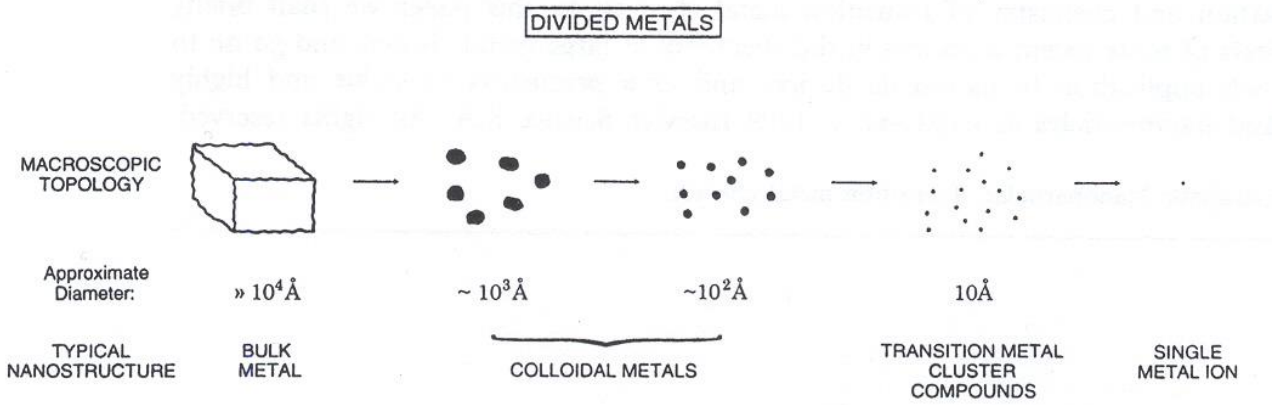

Figure 1.3 Representation of the size of bulk metal, colloidal metals, metal clusters and single metal ions.[3]

Up to now, the largest MCC structurally characterised is the hexa-anion $[Ni_{32}Pt_{24}(CO)_{56}]^{6-}$, which entered the nano regime (2.1 nm).[3] $[HNi_{38}Pt_6(CO)_{48}]^{5-}$ (1.9 nm) is another fascinating example of large MCC (Figure 1.4), whereas higher dimensions have been reached by using mixed $CO/PR_3/Pd$ clusters by Dahl et al. as shown by the giant $Pd_{145}(PR_3)_{30}(CO)_{60}$ (3 nm) (Figure 1.5).[4]

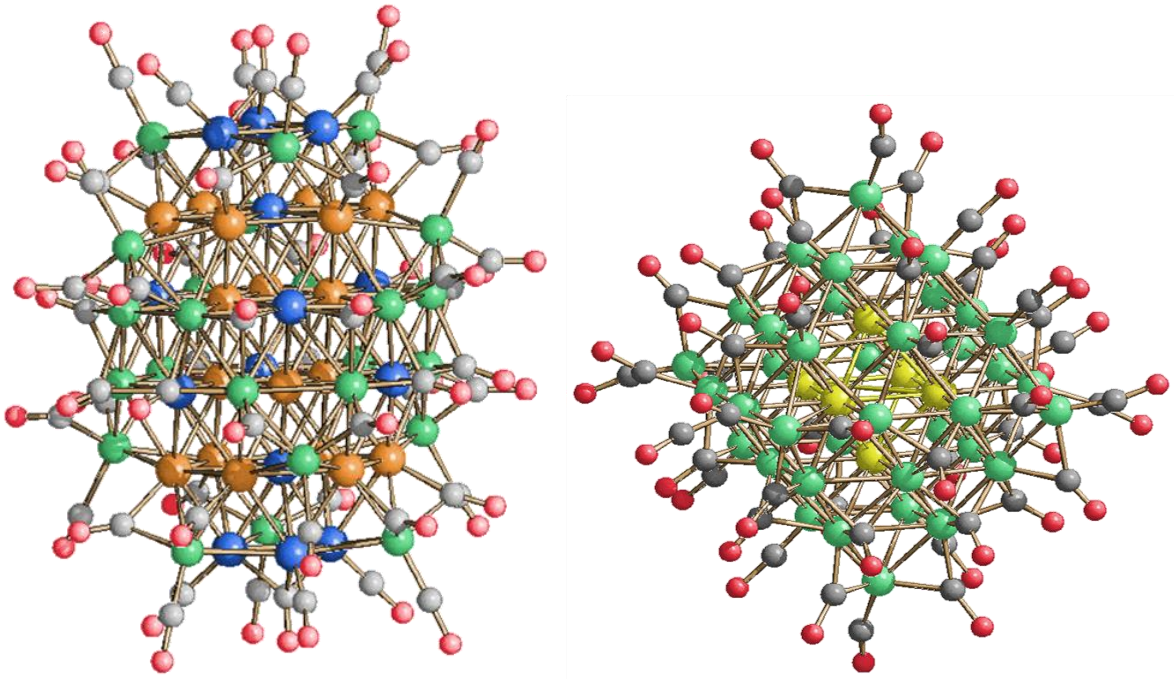

(a) (b)

Figure 1.4 Molecular structures of (a) $[Ni_{32}Pt_{24}(CO)_{56}]^{6-}$ (2.1 nm) and (b) $[HNi_{38}Pt_6(CO)_{48}]^{5-}$ (1.9 nm) (yellow, Pt (b); green, Ni; blue and orange, Ni/Pt (a); red, O; grey, C).

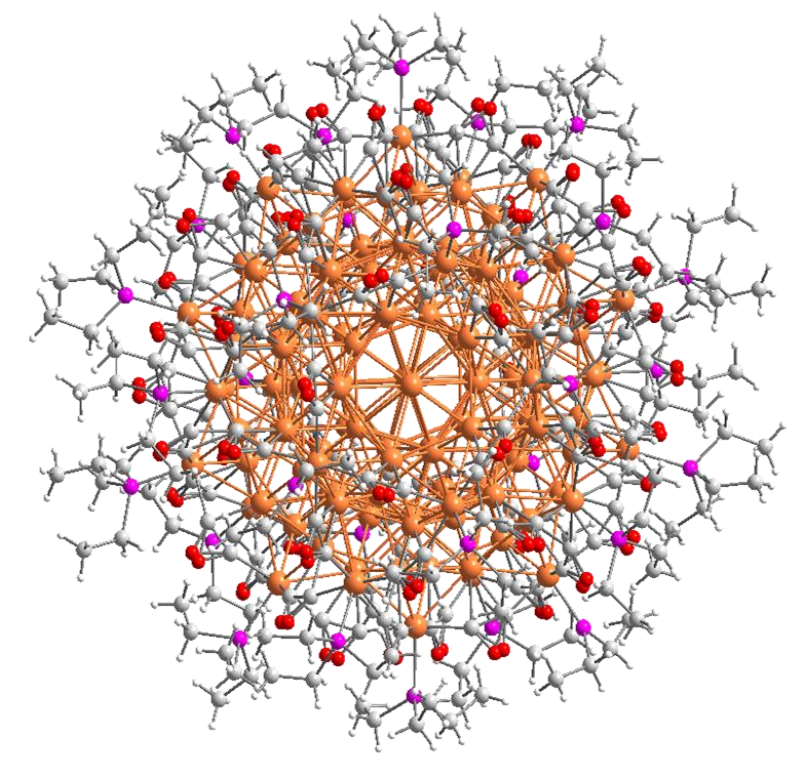

Figure 1.5 Molecular structure of $Pd_{145}(PR_3)_{30}(CO)_{60}$ (3 nm) (orange, Pd; purple, P; red, O; grey, C).[4]

1.2 Metal carbonyl clusters: Synthetic procedures

The scientific production regarding MCCs was quite fluctuating throughout the 1990s years, but it grew again with the explosion of the interest in nanochemistry. From that moment, several studies have been carried out aiming at developing new strategies for the syntheses of new MCCs. In general, the synthetic procedures for the preparation of MCCs may be grouped as follow:

- Direct (reductive) carbonylation.
- Thermal treatments.
- Redox processes.
- Other chemically induced methods.

It must be remarked that these strategies are not universal procedures. Indeed, depending on the nature of the metal or the ligand involved, a specific protocol should be adopted. Unfortunately, this does not permit to design *a priori* the preparation of a species with a predefined structure. Indeed, large MCCs show a wide variety of frameworks and even species with almost the same composition can adopt rather different geometries. This is due to the fact that M-M interactions are not very strong and are nondirectional compared to C-C bonds. This compounds are generally

anionic or neutral. Indeed, by employing solvents with different polarity it is possible to purify the crude mixture by separating the main product from the side products (this procedure is often referred as "work-up"). The ionic MCCs are generally isolated as tetra-substituted ammonium or phosphonium salts. Thus, depending on the nature of the organic fragments of the cation, it is possible to modulate the solubility of such compounds in organic solvents. This might also be of help for their crystallisation. Furthermore, the great variety of conditions that can be employed (nature of reagents, stoichiometry, reaction solvent, temperature, atmosphere, work-up) allows to obtain molecular frameworks with several combinations of metals and ligands. It is necessary to underline that neutral and anionic MCCs are oxygen sensitive, for this reason they must be stored under inert atmosphere. If exposed to O_2, MCCs are oxidise resulting in M^{n+} inorganic salts (M = non-noble metal) or bulk metal (M = noble metal).

Direct (reductive) carbonylation

Carbonylation is the main entry to the chemistry of metal carbonyls. Direct carbonylation works only with Fe and Ni. This procedure requires an intimate contact between fine metal particles and CO.

The most used synthetic method is the reductive carbonylation, which consists in the reduction of a metal salt or metal complex under CO atmosphere. Different reducing agents may be employed, and among these, CO itself in the presence of a base is often employed, in accordance with equation (1.1):

$$CO + 2OH^- \rightarrow CO_2 + H_2O + 2e^- \qquad (1.1)$$

Generally, this synthetic method leads to the formation of low nuclearity metal carbonyls, such as $Fe(CO)_5$, $Ni(CO)_4$, $Rh_4(CO)_{12}$ and $Co_2(CO)_8$. A well-known example of reductive carbonylation is that developed by Chini and Longoni that leads to the formation of the so-called "Chini clusters", of general formula $[Pt_{3n}(CO)_{6n}]^{2-}$ (n = 2-10).[5] The formation of the Chini clusters as sodium salts occurs by dissolving the Pt(IV) salt Na_2PtCl_6 in methanol at room temperature in the presence of CH_3COONa or NaOH. The nature of the resulting Chini cluster depends on the solvent, amount and strength of the base (see Chapter 6). Reductive carbonylation can also be performed in solid state with the "ship-in-a-bottle" method,[6] or in solution in the presence of PR_3 ligands affording, in the latter case, heteroleptic CO/PR_3 clusters.

Thermal treatment

Thermal treatments represent a very simple way to obtain larger MCCs. During this process, cleavage of M-CO bonds and formation of new M-M bonds occur, affording new species with higher nuclearity. For instance, a wide variety of products may be obtained by pyrolysis of $Os_3(CO)_{12}$, as pointed out in Scheme 1.1.[7,8]

Scheme 1.1 Preparation of Os carbonyl clusters by thermal methods.[7,8]

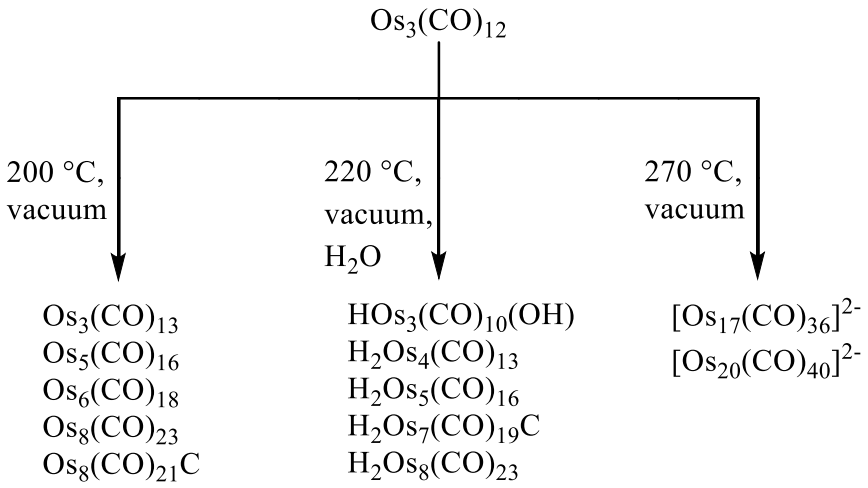

In the framework of this Thesis, there are several cases of large MCCs formed after heating up solutions of low nuclearity metal carbonyl clusters. Thermal treatments represent a good way to enhance the dimension of the cluster, but they have to be performed carefully, in order to avoid the complete decomposition of the product or the formation of complex mixtures of products.

Redox Processes

MCCs may also be synthesised by means of reduction, oxidation, redox condensation and disproportion processes. As far as the reduction is concerned, electrons are added to antibonding orbitals leading to the breakup of M-M bonds or CO loss. The reduction of Chini clusters $[Pt_{3n}(CO)_{6n}]^{2-}$ (n = 2-6) in the presence of a strong base and CO represents a perfect example of reduction of dimension (*n* value) without any perturbation of the molecular structure. CO atmosphere is of paramount importance to avoid CO removal and rearrangement of the metal framework during the reduction. MCCs may show different behaviour under reducing conditions, as in the case of multivalent compounds. Indeed, being able to undergo several reversible redox processes without any significant structural rearrangement, they cannot be transformed into larger or smaller compounds by redox reactions.

Reduction can also be performed by reacting MCCs with alkali metals or OH^-. In particular, Fe-CO clusters are actually synthesised from $Fe(CO)_5$ in the presence of bases. The general process is illustrated in Scheme 1.2.

Scheme 1.2 Condensation process induced by reduction.

Oxidation is another interesting way to increase the size of the cluster and its metal cage. Indeed, by using innocent oxidising species, such as tropylium or ferrocenium ions, new M-M bonds are formed. As far as coordinating oxidants (H^+) are concerned, the reactions may be more complex. The proton can add to the metal cage resulting in a stable hydride cluster or leave the compound as H_2. In this case an oxidative condensation of MCCs occurs, as shown in equations (1.2-1.3):

$$2[Rh_6C(CO)_{15}]^{2-} + 2H^+ \rightarrow [Rh_{12}C_2(CO)_{24}]^{2-} + 6CO + H_2 \quad (1.2)$$

$$2[Rh_6(CO)_{15}]^{2-} + 2H^+ \rightarrow [Rh_{12}(CO)_{30}]^{2-} + H_2 \quad (1.3)$$

Sometimes oxidation must be performed very gently, in order to avoid the complete oxidation of the metals and the formation of metal oxides. Some clusters are more resistant to oxidation than others. $[Pt_6(CO)_{12}]^{2-}$, for instance, is very sensitive and quickly reacts in the presence of oxidants affording the larger oligomers $[Pt_9(CO)_{18}]^{2-}$, $[Pt_{12}(CO)_{24}]^{2-}$ and $[Pt_{15}(CO)_{30}]^{2-}$. It is rather easy to follow this transformation, because the process is accompanied by a change of the colour of the solution (orange $[Pt_6(CO)_{12}]^{2-}$, red $[Pt_9(CO)_{18}]^{2-}$, emerald green $[Pt_{12}(CO)_{24}]^{2-}$, yellow-green $[Pt_{15}(CO)_{30}]^{2-}$).

Redox condensation is probably the most used approach for the synthesis of MCCs. It consists in a reaction between a reduced metal cluster (usually an anionic cluster) and a more oxidised species, that can be another cluster, a metal complex or a metal salt. The first example of redox condensation was reported by Hieber and Shubert in 1965,[9] and it is shown in equation (1.4):

$$[Fe_3(CO)_{11}]^{2-} + Fe(CO)_5 \xrightarrow[thf]{25\ ^\circ C} [Fe_4(CO)_{13}]^{2-} + 3CO \quad (1.4)$$

It seems reasonable to think that the first step gives rise to the unstable radicals $[Fe_3(CO)_{11}]^-$ and $[Fe(CO)_5]^-$, that subsequently reacts together affording the condensation product $[Fe_4(CO)_{13}]^{2-}$.[9]

By using reagents containing different metals, redox condensation can also be employed for the synthesis of heterometallic MCCs.

Finally, disproportion is the reverse process of the redox condensation. Indeed, it occurs when a neutral carbonyl compound $M_x(CO)_y$ is dissolved in a polar solvent (acetonitrile, dmf, dmso). For instance, $[Fe(dmf)_6][Fe_4(CO)_{13}]$ resulted after heating $Fe(CO)_5$ in dmf. A further example is that of $Co_2(CO)_8$, that in methanol at 50 °C disproportionates to $[Co(MeOH)_6][Co(CO)_4]_2$. The resulting salt is constituted by Co atoms in two different oxidation states, that is +2 and -1, according to equation (1.5).[10]

$$3Co_2(CO)_8 + 12MeOH \rightarrow 2[Co(MeOH)_6][Co(CO)_4]_2 + 8CO \quad (1.5)$$

The chemistry of octacarbonyl dicobalt is quite complex. The formation of larger clusters such as $Co_4(CO)_{12}$ and $[Co_6(CO)_{15}]^{2-}$ is regulated by equilibria that can be influenced by the polarity of the solvent.

In addition to the cases of Fe and Co that display disproportion in specific conditions (solvent polarity), $Rh_4(CO)_{12}$ exhibits the same behaviour in the presence of pyridine. The disproportion of the starting Rh carbonyl compound in CH_2Cl_2 under CO atmosphere leads to the formation of Rh(+1) and Rh(-1/5), as indicated in equation (1.6).[11]

$$3Rh_4(CO)_{12} + 4py \rightarrow 2[Rh(CO)_2(py)_2][Rh_5(CO)_{15}] + 2CO \quad (1.6)$$

Other Chemically Methods

The employment of anionic (OH^-, I^-) or neutral (PR_3, CO, amines) nucleophiles is considered an efficient strategy for the modification or preparation of MCCs. The interaction between the reagents may produce many effects, such as the addition to the metal cluster of the nucleophile as ligand, the rearrangement of the metal framework or its decomposition. The use of phosphines is rather interesting, because, as described in Chapter 6, allows to substitute CO ligands and, in some cases, also increases the dimension of the cluster. On the other hand, the purification step might be quite difficult in presence of products with different substitution degrees.

1.3 Characterisation and physical properties

Molecular metal carbonyl clusters display a great variety of features depending on the nature of the metals, the nuclearity, the bulkiness and type of ligands. It is not rare that very similar compounds show rather different reactivity or geometries. Sometimes just one negative charge can modify the

metal structure. In order to complete this brief overview, the physical and chemical properties of MCCs are herein briefly discussed.

Structural features

The metal cores of high nuclearity homo- and hetero-metallic MCCs often resemble to that of bulk metals, with close-packed geometries, such as body-centred cubic (bcc), hexagonal close-packed (hcp) and cubic close-packed (ccp) (Figure 1.6).

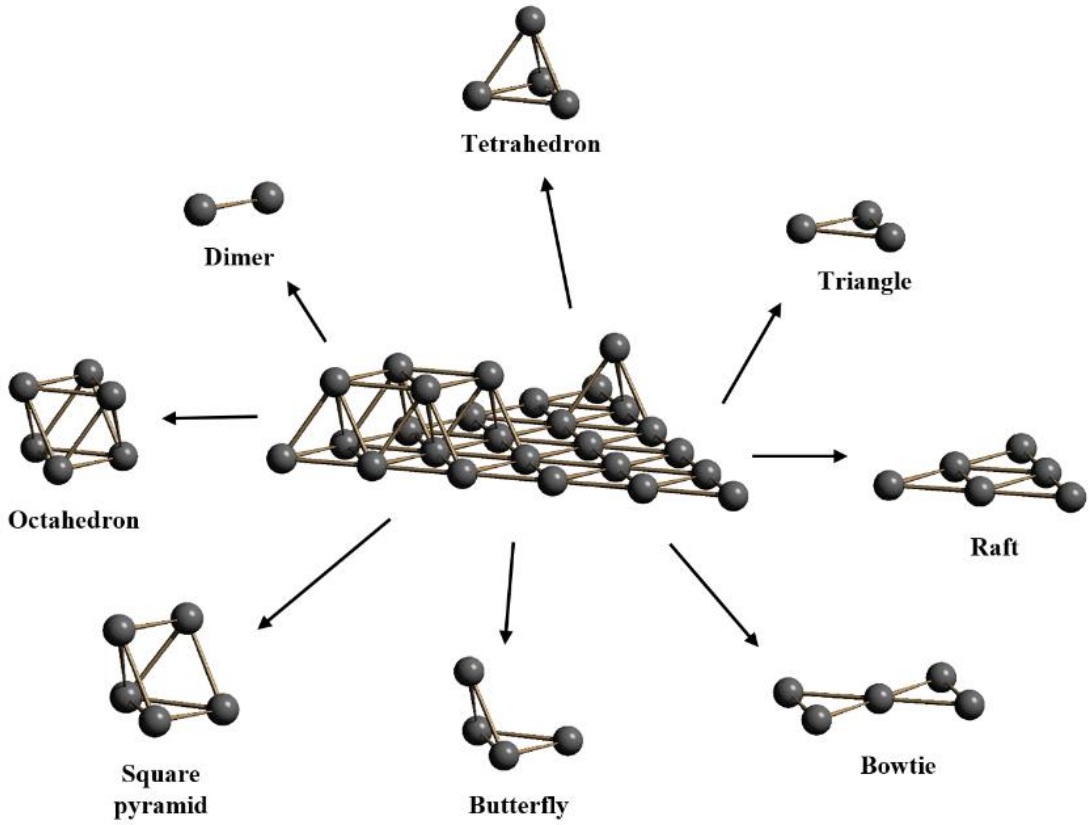

Figure 1.6 Comparison between fragments of a bulk metal and the metal frameworks of MCCs.

In addition to these, they can also adopt prismatic and antiprismatic frameworks. A well-known example of prismatic cage is that of Chini clusters. In particular, these compounds are based on triangular $[Pt_3(\mu\text{-}CO)_3(CO)_3]$ units stacked along a common C_3 axis with two electrons delocalised in the metal skeleton. The antiprismatic geometry and other complex structures are often adopted by heteronuclear species containing carbide ($[Ni_{32}C_6(CO)_{36}]^{2-}$ shown in Figure 1.7,[12] or $[Co_8C(CO)_{18}]^{2-}$) or hosting a heterometal (i.e. $[Rh_{10}As(CO)_{22}]^{3-}$). The presence of the latter within the metal cage may result in the formation of cavities with a specific geometry (trigonal

prismatic, square antiprismatic, octahedral). Icosahedral and poly-icosahedral structures are often found in non-carbonyl clusters, such as $[Au_{13}(PMe_2Ph)_{10}Cl_2]^{3+}$ (icosahedral) and $[Au_{13}Ag_{12}(PPh_3)_{10}Br_8]^{+}$ (biicosahedral).[13] Several examples are also found in MCCs, such as the icosahedral $[Pt_{13}(CO)_{12}]^{8-}$ (Figure 1.8) core of $[Pt_{13}(CO)_{12}\{Cd_5(\mu\text{-}Br\}_5Br_2(dmf)_3\}_2]^{2-}$ or the Ga-centred Ni_{12} cage of $[Ni_{12}Ga(CO)_{22}]^{3-}$.

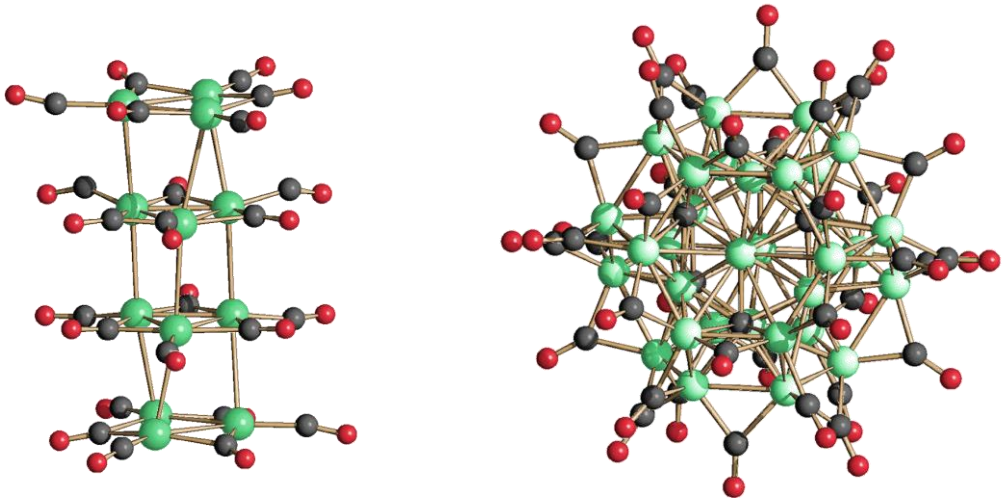

(a) (b)

Figure 1.7 Molecular structures of (a) $[Pt_{12}(CO)_{24}]^{2-}$ (trigonal prism) and (b) $[Ni_{32}C_6(CO)_{36}]^{6-}$ (six square anti-prismatic Ni_8C cages fused together).[12]

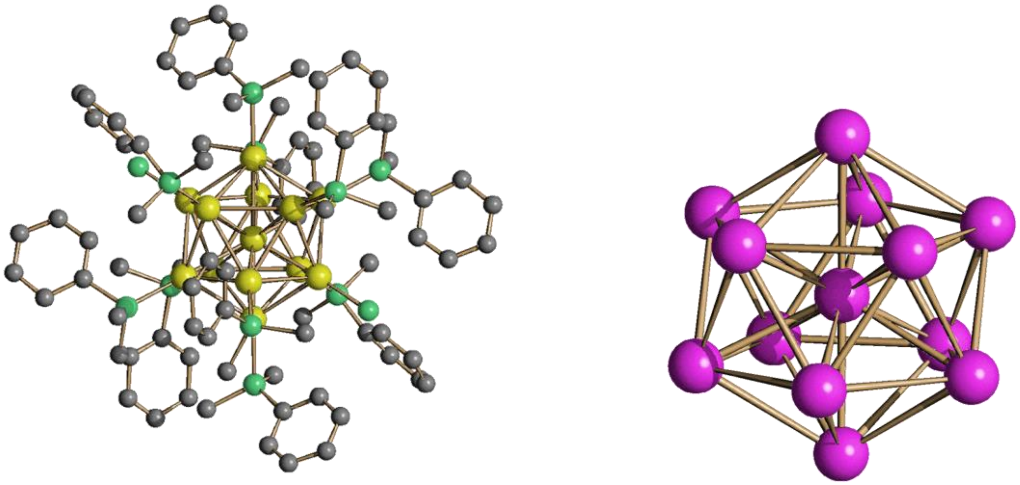

(a) (b)

Figure 1.8 Molecular structures of (a) $[Au_{13}(PMe_2Ph)_{10}Cl_2]^{3+}$ and (b) the $[Pt_{13}(CO)_{12}]^{8-}$ core of $[Pt_{13}(CO)_{12}\{Cd_5(\mu\text{-}Br\}_5Br_2(dmf)_3\}_2]^{2-}$ (purple, P; yellow, Au; green, P and Cl; grey, C). Both species are isoelectronic (162 CV) and adopt the same icosahedral geometry.[13]

The reason for which a MCC prefers a specific molecular structure rather than another one is not simple. It depends on many factors, such as the nature and number of metals, the metal/CO ratio

and the presence of ancillary ligands. In order to unravel the molecular structure, crystallographic studies are necessary (Single Crystal X-Ray Diffractometry, SC-XRD).

Physical properties

Small and larger MCCs may exhibit different physical properties, since they depend on the nuclearity of the cluster and the CO/M ratio. When the nuclearity is high, CO/M decreases, M-M bonds become predominant over M-CO interactions and the cluster assumes a bulk metal like behaviour. As a consequence, metallisation occurs, the electrons become more delocalised and the HOMO-LUMO gap decreases, passing from an insulating to a semi-conductor regime. This phenomenon may be observed in MCCs with nuclearity between 20 and 60. Electrochemical properties, NMR spectroscopy and magnetic measurements are required in order to fully characterise these species.

From an electrochemical point of view, larger MCCs are often multivalent, and display two or more redox processes as a consequence of the reversible addition/removal of electrons in their frontier orbitals. At this regard, cyclovoltammetry represents a useful method for the determination of the redox processes. As shown in Figure 1.9, a voltammetric profile of a redox-active MCC displays almost equally spaced redox waves, as in the case of $[Ni_{32}C_6(CO)_{36}]^{6-}$.

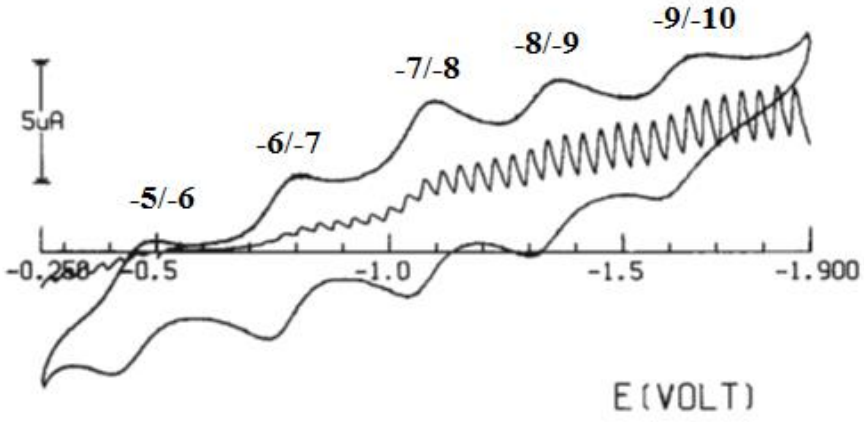

Figure 1.9 Voltammetric profile of $[Ni_{32}C_6(CO)_{36}]^{6-}$. One oxidative and four reductive processes were detected.[3]

The possibility of modulating the electronic charge of multivalent MCCs makes them feasible candidates as molecular nanocapacitors. The oxidation state of such clusters can be controlled by chemical redox reactions or by means of electrochemical methods. Addition of acids

may result in oxidation of the cluster or formation of mono- or poly-protonated MCCs. Indeed, hydride atoms in MCCs are usually slightly acidic and can be removed by the use of bases.

Unfortunately, hydrides in high nuclearity MCCs cannot be detected by NMR spectroscopy. Indeed, beyond a nuclearity of 22-30 metal atoms, these species become NMR silent. IR spectroscopy may be of help in the (indirect) observation of protonation/deprotonation processes. In the case of MCC poly-hydrides, by changing the polarity of the solvent it is possible to distinguish the different poly-protonated forms, as shown in Scheme 1.3.

Scheme 1.3 Protonation/deprotonation of $[HN_{22}(C_2)_4(CO)_{28}(CdBr)_2]^{3-}$ in different solvents.

$$[H_2N_{22}(C_2)_4(CO)_{28}(CdBr)_2]^{2-} \underset{+\,H^+}{\overset{-\,H^+}{\rightleftharpoons}} [HN_{22}(C_2)_4(CO)_{28}(CdBr)_2]^{3-} \underset{+\,H^+}{\overset{-\,H^+}{\rightleftharpoons}} [N_{22}(C_2)_4(CO)_{28}(CdBr)_2]^{4-}$$

2031(s), 1862(m) cm^{-1} — 2017(s), 1849(m) cm^{-1} — 2008(s), 1837(m) cm^{-1}

in thf — in CH_3CN — in dmf

As far as low nuclearity MCC poly-hydrides are concerned, the presence of hydride atoms can be recognised by means of ^1H NMR spectroscopy in a range of chemical shift between 0 and -40 ppm. The resolution of ^1H NMR spectra may be complex when fluxional phenomena occur. In this case, NMR analyses at very low temperature are recommended, in order to freeze the hydride movements and avoid broad resonances in the ^1H NMR spectrum.

The last important property of MCC regards their magnetic behaviour. In this perspective, a first distinction between odd- and even-electron MCCs may be useful. Odd-electron clusters presenting one unpaired electron are paramagnetic compounds, whereas even-electron MCCs display a more controversial behaviour, that may arise from incipient metallisation of the metal core and from the decrease of HOMO-LUMO energy gap to values close to kT.[14] The increase of nuclearity accompanied by the tightening of the frontier energy gap seems to induce magnetism in several MCCs, regardless of the fact that they possess an even or odd number of electrons.

The development of electronic and magnetic properties of molecular MCCs make them candidates for applications in nanosciences, superparamagnetic quantum dots and nanomagnets, as well as precursors of narrowly dispersed magnetic alloy and metal oxide nanoparticles of corresponding composition.

Self-Assembly

MCCs can be employed as nanometric or subnanometric building blocks for self-assembly. In order to achieve it, several strategies can be used, such as:

- Formation of functionalised ionic materials by assembly of functional MCC anions with suitable cations.
- Polymerisation of MCCs with formation of M-M bonds.
- Aggregation of MCCs through heterometallic M-M' bonds by using suitable M'^{n+} cations.
- Self-assembly through inorganic linkers.
- Aggregation of clusters by polydentate organic linkers.
- Formation of isocarbonyl linkages.

A very fascinating example of the second strategy is that represented by Chini clusters. Indeed, it is well-known that stepwise oxidation of $[Pt_{3n}(CO)_{6n}]^{2-}$ species results in the 1-D growth of the cluster by formal progressive addition of $[Pt_3(\mu\text{-}CO)_3(CO)_3]$ units along the common C_3 axis (Figure 1.10).

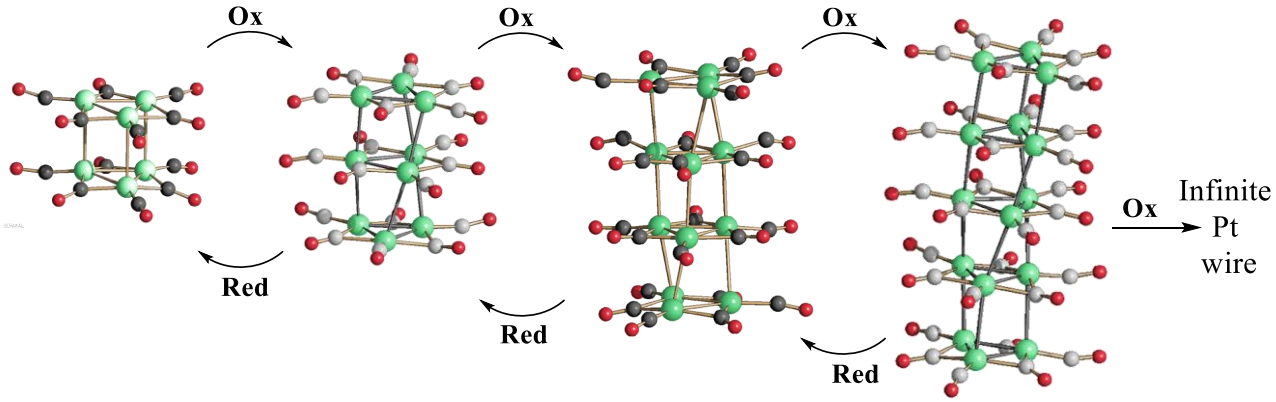

Figure 1.10 Stepwise oxidation of $[Pt_{3n}(CO)_{6n}]^{2-}$ clusters to form infinite wires (green, Pt; red, O; grey, C).

The morphological aspect of the resulting $[M]_x[Pt_{3n}(CO)_{6n}]$ (M = mono- or bivalent cation; x = 1, 2; n = 2-8) material depends on the nature and dimension of the cation, as well as the nuclearity *n* of the cluster. Low nuclearity species ($n \leq 4$) adopt ionic 0-D packing during crystallisation, whereas higher nuclearity compounds ($n \geq 5$) approach each other by giving rise to infinite chains, that can be discontinuous, semicontinuous or continuous (Figure 1.11). This is due to fact that while the nuclearity increases, the negative charge remains constant (2 electrons), electrostatic repulsion decreases, and the clusters can come closer. The tendency of larger compounds (n = 5-8) to produce infinite wires is also macroscopically observable during the crystallisation process, when they form

crystals that resemble whiskers. A further interesting point regards the electrical behaviour. It was observed that ionic 0-D materials are insulator, whereas the resistivity drops from approximatively 10^5 to 10^3 and 10^2 Ω cm on passing from discontinuous to semicontinuous to continuous materials, respectively.[3]

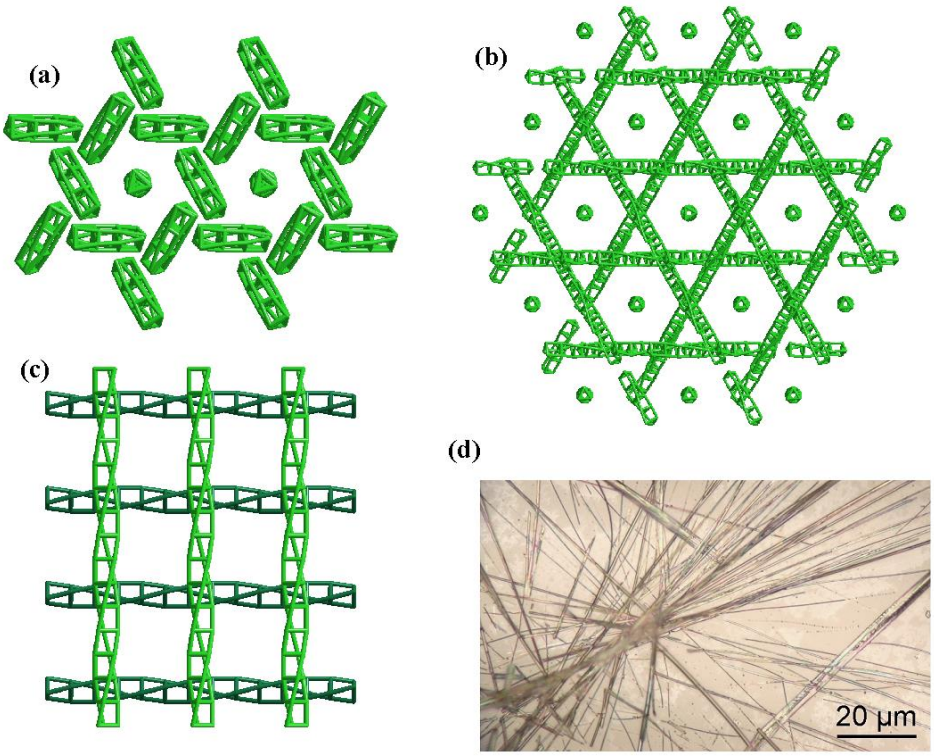

Figure 1.11 Crystal packing of (a) $[NBu_4]_2[Pt_{12}(CO)_{24}]$ (isolated ions, 0-D packing), (b) $[NEt_4]_2[Pt_{15}(CO)_{30}]$ (discontinuous chains, 3-D network) and (c) $[NEt_4]_2[Pt_{24}(CO)_{48}]$ (continuous chains, 2-D network). Only Pt atoms are represented for clarity. (d) Optical micrographs (magnification 50×) of whisker-like crystals of $[NBu_4]_2[Pt_{15}(CO)_{30}]$.[3]

MCCs as Precursors of Metal Nanoparticles

MCCs can be used as starting material for the preparation of metal nanoparticles, metal nanowires and other nanostructured materials. The thermal decomposition under mild conditions represent an efficient approach for the synthesis of small metal nanoparticles with controlled dimension and composition (Figure 1.12 (a)). It is well-known that both homo- and bimetallic MCCs can be formed in cavities of zeolites through "ship-in-a-bottle" syntheses and then transformed into metal nanoparticles of controlled size (Figure 1.12 (b)).[6] The "ship-in-bottle" technology using zeolites as microsized reactors gives an ordered basis for better control of particle size, metal compositions and morphology. Through the years several platinum MCCs have been synthesised, extracted and characterised, and transformed into nanoparticles and nanowires encapsulated in micro/mesoporous cavities and channels. The resulting nanostructured platinum-based materials exhibit higher

catalytic performances and stabilities for various catalytic reactions as well as having unique magnetic properties, compared to conventional metals. The employment of a second metal within the metal cage can contribute to the catalytic performance. This is the case of the bimetallic Pt-Sn carbonyl clusters used for the preparation of nanostructured materials for the selective oxidation of HMF (hydroxymethylfurfural).[15]

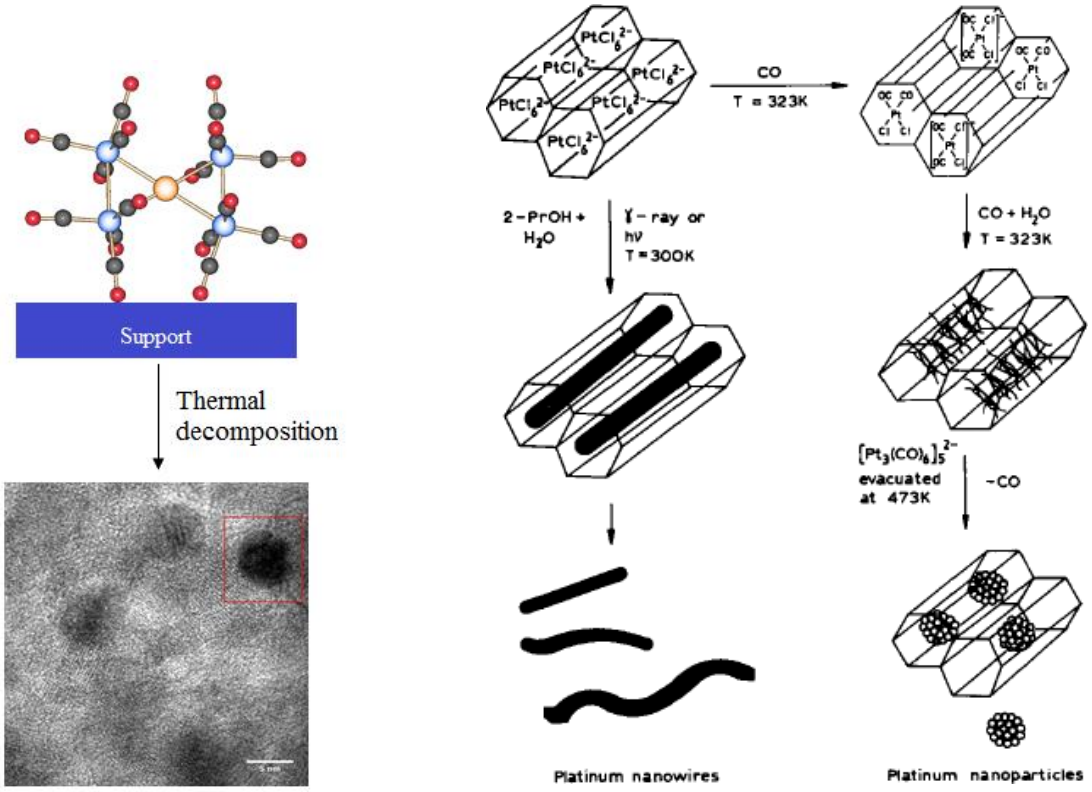

(a) (b)

Figure 1.12 (a) Fabrication of Au-Fe_x catalysts on TiO_2 from $[AuFe_4(CO)_{16}]^-$ clusters: the molecular precursors are adsorbed on the support and converted into active phase by thermal treatment (blue, Fe; orange, Au; red, O; grey, C). The TEM image displays the presence of small Au nanoparticles (< 5 nm) well dispersed on the support. (b) Ship-in-a-bottle fabrication of Pt nanowires and nanoparticles.[3]

Finally, bimetallic MCCs can be useful precursors for the preparation of magnetic bimetallic nanoparticles protected by ligands and dispersed in organic solvents or water, as well as embedded in mesoporous matrices. The thermal decomposition of bimetallic Fe–Co, Fe–Ni and Fe–Pt MCCs in 1,2-dichlorobenzene solution in the presence of surfactants (i.e. oleic acid, myristic acid, oleylamine) leads to the formation of magnetic nanoalloys with controlled size and composition (Figure 1.13).

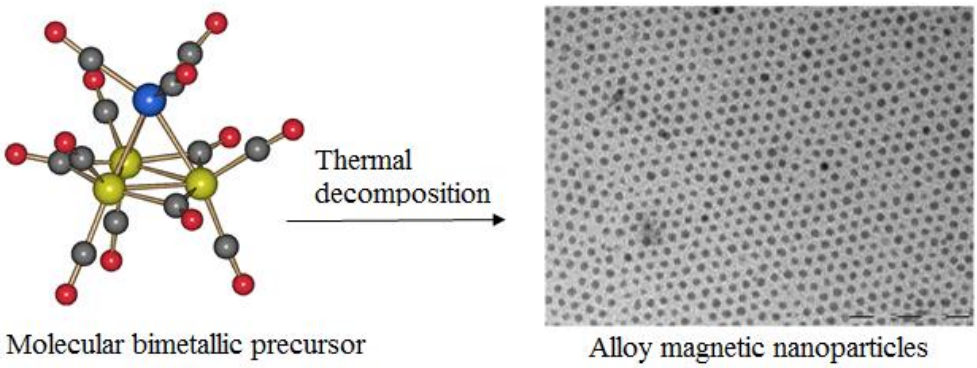

Figure 1.13 Preparation of bimetallic nanoparticles from MCCs.[3]

1.4 Aim of the Thesis

The aim of this Thesis was to explore new synthetic routes for the preparation of new homo- and heterometallic carbonyl clusters, their characterisation from a structural point of view and the investigation of their physical and chemical properties, as well as their potential catalytic activity. Particular attention was focused on transition metal molecular clusters and nanoclusters showing different sizes, compositions, and properties. In order to shed some light on their reactivity and type of interactions (i.e. metallophilic), several metallic systems have been investigated.

At first, low nuclearity MCCs have been studied. At this regard, the employment of N-Heterocyclic carbene (NHC) ligands in addition to carbonyls was of paramount importance for the stabilisation and isolation of new species. The research started with the investigation of low nuclearity Fe-Au(NHC) carbonyl clusters (Chapter 2), followed by the study of the congeners Fe-Cu(NHC) and Fe-Ag(NHC) carbonyl compounds (Chapter 3). The metallophilic interactions (aurophilicity, argentophilicity and cuprophilicity) observed in these new Fe-M (M = Cu, Ag, Au) species have been investigated and thermal treatments performed in order to achieve higher nuclearity products. Amongst these species, those of the type $[M_3Fe_3(CO)_{12}]^{3-}$ and $[M_4Fe_4(CO)_{16}]^{4-}$ (M = Ag, Au) occurred as a consequence of the loss of the ancillary ligands. This observation inspired the investigation of promising reaction paths for the synthesis of new iron bimetallic carbonyl clusters (M = Ag, Cu, Au) devoid of ancillary ligands (Chapter 4). This study was, then, extended to Co-M(NHC) species (Chapter 5). The interesting results obtained allowed a better understanding of the differences and similarities between the Fe-M(NHC) and Co-M(NHC) systems (M = Cu, Ag, Au), and their application in homogeneous catalysis (ammonia-borane dehydrogenation).

Subsequently, the attention was focused on larger transition metal clusters. It is noteworthy that platinum Chini clusters are good starting materials for the preparation of higher nuclearity compounds. In these perspective, new strategies for the growth of platinum carbonyl clusters have been developed, by employing, for instance, bidentate phosphines (Chapter 6). Some bimetallic Ni-Pt and Ni-Pd carbonyl clusters can reach great dimensions, as reported in the literature. For this reason, the syntheses on new Ni-M (Pd, Pt) carbonyl clusters have been explored, as well as their thermal decomposition (Chapter 7).

CHAPTER 2

Heterobimetallic Fe-Au Carbonyl Clusters Stabilised by N-Heterocyclic Carbene Ligands

In this chapter the synthesis and characterisation of new Fe-Au carbonyl clusters containing N-Heterocyclic carbene ligands are reported. The compounds presented in this Section are summarised in Table 2.1.

Table 2.1 Clusters described in this chapter.

Compound	Compound number
$[Fe(CO)_4(AuIMes)]^-$	**1**
$[Fe(CO)_4(AuIPr)]^-$	**2**
$Fe(CO)_4(AuIMes)_2$	**3**
$Fe(CO)_4(AuIPr)_2$	**4**
$Fe(CO)_4(AuIMes)(AuIPr)$	**5**
$Fe(CO)_4(AuIMes)(AuPPh_3)$	**6**
$Fe(CO)_4(AuIPr)(AuPPh_3)$	**7**
$Fe(CO)_4(AuPPh_3)_2$	**8**
$[Au_3\{Fe(CO)_4\}_2(AuPPh_3)_2]^-$	**9**
$[Fe(CO)_4(AuPPh_3)]^-$	**10**
$[Fe_2(CO)_8(AuIMes)]^-$	**11**
$[Fe_2(CO)_8(AuIPr)]^-$	**12**
$[Fe_3(CO)_{10}(CCH_3)]^-$	**13**
$[Au_3Fe_3(CO)_{12}]^{3-}$	**14**
$[Au_3Fe_2(CO)_8(IMes)_2]^-$	**15**
$[Fe_3S(CO)_9]^-$	**16**
$[HFe(CO)_4]^-$	**17**
$[Au_{16}S\{Fe(CO)_4\}_4(IPr)_4]^{2+}$	**18**

2.1 Introduction

Heterometallic complexes and clusters containing coinage metals in the +1 oxidation state are very attractive since they present heterometallic bonds and metallophilic interactions, that are attractive interactions between the closed shell d^{10} centres. Au(I) displays a $5d^{10}$ valence shell electron configuration and tends to form compounds with a linear coordination. This tendency can be explained on the basis of the d-s-p hybridisation scheme proposed by Orgel (Figure 2.1).

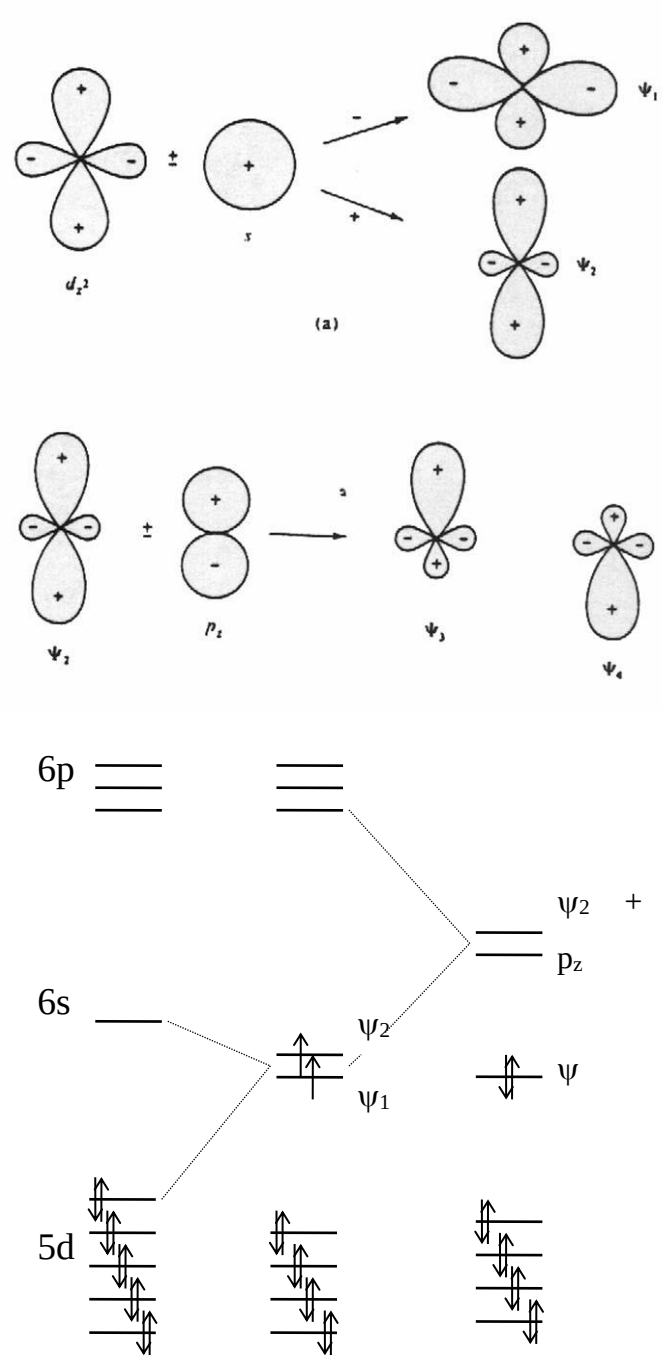

Figure 2.1 Representation of d-s-p hybridisation of Au(I).

Indeed, the hybridisation of the full $5d_z^2$ orbital with the empty 6s orbital leads to the formation of the two ψ_1 and ψ_2 hybrid orbitals. Further hybridisation of ψ_2 with the p_z orbital generates two empty orbitals that can be employed to form two coordinative bonds with an angle of 180° along the z-axis. Moreover, the high electron density located on ψ_1 shows a repulsive effect by preventing ligands from getting closer to the metal on the xy plane.

Gold is stable in the +3 oxidation state, while in the +1 oxidation state as aquo complex it spontaneously disproportionates to Au(0) and Au(III). As shown in the Latimer diagram depicted in Scheme 2.1, the standard reduction potential of the Au(I)/Au(0) couple is higher than Au(III)/Au(I), indicating spontaneous disproportion of Au(I) to Au(0) and Au(III).

Scheme 2.1. Latimer diagram for Au.

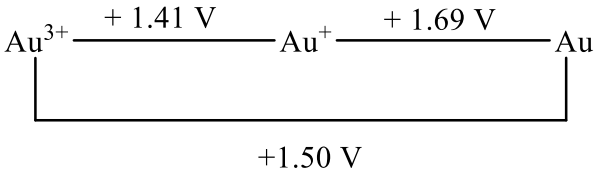

In order to stabilise Au(I) it is necessary to use appropriate ligands, such as halides, S or P based ligands, or N-Heterocyclic carbene ligands (NHC). Phosphines are the most efficient ones; indeed, $Au(PR_3)X$ (X = Cl, Br, I) complexes are stable at room temperature, in air, to the light, in solid and in solution. Conversely, complexes such as $[AuX_2]^-$, Au(CO)X and $Au(SR_2)X$ are less stable and they need to be stored in an inert atmosphere, in the darkness and/or at low temperature. Recently, the interest for NHCs as ligands in organometallic, inorganic, coordination chemistry and catalysis has considerably grown.[16] NHC ligands have been also employed for the stabilisation of metal nanoparticles (NPs) and ultra-small metal nanoparticles (UNPs),[17] whereas their use as ligands for molecular metal clusters was, up to now, limited.[18] However, NHC carbenes are very good ligands for Au(I) and they are entirely comparable to phosphines.

In general, metal-carbene complexes can be divided as follows:

- Fischer's carbene: they are characterised by a C-M bond with the metal in a low oxidation state linked to π acceptor ligands, and by π donor substituents at the C atom. Moreover, this displays the singlet electronic configuration that makes it a very good σ donor and a bad π acceptor. For this reason, the carbene C-atom presents electrophilic properties, becoming an excellent ligand for the late transition metals (Figure 2.2).

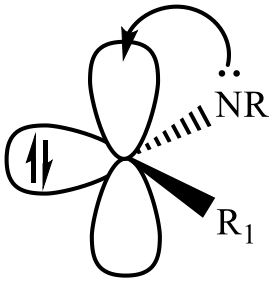

Figure 2.2 Representation of a Fischer's carbene.

- Schrock's carbenes: they are characterised by a C-M bond with a metal in a high oxidation state linked to non π acceptor ligands, and by non π donor substituents on the C atom. The lack of stability provided by the resonance effect induces a triplet state, which makes the C-M bond covalent and polarised towards the carbenic C, which becomes a nucleophile (Figure 2.3).

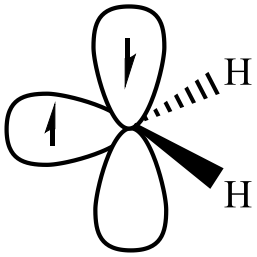

Figure 2.3 Representation of a Schrock's carbene.

NHC carbenes belong to the first group of carbene, the Fischer's ones (Figure 2.4). They are composed of a single C atom which is stabilised by two N atoms within a heterocyclic ring.[19]

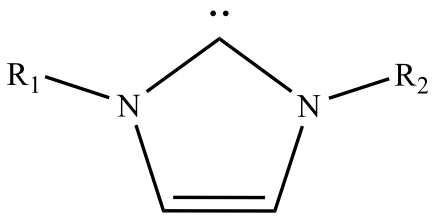

Figure 2.4 Representation of a generic NHC carbene.

NHC carbenes tend to form stable bonds, are more resistant to the heat and are less prone to oxidation than analogous ligands, like phosphines. Moreover, it is possible to modulate their chemical and steric properties by changing the substituents on the N atoms. They are very good σ donor and can stabilise metals in a low oxidation state with a low back-donation tendency, such as Au, Cu and Ag. NHC carbenes represent an important class of ligands for the metals of group 11 in the +1 oxidation state, by allowing the formation of several stable complexes.

Amongst these complexes, those of general formula M(NHC)Cl (M= Au, Cu, Ag) are the main focus of Chapters 2, 3 and 5. The use of these ligands in transition metal cluster compounds allows to study a very interesting type of interaction, that is the metallophilic ones. In particular, aurophilicity was investigated at first, in relation also to relativistic phenomena, followed by argentophilicity and cuprophilicity. Several homoleptic and heteroleptic carbonyl clusters containing 2-8 coinage metals (also mixed ones) supported by Fe, Co, Mo, V and Ru carbonyl moieties were reported.[20–24] These allowed to study the effects of the coinage metal, heterometal and ancillary ligands on the bonding within such heterometallic clusters.

In the framework of this Thesis, CO is the main ligand used to stabilise metals in a low oxidation state, except for Au. Indeed, Au does not form any neutral binary compound with CO. However, the neutral mixed Au(CO)Cl and the cationic $[Au(CO)_x]^+$ (x= 1-3) complexes are well-known, but all of them are not very stable. In general, the stabilisation of the M-CO interaction is guaranteed by the σ donation of the electron pair from CO to an empty orbital of M, and by the π back-donation of the electron density from the full orbitals of M to the anti-bonding orbitals of CO. This phenomenon stabilises the molecular structure and enforces the M-CO bond. Au is a metal with high ionisation energy and electronegativity, that prevent the π back-donation and destabilise M-CO bond. The reason why Au(CO)Cl and $[Au(CO)_x]^+$ (x= 1-3) complexes exist is due to the fact that Au(I) is a stronger σ-acid than Au(0), enforcing the σ donation while the π back-donation is almost absent.

The only way to synthesise Au-containing carbonyl clusters is by using a second metal with high affinity to CO. For these heterometallic systems, Fe is widely employed: indeed, it can form several carbonyl compounds, both neutral and anionic, by starting from a wide variety of reagents that can be easily prepared from $Fe(CO)_5$, which is a commercial product.

Au-Fe carbonyl clusters can be divided into three categories:

- Clusters containing only Au(I), Fe and CO: such as $[Au_4Fe_4(CO)_{16}]^{4-}$ and $[Au_5Fe_4(CO)_{16}]^{3-}$, which are composed by Au(I) ions exclusively bonded to $[Fe(CO)_4]^{2-}$ fragments.
- Clusters containing Au(I), Fe, CO and phosphines (or NHC ligands): such as $Fe(CO)_4(AuPPh_3)_2$, $[Au_3Fe_2(CO)_8(dppm)]^-$, $Au_4Fe_2(CO)_8(dppm)_2$, $[Au_5Fe_2(CO)_8(dppm)_2]^+$, $[Au_3Fe(CO)_4(dppm)_2]^+$ and $Fe_4C(CO)_{12}(AuPPh_3)_2$. These species are composed by Au(I) ions bonded to $[Fe(CO)_4]^{2-}$ fragments and phosphines.
- Clusters containing only Au(<I), Fe and CO: such as $[Au_{21}Fe_{10}(CO)_{40}]^{5-}$, $[Au_{22}Fe_{12}(CO)_{48}]^{6-}$, $[Au_{28}Fe_{14}(CO)_{52}]^{8-}$ and $[Au_{34}Fe_{14}(CO)_{50}]^{8-}$. These are metalloid nanoclusters where an Au_n

core is stabilised by $Fe(CO)_4$ and $Fe(CO)_3$ groups present on their surface. Au displays an oxidation state between +1 and 0.

Before this work, the number of Au-Fe carbonyl clusters containing NHC ligands was limited. In the past, my research group synthesised a few species, that is $Fe(CO)_4(AuNHC)_2$ (NHC = IMes, IPr, IBu; IMes = $C_3N_2H_2(C_6H_2Me_3)_2$; IPr = $C_3N_2H_2(C_6H_3{}^iPr_2)_2$; IBu = $C_3N_2H_2(CMe_3)_2$) and $[Au_3Fe_2(CO)_8(IMes)_2]^-$.[25]

Aiming at developing a general strategy for the preparation of bimetallic carbonyl clusters containing NHC ligands, we have considered the reactions of Au(NHC)Cl complexes with anionic metal carbonyl compounds. Herein, we report our results on Fe-Au clusters obtained by reacting the Collman's reagent $Na_2[Fe(CO)_4]\cdot 2thf$ with Au(NHC)Cl complexes. Depending on the stoichiometry of the reaction, neutral $Fe(CO)_4(AuNHC)_2$ and mono-anionic $[Fe(CO)_4(AuNHC)]^-$ clusters may be obtained. These, in turn, can be transformed into larger clusters *via* reactions with cationic complexes or thermal treatment. This entire work has been extended to Ag and Cu, in order to study all the metallophilic interactions and to investigate the similarities and the differences amongst the three coinage metals (Au, Cu and Ag) (see Chapter 3).

2.2 General results

The following Sections 2.3-2.6 report the synthesis and the characterisation of $[Fe(CO)_4(AuNHC)]^-$ (NHC = IMes, **1**; IPr, **2**), $Fe(CO)_4(AuNHC)_2$ (NHC = IMes, **3**; IPr, **4**), $Fe(CO)_4(AuIMes)(AuIPr)$ (**5**) and $Fe(CO)_4(AuNHC)(AuPPh_3)$ (NHC = IMes, **6**; IPr, **7**) clusters.

Moreover, the new $[Fe_2(CO)_8(AuNHC)]^-$ (NHC = IMes, **11**; IPr, **12**), $[Fe_3(CO)_{10}(CCH_3)]^-$ (**13**), $[Au_3Fe_3(CO)_{12}]^{3-}$ (**14**), $[Au_3\{Fe(CO)_4\}_2(PPh_3)_2]^-$ (**9**) and $[Au_{16}S\{Fe(CO)_4\}_4(IPr)_4]^{n+}$ (**18**) clusters deriving from the thermal decomposition of the previous compounds are presented in the Sections 2.7-2.8.

2.3 Synthesis and characterisation of $[Fe(CO)_4(AuNHC)]^-$ (NHC = IMes, 1; IPr, 2)

The reaction of the Collman's reagent $Na_2[Fe(CO)_4]\cdot 2thf$ with one equivalent of Au(NHC)Cl (NHC = IMes, IPr) in dmso resulted in the $[Fe(CO)_4(AuNHC)]^-$ (NHC = IMes, **1**; IPr, **2**; IMes = $C_3N_2H_2(C_6H_2Me_3)_2$; IPr = $C_3N_2H_2(C_6H_3{}^iPr_2)_2$) mono-anions in accord to the equation (2.1):

$$Na_2[Fe(CO)_4]\cdot 2thf + Au(NHC)Cl \xrightarrow[2.\ [NEt_4]Br + H_2O]{1.\ dmso,\ RT} [NEt_4][Fe(CO)_4(AuNHC)] \quad \begin{matrix} NHC = IMes\ \mathbf{1} \\ IPr\ \ \mathbf{2} \end{matrix} \qquad (2.1)$$

The reactions were monitored by means of IR spectroscopy, by adding Au(NHC)Cl in small portions to the $Na_2[Fe(CO)_4]\cdot 2thf$ solution, up to the complete disappearance of the signal at 1740 cm^{-1}, due to the Collman's reagent.

Then, the mono-anionic species **1** and **2** were isolated as $[NEt_4]^+$ salts, washed with water and toluene in order to remove the excess of cation and neutral species, such as $Fe(CO)_4(AuNHC)_2$ (NHC = IMes, **3**; IPr, **4**). Crystals of $[NEt_4][\mathbf{1}]$ and $[NEt_4][\mathbf{2}]$ were obtained by slow diffusion of *n*-hexane into their acetone solutions. Both were characterised by means of IR, ^1H NMR and $^{13}C\{^1H\}$ NMR spectroscopy, and their structures determined by X-ray crystallography.

IR spectra of **1** and **2** in CH_3CN solutions are similar and show ν_{CO} bands at 1927 cm^{-1} and 1821 cm^{-1}, and 1926 cm^{-1} and 1819 cm^{-1} for **1** and **2**, respectively. According to the -1 charge of the clusters, their ν_{CO} bands are intermediate between those of $[Fe(CO)_4]^{2-}$ (1740 cm^{-1}) and $Fe(CO)_4(AuNHC)_2$ (1974 and 1884 cm^{-1}).

^1H and $^{13}C\{^1H\}$ NMR spectra of **1** and **2** show the typical resonances related to NHC and CO ligands, according to the cluster structures. In particular, in the ^1H NMR spectrum of **1** there are: two singlets in the aromatic region due to the presence of four equivalent aromatic protons and two imidazoles protons; one singlet for the two *p*-CH_3 and one singlet for the four *o*-CH_{3g} groups, and two broad resonances for the cation. This broadening is due to paramagnetic impurities, which are often present in Fe-CO compounds. The same effect can be observed in the ^1H NMR spectrum of **2**. Nevertheless, it is possible to assign all the signals in accordance to the molecular structure of the compound. Finally, $^{13}C\{^1H\}$ NMR spectra confirm the presences of CO and NHC bonded to Fe and Au, respectively. The Au-coordinated carbene resonates in the $^{13}C\{^1H\}$ NMR spectra at δ_C 196.3 and 198.3 ppm for **1** and **2**, respectively. A singlet was present at all temperatures in the CO region of the $^{13}C\{^1H\}$ NMR spectra of the two species, suggesting a fluxional behaviour for the carbonyl ligands. This rapid exchange process made the equatorial and apical CO ligands equivalent also at low temperature.

Although **1** and **2** present almost identical ν_{CO} frequencies, IMes and IPr-containing species show a different reactivity, that should be attributed mainly to steric effects. This prompted a computational investigation, whose results are described at the end of this Section.

Crystal structures

The molecular structures of **1** and **2** have been determined as their $[NEt_4]^+$ salts (Figure 2.5 and Table 2.2). The mono-anions **1** and **2** adopted a trigonal bipyramidal structure, with the AuNHC

fragment in an axial position. **1** and **2** contained strong Au-Fe, Fe-C(O) and Au-$C_{carbene}$ interactions as well as some weak Au···C(O) contacts (see Table 2.2). Regarding the latter contacts, their detection in the solid state structures could merely be the consequence of the preferred arrangement of the CO ligands about the Fe centre, which brings the CO ligands in closer proximity to the Au centre, rather than any attraction (even van der Waals) between the carbonyls and Au.

The Au-Fe distances [2.50-2.52 Å] found in these mono-anionic complexes were very similar to those previously reported for the neutral complexes $Fe(CO)_4(AuNHC)_2$ [2.51-2.53 Å] (Table 2.3).

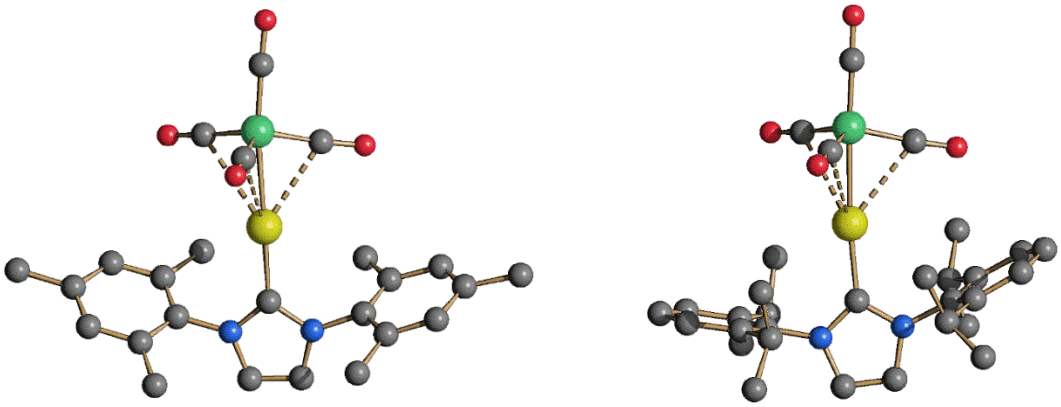

(a) (b)

Figure 2.5 Molecular structures of (a) $[Fe(CO)_4(AuIMes)]^-$ (**1**) and (b) $[Fe(CO)_4(AuIPr)]^-$ (**2**). Au-C(O) contacts [2.630(4)-2.900(4) Å for **1**; 2.688(4)-2.805(3) Å for **2**] are represented as fragmented lines. Hydrogen atoms have been omitted for clarity (green, Fe; yellow, Au; blue, N; red, O; grey, C).[26]

Table 2.2 Main bond distances (Å) and angles (°) of $[Fe(CO)_4(AuIMes)]^-$ (**1**) and $[Fe(CO)_4(AuIPr)]^-$ (**2**).

	$[Fe(CO)_4(AuIMes)]^-$	**$[Fe(CO)_4(AuIPr)]^-$**
Fe-Au	2.5244(6)	2.5015(4)
Au-$C_{carbene}$	2.029(4)	2.019(2)
Fe-C(O)	1.755(5)-1.780(4)	1.757(3)-1.778(3)
Au···C(O)	2.565(5)-2.931(4)	2.688(4)-2.805(3)
Fe-Au-$C_{carbene}$	174.96(11)	175.21(7)

Computational studies

The space occupied by the NHC ligands in the first coordination sphere of gold can be described by the buried volume, $\%V_{Bur.}$ The calculated $\%V_{Bur}$ values for IMes and IPr in the DFT-optimised structures of **1** and **2** were respectively 36.0% and 42.9%, and the different reactivity of the IPr

derivatives was probably related to the higher $\%V_{Bur}$. Figure 2.6 shows plots of the electron density surfaces for **1** and **2**. The LUMO of the complexes were localised on the carbene donor atom and on gold, and in the case of NHC = IPr the substituents seemed to better protect the unoccupied orbital from incoming nucleophiles. We might therefore conclude that the different stability observed could be ascribed to the different reactivity of the Au-NHC groups on changing the bulkiness of the carbene substituents. For what concerns the Au···CO, the electron density minima between gold and carbon are comprised between $0.35 \cdot 10^{-1}$ and $0.39 \cdot 10^{-1}$ a.u. in **1** and **2** and suggest the lack of Au-CO bonds.

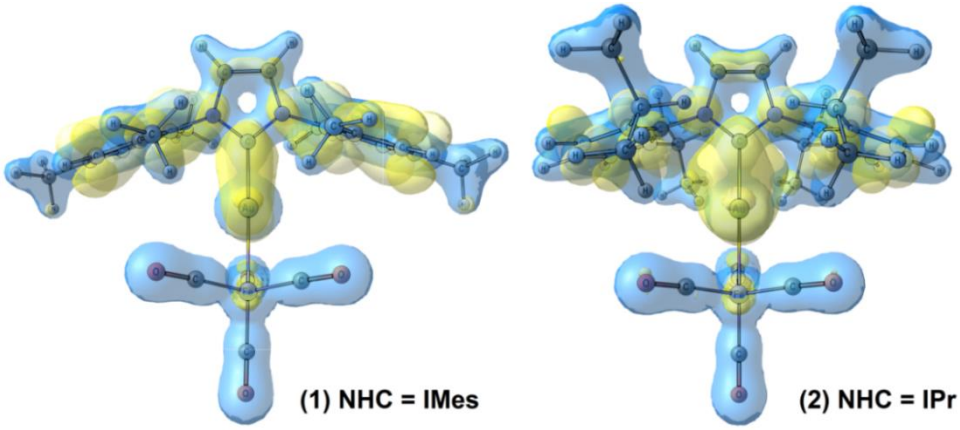

Figure 2.6 Electron density surfaces (light blue, isovalue = 0.1 a.u.) and LUMOs (yellow tones, isovalue = 0.03 a.u.) for compounds **1** and **2**. The high isovalue for electron density surfaces was chosen to make the plot clear.[26]

2.4 Synthesis and characterisation of $Fe(CO)_4(AuNHC)_2$ (NHC = IMes, 3; IPr, 4)

The reaction between the mono-anion $[NEt_4][Fe(CO)_4(AuNHC)]$ and one equivalent of Au(NHC)Cl leads to the formation of the bimetallic $Fe(CO)_4(AuNHC)_2$ (NHC = IMes, **3**; IPr, **4**) clusters in accord to the equation (2.2):

$$[NEt_4][Fe(CO)_4(AuNHC)] + Au(NHC)Cl \xrightarrow[\text{Acetone, RT}]{} Fe(CO)_4(AuNHC)_2 \quad \text{NHC = IMes } \mathbf{3},\ \text{IPr } \mathbf{4} \tag{2.2}$$

Alternatively, as previously reported,[25] **3** and **4** may be obtained by reacting the Collman's reagent $Na_2[Fe(CO)_4]\cdot 2thf$ with two equivalents of Au(NHC)Cl (NHC = IMes, IPr) in thf, in accord to equation (2.3):

$$Na_2[Fe(CO)_4]\cdot 2thf + 2Au(NHC)Cl \xrightarrow[\text{thf, RT}]{} Fe(CO)_4(AuNHC)_2 \quad \text{NHC = IMes } \mathbf{3},\ \text{IPr } \mathbf{4} \tag{2.3}$$

Crystals of **4** suitable for X-ray crystallography were obtained after work up by slow diffusion of *n*-pentane on the toluene solution, whereas crystals of **3** were obtained by slow diffusion of *n*-hexane into its thf solution. Both compounds were characterised by means of IR, ^{1}H NMR and ^{13}C{^{1}H} NMR spectroscopy, and their structures determined by X-ray crystallography.

Compounds **3** and **4** displayed ν_{CO} bands in acetone solution at ca. 1974(s) and 1884(vs) cm^{-1}, considerably shifted towards higher wavenumbers compared to **1** and **2** (ν_{CO} 1924(s) and 1820(vs) cm^{-1}) in view of their neutral charges. In the ^{13}C{^{1}H} NMR spectra, the neutral complexes **3** and **4** displayed carbene resonances at very similar chemical shifts to **1** and **2**, that is 194.5 and 194.3 ppm, respectively.

Crystal structures

The molecular structures of **3** and **4** have been determined by means of X-ray crystallography (Figure 2.7 and Table 2.3). **3** and **4** are composed of a C_{2v}-Fe(CO)$_4$ sawhorse/seesaw unit coordinated to two AuNHC fragments in relative *cis* position. Their structures are similar to that previously reported for Fe(CO)$_4$(AuPPh$_3$)$_2$ (**8**).[27–29] The Fe-Au [2.5158(15) and 2.5312(15) Å (**3**); 2.512(2) and 2.524(2) Å (**4**)] and Fe-CO [1.756(13)-1.783(13) Å (**3**); 1.737(15)-1.781(15) Å (**4**)] distances are very similar to those reported for **8** [2.522-2.553 and 1.73-1.79 Å, respectively]. **3** displays also a weak aurophilic Au···Au interaction [3.2015(8) Å] as well as four sub-van der Waals Au···C(O) contacts [2.609(12)–2.764(13) Å]. Conversely, the Au···Au distance of **4** [4.082(1) Å] is completely non-bonding and six sub-van der Waals Au···C(O) contacts are present [2.572(14)-2.873(18) Å]. The long Au···Au contact found in **3** may be ascribed to the presence of the bulky IMes ligand, whereas the presence of the even bulkier IPr ligand in **4** causes the complete loss of any Au···Au interaction.[30] The Au–Fe-Au angle increases by increasing the Au···Au distance in the series. The Au–C(NHC) distances agree with those previously reported for other Au(I)NHC complexes.[25]

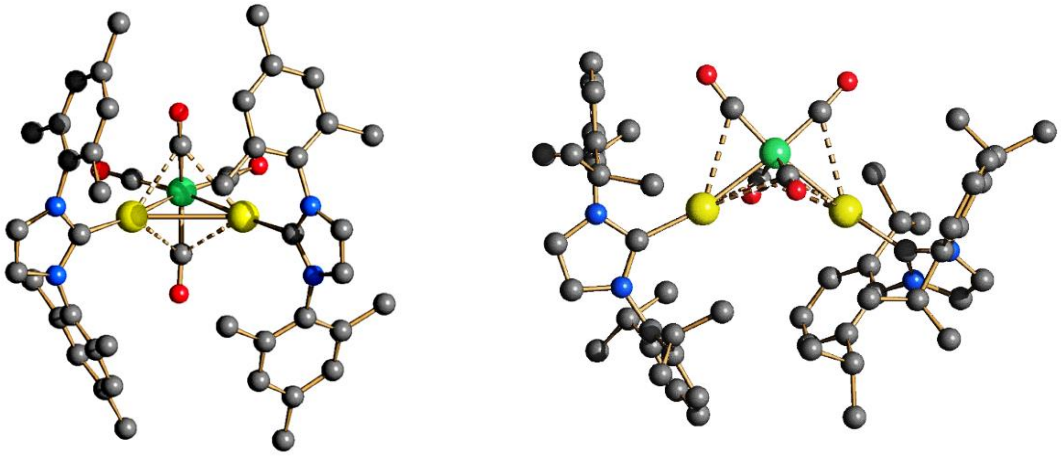

(a) (b)

Figure 2.7 Molecular structures of (a) $Fe(CO)_4(AuIMes)_2$ (**3**) and (b) $Fe(CO)_4(AuIPr)_2$ (**4**). Au-C(O) contacts [2.609(12)–2.764(13) Å for 3; 2.572(14)–2.873(18) Å for 4] are represented as fragmented lines. Hydrogen atoms have been omitted for clarity (green, Fe; yellow, Au; blue, N; red, O; grey, C).[25]

Table 2.3 Main bond distances (Å) and angles (deg) of $Fe(CO)_4(AuIMes)_2$ (**3**) and $Fe(CO)_4(AuIPr)_2$ (**4**).

	$Fe(CO)_4(AuIMes)_2$	**$Fe(CO)_4(AuIPr)_2$**
Au(1)-Fe(1)	2.5158(15)	2.512(2)
Au(2)-Fe(1)	2.5312(15)	2.524(2)
Au(1)-Au(2)	3.2015(8)	4.082(1)
Au(1)-X(1)	2.008(10)	2.012(11)
Au(2)-X(2)	2.020(10)	1.949(14)
Fe(1)-CO	1.756(13)-1.783(13)	1.737(15)-1.781(15)
Au···C(O)	2.609(12)-2.764(13)	2.572(14)-2.873(18)
Fe(1)-Au(1)-X(1)	177.8(3)	168.3(3)
Fe(1)-Au(2)-X(2)	165.9(3)	168.4(5)
Au(1)-Fe(1)-Au(2)	78.74(4)	107.90(9)
Fe(1)-Au(1)-Au(2)	50.84(4)	36.15(5)
Fe(1)-Au(2)-Au(1)	50.42(3)	35.95(5)

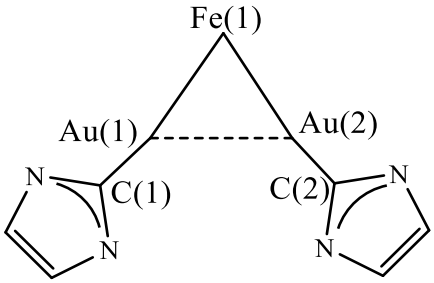

2.5 Syntheses and characterisation of $Fe(CO)_4(AuIMes)(AuIPr)$ (5) and $Fe(CO)_4(AuNHC)(AuPPh_3)$ (NHC = IMes, 6; IPr, 7)

Scheme 2.2 shows the different reaction paths for the synthesis of the neutral complexes $Fe(CO)_4(AuNHC)_2$ (NHC = IMes, **3**; IPr, **4**), $Fe(CO)_4(AuIMes)(AuIPr)$ (**5**) and $Fe(CO)_4(AuNHC)(AuPPh_3)$ (NHC = IMes, **6**; IPr, **7**), by starting from the Collman's reagent.

The mixed complex **5** was obtained by adding Au(IMes)Cl to a solution of **2** in acetone. The formation of the neutral mixed complex was confirmed by the comparison of its IR spectrum with those of **3** and **4**. An unique resonance was observed in the $^{13}C\{^1H\}$ NMR spectrum of **5** at δ_C 217.8 ppm for the CO ligands, whereas two distinct resonances were observed in the Au-$C_{carbene}$ region (δ_C 195.1 and 193.7 ppm) in view of the presence of both AuIMes and AuIPr fragments. Similarly, **6** and **7** were obtained from the reaction of **1** and **2** with $Au(PPh_3)Cl$.

Scheme 2.2 Syntheses of the neutral complexes **3**-**7**.

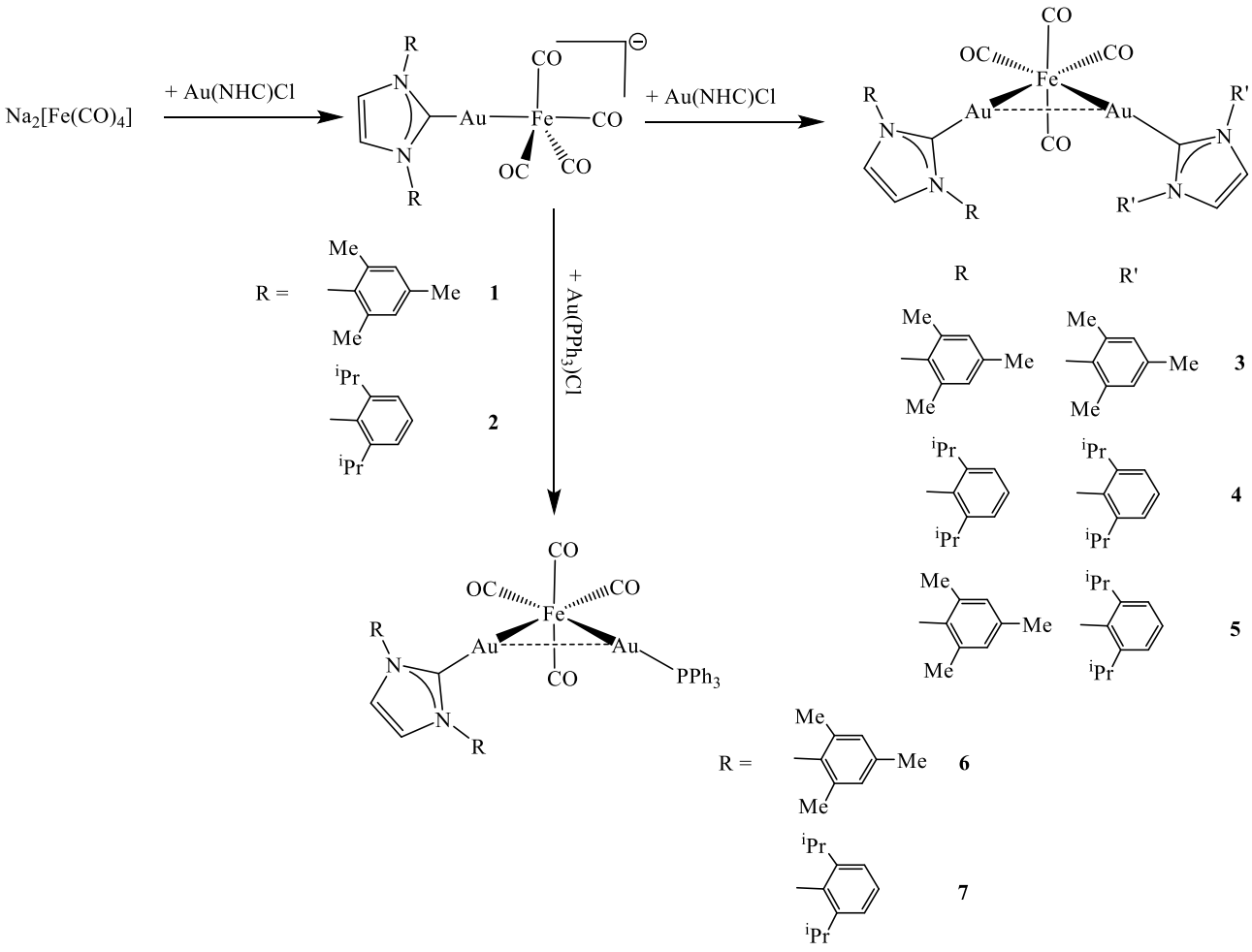

Crystal structures

Crystals of **6** and **7** suitable for X-ray crystallography were obtained by slow diffusion of *n*-pentane on their CH_2Cl_2 solutions (Figures 2.8-2.9 and Table 2.4).

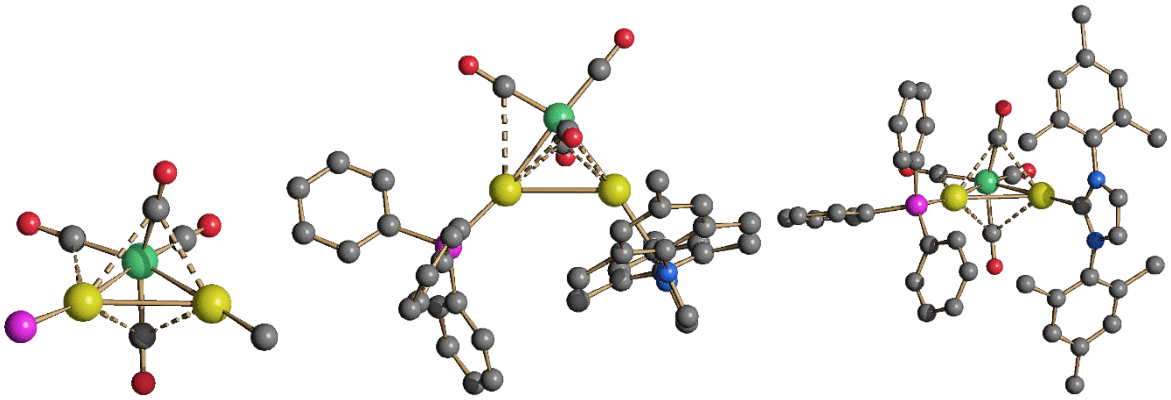

Figure 2.8 Molecular structure of $Fe(CO)_4(AuIMes)(AuPPh_3)$ (**6**). Two different views as well as its core are reported. Au-C(O) contacts [2.621(8)-2.885(7) Å] are represented as fragmented lines. Hydrogen atoms have been omitted for clarity (green, Fe; yellow, Au; purple, P; blue, N; red, O; grey, C).[26]

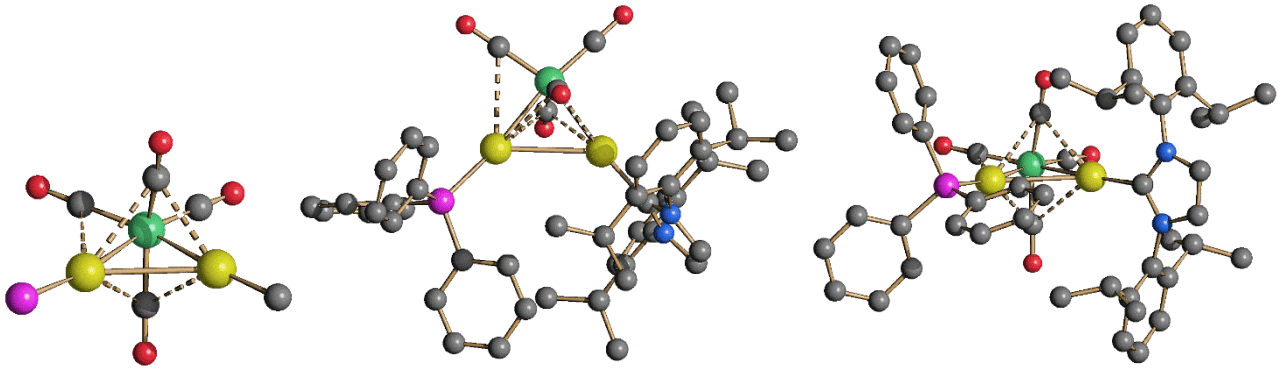

Figure 2.9 Molecular structure of $Fe(CO)_4(AuIPr)(AuPPh_3)$ (**7**). Two different views as well as its core are reported. Au-C(O) contacts [2.573(3)-2.955(3) Å] are represented as fragmented lines. Hydrogen atoms have been omitted for clarity (green, Fe; yellow, Au; purple, P; blue, N; red, O; grey, C).[26]

These two new species, containing both an AuNHC and $AuPPh_3$ fragment, display very similar spectroscopic features. They are composed of a C_{2v}-$Fe(CO)_4$ sawhorse/seesaw unit coordinated to one AuNHC and one $AuPPh_3$ fragment in relative *cis* position. The structures of **6** and **7** are similar to those reported for the homoleptic complexes **3**, **4** and $Fe(CO)_4(AuPPh_3)_2$ (**8**).[25,27] The Au···Au contacts [3.0471(4) Å for **6**, 3.0479(2) Å for **7**] were indicative of weak aurophilic interactions, which were intermediate between those found in **8** [2.8750(3)-3.0698(2) Å, depending of the polymorph] and **3** [3.2015(8) Å]. The fact that the Au···Au distance was strongly affected by the steric properties of the Au-bonded ligands as well as packing effects pointed out that

such aurophilic interactions were rather deformable. In particular, the Au···Au distance increased with the increasing bulkiness of the ligands when passing from PPh_3 to IMes and eventually IPr. All complexes **3**, **4** and **6**-**8** display also some sub-van der Waals Au···C(O) contacts.

Table 2.4 Main bond distances (Å) and angles (deg) of $Fe(CO)_4(AuIMes)_2$ (**3**), $Fe(CO)_4(AuIPr)_2$ (**4**), $Fe(CO)_4(AuIMes)(AuPPh_3)$ (**6**), $Fe(CO)_4(AuIPr)(AuPPh_3)$ (**7**) and $Fe(CO)_4(AuPPh_3)_2$ (**8**).

	3 [a]	**4** [a]	**4** [b]	**6**	**7**	**8** [c]	**8** [d]
Au(1)-Fe(1)	2.5158(15)	2.512(2)	2.5203(9)	2.5471(9)	2.5371(4)	2.5344(6)	2.5329(4)
Au(2)-Fe(1)	2.5312(15)	2.524(2)	2.5326(9)	2.5089(9)	2.5107(4)	2.5555(6)	2.5181(4)
Au(1)-Au(2)	3.2015(8)	4.082(1)	3.984(1)	3.0471(4)	3.0479(2)	2.8750(3)	3.0698(2)
Au(1)-X(1)	2.008(10)	2.012(11)	2.018(6)	2.020(6)	2.011(3)	2.2696(10)	2.2756(7)
Au(2)-X(2)	2.020(10)	1.949(14)	2.023(6)	2.2661(16)	2.2621(8)	2.2707(10)	2.2646(7)
Fe(1)-CO	1.756(13)-1.783(13)	1.737(15)-1.781(15)	1.727(8)-1.769(8)	1.768(8)-1.777(8)	1.772(3)-1.786(3)	1.787(4)-1.800(4)	1.772(3)-1.790(3)
Au···C(O)	2.609(12)-2.764(13)	2.572(14)-2.873(18)	2.629(7)-2.827(8)	2.621(8)-2.885(7)	2.573(3)-2.955(3)	2.604(6)-3.069(5)	2.638(3)-3.050(3)
Fe(1)-Au(1)-X(1)	177.8(3)	168.3(3)	172.75(18)	175.77(17)	174.65(8)	172.02(3)	177.55(2)
Fe(1)-Au(2)-X(2)	165.9(3)	168.4(5)	168.16(17)	170.15(5)	171.12(2)	173.45(3)	173.71(2)
Au(1)-Fe(1)-Au(2)	78.74(4)	107.90(9)	104.08(3)	74.12(3)	74.284(12)	68.781(14)	74.855(12)
Fe(1)-Au(1)-Au(2)	50.84(4)	36.15(5)	38.07(2)	52.37(2)	52.462(10)	55.956(13)	52.354(10)
Fe(1)-Au(2)-Au(1)	50.42(3)	35.95(5)	37.85(2)	53.51(2)	53.254(10)	55.263(13)	52.791(9)

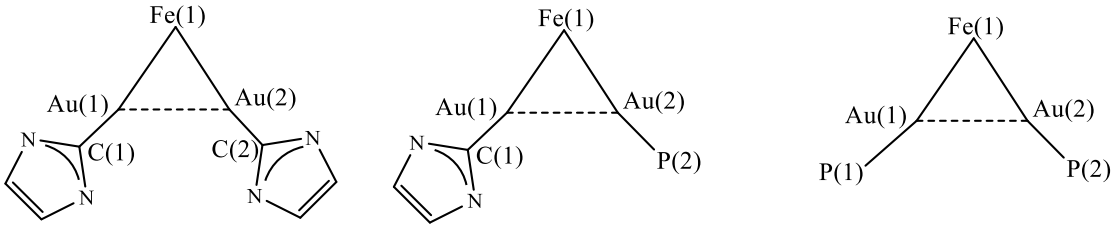

[a] See ref. [25] [b]As found in $Fe(CO)_4(AuIPr)_2 \cdot 1.5$toluene. [c] As found in $Fe(CO)_4(AuPPh_3)_2$ ($P\bar{1}$). [d] As found in $Fe(CO)_4(AuPPh_3)_2$ ($P2_1/n$).

2.6 Reactivity of $Fe(CO)_4(AuNHC)(AuPPh_3)$ (NHC = IMes, 6; IPr, 7)

Despite the structural analogies between **6** and **7**, their chemical behaviour is rather different. **7** is very stable and can be easily obtained in a very pure form, as indicated by the presence of a single resonance at δ_P 40.8 ppm in the $^{31}P\{^1H\}$ NMR spectrum. Conversely, **6** is less stable and its synthesis is not so straightforward. Thus, it was often obtained in mixtures with minor amounts of **8** and the new compound $[Au_3\{Fe(CO)_4\}_2(AuPPh_3)_2]^-$ (**9**) (see Section 2.7), as evidenced by the

presence of three distinct resonances in the $^{31}P\{^{1}H\}$ NMR spectrum at δ_P 40.8 ppm (**6**), 40.1 ppm (**8**) and 38.5 ppm (**9**).

In more detail, the addition of increasing amounts of $Au(PPh_3)Cl$ to an acetone solution of **1** results in the partial substitution of the AuIMes fragment with $AuPPh_3$ (Scheme 2.3). Thus, after the addition of one equivalent of $Au(PPh_3)Cl$ a mixture of $[Fe(CO)_4(AuPPh_3)]^-$ (**10**) (major) and **1** (minor) is present in solution. Further addition of $Au(PPh_3)Cl$ results in the formation of the neutral species $Fe(CO)_4(AuPPh_3)_2$ (**8**) as the major product. Compound **8** was spectroscopically detected and, moreover, its molecular structure was corroborated by X-ray crystallography on two new polymorphs, that are $Fe(CO)_4(AuPPh_3)_2$ ($P\bar{1}$) and $Fe(CO)_4(AuPPh_3)_2$ ($P2_1/n$).

Scheme 2.3 Reactivity of **1** and **3** with $Au(PPh_3)Cl$.

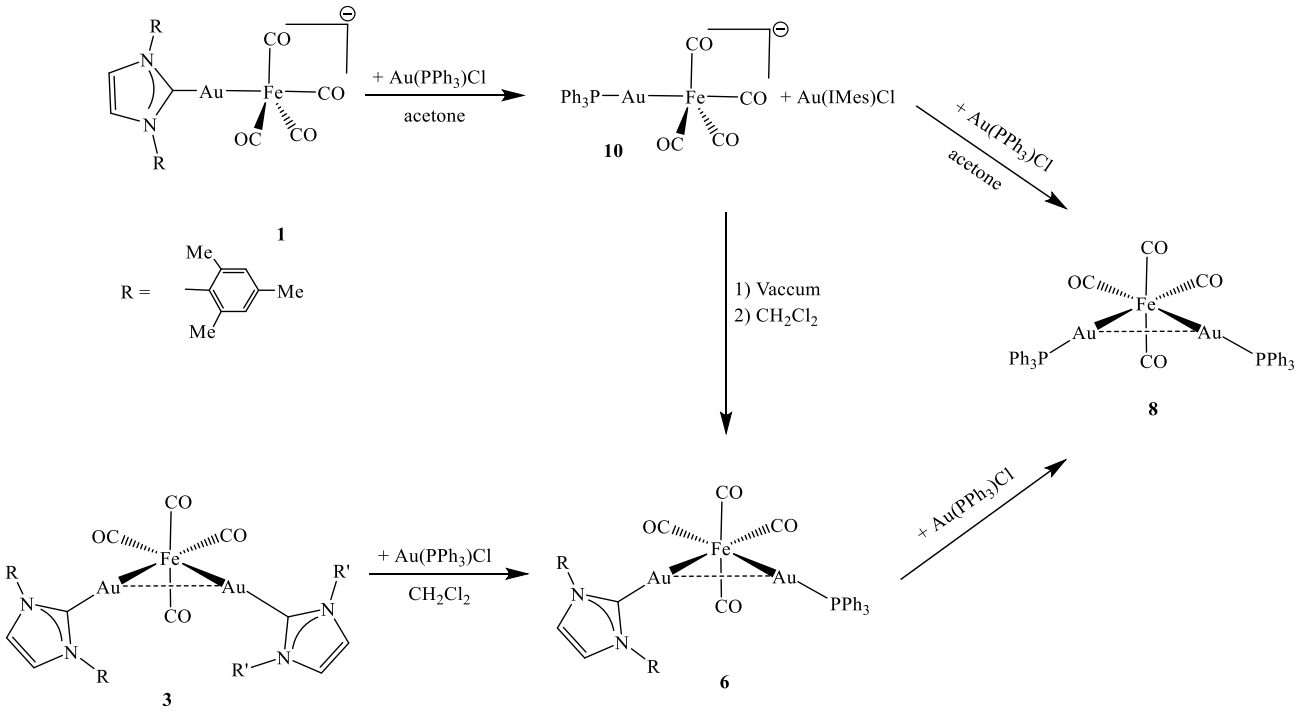

Concerning the ability of the $AuPPh_3$ fragment to replace AuIMes in the coordination sphere of $Fe(CO)_4$, this suggests that the $AuPPh_3$ fragment is more electrophilic than AuIMes. To demonstrate this point, **3** was reacted with increasing amounts of $Au(PPh_3)Cl$. As a result, **6** and then, **8** were formed in sequence. During this study, a few crystals of $[Au(IMes)_2][Fe_2(CO)_8(AuPPh_3)]\cdot CH_2Cl_2$ were obtained and characterised by single crystal X-ray crystallography. It is likely that some $[Fe_2(CO)_8]^{2-}$ was formed by oxidation of $[Fe(CO)_4]^{2-}$ at some stage of the reaction that, eventually, reacted with $Au(PPh_3)Cl$. The structure of the $[Fe_2(CO)_8(AuPPh_3)]^-$ mono-anion was previously reported as $[NEt_4]^+$ salt,[29] displaying almost

identical geometry and bonding parameters. It must be remarked that **8** did not react with Au(IMes)Cl even when used in large excess.

Therefore, the best way in order to obtain **6** is to mix **1** and $Au(PPh_3)Cl$ in a 1:1 ratio in acetone, remove the solvent *in vacuum* and let the reaction to continue in CH_2Cl_2. This allows to obtain **6** in a pure crystalline form, after slow diffusion of *n*-pentane. Conversely, the reaction of **2** with $Au(PPh_3)Cl$ directly affords **7**, without any evidence of the formation of **10**. Only after the addition of a slight excess of $Au(PPh_3)Cl$, **7** was eventually transformed into **8** (Scheme 2.4).

Scheme 2.4 Reactivity of **2** with $Au(PPh_3)Cl$.

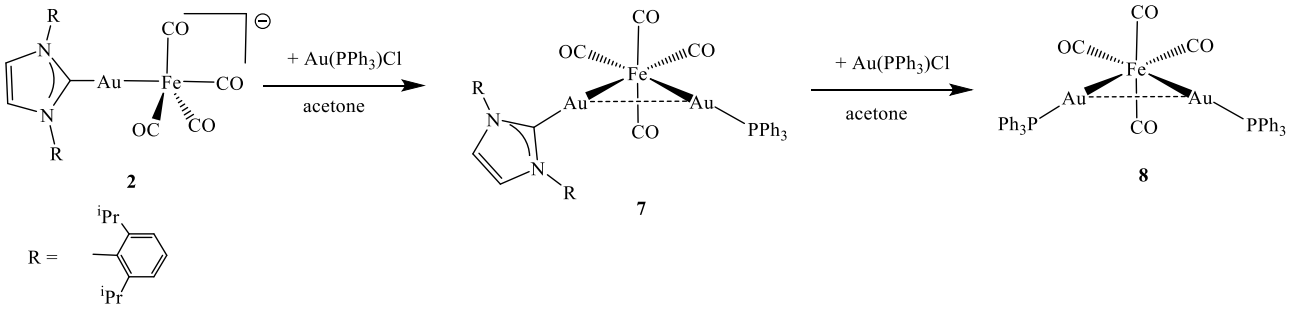

From a mechanistic point of view, the substitution reaction, which transformed **1** into **10** (Scheme 2.3), was likely to proceed *via* an associative mechanism involving **6** as an intermediate. Since **6** was not very stable in polar solvents such as acetone, it rapidly dissociated a $[Au(IMes)]^+$ fragment, affording **10** as the major product. Therefore, in order to favour the formation of **6**, a less polar solvent such as CH_2Cl_2 must be employed in order to hamper the dissociation. Conversely, because of the greater stability of **7** compared to **6**, addition was observed rather than substitution, regardless of the solvent employed.

To address the point of whether in some cases the whole AuL (L = NHC, PPh_3) fragment migrates or only the ligand L, **3** and **4** were reacted with increasing amounts of PPh_3 and the reaction monitored *via* IR and ^{31}P NMR spectroscopies. No reaction was observed, suggesting that substitution of the whole Au(NHC) fragment by $AuPPh_3$ occurred.

2.7 Synthesis and characterisation of $[Au_3\{Fe(CO)_4\}_2(PPh_3)_2]^-$ (9)

The mixed neutral species $Fe(CO)_4(AuIMes)(AuPPh_3)$ (**6**) was not very stable in polar solvents already at room temperature. Indeed, its $^{31}P\{^1H\}$ NMR spectrum in CD_3COCD_3 solution displayed a major resonance at δ_P 40.8 ppm attributable to **6**, accompanied by minor resonances at 40.1 ppm

and 38.5 ppm (spectrum (a) Figure 2.10). These resonances corresponded to $Fe(CO)_4(AuPPh_3)_2$ (**8**) and the new species **9**, respectively. The former was a by-product of the synthesis of **6** as previously reported,[26] whereas the formation of **9** arose from partial decomposition (ionisation) of **6**. Indeed, after heating this mixture in CH_3CN at 80 °C for 3 h, the resonance at δ_P 40.8 ppm considerably decreased, whereas the resonance at δ_P 38.5 ppm became the major one (spectrum (b) Figure 2.10). This indicated an almost complete conversion of **6** into **9**. This new compound was completely characterised by means of IR, ^1H, $^{13}C\{^1H\}$ and $^{31}P\{^1H\}$ NMR spectroscopy.

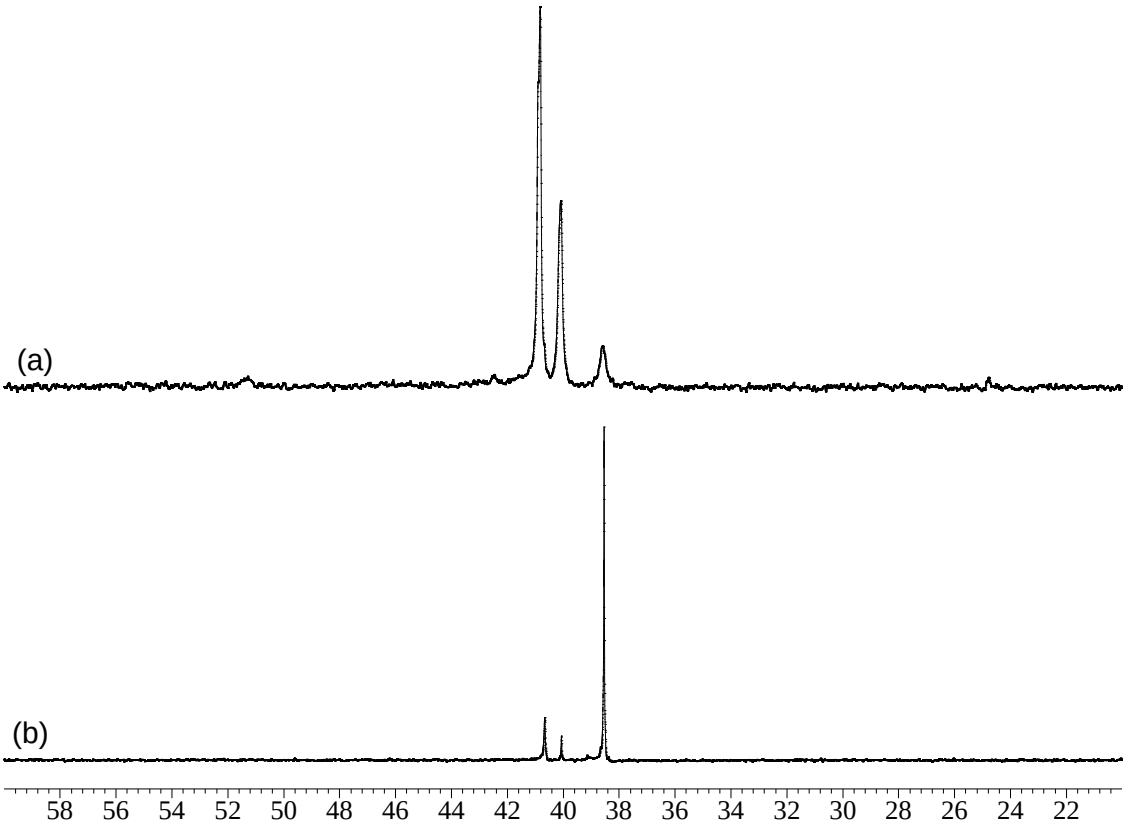

Figure 2.10 $^{31}P\{^1H\}$ NMR spectra in CD_3COCD_3 at 298 K of (a) $Fe(CO)_4(AuIMes)(AuPPh_3)$ (**6**) and (b) the mixture obtained after thermal treatment of **6**. The three resonances at δ_P 40.8, 40.1 and 38.5 ppm in (a) and (b) corresponded to **6**, **8** and **9**, respectively.

Crystal structure

The molecular structure of **9** was determined by single crystal X-ray diffraction as its $[Au(IMes)_2][\mathbf{9}]\cdot 0.67CH_2Cl_2$ salt (Figures 2.11-2.12). The latter was composed of $[Au(IMes)_2]^+$ cations and $[Au_3\{Fe(CO)_4\}_2(PPh_3)_2]^-$ anions (**9**), in accord to equation (2.4).

$$\underset{\mathbf{6}}{2Fe(CO)_4(AuIMes)(AuPPh_3)} \longrightarrow [Au(IMes)_2]^+ + \underset{\mathbf{9}}{[Au_3\{Fe(CO)_4\}_2(PPh_3)_2]^-} \qquad (2.4)$$

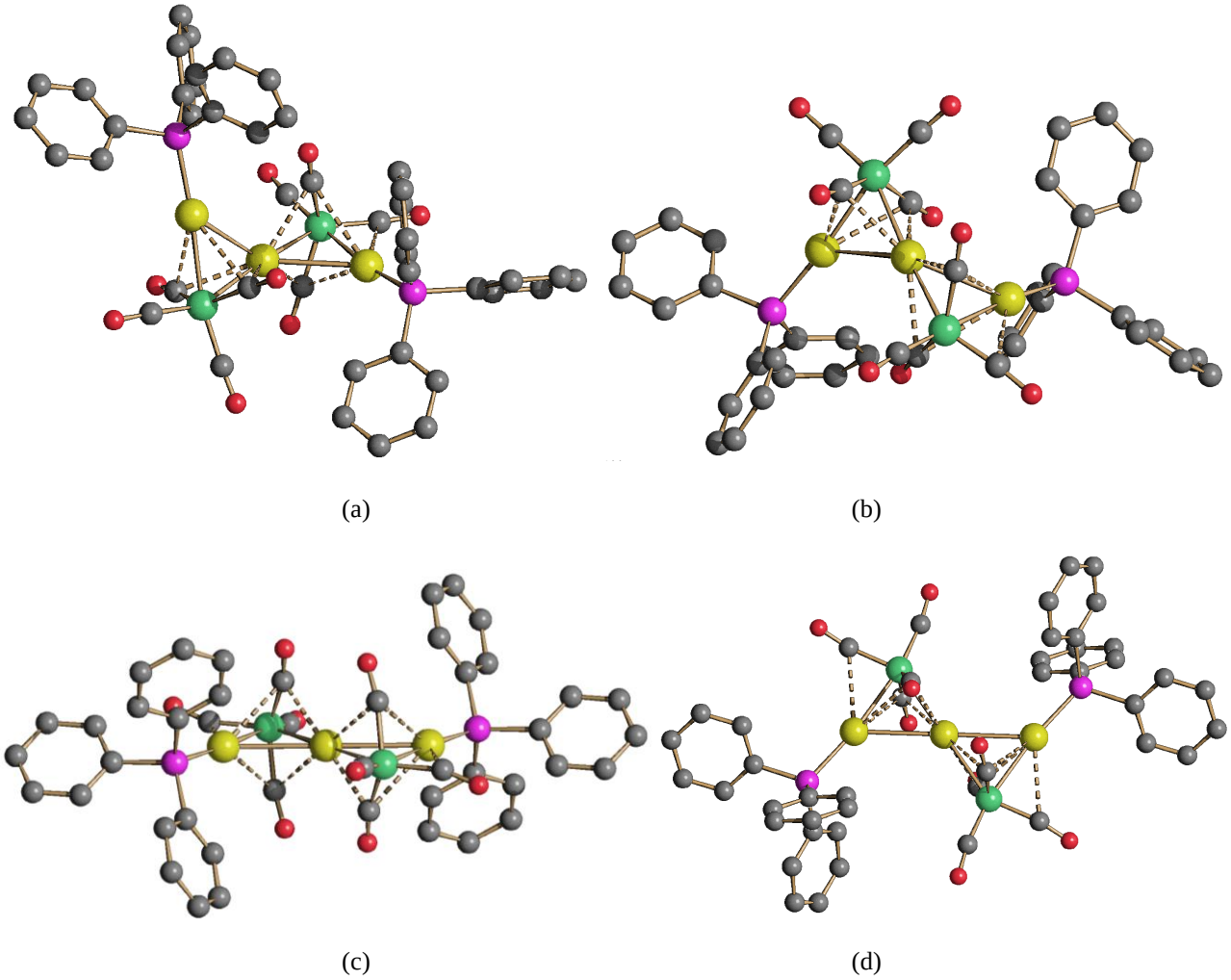

Figure 2.11 Molecular structures of the two isomers of **9**. The two isomers were present within the crystal in the ratio **9a:9b** = 2:1. Two views of isomer **9a** are reported in (a) and (b), two views of isomer **9b** are reported in (c) and (d). Au-C(O) contacts [2.34(6)-2.87(8)Å for **9a**; 2.56(3)-2.89(3) Å for **9b**] were represented as fragmented lines. Hydrogen atoms have been omitted for clarity (green, Fe; yellow, Au; purple, P; blue, N; red, O; grey, C).[31]

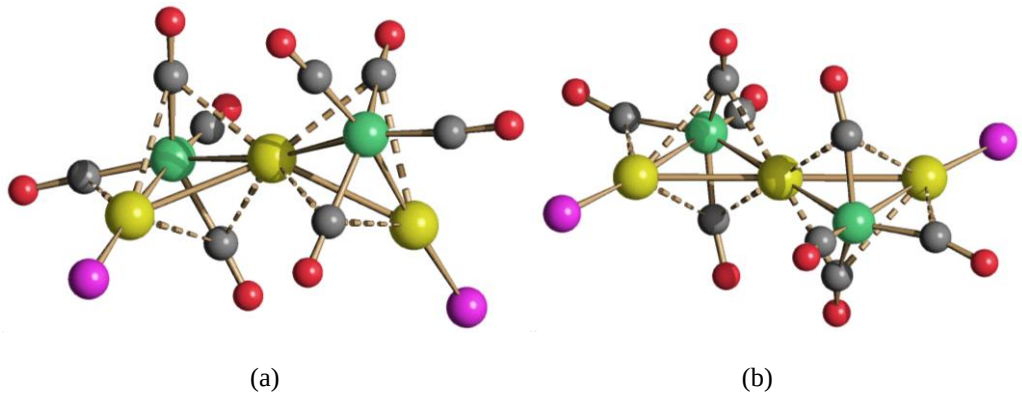

Figure 2.12 The $Au_3Fe_2(CO)_8P_2$ cores of (a) **9a** and (b) **9b** (green, Fe; yellow, Au; purple, P; red, O; grey, C).[31]

Within the crystals of $[Au(IMes)_2][\mathbf{9}]\cdot 0.67CH_2Cl_2$, two isomers of the anion **9** were present in a 2:1 ratio (referred as isomers **9a** and **9b**, respectively). Both isomers were composed of an Au_3 core bonded to two μ-$Fe(CO)_4$ units and two terminal PPh_3 ligands. The Au_3 core of **9a** displayed a V-shaped geometry [<Au-Au-Au 132.00(4)°], whereas it adopted a linear arrangement in **9b** with the central Au atom located on an inversion centre [<Au-Au-Au 180.00(10)°]. The structure of the isomer **9b** was similar to that previously reported for **15**.[25] Both isomers displayed two aurophilic Au···Au contacts [2.9353(13) and 2.8855(14) Å for **9a**; 2.9177(14) and 2.9177(14) Å for **9b**] as well as sub-van der Waals Au···C(O) contacts [2.34(6)-2.87(8) Å for **9a**; 2.56(3)-2.89(3) Å for **9b**].

The presence in the solid state of two isomers of **9** prompted a variable temperature $^{31}P\{^1H\}$ NMR investigation. Unfortunately, a single resonance was observed at all the temperatures examined (193-298 K) suggesting a fast exchange between **9a** and **9b** in solution.

The structures of **9a** and **9b** were also optimised by means of DFT calculations. The RMSD (Root Mean Square Deviation) of the computed $[Fe_2Au_3]$ cores with respect to the experimental data were 0.129 and 0.064 Å respectively for **9a** and **9b**. The deviations were mainly attributable to a slight overestimation of the Au−Au distances, caused by the known weakness of DFT methods in predicting dispersion interactions such as the aurophilic one. Despite this limit, the computed energy difference between the two isomers was 0.9 kcal mol^{-1}, **9a** resulting slightly more stable than **9b**, in agreement with the fast exchange observed. In both the clusters, no (3,-1) bond critical point (b.c.p.) for Au−Au interactions was found, being the gradient norm of electron density higher than zero along the Au−Au bonds (minimum gradient values were 0.005 and 0.004 a.u. for **9a** and **9b**, respectively). This result, that suggested a delocalised dispersion interaction, was in line with the data previously reported for **8**.[32] (3,-1) b.c.p. were instead found for the Fe-Au bonds, and relevant data were collected in Table 2.5 and compared with those obtained for compounds $[Fe_2(CO)_8(AuIMes)]^-$ (**11**) and $[Fe_2(CO)_8(AuIPr)]^-$ (**12**). All Fe-Au b.c.p. were characterised by negative energy density (E) values, while the Laplacian of electron density ($\nabla^2\rho$) was positive, in agreement with Bianchi's definition of M-M bonds.[33] ρ and V values of **9a** and **9b** were closely comparable, and the bonds with terminal Au atoms were stronger than those with the central Au.

The data collected in Table 2.5 indicated that the different binding mode of Au in **11** and **12** caused a slightly lowering of the Fe-Au bond strength. For what concerns the charge distribution, the three Au atoms in **9a** and **9b** had very similar Hirshfeld partial charge, in the range 0.060 – 0.064 a.u. for **9a** and 0.057 – 0.065 a.u. for **9b**, as expected on considering the formal homogeneity of the oxidation states.

Table 2.5 Properties of the Fe-Au (3,-1) b.c.p in **9a**, **9b**, **11**, and **12** (electron density, ρ; potential energy density, V; energy density, E; Laplacian of electron density, $\nabla^2 \rho$). All the quantities were reported in a.u.

Compound	Bond	ρ	V	E	∇^2 ρ
10	Fe-Au	0.047	-0.039	-0.013	0.054
11	Fe-Au	0.046	-0.038	-0.012	0.054
15a	$Fe\text{-}Au_{central}$	0.050	-0.043	-0.014	0.064
	$Fe\text{-}Au_{terminal}$	0.060	-0.053	-0.017	0.077
15b	$Fe\text{-}Au_{central}$	0.049	-0.043	-0.013	0.064
	$Fe\text{-}Au_{terminal}$	0.060	-0.052	-0.017	0.076

2.8 Thermal decomposition

2.8.1 General results

In this Section the thermal treatment of the clusters previously described is reported. The thermal reactions of the compounds **1-7** were investigated aiming at obtaining higher nuclearity species. As a general strategy, **1-7** were heated in different solvents (CH_2Cl_2, CH_3CN, dmf, dmso) at temperatures in the range 50-160 °C monitoring the time-evolution of the reactions by IR spectroscopy in the ν_{CO} region. All the results obtained are shown in Scheme 2.5. The new results herein obtained can be summarised as follow:

- Heating the mono-anions **1** and **2** as $[NEt_4]^+$ salts in CH_2Cl_2 at refluxing temperature resulted in the formation of $[Fe_2(CO)_8(AuNHC)]^-$ (NHC = IMes, **11**; IPr, **12**). Traces of $[Fe_3(CO)_{10}(CCH_3)]^-$ (**13**) were obtained as side-product.
- $[Au_3Fe_3(CO)_{12}]^{3-}$ (**14**) was the final product of the thermal treatment of **1**, **2**, **3** and **5** in dmso at high temperature.
- Heating **3** at lower temperatures (≤ 100 °C) in dmf or dmso resulted in **15**, that might be viewed as an intermediate in the transformation of **3** into **14**.
- **4** was only partially decomposed after prolonged heating in dmso at 130-160 °C resulting in a mixture of $[Fe_3S(CO)_9]^{2-}$ (**16**), $[HFe(CO)_4]^-$ (**17**) and $[Au_{16}S\{Fe(CO)_4\}_4(IPr)_4]^{n+}$ (**18**).
- The thermal decomposition of **6** in CH_3CN at 80 °C afforded the larger $[Au_3\{Fe(CO)_4\}_2(PPh_3)_2]^-$ (**9**) cluster which was present as two isomers in the solid state structure, as described in the previous Section.
- Compound **7** is stable in dmso at high temperature.

Further details are given in the next Sections.

Scheme 2.5 Thermal reactions of **1-7.**

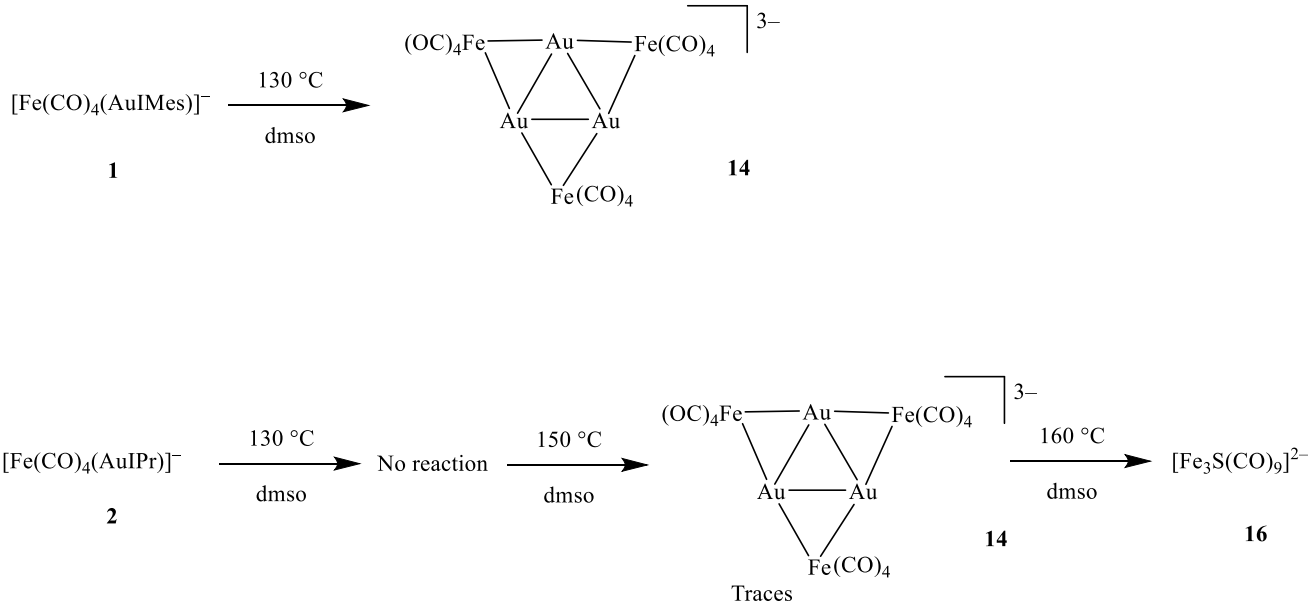

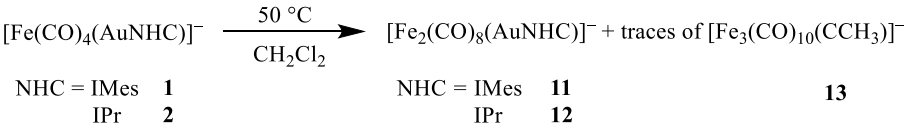

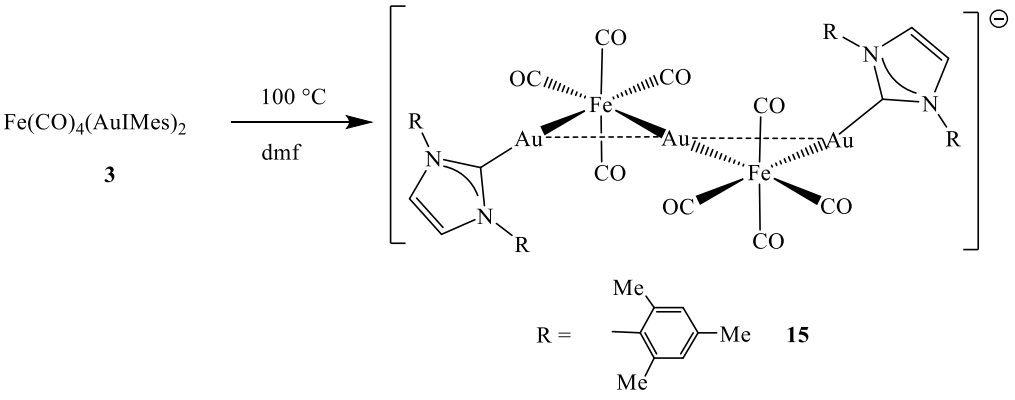

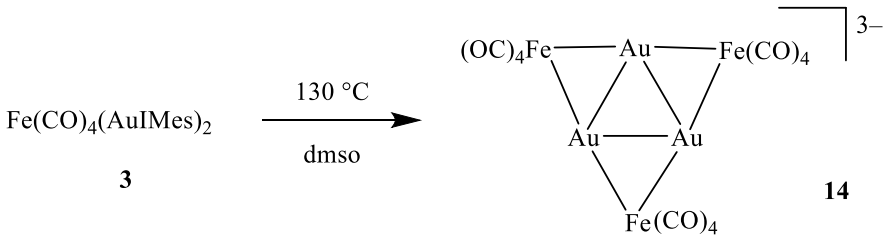
Fe(CO)4(AuIMes)2
3
130 °C
dmso
(OC)4Fe
Au
Fe(CO)4
3–
Au
Au
Fe(CO)4
14

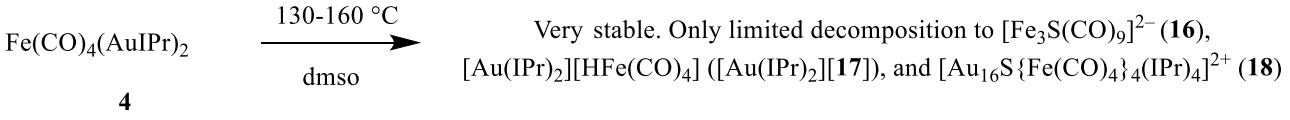
Fe(CO)4(AuIPr)2
4
130-160 °C
dmso
Very stable. Only limited decomposition to [Fe3S(CO)9]2– (16),
[Au(IPr)2][HFe(CO)4] ([Au(IPr)2][17]), and [Au16S{Fe(CO)4}4(IPr)4]2+ (18)

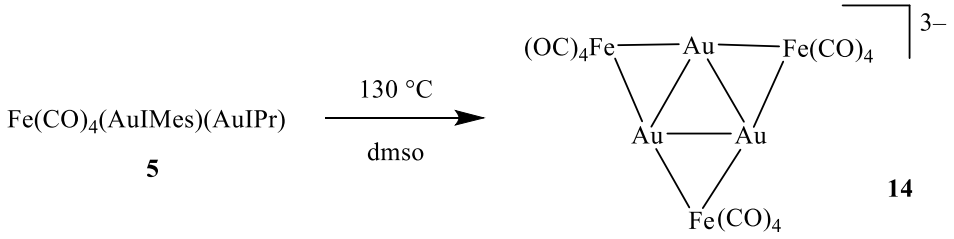
Fe(CO)4(AuIMes)(AuIPr)
5
130 °C
dmso
(OC)4Fe
Au
Fe(CO)4
3–
Au
Au
Fe(CO)4
14

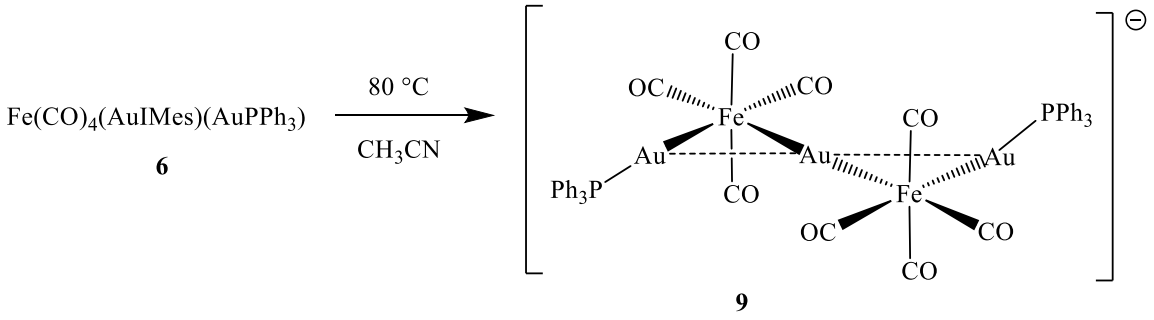
Fe(CO)4(AuIMes)(AuPPh3)
6
80 °C
CH3CN
CO
OC
CO
Fe
CO
PPh3
Au
Au
Au
Ph3P
CO
Fe
OC
CO
CO
⊖
9

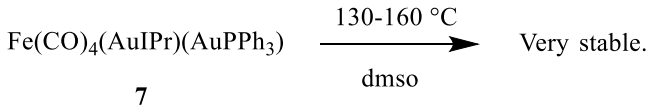
Fe(CO)4(AuIPr)(AuPPh3)
7
130-160 °C
dmso
Very stable.

2.8.2 Syntheses and characterisation of $[Fe_2(CO)_8(AuNHC)]^-$ (NHC = IMes, 11; IPr, 12) and $[Fe_3(CO)_{10}(CCH_3)]^-$ (13)

The anionic species **1** and **2** were not stable in chlorinated solvents such as CH_2Cl_2 already at room temperature. Complete decomposition occurred after heating at 50 °C, resulting in the formation of the new species $[Fe_2(CO)_8(AuNHC)]^-$ (NHC = IMes, **11**; IPr, **12**). Formation of **11** and **12** required the formal oxidation of Fe from -2, as present in **1** and **2**, to -1, as found in the final products. Since this reaction did not occur in non-chlorinated solvents even after heating for several hours, we could rule out that adventitious oxygen was the oxidising species. Thus, the oxidant should be CH_2Cl_2 itself.[34] Unfortunately, all attempts to identify the products of the reduction of CH_2Cl_2 by GC-MS analyses failed. Therefore, it was not possible to deduce the mechanism of the reaction.

Moreover a few crystals of $[NEt_4][Fe_3(CO)_{10}(CCH_3)]$, $[NEt_4]$[**13**], were isolated as side products of the thermal decomposition of **2** in CH_2Cl_2, and their nature completely revealed by means of X-ray crystallography. The mechanism for the formation of **13** as side product along the thermal decomposition of **2**, that afforded **12** as major product, was not clear. It probably involved the oxidation of **2** by means of CH_2Cl_2 as described above followed by removal of the AuIPr fragment and rearrangement of the cluster core. Unfortunately, due to the very low yields, it was not possible to further elucidate the mechanism.

Crystal structures

Compounds **11** and **12** have been characterised by means of IR and multinuclear NMR spectroscopy, and the molecular structure of **12** crystallographycally determined as its $[NEt_4]$[**12**]·1.5toluene salt (Figure 2.13). The molecular structure of **12** may be viewed as the result of the addition of a $[AuIPr]^+$ fragment to $[Fe_2(CO)_8]^{2-}$. It displayed six terminal and two edge bridging carbonyl ligands and some short sub-van der Waals Au···C(O) contacts. The structure of **12** was an interesting addition to the limited number of compounds with the $Fe_2(CO)_6(\mu\text{-}CO)_2$ unit. The Fe-Fe bond distance of such compounds spanned a very large range [2.39-2.62 Å]. In the case of **12**, the Fe-Fe distance [2.573(4) Å] was in the middle between $Fe_2(CO)_9$ [2.52 Å] and $[Fe_2(CO)_8(AuPPh_3)]^-$ [2.605 Å].

The ^1H and $^{13}C\{^1H\}$ NMR spectra of **12** displayed all the expected resonances due to the IPr group. Conversely, in the carbonyl region of the $^{13}C\{^1H\}$ NMR spectra recorded at 298 and 273 K, only a single sharp resonance at 230.5 ppm was detected. Coalescence was, then, observed at 213 K suggesting the presence of a fluxional behaviour that made the eight CO ligands equivalent at higher temperatures.

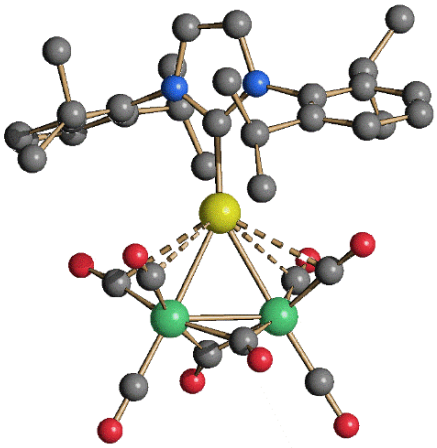

Figure 2.13 Molecular structure of **12**. Au-C(O) contacts [2.830(19)-2.977(19) Å] were represented as fragmented lines. Hydrogen atoms were omitted for clarity (green, Fe; yellow, Au; blue, N; red, O; grey, C). Selected bond lengths (Å): Fe-Fe 2.573(4); Fe-Au 2.665(3) and 2.677(3); Au-$C_{carbene}$ 2.013(18); Fe-$C(O)_{bridge}$ 1.90(2)-1.969(18); Fe-$C(O)_{terminal}$ 1.73(2)-1.83(3).[31]

Crystals of [NEt_4][**13**] contained the μ_3-ethylidyne cluster $[Fe_3(CO)_{10}(CCH_3)]^-$ (**13**) (Figure 2.14), whose synthesis was previously reported, whereas its structure, at the best of our knowledge, was not described before.[35]

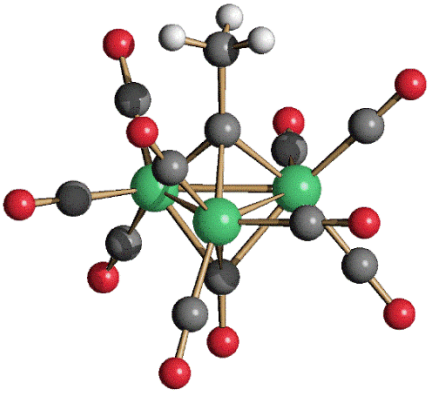

Figure 2.14 Molecular structure of **13** (green, Fe; red, O; grey, C; white, H). Selected bond lengths (Å): Fe-Fe 2.5285(5)-2.5458(5); Fe-$C_{ethylidyne}$ 1.940(2)-1.960(2); Fe-$C(O)_{bridging}$ 2.015(2)-2.077(2); Fe-$C(O)_{terminal}$ 1.766(3)-1.811(3); C-$C_{ethylidyne}$ 1.497(3).[31]

The molecular structure of **13** was composed of a triangular Fe_3 core, bonded to nine terminal CO ligands (three per each Fe atom), one μ_3-ethylidyne and one μ_3-CO. The bonding parameters of **13** (see caption of Figure 2.14) were similar to those previously reported for related clusters.[36] The μ_3-CO [Fe-$C(O)_{bridging}$ 2.015(2)-2.077(2) Å] and μ_3-CCH_3 ligands [Fe-$C_{ethylidyne}$

1.940(2)-1.960(2) Å] were symmetrically bonded to the Fe_3-triangle and the C-$C_{ethylidyne}$ distance [1.497(3) Å] was as expected for a single bond.

2.8.3 Synthesis and characterisation of $[Au_3Fe_3(CO)_{12}]^{3-}$ (14)

The thermal decomposition of **3** in dmso at 130 °C led to the formation of the tri-anionic species $[Au_3Fe_3(CO)_{12}]^{3-}$ (**14**), in accord to the equation (2.5):

$$\underset{\mathbf{3}}{Fe(CO)_4(AuIMes)_2} \xrightarrow[\text{2. } [NMe_4]Br + H_2O]{\text{1. dmso, 130 °C, 30 min}} [Au(IMes)_2][NMe_4]_2\underset{\mathbf{14}}{[Au_3Fe_3(CO)_{12}]} \quad (2.5)$$

The product was isolated as $[NMe_4]^+$ salt, washed with water and crystallised by a slow diffusion of *n*-hexane on the acetone solution.

From a stoichiometric point of view, the formation of **14** can be explained as follow (equation (2.6)):

$$\underset{\mathbf{3}}{3Fe(CO)_4(AuIMes)_2} \longrightarrow 3[Au(IMes)_2]^+ + \underset{\mathbf{14}}{[Au_3Fe_3(CO)_{12}]^{3-}} \quad (2.6)$$

This is the only way to synthesise **14**, because by reacting the Collman's reagent with Au(I) complexes, $[Au_4Fe_4(CO)_{16}]^{4-}$ is obtained instead.

14 has been characterised by means of IR, ^{1}H NMR and $^{13}C\{^1H\}$ NMR spectroscopy, and its structure determined by X-ray crystallography.

It must be remarked that, as previously reported,[25] the thermal reaction of **3** at lower temperatures (≤ 100 °C) in dmf or dmso, afforded **15**, and only at higher temperatures **3** was converted into **14**. The computed Gibbs energy variations (C-PCM/PBEh-3c calculations) for the reactions (2.7) and (2.8) were -13.1 and -23.1 kcal mol^{-1}, respectively, and suggested that the formation of $[Au(IMes)_2]^+$ was the driving force.

$$\underset{\mathbf{3}}{6Fe(CO)_4(AuIMes)_2} \longrightarrow 3[Au_3\{Fe(CO)_4\}_2(IMes)_2]^- + \underset{\mathbf{15}}{3[Au(IMes)_2]^+} \quad (2.7)$$

$$\underset{\mathbf{15}}{3[Au_3Fe_2(CO)_8(IMes)_2]^-} + 3[Au(IMes)_2]^+ \longrightarrow 2\underset{\mathbf{14}}{[Au_3Fe_3(CO)_{12}]^{3-}} + 6[Au(IMes)_2]^+ \quad (2.8)$$

Crystal structure

Crystals of **14** suitable for X-ray diffraction were obtained as $[Au(IMes)_2][NMe_4]_2$[**14**] salt (Figure 2.15).

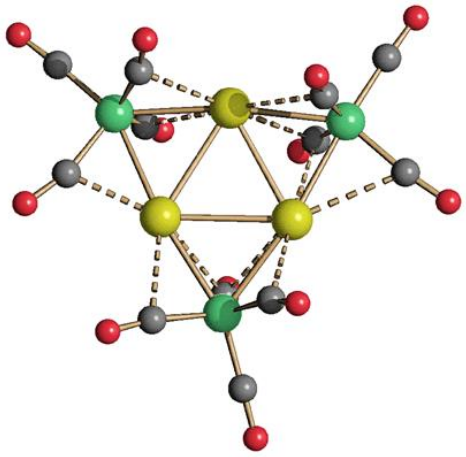

Figure 2.15 Molecular structure of $[Au_3Fe_3(CO)_{12}]^{3-}$ (**14**) (green, Fe; yellow, Au; red, O; grey, C). Au-C(O) contacts were represented as fragmented lines.

The molecular structure of **14** is based on a planar ν_2-triangular M_3Fe_3 core which consists of a M_3-triangle with edge-bridging $Fe(CO)_4$ groups. This structure can be compared to the previously reported $[Au_4Fe_4(CO)_{16}]^{4-}$. $[Au_3Fe_3(CO)_{12}]^{3-}$ and $[Au_4Fe_4(CO)_{16}]^{4-}$ may be viewed as the trimer and the tetramer, respectively, of the same $[AuFe(CO)_4]^-$ unit.

The next chapter presents a Section dedicated to this topic, exploring a unique case of polymerisation isomerism in $[\{MFe(CO)_4\}_n]^{n-}$ (M = Cu, Ag, Au; n = 3, 4) molecular clusters supported by metallophilic interactions.

2.8.4 Synthesis and characterisation of $[Au_{16}S\{Fe(CO)_4\}_4(IPr)_4]^{n+}$ (18)

4 was very stable in dmso at 140 °C, but by pushing the thermal treatment at 150 °C for a prolonged time a partial decomposition of the cluster was observed. Among the decomposition products, it was possible to isolate a few crystals of $[NEt_4]_2[Fe_3S(CO)_9]$ ($[NEt_4]$[**16**]), $[Au(IPr)_2][HFe(CO)_4]$ ($[Au(IPr)_2]$[**17**]) and $[Au_{16}S\{Fe(CO)_4\}_4(IPr)_4][BF_4]_n$·solv ([**18**]$[BF_4]_n$·solv). The presence of $[BF_4]^-$ anions in the latter salt was due to the use of $[NEt_4][BF_4]$ during workup of the reaction mixture.

Formation of **16** was rather interesting since it suggested that S atoms were somehow generated from dmso after the prolonged thermal treatment of **4**. This was in keeping with the formation of the new species **18**, which contained an interstitial sulphur atom.

Despite the fact that **18** was obtained in low yields, it was possible to characterise it also by means of multinuclear NMR techniques. ^{1}H and $^{13}C\{^{1}H\}$ NMR analyses were in agreement with the presence of CO and IPr ligands. More interestingly, the ^{19}F NMR spectrum of **18** (Figure 2.16) displayed the typical resonance of the $[BF_4]^-$ anion. Therefore, **18** was better formulated as a cationic species and because of this, its crystals were referred as [**18**][BF_4]$_n$·solv.

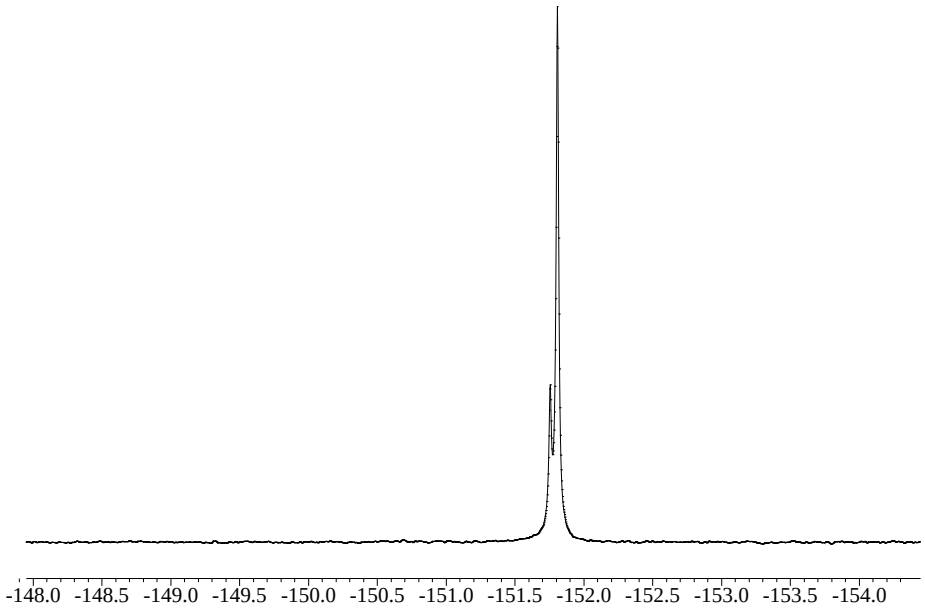

Figure 2.16 ^{19}F NMR spectrum of $[Au_{16}S\{Fe(CO)_4\}_4(IPr)_4]^{n+}$ (**18**) in CD_3COCD_3 at 298 K, which shows the typical resonances of $[BF_4]^-$.

Crystal structure

18 was formed only in trace amounts and because of this, only very few small crystals were grown. This allowed the complete determination of the molecular structure of the cluster molecule (Figure 2.17 and Table 2.6), which occupied 78% of the unit cell volume. The remaining 22% of the volume of the unit cell was likely to be occupied by cations/anions and/or solvent molecules (Figure 2.18), whose nature was not determined. Based on the ^{19}F NMR spectrum (see above), the presence of $[BF_4]^-$ anions was inferred.

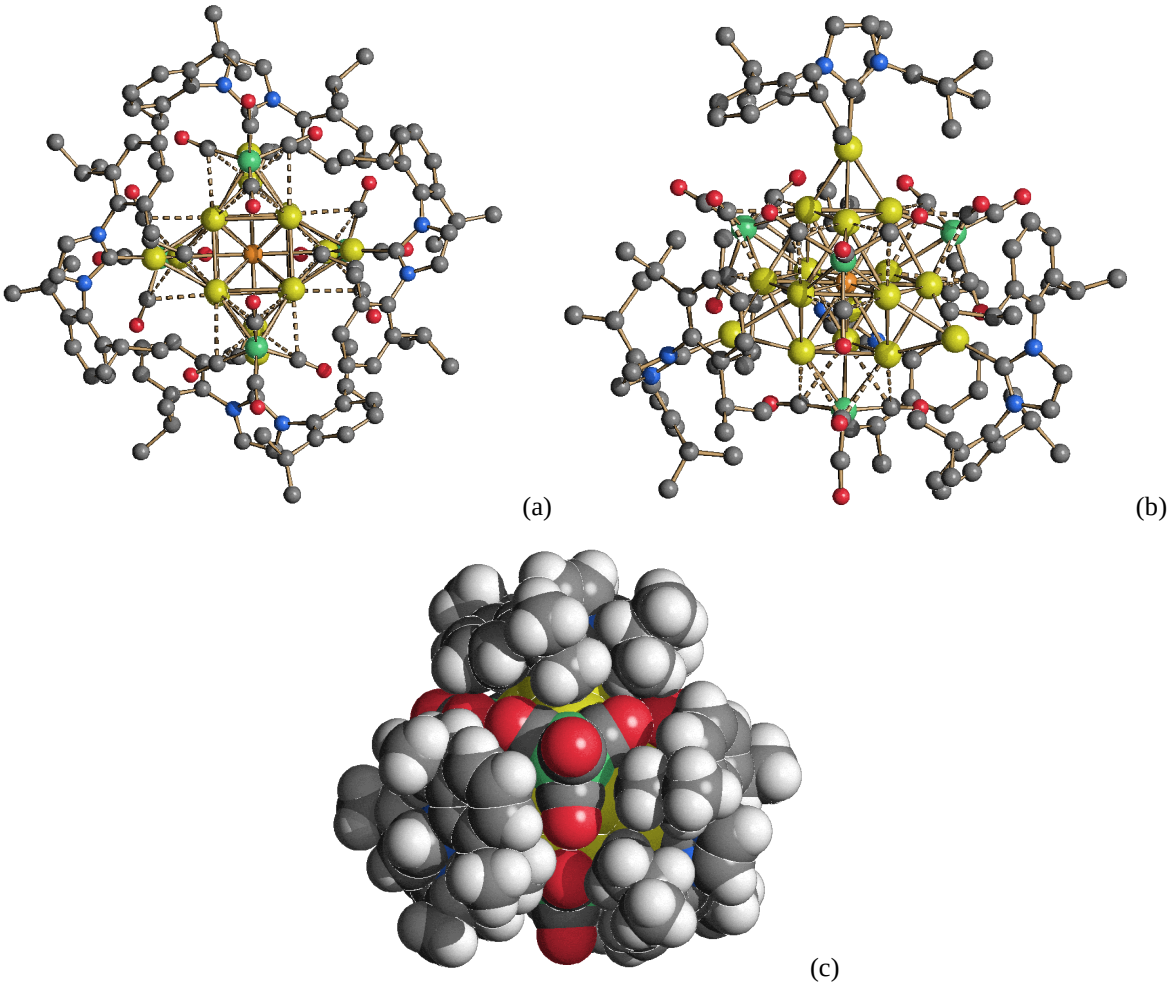

Figure 2.17 Molecular structure of **18**. Two different views (a,b) as well as the space filling model (c) were reported. Au-C(O) contacts [2.636(4)-2.723(4) Å] were represented as fragmented lines. Hydrogen atoms have been included only in the space filling model (green, Fe; yellow, Au; orange, S; blue, N; red, O; grey, C; white, H).[31]

Table 2.6 Main bond distances (Å) and angles (deg) of $[Au_{16}S\{Fe(CO)_4\}_4(IPr)_4]^{n+}$ (**18**).

	Range	**Average**
Au_c-Au_c	2.702(2)-2.874(2)	2.753(6)
Au_c-Au_s	2.724(2)-2.733(2)	2.728(3)
Au_c-Fe	2.625(5)-2.650(5)	2.636(9)
Au_c-S	2.7641(13)-2.7995(16)	2.777(3)
Au_s-$N_{carbene}$	2.04(4)	2.04(4)
Au_c···C(O)	2.636(4)-2.723(4)	2.684(10)

Au_c = Au atoms of the Au_{12} cuboctahedron.

Au_s = Au atoms of the AuIPr fragments.

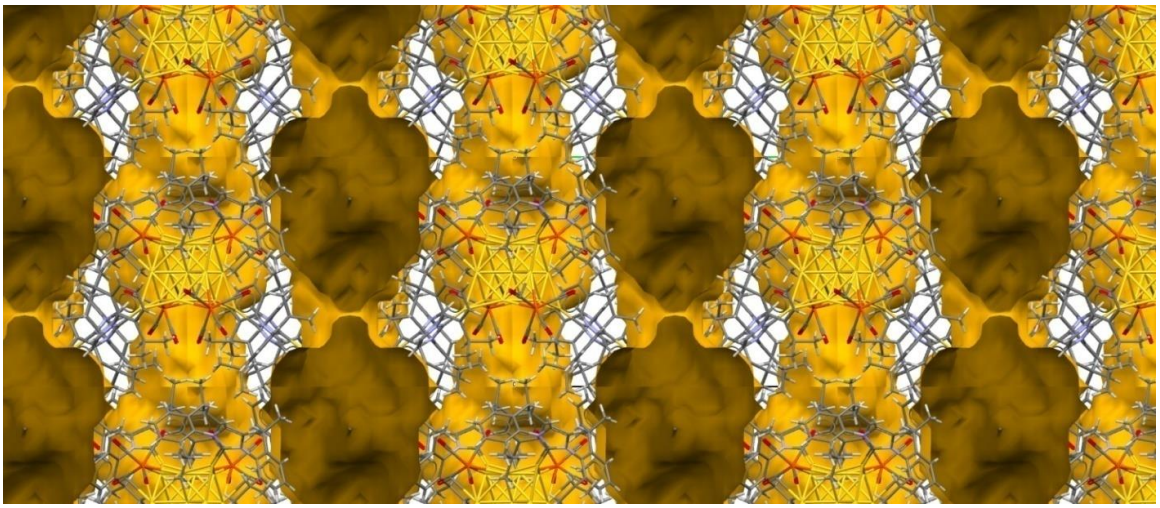

(a)

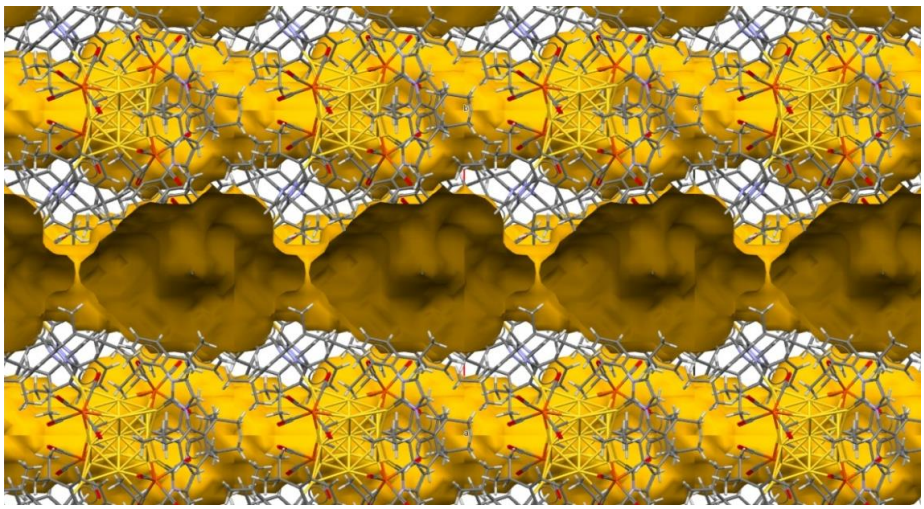

(b)

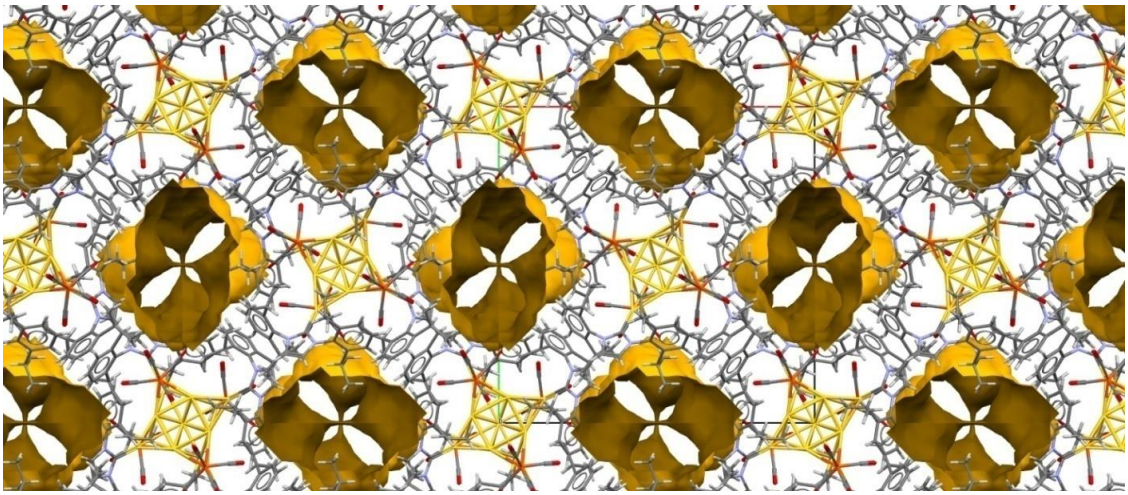

(c)

Figure 2.18 Views of the potential solvent accessible voids present within the crystal packing of $[Au_{16}S\{Fe(CO)_4\}_4(IPr)_4]^{n+}$ (**18**) along the crystallographic axes a, b, and c.

18 consisted of an Au_{12}-cuboctahedron centred by a μ_{12}-S atom, whose surface was decorated by four μ_3-$Fe(CO)_4$ and four μ_3-AuIPr fragments with a pseudo-T_d symmetry (Figure 2.19). A related structure, where a μ_{12}-S atom was encapsulated within a Cu_{12}-cuboctahedral cage, was recently reported for the neutral $[Cu_{12}(\mu_{12}\text{-}S)(S_2CN^nBu_2)_6(C{\equiv}CPh)_4]$ cluster.[37] As in the case of $[Cu_{12}(\mu_{12}\text{-}S)(S_2CN^nBu_2)_6(C{\equiv}CPh)_4]$, the Au-S distances [2.7641(13)-2.7995(16) Å, average 2.777(3) Å] of **18** were rather elongated in view of the high coordination number of the interstitial μ_{12}-S atom. For comparison, the sums of the covalent and van der Waals radii of Au and S were 2.38 and 3.46 Å, respectively. Prior of the isolation of **18**, the highest coordination number observed for S with Au was four, and the corresponding Au-S distances were considerably shorter [2.30-2.42 Å].[32]

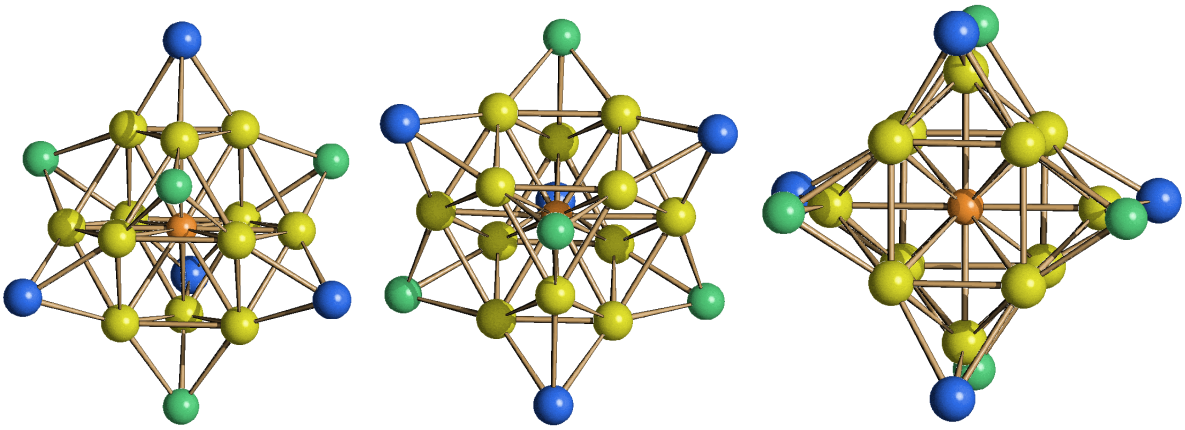

Figure 2.19 Three different views of the $Au_{16}S$ core of **18** (green, Fe; yellow, Au atoms of the Au_{12} cuboctahedron; blue, Au atoms of the μ_3-AuIPr fragments; orange, S).[31]

The tangential Au-Au contacts [2.702(2)-2.874(2) Å, average 2.753(6) Å] were more dispersed compared to the more localised Au-Au contacts involving the μ_3-AuIPr fragments [2.724(2)-2.733(2) Å, average 2.728(3) Å]. Similarly, the Au-Fe distances [2.625(5)-2.650(5) Å, average 2.636(9) Å] displayed by **18** that presented μ_3-$Fe(CO)_4$ groups were significantly longer than those found in clusters containing μ_2-$Fe(CO)_4$ fragments such as **9** [2.529(3)-2.601(11) Å, average 2.564(8) Å].

Computational study

DFT calculations were carried out on models of compound **18**. The substituents on the N atoms of the NHC ligands were replaced by methyl groups to reduce the computational effort. The coordinates of the other atoms were obtained from X-ray data. DFT calculations demonstrated that

the most stable electronic structure of **18** was the 2+. The 4+ and 6+ cations were less stable by 0.9 and 2.2 a.u., respectively. For this reason, the formula $[Au_{16}S\{Fe(CO)_4\}_4(IPr)_4]^{2+}$ was proposed. The computed energy gap between frontier orbitals in the model compound was quite high, 3.9 eV.

The approximate T_d symmetry was confirmed by all the population analyses, and the four C_3 axes were reported in Figure 2.20 for clarity.

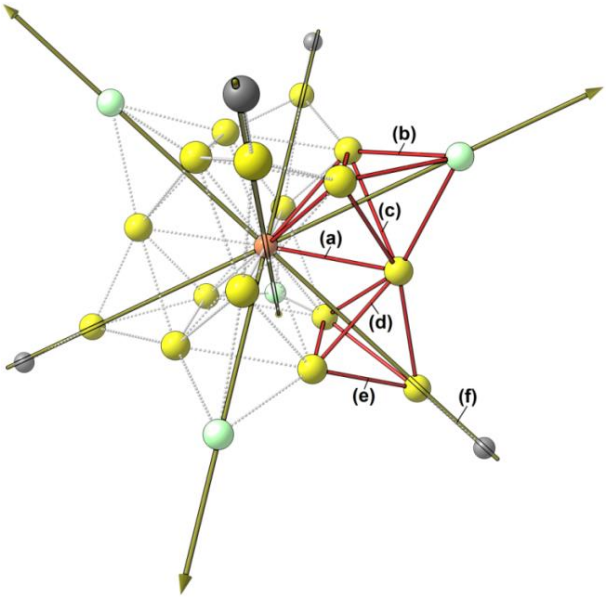

Figure 2.20 Structure of **18** with highlighted one $[FeAu_3]$ and one $[Au_4]$ tetrahedron. The CO ligands were removed for clarity. Only the donor atoms of the NHC ligands were depicted. The four C_3 axes were shown. Different types of bonds involving the Au centres were labelled (yellow, Au; orange, S; green, Fe; grey, C).[31]

The compound can be thought as composed of four $[FeAu_3]$ tetrahedra, each one forming three bonds with the central sulphur (in red in Figure 2.20). The $[FeAu_3]$ tetrahedra were interconnected by Au-Au bonds, and each [AuIPr] fragment was bonded to three Au atoms belonging to different $[FeAu_3]$ tetrahedra, with the formation of $[Au_4]$ tetrahedra, one of them highlighted in Figure 2.20.

The electron count of **18** was based on the following assumptions. The μ_3-AuIPr fragments were considered to contribute one electron each, being isolobal to μ_3-H. The μ_3-$Fe(CO)_4$ groups were usually described in the literature as four electron donors.[38] The interstitial μ_6-S atom was considered to contribute with all its six valence electrons. Therefore, if **18** was a di-cation, as inferred from DFT calculations, it should possess 156 [11×12 (Au) + 6×1 (μ_6-S) + 4×1 (μ_3-AuIPr) + 4×4 (μ_3-$Fe(CO)_4$)– 2 (charge +2)] cluster valence electrons (CVE). The expected CVEs depended on the model adopted. According to the EAN (Effective Atomic Number) rule, a cuboctahedron

should have 168 CVE. PSEPT (Polyhedral Skeletal Electron Pair Theory) predicted 170 CVE by interpreting a cuboctahedron as a four-connected polyhedron. Conversely, assuming that radial bonding predominates, on the basis of Mingos Rules a cuboctahedron should have 162 CVE.[32] In this respect, **18** appeared to be electron poor, as often happened for gold clusters. These are often electron poor because Au has already a high electron density and, therefore, tends to form fewer bonds compared to other transition metals.

Final Remarks

In this chapter a general strategy for the syntheses of new Fe-Au carbonyl clusters supported by NHC and PPh_3 ligands has been reported, starting from the Collman's reagent and Au(I) complexes, such as Au(NHC)Cl and Au(PPh_3)Cl. The new species were fully characterised by means of IR, ^1H NMR and $^{13}C\{^1H\}$ NMR spectroscopy, and their structures determined by X-ray crystallography.

Depending on the stoichiometry of the reaction and the solvent, mono-anionic or neutral species are formed. The formation of $[Fe(CO)_4(AuNHC)]^-$ (NHC = IMes, **1**; IPr, **2**) is favoured with 1:1 stoichiometry in polar solvents, such as dmso, while the neutral compounds $Fe(CO)_4(AuNHC)_2$ (NHC = IMes, **3**; IPr, **4**) may be easily obtained in less polar solvent, such as thf or acetone, with an excess of Au(I) complex. These clusters show different behaviour and reactivity, that strictly depend on the nature of the carbene ligand. Indeed, species containing the IPr group are more stable than the analogous containing the IMes group. DFT calculations highlighted that the different reactivity of these compounds was due to the steric effect of the IMes and IPr groups. Indeed, the bulkier is the substituent on the aromatic group of the carbene, the more protected the LUMO localised on the AuNHC fragment is. This protection permits to avoid attacks from nucleophiles, enhancing the stability of the compound. Moreover, DFT studies pointed out that the Au···Au interactions in such heterobimetallic clusters were not covalent bonds but mainly dispersion-driven.

Another interesting aspect of these compounds is the possibility to modulate their chemical and physical properties by changing and mixing the ligands. Indeed, in this chapter we reported different reaction paths for the preparation of mixed neutral compounds, such as $Fe(CO)_4(AuIMes)(AuIPr)$ (**5**), $Fe(CO)_4(AuIMes)(AuPPh_3)$ (**6**) and $Fe(CO)_4(AuIPr)(AuPPh_3)$ (**7**).

The species obtained in this work might be good starting material for the preparation of larger clusters. Their thermal decomposition has been investigated with the attempt to isolate new clusters with higher nuclearity. The obtained Fe-Au products could be grouped within the following categories:

- $[Fe_2(CO)_8(AuNHC)]^-$ (NHC = IMes, **11**; IPr, **12**) resulted from oxidation of Fe from -2 to -1, whereas Au retained the original +1 oxidation state.
- Anions $[Au_3Fe_3(CO)_{12}]^{3-}$ (**14**), $[Au_3Fe_2(CO)_8(IMes)_2]^-$ (**15**) and $[Au_3\{Fe(CO)_4\}_2(PPh_3)_2]^-$ (**9**) were the result of ionisation and rearrangement of the starting species. Thus, they retained the original oxidation states of the metals, that is Au(+1) and Fe(-2).
- The unique species $[Au_{16}S\{Fe(CO)_4\}_4(IPr)_4]^{2+}$ (**18**) (even if obtained in very low yields) formally contained Fe(-2) whereas the oxidation state of Au was comprised between 0 and

+1. This assignment was based on the assumption that, as usually found in Au-Fe carbonyl clusters, the $Fe(CO)_4$ fragments retained the original di-anionic nature.

CHAPTER 3

Heterometallic Fe-M (Cu, Ag, Au) Carbonyl Clusters Stabilised by N-Heterocyclic Carbene Ligands

In this chapter the syntheses and characterisation of new heterometallic Fe-M (Cu, Ag, Au) carbonyl clusters containing N-Heterocyclic carbene ligands are reported. The compounds presented in this Section are summarised in Tables 3.1-3.2.

Table 3.1 Clusters discussed in this chapter.

Compound	Compound number
$[Fe(CO)_4(CuIMes)]^-$	**1**
$[Fe(CO)_4(CuIPr)]^-$	**2**
$[Fe(CO)_4(AgIMes)]^-$	**3**
$[Fe(CO)_4(AgIPr)]^-$	**4**
$[Fe(CO)_4(AuIMes)]^-$	**5**
$[Fe(CO)_4(AuIPr)]^-$	**6**
$[Ag_3Fe_3(CO)_{12}]^{3-}$	**7**
$[Ag_4Fe_4(CO)_{16}]^{4-}$	**8**
$[Ag_5Fe_4(CO)_{16}]^{3-}$	**9**
$[Fe_2(CO)_8(AgIPr)]^-$	**10**
$Fe(CO)_4(CuIMes)_2$	**11**
$Fe(CO)_4(CuIPr)_2$	**12**
$Fe(CO)_4(AgIMes)_2$	**13**
$Fe(CO)_4(AgIPr)_2$	**14**
$Fe(CO)_4(AuIMes)_2$	**15**

Table 3.2 Clusters discussed in this chapter.

Compound	Compound number
$Fe(CO)_4(AuIPr)_2$	**16**
$[Cu_3Fe_3(CO)_{12}]^{3-}$	**17**
$[Au_3Fe_3(CO)_{12}]^{3-}$	**18**
$[Au_4Fe_4(CO)_{16}]^{4-}$	**19**
$Fe(CO)_4(CuIPr)(AgIPr)$	**20**
$Fe(CO)_4(CuIPr)(AuIPr)$	**21**
$Fe(CO)_4(AgIPr)(AuIPr)$	**22**
$Fe(CO)_4(CH_2IMes)$	**23**

3.1 Introduction

Chapter 2 introduced the importance that the heterometallic complexes and clusters containing Au(I) have gained in the recent years. The reason of this interest is linked to metallophilic interactions. Aurophilicity was explored and discussed in the previous chapter. The information obtained by studying Fe-Au carbonyl clusters allowed us to extend this research to the other two coinage metals, that is Ag and Cu, in order to investigate and better understand all the metallophilic interactions amongst the three metals (Au, Cu and Ag).

As described previously, metals in the +1 oxidation state of the 11th group of the periodic table present a low affinity to the CO ligand, which is due to the high ionisation energy and electronegativity that hamper a good π back-donation to the anti-bonding orbitals of CO. For this reason, the chemistry of the carbonyls of these M(I) ions is quite limited. In particular, in the literature few carbonyl species with the formula $[M(CO)_x]^+$ (M = Au, Ag; x = 1-3) are known, and all of them display a low stability. As regards the iron bimetallic carbonyl clusters, several Fe-Cu compounds are known, such as $[Cu_6\{Fe(CO)_4\}_4]^{2-}$, $[Cu_5\{Fe(CO)_4\}_4]^{3-}$, $[Cu_3\{Fe(CO)_4\}_3]^{3-}$, $[Fe_3(CO)_9(CCO)(CuI)]^{2-}$ and $[Fe_4(CO)_{13}(CuPPh_3)]^-$. As far as Ag is concerned, less structures were obtained because of the lower stability of the Fe-Ag bond, which is weaker than Fe-Cu and Fe-Au. Some important examples include $[Ag_4Fe_4(CO)_{16}]^{4-}$, $[Ag_5Fe_4(CO)_{16}]^{3-}$ and $[Ag_{13}Fe_8(CO)_{32}]^{n-}$ (n = 3, 4, 5) (Figure 3.1).

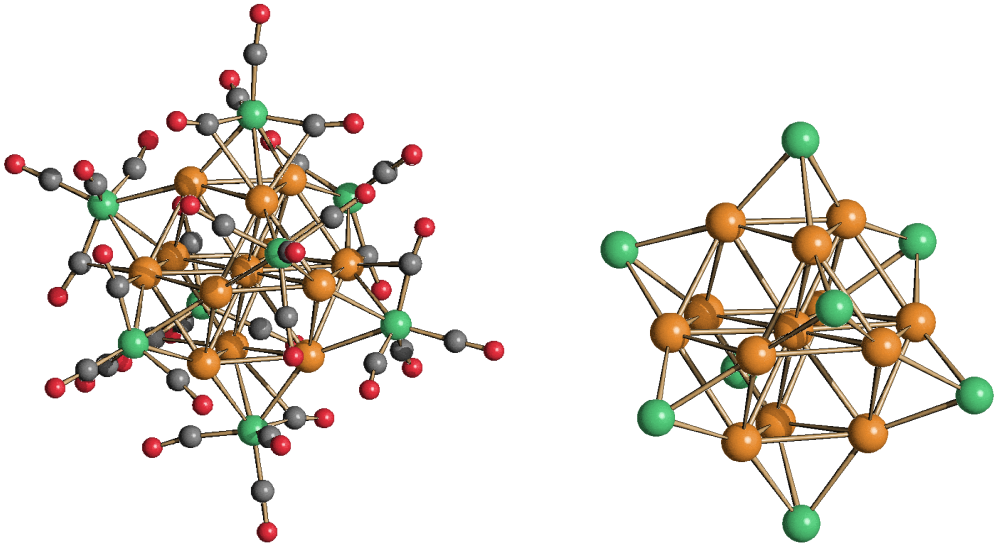

(a) (b)

Figure 3.1 (a) Molecular structure of $[Ag_{13}Fe_8(CO)_{32}]^{n-}$ and (b) its $Ag_{13}Fe_8$ metal cage (green, Fe; orange, Ag; red, O; grey, C).

These compounds resulted from the reactions between the Collman's reagent $Na_2[Fe(CO)_4]$·2thf and Ag(I) salts or Ag(L)X (L = phosphine; X = anion) complexes. The breaking of Ag-P bond due to the presence of a strong nucleophile such as $[Fe(CO)_4]^{2-}$, led to the formation of these clusters composed only by Ag, Fe and CO. Unlike Ag, in the case of Au it is possible to synthesise Fe-Au carbonyl clusters stabilised by phosphines ligands by using Au(L)X complexes, due to the greater stability of Au-P bonds compared to Ag-P. Indeed, only two examples of Fe-Ag carbonyl clusters containing phosphines are known: $Ag_6Fe_3(CO)_{12}[CH(PPh_2)_3]$ and $[Ag_3Fe(CO)_4(dppm)_3]^+$ (Figure 3.2). It is important to underline that these two compounds contain polydentate phosphines, that stabilise the Ag-P bond with the chelating effect.

Aiming at widening the library of the iron bimetallic carbonyl clusters and investigating all the metallophilic interactions, the general strategy presented in the previous chapter was also applied for Ag and Cu.

Herein, the results obtained by reacting the Collman's reagent with M(I) complexes, such as M(NHC)Cl, are reported.

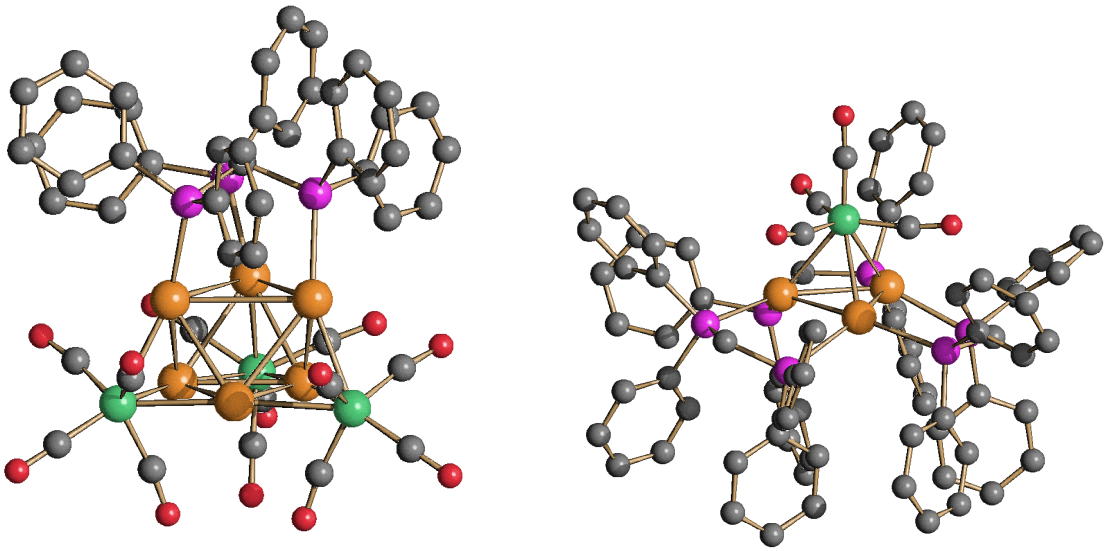

(a) (b)

Figure 3.2 Molecular structures of (a) $Ag_6Fe_3(CO)_{12}[CH(PPh_2)_3]$ and (b) $[Ag_3Fe(CO)_4(dppm)_3]^+$. Hydrogen atoms have been omitted for clarity (green, Fe; orange, Ag; purple, P; red, O; grey, C).

3.2 General results

The following Sections 3.3, 3.4 and 3.6 report the synthesis and the characterisation of $[Fe(CO)_4(MNHC)]^-$ (M = Cu, NHC = IMes, **1**; IPr, **2**; M = Ag, NHC =IMes, **3**; IPr, **4**), $Fe(CO)_4(MNHC)_2$ (M = Cu, NHC = IMes, **11**; IPr, **12** M = Ag, NHC =IMes, **13**; IPr, **14**), $Fe(CO)_4(CuIPr)(AgIPr)$ (**20**), $Fe(CO)_4(CuIPr)(AuIPr)$ (**21**), $Fe(CO)_4(AgIPr)(AuIPr)$ (**22**) and $[M_3Fe_3(CO)_{12}]^{3-}$ (M = Cu, **17**; Ag, **7**).

The thermal decomposition of **1-11** have been studied, leading, among the others, the formation of the new species $[Fe_2(CO)_8(AgIPr)]^-$ (**10**) and $Fe(CO)_4(CH_2IMes)$ (**23**).

3.3 Synthesis and characterisation of mono-anionic $[Fe(CO)_4(MNHC)]^-$ complexes (M = Cu, Ag; NHC = IMes, IPr)

The reaction of the Collman's reagent $Na_2[Fe(CO)_4]\cdot 2thf$ with one equivalent of M(NHC)Cl (M = Cu, Ag; NHC = IMes, IPr) in dmso resulted in the $[Fe(CO)_4(MNHC)]^-$ (M = Cu, NHC = IMes, **1**; M = Cu, NHC = IPr, **2;** M = Ag, NHC = IMes, **3**; M = Ag, NHC = IPr, **4**) mono-anions, in accord to Scheme 3.1.

Scheme 3.1 Syntheses of the mono-anionic $[Fe(CO)_4(MNHC)]^-$ complexes.

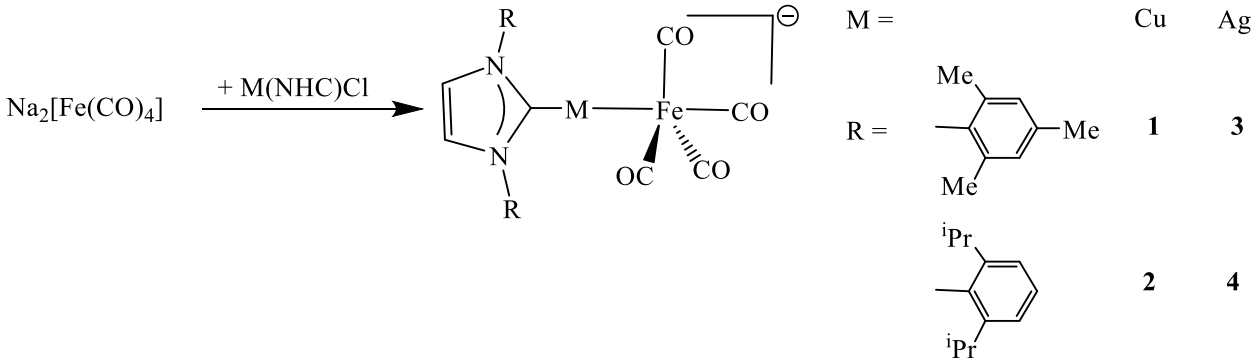

Compounds **1**-**4** are less stable than the analogous species $[Fe(CO)_4(AuNHC)]^-$ (NHC = IMes, **5**; IPr, **6**). The isolation and crystallisation of the new mono-anions were difficult. For this reason, they were characterised directly in the crude reaction mixtures by means of IR, ^1H and $^{13}C\{^1H\}$ NMR spectroscopies.

The ^1H and $^{13}C\{^1H\}$ NMR data of **1**-**4** were in agreement with the proposed structures and similar to those previously reported for **5** and **6**.[26] Compounds **1**-**4** displayed two ν_{CO} bands in dmso solution at 1909-1913(s) and 1796-1801(vs) cm^{-1}, significantly shifted towards lower wavenumbers compared to the Au-congeners **5** and **6** (ν_{CO} 1924(s) and 1820(vs) cm^{-1}).

The ν_{CO} shifts related to the change of the coinage metal were confirmed by the IR simulations on the DFT-optimised geometries (Figure 3.3).

The AIM (Atoms in Molecules) analyses of the Fe-C bonds in **1**, **3** and **5** highlighted the slight reduction of electron density (ρ) and the less negative values of potential energy density (V) at Fe-C bond critical points (b.c.p.) in the case of the Au derivative **5**. This may be explained on the basis of the greater electronegativity of Au (2.4) compared to Ag (1.9) and Cu (1.9), which resulted in a decrease of the electron density on Fe bonded to Au greater than in the case of Cu and Ag. This, in turn, reduced the π-Fe-CO back-donation in the Fe-Au complexes compared to Fe-Cu and Fe-Ag, in agreement with the experimental and computed IR frequencies of the ν_{CO} stretchings.

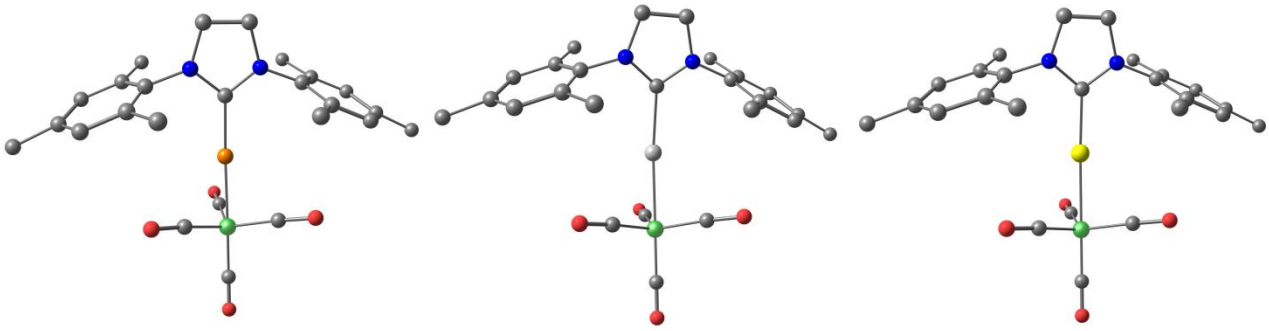

1 **3** **5**

Figure 3.3 DFT-optimised geometries of **1**, **3** and **5** (PBEh-3c method). Hydrogen atoms were omitted for clarity (green, Fe; orange, Cu; light grey, Ag; yellow, Au; blue, N; red, O; grey, C). Selected computed bond lengths (Å) for **1**: Fe-Cu 2.295, Fe-CO(axial) 1.720, Fe-CO(equatorial, average) 1.726, Cu-C(IMes) 1.929. Selected computed bond lengths (Å) for **3**: Fe-Ag 2.477, Fe-CO(axial) 1.718, Fe-CO(equatorial, average) 1.733, Ag-C(IMes) 2.135. Selected computed bond lengths (Å) for **5**: Fe-Au 2.401, Fe-CO(axial) 1.723, Fe-CO(equatorial, average) 1.735, Au-C(IMes) 2.047.[39]

The electronegativity of the coinage metal plays an important role in terms of stability of the compound. Indeed, the stronger the Fe-M bond is, the more stable and less reluctant to dissociate into $[Fe(CO)_4]^{2-}$ and $[MIMes]^+$ the species is. It might also be concluded that Fe-Au bonds are stronger than Fe-Cu and Fe-Ag bonds, in accordance with the greater stability of **5** and **6** compared to **1**-**4**.

*Crystal structure of **2***

The molecular structure of **2** has been determined as its $[NEt_4]^+$ salt (Figure 3.4) corroborating the nature of compounds **1**-**4**. Crystals of $[NEt_4][\mathbf{2}]$ were obtained by addition of a saturated solution of $[NEt_4]Br$ in water to the dmso reaction mixture, the solid recovered by filtration and extracted in toluene. Crystals of $[NEt_4][\mathbf{2}]$ suitable for X-ray analyses were obtained by slow diffusion of *n*-pentane on the toluene solution.

Similarly to **5** and **6**, **2** adopted a trigonal bipyramidal structure, with the CuIPr fragment in an axial position. **2** contained strong Cu-Fe, Fe-C(O) and Cu-$C_{carbene}$ interactions as well as some weak Cu···C(O) contacts. In general, it was rather debated if such M···C(O) (M = Cu, Ag, Au) contacts were due to the steric arrangement of the CO ligands, or they were the consequence of any attraction (even van der Waals) between the carbonyls and M(I).[40]

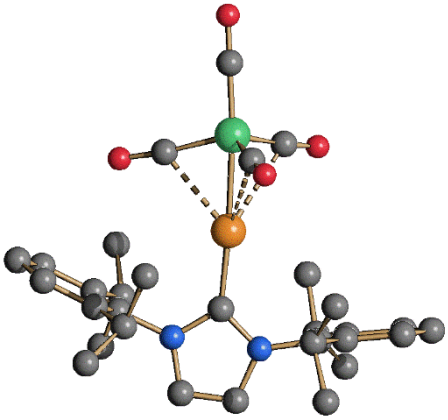

Figure 3.4 Molecular structure of $[Fe(CO)_4(CuIPr)]^-$ (**2**). Cu···C(O) contacts [2.462(5)-2.670(5) Å] are represented as fragmented lines. Hydrogen atoms have been omitted for clarity (green, Fe; orange, Cu; blue, N; red, O; grey, C). Main bond distances (Å) and angles (°): Fe-Cu 2.3216(7), Cu-$C_{carbene}$ 1.903(3), Fe-C(O) 1.749(6)-1.773(5), Fe-Cu-$C_{carbene}$ 176.80(11).[39]

Isolation of **2** was possible because of the enhanced steric stability of IPr-derivatives compared to IMes-derivatives, as well as the (slightly) greater stability of Fe-Cu species compared to Fe-Ag.[26] Indeed, all attempts to isolate **1**, **3** and **4** following a similar procedure failed, leading to the formation of complex mixtures of decomposition products.

*Attempt of crystallisation of **3***

Attempting the isolation of **3**, crystals of $[NEt_4]_2[Ag(IMes)_2][Ag_3Fe_3(CO)_{12}]$·solv,[32] $[NEt_4]_2[HIMes]_2[Ag_4Fe_4(CO)_{16}]$, $[NEt_4]_4[Ag_4Fe_4(CO)_{16}]$·$2CH_3CN$ and $[NEt_4]_3[Ag_5Fe_4(CO)_{16}]$ were obtained (Figure 3.5).

All these salts contained the $[Ag_3Fe_3(CO)_{12}]^{3-}$ (**7**),[32] $[Ag_4Fe_4(CO)_{16}]^{4-}$ (**8**), and $[Ag_5Fe_4(CO)_{16}]^{3-}$ (**9**) cluster anions.[41] Their formation suggested that the Ag-IMes bond was mainly broken during work-up, leading to homoleptic Ag-Fe-CO clusters. The presence among the decomposition products of the imidazolium $[HIMes]^+$ cation indicated that, once liberated in solution, the IMes carbene may be readily protonated by traces of humidity present in the solvent. The molecular structures of Ag-Fe compounds displayed in Figure 3.5 are similar to those of Ag-Fe, Cu-Fe and Au-Fe species reported in the literature.[20,21]

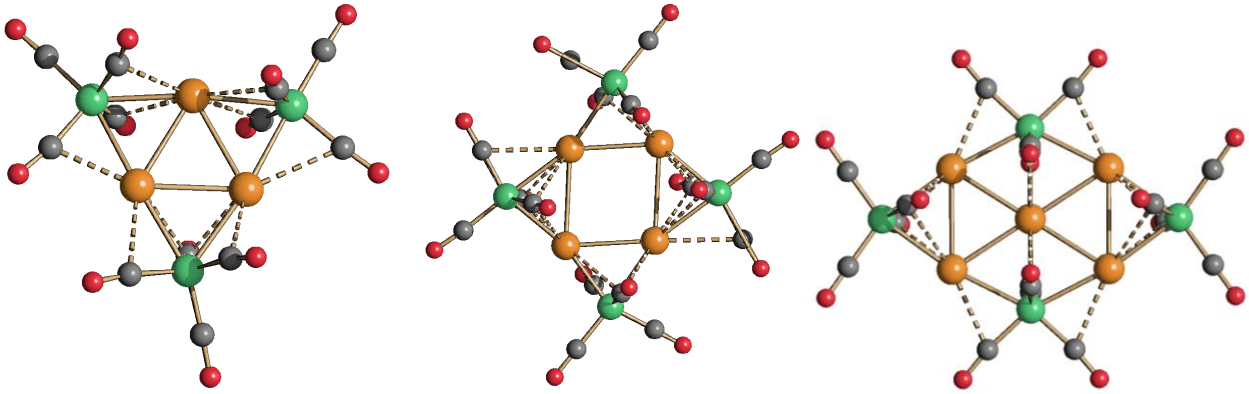

7 **8** **9**

Figure 3.5 Molecular structures of $[Ag_3Fe_3(CO)_{12}]^{3-}$ (**7**), $[Ag_4Fe_4(CO)_{16}]^{4-}$ (**8**) and $[Ag_5Fe_4(CO)_{16}]^{3-}$ (**9**). Ag···C(O) contacts are represented as fragmented lines (green, Fe; orange, Ag; red, O; grey, C).[32,39] Main bond distances (Å): Ag-Fe 2.6105(9)-2.6632(9) (**7**), 2.581 (**8**) and 2.58-2.70 (**9**), Ag-Ag 2.8515(7)-2.8801(7) (**7**), Ag 3.149 (**8**) and 2.79-3.01 (**9**).

*Attempt of crystallisation of **4***

During the attempts of isolating **4**, crystals of $[Ag(IPr)_2][Fe_2(CO)_8(AgIPr)]\cdot CH_2Cl_2$, $[NEt_4]_2[HIPr][Fe_2(CO)_8(AgIPr)]_2[Cl]\cdot 2CH_2Cl_2$ and $[NEt_4]_4[Ag_4Fe_4(CO)_{16}]$ were obtained. A part $[Ag_4Fe_4(CO)_{16}]^{4-}$ (**8**) which did not contain the IPr ligand, all the other products retained the AgIPr fragment. This confirmed the different reactivity of the IPr-containing species compared to IMes-ones, mainly imputable to their different steric properties. Formation of the $[Fe_2(CO)_8]^{2-}$ moiety was due to oxidation of the $[Fe(CO)_4]^{2-}$ unit present in **4**.

The molecular structure of the new $[Fe_2(CO)_8(AgIPr)]^-$ (**10**) anion, as found in both $[Ag(IPr)_2][\mathbf{10}]\cdot CH_2Cl_2$ and $[NEt_4]_2[HIPr][\mathbf{10}]_2[Cl]\cdot 2CH_2Cl_2$, is reported in Figure 3.6.

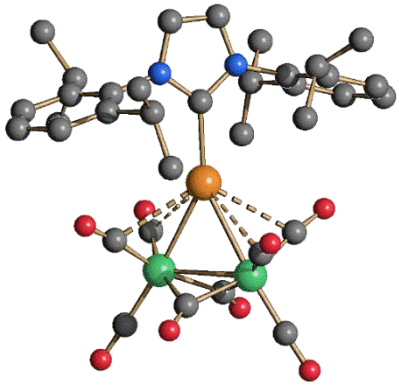

Figure 3.6 Molecular structure of $[Fe_2(CO)_8(AgIPr)]^-$ (**10**). Ag···C(O) contacts [2.775(5)-3.012(7) Å] are represented as fragmented lines. Hydrogen atoms have been omitted for clarity (green, Fe; orange, Ag; blue, N; red, O; grey, C). Selected bond lengths (Å): Fe-Fe 2.5927(9); Fe-Ag 2.7159(7) and 2.7201(7); Ag-$C_{carbene}$ 2.142(4); Fe-$C(O)_{bridge}$ 1.927(5)-1.993(5); Fe-$C(O)_{terminal}$ 1.750(5)-1.807(5).[39]

This structure may be viewed as the result of the addition of a $[AgIPr]^+$ fragment to $[Fe_2(CO)_8]^{2-}$. It displayed six terminal and two edge bridging CO ligands. The Fe-Fe distance found in **10** [2.5927(9) Å] was in keeping with those of $[Fe_2(CO)_8(AuIPr)]^-$ [2.573(4) Å] and $[Fe_2(CO)_8(AuPPh_3)]^-$ [2.605 Å].

3.4 Synthesis and characterisation of neutral bimetallic $Fe(CO)_4(MNHC)_2$ complexes (M = Cu, Ag; NHC = IMes, IPr)

The neutral bimetallic $Fe(CO)_4(MNHC)_2$ (M = Cu, NHC = IMes, **11**; M = Cu, NHC = IPr, **12**; M = Ag, NHC = IMes, **13**; M = Ag, NHC = IPr, **14**) compounds were obtained by reacting $Na_2[Fe(CO)_4]\cdot 2thf$ with two equivalents of M(NHC)Cl in thf, as shown in Scheme 3.2.

Scheme 3.2 Synthesis of **11-14**.

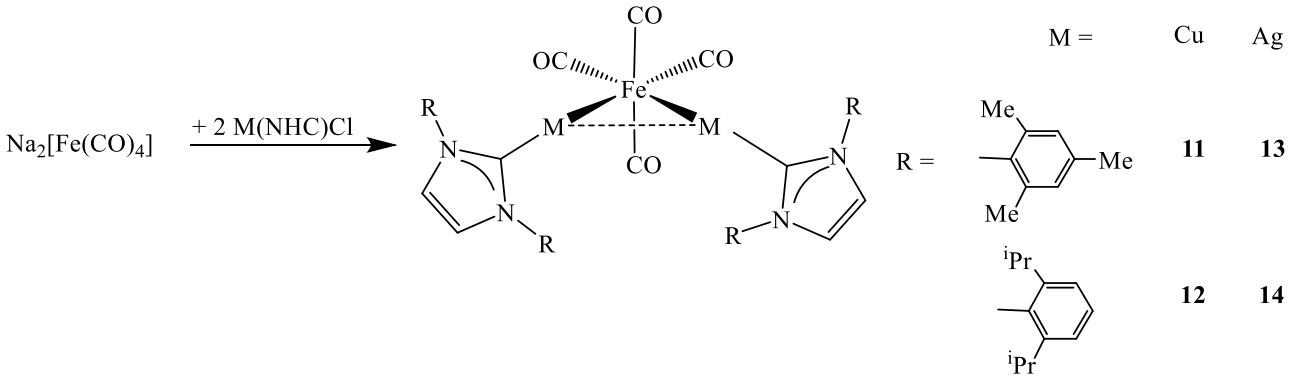

After the work-up, compounds **11-14** were spectroscopically characterised by means of IR, ^1H and $^{13}C\{^1H\}$ NMR techniques. The IR spectra of these species displayed ν_{CO} bands in CH_2Cl_2 at 1943-1950 and 1849-1878 cm^{-1}, significantly downshifted compared to $Fe(CO)_4(AuNHC)_2$ (NHC = IMes, **15**; IPr, **16**) [*ca.* 1974(m), 1884(s) cm^{-1}]. As explained in Section 3.3, this was related to the greater electronegativity of Au compared to Cu and Ag. The IR simulations on the DFT-optimised structures of **11**, **13** and **15** confirmed the variations to the ν_{CO} stretchings on changing the coinage metal in agreement with the lower ρ and less negative V values at Fe-C b.c.p. for the Au compound **15**.

The two NHC ligands were equivalent in the ^1H and ^{13}C NMR spectra at all temperatures, in agreement with the solid state structures. The M-coordinated carbene resonated at δ_C 177.3, 181.5, 182.6 and 189.2 ppm for **11**, **12**, **13** and **14**, respectively. The expected coupling to ^{107}Ag and ^{109}Ag was detected in the Ag-complexes **13** and **14** ($^1J_{C\text{-}Ag}$ = 209 and 180 Hz for **13** and $^1J_{C\text{-}Ag}$ = 204 and 182 Hz for **14**). A singlet was present at all temperatures in the CO region of the ^{13}C NMR spectra

of **11-14**, suggesting a fluxional behaviour for the carbonyl ligands. This rapid exchange process made the equatorial and apical CO ligands equivalent also at low temperature and hampered the spectroscopic detection in solution of possible M···C(O) interactions.

Crystal structures

The molecular structures of **11-13** were crystallographycally determined (Figure 3.7 and Table 3.3).[32] Conversely, we were not able to obtain crystals of **14**. **11-13** were composed of a C_{2v}-$Fe(CO)_4$ sawhorse/seesaw unit coordinated to two MNHC fragments in relative *cis* position, as previously found in **15** and **16**.[25] All these compounds displayed short Fe-M, Fe-CO and M-$C_{carbene}$ contacts, as well as sub-van der Waals M···C(O) contacts (Table 3.3).

Regarding the M···M distances, they were shorter in the IMes-derivatives and rather longer in the IPr-derivatives. Thus, the former contacts may be viewed as weak metallophilic interactions, whereas they were completely non-bonding in the latter compounds. These differences were explained on the basis of the greater steric demand of IPr compared to IMes, which caused the complete loss of any M···M interaction. As a consequence, the M-Fe-M angles were considerably smaller in the IMes-derivatives [73.53(7)-78.74(4)°] than in the IPr-congeners [107.90(9)-127.75(3)°]. The results herein described and summarised in Table 3.3 further pointed out that metallophilic M···M interactions were rather deformable and adapted themselves to the steric properties of the ancillary ligands employed in such complexes.

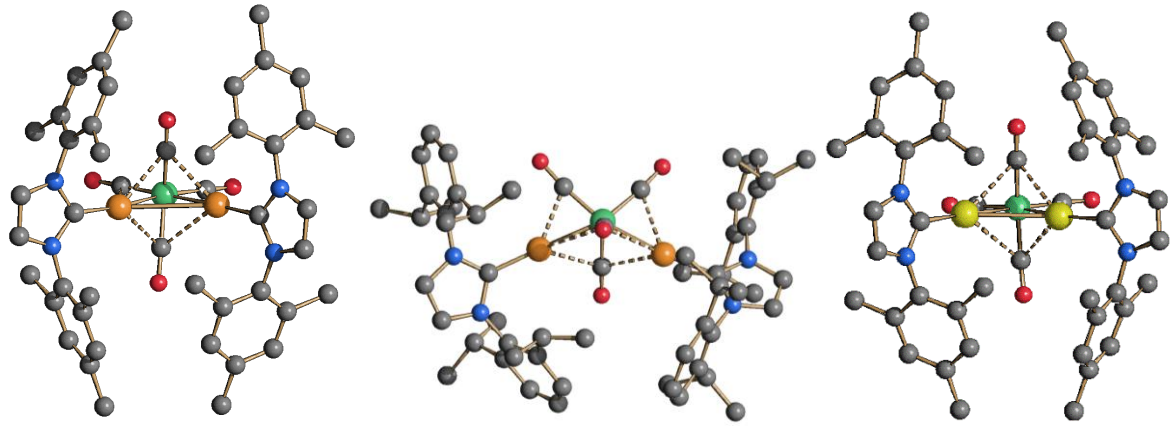

11 **12** **13**

Figure 3.7 Molecular structures of $Fe(CO)_4(CuIMes)_2$ (**11**), $Fe(CO)_4(CuIPr)_2$ (**12**) and $Fe(CO)_4(AgIMes)_2$ (**13**). Cu···C(O) contacts [2.359(3)-2.907(3) Å] (**11**), [2.345(5)-2.9742(6) Å] (**12**) and Ag···C(O) contacts [2.576(4)-2.767(4) Å] (**13**) are represented as fragmented lines. Hydrogen atoms have been omitted for clarity (green, Fe; orange, Cu; yellow, Ag; blue, N; red, O; grey, C).[39]

Table 3.3 Main bond distances (Å) and angles (deg) of $Fe(CO)_4(CuIMes)_2$ (**11**), $Fe(CO)_4(CuIPr)_2$ (**12**) and $Fe(CO)_4(AgIMes)_2$ (**13**) compared to $Fe(CO)_4(AuIPr)_2$ (**16**)[25] and $Fe(CO)_4(AuIMes)_2$ (**15**).[25,32]

	$Fe(CO)_4(CuIMes)_2$	**$Fe(CO)_4(CuIPr)_2$**	**$Fe(CO)_4(AgIMes)_2$**	**$Fe(CO)_4(AuIPr)_2$**	**$Fe(CO)_4(AuIMes)_2$**
	11	**12**	**13**	**16**	**15**
M(1)-Fe(1)	2.3586(4)	2.3603(8)	2.5292(4)	2.512(2)	2.5158(15)
M(2)-Fe(1)	2.3582(4)	2.3438(8)	2.5423(4)	2.524(2)	2.5312(15)
M(1)-M(2)	3.1990(9)	4.223(2)	3.1185(3)	4.082(1)	3.2015(8)
M(1)-C(1)	1.903(2)	1.911(4)	2.105(2)	2.012(11)	2.008(10)
M(2)-C(2)	1.908(2)	1.889(4)	2.104(2)	1.949(14)	2.020(10)
Fe(1)-CO	1.770(2)-1.776(2)	1.775(5)- 1.785(5)	1.770(2)-1.781(2)	1.737(15)-1.781(15)	1.756(13)-1.783(13)
Fe(1)-M(1)-C(1)	168.64(7)	170.67(12)	178.02(6)	168.3(3)	177.8(3)
Fe(1)-M(2)-C(2)	178.04(7)	171.36(13)	165.05(6)	168.4(5)	165.9(3)
M(1)-Fe(1)-M(2)	73.53(7)	127.75(3)	75.890(12)	107.90(9)	78.74(4)
Fe(1)-M(1)-M(2)	47.30(2)	26.03(2)	52.245(9)	36.15(5)	50.84(4)
Fe(1)-M(2)-M(1)	47.31(2)	26.23(2)	51.865(9)	35.95(5)	50.42(3)

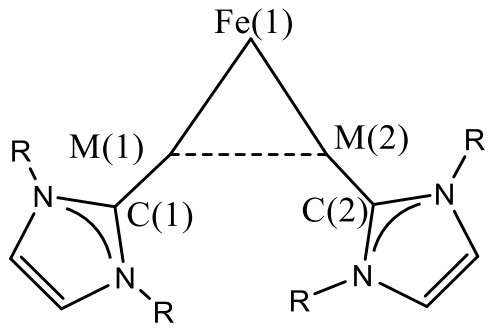

3.5 Thermal decomposition

Aiming at studying their reactivity and enhancing the nuclearity, the thermal treatments of **11**-**14** in dmso at 130 °C were performed. The results can be summarised as follow (Scheme 3.3):[25]

- Compounds **11**, **13** and **14** rapidly decomposed affording the triangular clusters $[M_3Fe_3(CO)_{12}]^{3-}$ (M = Cu, **17**; Ag, **7**).
- Complex **12** was thermally stable and displayed only limited dissociation of one $[CuIPr]^+$ group and resulted in a mixture of unreacted **12** (major) and **2** (minor). These results were in keeping with our previous observations, that indicated that IPr-containing species were more stable than IMes-ones and Cu complexes were more stable than Ag ones. From this point of view, Cu-containing complexes resembled more to Au-complexes than Ag-complexes.

Scheme 3.3 Thermal decomposition of **11**-**14**.

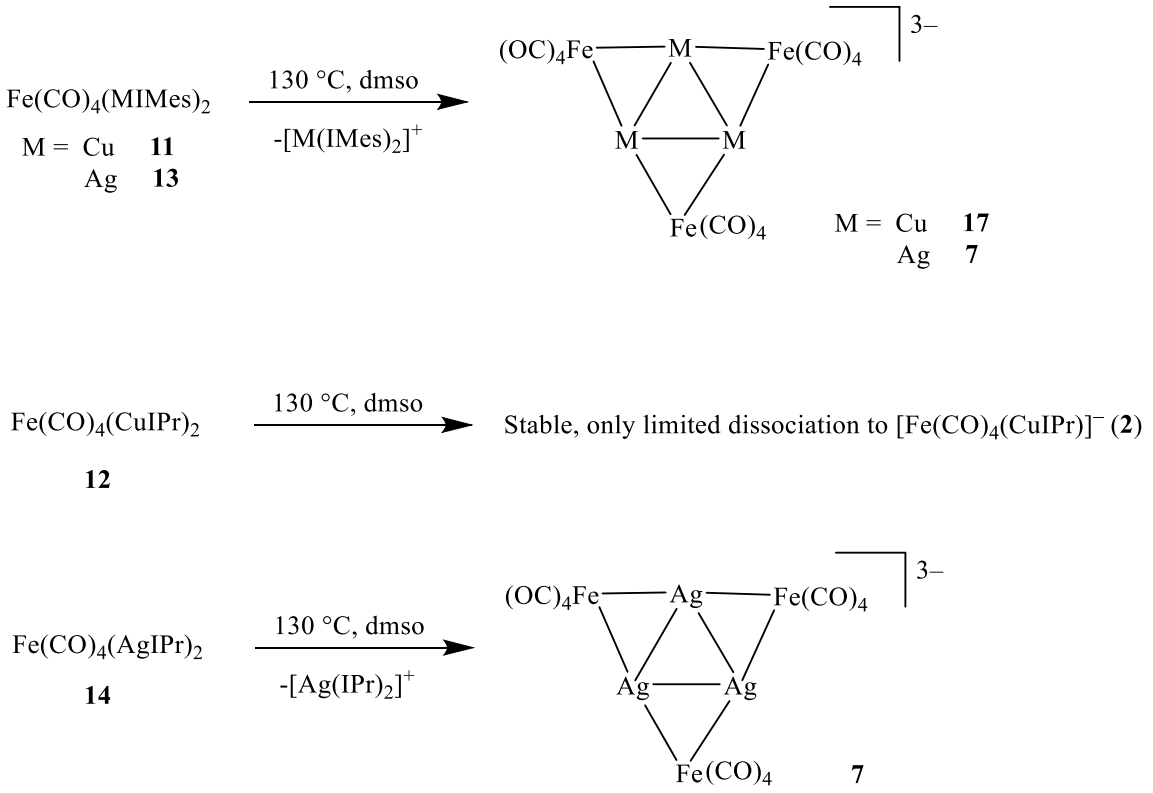

Independently of the coinage metal, IMes-complexes **11**, **13** and **15** rapidly decomposed after heating in dmso at 130 °C affording the higher nuclearity $[\{MFe(CO)_4\}_3]^{3-}$ (M = Ag, **7**; Cu, **17**; Au, **18**) clusters (Scheme 3.3). The case of Au was already presented in Chapter 2.

Formation of the $[\{MFe(CO)_4\}_3]^{3-}$ clusters from the neutral ones may be accounted by the decomposition-ionisation reaction depicted in equation (3.1):

$$3Fe(CO)_4(MIMes)_2 \longrightarrow [\{MFe(CO)_4\}_3]^{3-} + 3[M(IMes)_2]^+ \quad (3.1)$$

M = Cu **11**, Ag **13**, Au **15** → M = Cu **17**, Ag **7**, Au **18**

Compounds **7**, **17** and **18** were based on a M_3Fe_3 core which consisted of a M_3-triangle with edge-bridging $Fe(CO)_4$ groups. Such a triangular structure was unprecedented for Ag and Au, whereas the hexa-nuclear copper cluster $[\{CuFe(CO)_4\}_3]^{3-}$ was previously obtained by reaction of $Na_2[Fe(CO)_4]\cdot 2thf$ with Cu(I) salts. Conversely, analogous reactions of Collman's reagent with Ag(I) and Au(I) salts afforded the square-in-a-square-type clusters $[\{MFe(CO)_4\}_4]^{4-}$ (M = Ag, **8**; Au, **19**) as previously reported in the literature.[41,42] Thus, depending on the synthetic protocol adopted, both the triangular $[\{MFe(CO)_4\}_3]^{3-}$ and square $[\{MFe(CO)_4\}_4]^{4-}$ polymerisation isomers can be selectively obtained, at least for Ag and Au. Polymerisation isomerism, that is two compounds having the same elemental compositions but different molecular weights, was investigated in $[\{MFe(CO)_4\}_n]^{n-}$ (n = 3, 4; M = Cu, Ag, Au) by means of structural and theoretical methods and the role of metallophilic interactions was computationally studied throughout the atoms-in-molecules (AIM) approach.

As far as Cu was concerned, only the $[\{CuFe(CO)_4\}_3]^{3-}$ triangular cluster was obtained independently of the synthetic strategy adopted. $[\{MFe(CO)_4\}_4]^{4-}$ and $[\{MFe(CO)_4\}_3]^{3-}$ (M = Ag, Au) represented the first examples of polymerisation isomers for molecular clusters, having the same elemental compositions but different molecular weights.

The M_3 and M_4 cores of the clusters were supported by metallophilic interactions, which were lower in M_4 clusters with respect to the analogous M_3 species, as inferred by DFT calculations. This lowering was more accentuated for $[\{CuFe(CO)_4\}_4]^{4-}$, where cuprophilic interactions were weaker. This explained the tendency of Cu to form the triangular compound, while the softer and flexible character of Ag and Au allowed the formation of both triangular and square isomers without altering the Fe-M-Fe frameworks.

The molecular structures and the electron densities associated to the coinage metals in the $[\{MFe(CO)_4\}_3]^{3-}$ and $[\{MFe(CO)_4\}_4]^{4-}$ clusters are shown in Figures 3.8-3.9, respectively.

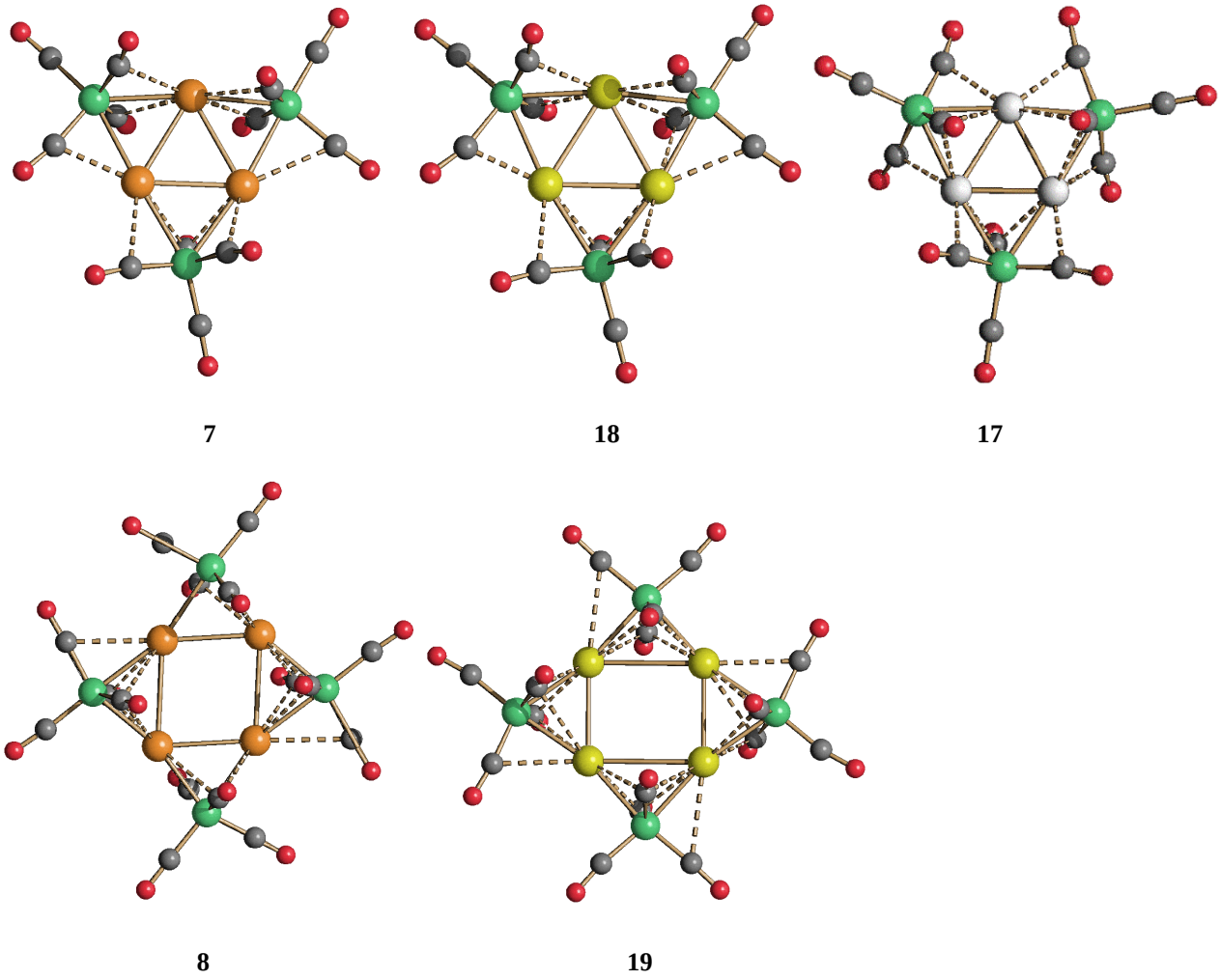

Figure 3.8 Molecular structures of $[\{MFe(CO)_4\}_3]^{3-}$ (M = Ag, **7**; Au, **18**; Cu, **17**) and $[\{MFe(CO)_4\}_4]^{4-}$ (M = Ag, **8**; Au, **19**) as determined by SC-XRD analysis *(*green, Fe; orange, Ag; yellow, Au; light grey, Cu; red, O; grey, C).[32]

.

As shown in Figure 3.9, metallophilic interactions are lower in M_4 clusters with respect to the analogous M_3 species, but this lowering is more accentuated for $[\{CuFe(CO)_4\}_4]^{4-}$, where cuprophilic interactions are weak.

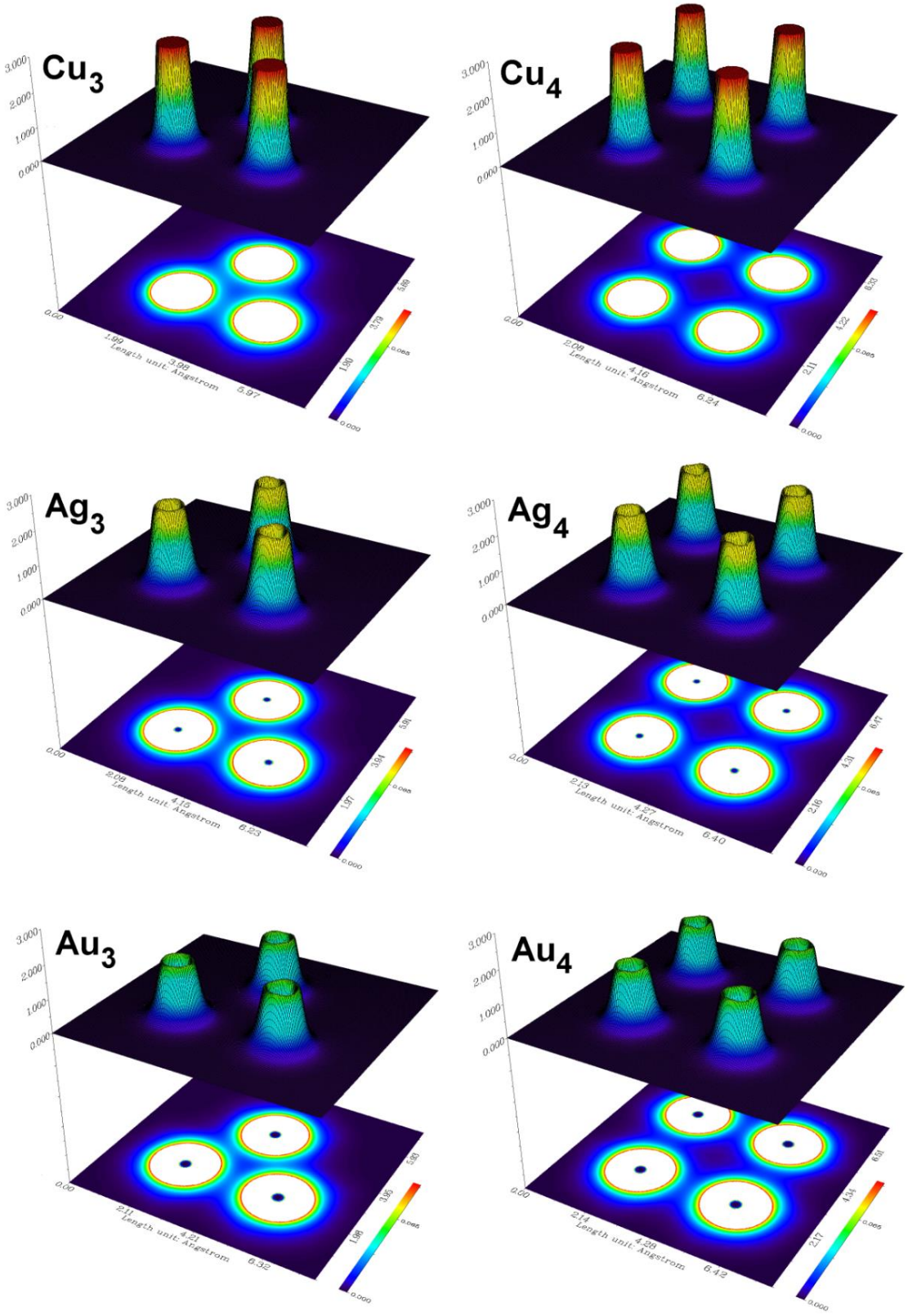

Figure 3.9 Surface maps with projections of the coinage metal electron densities (a.u.) in the $[\{MFe(CO)_4\}_3]^{3-}$ and $[\{MFe(CO)_4\}_4]^{4-}$ clusters.[32]

3.6 Synthesis and characterisation of neutral trimetallic $Fe(CO)_4(MNHC)(M'NHC)$ complexes (M = Cu, Ag; M' = Cu, Ag, NHC = IMes, IPr)

The reaction between the mono-anions $[Fe(CO)_4(MNHC)]^-$ (**1**-**6**) and one equivalent of M'(NHC)Cl were performed in the attempt to prepare neutral trimetallic clusters of the general type $Fe(CO)_4(MNHC)(M'NHC)$ (NHC = IMes, IPr; M, M' = Cu, Ag, Au; M ≠ M'). Depending on the nature of the NHC carbene ligands, different results were obtained (Scheme 3.4). When NHC = IPr, it was possible to isolate in satisfactory yields all the new three species $Fe(CO)_4(CuIPr)(AgIPr)$ (**20**), $Fe(CO)_4(CuIPr)(AuIPr)$ (**21**) and $Fe(CO)_4(AgIPr)(AuIPr)$ (**22**).

Scheme 3.4 Synthesis of **20**-**22**.

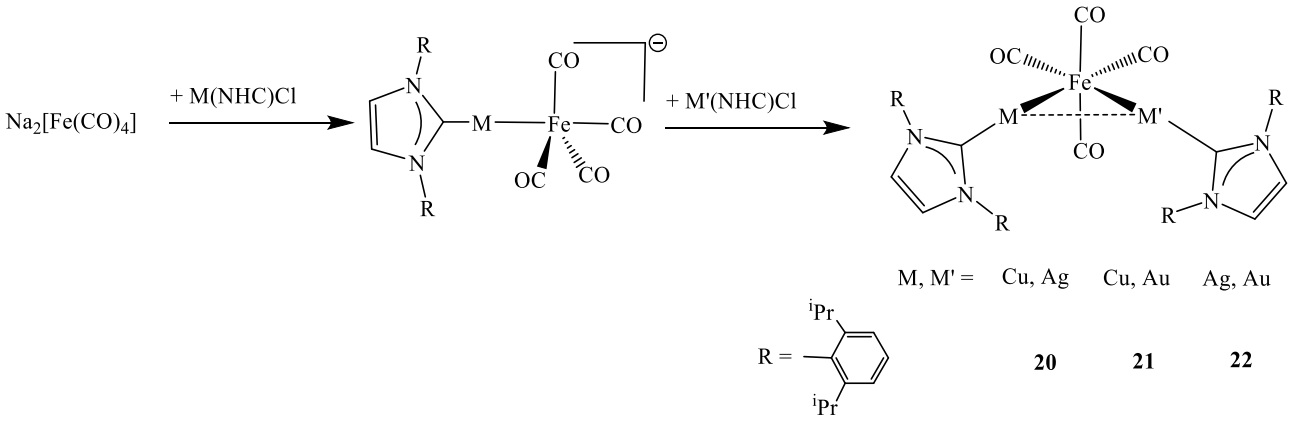

20-**22** were quite stable both in the solid state and in solution, and were fully characterised through IR, ^1H and $^{13}C\{^1H\}$ NMR spectroscopies.

Crystal structures

The molecular structures of **20**-**22** were determined by means of single crystal X-ray diffraction as their isomorphous $Fe(CO)_4(CuIPr)_{1.27}(AgIPr)_{0.73}\cdot 1.5$toluene (**I**), $Fe(CO)_4(CuIPr)_{0.71}(AuIPr)_{1.29}\cdot 1.5$toluene (**II**) and $Fe(CO)_4(AgIPr)_{0.95}(AuIPr)_{1.05}\cdot 1.5$toluene (**III**) solvates (Figures 3.10-3.12, Table 3.4).

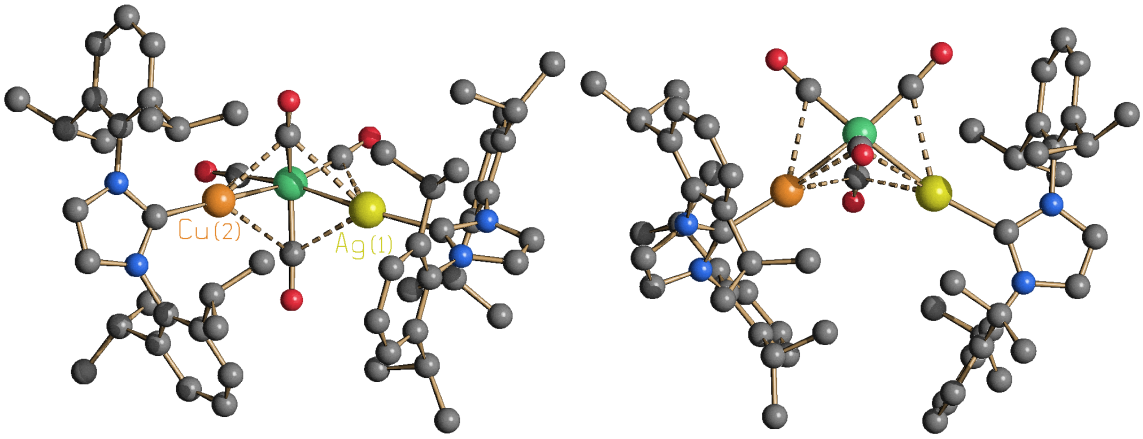

Figure 3.10 Molecular structure of $Fe(CO)_4(CuIPr)(AgIPr)$ (**20**). Two different views of the molecule are reported. M···C(O) contacts [2.414(5)-2.787(5) Å] are represented as fragmented lines. Hydrogen atoms have been omitted for clarity (green, Fe; orange, Cu; yellow, Ag; blue, N; red, O; grey, C).[39]

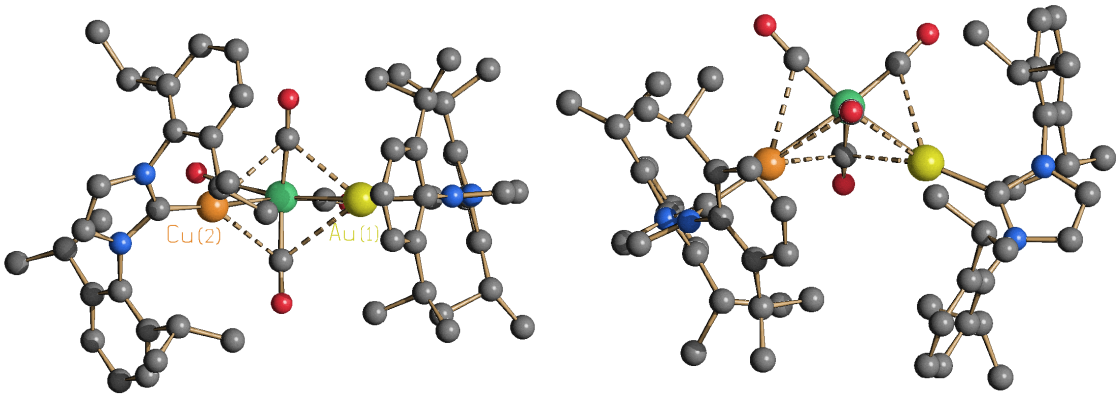

Figure 3.11 Molecular structure of $Fe(CO)_4(CuIPr)(AuIPr)$ (**21**). Two different views of the molecule are reported. M···C(O) contacts [2.556(5)-2.842(5) Å] are represented as fragmented lines. Hydrogen atoms have been omitted for clarity (green, Fe; orange, Cu; yellow, Au; blue, N; red, O; grey, C).[39]

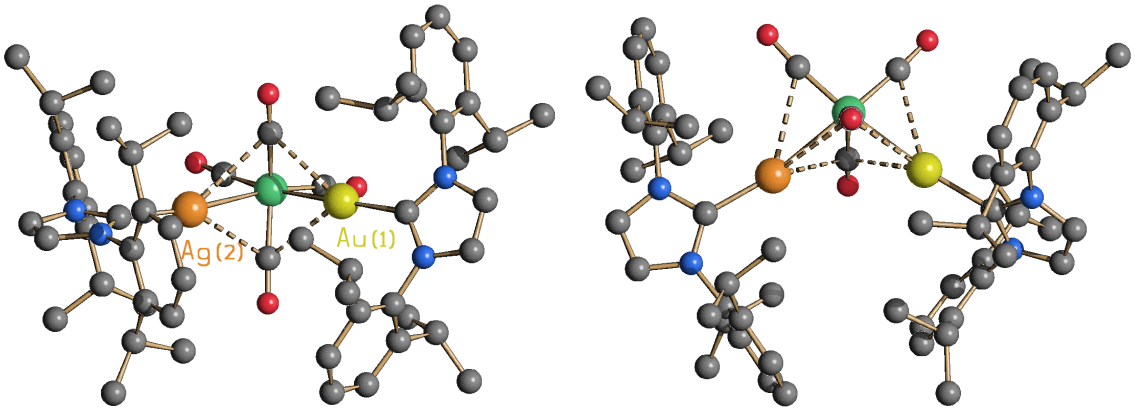

Figure 3.12 Molecular structure of $Fe(CO)_4(AgIPr)(AuIPr)$ (**22**). Two different views of the molecule are reported. M···C(O) contacts [2.588(4)-2.912(4) Å] are represented as fragmented lines. Hydrogen atoms have been omitted for clarity (green, Fe; orange, Ag; yellow, Au; blue, N; red, O; grey, C).[39]

Table 3.4 Main bond distances (Å) and angles (deg) of $Fe(CO)_4$(CuIPr)(AgIPr) (**20**), $Fe(CO)_4$(CuIPr)(AuIPr) (**21**) and $Fe(CO)_4$(AgIPr)(AuIPr) (**22**) as found in **I-III**.

	$Fe(CO)_4$(CuIPr)(AgIPr)	**$Fe(CO)_4$(CuIPr)(AuIPr)**	**$Fe(CO)_4$(CuIPr)(AuIPr)**	**$Fe(CO)_4$(AgIPr)(AuIPr)**
	20	**21 (crystal 1)**	**21 (crystal 2)**	**22**
M(1)-Fe(1)	2.404(7)	2.4848(13)	2.4962(11)	2.500(4)
M(2)-Fe(1)	2.411(13)	2.488(10)	2.485(9)	2.536(3)
M(1)-M(2)	3.763(6)	3.948(8)	3.958(8)	3.911(7)
M(1)-C(1)	2.079(9)	2.001(4)	2.001(4)	2.067(6)
M(2)-C(2)	1.953(13)	1.933(11)	1.950(10)	2.027(7)
Fe(1)-CO	1.751(6)-1.774(5)	1.763(5)-1.779(5)	1.766(4)-1.780(4)	1.765(4)-1.786(4)
Fe(1)-M(1)-C(1)	168.9(5)	167.37(13)	167.34(11)	171.7(2
Fe(1)-M(2)-C(2)	172.2(8)	175.9(6)	177.8(5)	169.6(3)
M(1)-Fe(1)-M(2)	101.5(6)	101.71(5)	101.51(4)	101.5(2)
Fe(1)-M(1)-M(2)	38.65(5)	37.47(7)	37.30(8)	39.94(8)
Fe(1)-M(2)-M(1)	38.52(5)	37.41(4)	37.49(8)	38.82(8)

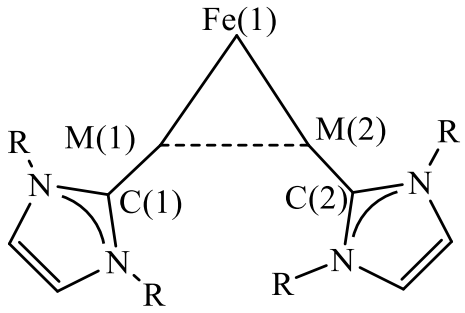

20-**22** presented similar molecular structures, geometries, and bonding parameters to those reported for the related bimetallic clusters $Fe(CO)_4(MIPr)_2$. The most interesting point was that, within the solid state structures of **I**-**III**, the positions occupied by M(1) and M(2) were disordered Cu/Ag for **I**, Cu/Au for **II**, and Ag/Au for **III**. This can be explained assuming the presence of a mixture of $Fe(CO)_4(AgIPr)_2$ (**14**), $Fe(CO)_4(CuIPr)(AgIPr)$ (**20**) and $Fe(CO)_4(CuIPr)_2$ (**12**) for **I**, $Fe(CO)_4(AuIPr)_2$ (**16**), $Fe(CO)_4(CuIPr)(AuIPr)$ (**21**) and $Fe(CO)_4(CuIPr)_2$ (**12**) for **II**, and $Fe(CO)_4(AuIPr)_2$ (**16**), $Fe(CO)_4(AgIPr)(AuIPr)$ (**22**) and $Fe(CO)_4(AgIPr)_2$ (**14**) for **III**, as also indicated by NMR analyses. Indeed, after dissolving the crystals in CD_2Cl_2, three resonances were present in the CO region of the $^{13}C\{^1H\}$ NMR spectra of **I** (δ_{CO} 217.6, 216.5 and 215.6 attributable to **14**, **20** and **12**, respectively), **II** (δ_{CO} 216.8, 216.1 and 215.6 attributable to **16**, **21** and **12**, respectively) and **III** (δ_{CO} 220.1, 217.6 and 217.1 attributable to **14**, **22** and **16**, respectively).

The resulting composition of the new trimetallic neutral compounds were Ag 0.731(6) and Cu 1.269(6) for **I**, Au 1.287(2) and Cu 0.713(2) for **II**, and Au 1.052(3) and Ag 0.948(3) for **III**. A second crystal was collected in the case of **II**, and the free variables refined as follows: 0.734(2) Au(1), 0.628(2) Au(2). The resulting composition was Au 1.362(2) and Cu 0.638(2), quite similar to that found in the first crystal.

Unlike NHC = IPr, the reactions between the mono-anions **1**, **3** and **5** with one equivalent of M'(IMes)Cl in dmso or thf did not allow to isolate any $Fe(CO)_4(MIMes)(M'IMes)$ species. Although in some cases there was the *in-situ* spectroscopic evidence of the trimetallic cluster (by comparison with the IR spectra of **20**-**22**), after work-up of the reaction mixtures, $[M_3Fe_3(CO)_{12}]^{3-}$ (M = Cu, **17**; Ag, **7**) clusters, or their oxidised products $[M_5Fe_4(CO)_{16}]^{3-}$, were always isolated. Indeed, **7** and **17** clusters were often detected (by IR spectroscopy) as the major species in solution in the crude reaction mixtures prior to work-up.

In particular, by reacting **3** with one equivalent of Au(IMes)Cl in dmso, followed by precipitation with water, extraction of the residue in acetone and slow diffusion of *n*-hexane, crystals of $[Au(IMes)_2]_3[\mathbf{7}]\cdot$solv suitable for X-ray analyses were obtained. Following the same procedure but using a saturated solution of $[NEt_4]Br$ in water for precipitation, crystals of $[NEt_4]_2[Au(IMes)_2][\mathbf{7}]\cdot$dmf were isolated. The molecular structures of the $[Au(IMes)_2]^+$ cations and **7** anions were already reported in the literature as miscellaneous salts (Figure 3.13).

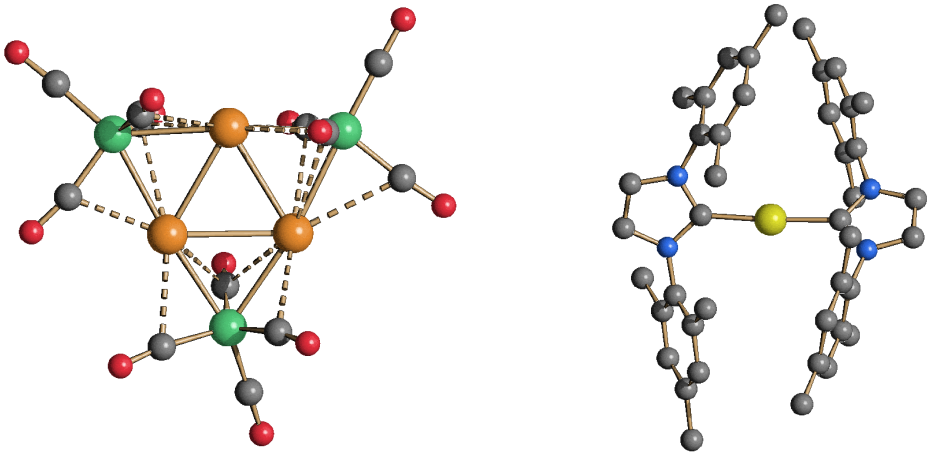

(a) (b)

Figure 3.13 Molecular structures of (a) $[Ag_3Fe_3(CO)_{12}]^{3-}$ (**7**) and (b) $[Au(IMes)_2]^+$ as found in $[Au(IMes)_2]_3[Ag_3Fe_3(CO)_{12}]\cdot$solv and $[NEt_2]_2[Au(IMes)_2][Ag_3Fe_3(CO)_{12}]\cdot$dmf. Ag···C(O) contacts [2.453(4)-2.993 (4) Å] are represented as fragmented lines. Hydrogen atoms have been omitted for clarity (green, Fe; orange, Ag; yellow, Au; blue, N; red, O; grey, C).[39]

Similarly, the reaction of **3** with one equivalent of Cu(IMes)Cl under analogous experimental conditions, resulted in crystals of $[NEt_4]_2[Cu(IMes)_2][\mathbf{7}]\cdot CH_3COCH_3$ and $[NEt_4]_2[Cu(IMes)_2][\mathbf{7}]\cdot$solv, suitable for X-ray crystallography (Figure 3.14).

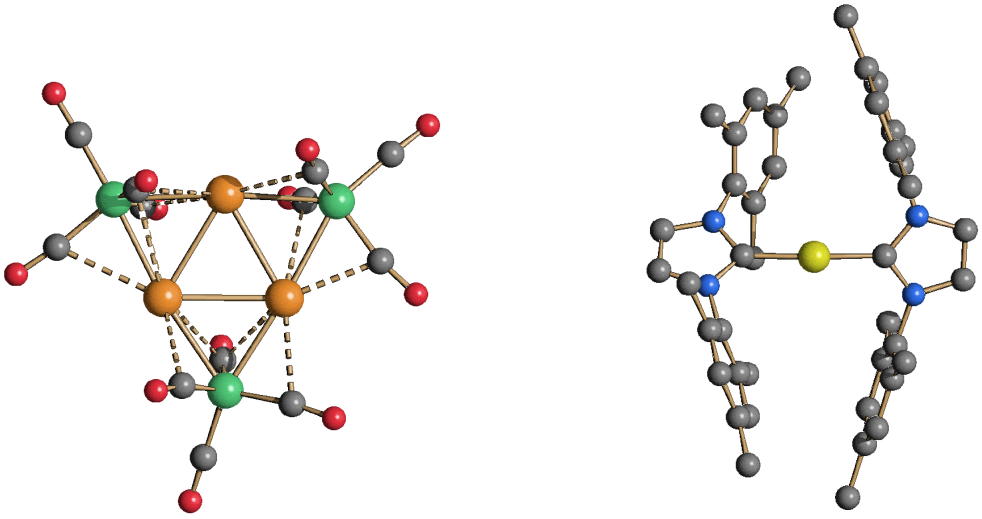

(a) (b)

Figure 3.14 Molecular structures of (a) $[Ag_3Fe_3(CO)_{12}]^{3-}$ (**7**) and (b) $[Cu(IMes)_2]^+$ as found in $[NEt_2]_2[Cu(IMes)_2][\mathbf{7}]\cdot CH_3COCH_3$ and $[NEt_2]_2[Cu(IMes)_2][\mathbf{7}]\cdot$solv. Ag···C(O) contacts [2.447(4)-3.001(4) Å] are represented as fragmented lines. Hydrogen atoms have been omitted for clarity (green, Fe; orange, Ag; yellow, Cu; blue, N; red, O; grey, C).

It must be remarked that **7** was easily oxidised to $[Ag_5Fe_4(CO)_{16}]^{3-}$ (**9**) by adventitious air and, therefore, particular attention must be used during work-up. As a proof of this point, crystals of $[NEt_4][M(IMes)_2]_2$[**9**]·4thf (M= 0.94 Au, 1.06 Ag) were once obtained due to problems during work-up.

Formation of $[M_3Fe_3(CO)_{12}]^{3-}$ species during the attempts to isolate $Fe(CO)_4(MIMes)(M'IMes)$ was not surprising. Indeed, as previously reported,[32] thermal treatment, even under gentle conditions, of $Fe(CO)_4(MIMes)_2$ (M = Cu, Ag, Au) species resulted in $[M_3Fe_3(CO)_{12}]^{3-}$ in accord to equation (3.2):

$$3Fe(CO)_4(MIMes)_2 \rightarrow [M_3Fe_3(CO)_{12}]^{3-} + 3[M(IMes)_2]^{+} \quad (3.2)$$

The thermal treatment of $Fe(CO)_4(MIMes)_2$ was the only way to prepare $[Ag_3Fe_3(CO)_{12}]^{3-}$ and $[Au_3Fe_3(CO)_{12}]^{3-}$, since the reaction of $[Fe(CO)_4]^{2-}$ with M(I) (M = Ag, Au) salts afforded $[Ag_4Fe_4(CO)_{16}]^{4-}$ and $[Au_4Fe_4(CO)_{16}]^{4-}$. Conversely, $[Cu_3Fe_3(CO)_{12}]^{3-}$ was obtained by thermal decomposition of $Fe(CO)_4(CuIMes)_2$ as well as reaction of $[Fe(CO)_4]^{2-}$ with Cu(I) salts. In the case of $Fe(CO)_4(MIMes)(M'IMes)$, it was interesting to notice that complete segregation of the two group 11 metals was observed during the decomposition, at least in the case of Cu/Ag and Ag/Au. Unfortunately, crystals were not obtained for the Cu/Au-IMes system. As summarised in equation (3.3), these reactions selectively afforded $[Ag_3Fe_3(CO)_{12}]^{3-}$ anions and $[M(IMes)_2]^{+}$ (M = Cu, Au) cations.

$$3Fe(CO)_4(AgIMes)(MIMes) \rightarrow [Ag_3Fe_3(CO)_{12}]^{3-} + 3[M(IMes)_2]^{+} \quad (3.3)$$

Another interesting compound was isolated after reacting $Na_2[Fe(CO)_4]$·2thf with Cu(IMes)Cl and Ag(IMes)Cl in thf. In particular, few crystals of $Fe(CO)_4(CH_2IMes)$ (**23**) suitable for X-ray crystallography were obtained after slow diffusion of *n*-pentane on the CH_2Cl_2 solution (Figure 3.15). These were likely to arise from the decomposition of $Fe(CO)_4(CuIMes)(AgIMes)$ and activation of CH_2Cl_2, as reported in Chapter 2 for related Fe-Au-NHC complexes.[31] **23** contained the zwitterionic (1,3-di-mesitylimidazolium-2-yl)methyl ligand (formally a two-electron donor) bonded to $Fe(CO)_4$. Some examples of related zwitterionic ligands derived by NHC carbene bonded to miscellaneous metals have been previously reported in the literature.[43–45]

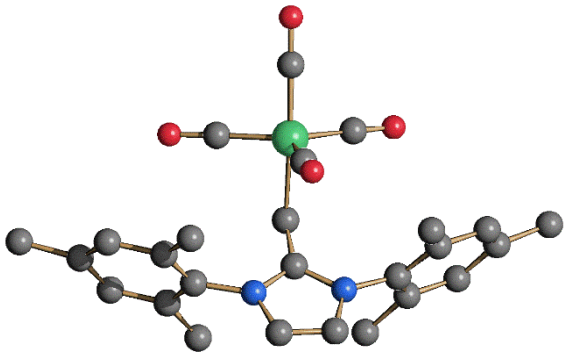

Figure 3.15 Molecular structure of $Fe(CO)_4(CH_2IMes)$ (**23**). Hydrogen atoms have been omitted for clarity (green, Fe; blue, N; red, O; grey, C). Main bond distances (Å) and angles (°): Fe-C_{CH2} 2.158(2), Fe-CO 1.771(3)-1.796(3), C_{CH2}-C_{IMes} 1.448(5), Fe-C_{CH2}-C_{IMes} 111.24(16).[39]

Computational study

In order to shed light on the decomposition products of $Fe(CO)_4(MIMes)(M'IMes)$ clusters, the Gibbs energy variations of the reactions were computationally estimated by means of PBEh-3c calculations. The reactions are summarised in Table 3.5. As observable, in the case of M = Ag and M' = Cu or Au, the formation of $[Ag_3Fe_3(CO)_{12}]^{3-}$ is thermodynamically favoured with respect to $[Cu_3Fe_3(CO)_{12}]^{3-}$ or $[Au_3Fe_3(CO)_{12}]^{3-}$. Despite the fact that there is no experimental evidence, DFT calculations suggest the formation of $[Cu_3Fe_3(CO)_{12}]^{3-}$ instead of $[Au_3Fe_3(CO)_{12}]^{3-}$ for the decomposition of $Fe(CO)_4(CuIMes)(AuIMes)$. The data in Table 3.5 can be rationalised on the basis of the different stability of the M-IMes bonds on changing the coinage metal. The computed dissociation energy for the reaction $[Au(IMes)_2]^+ \rightarrow [AuIMes]^+ + IMes$ is 6.5 kcal mol^{-1} higher than that for the corresponding reaction with M = Cu and 19.5 kcal mol^{-1} higher on comparing M = Au with M = Ag. The stability of the M-IMes bonds therefore follows the order Au > Cu > Ag, and the decompositions of the $Fe(CO)_4(MIMes)(M'IMes)$ clusters afford the most stable $[M(IMes)_2]^+$ complex as product. The computed data here reported are in line with the previously stated experimental observation that Cu-containing complexes resembled more to Au-complexes than Ag-complexes.

Table 3.5 Relative Gibbs energy variations (kcal mol^{-1}) between the possible products of the decomposition reactions of $Fe(CO)_4(MIMes)(M'IMes)$ clusters.

Reactants	First set of products (R1)	Second set of products (R2)	ΔG(R2)-ΔG(R1)
$3Fe(CO)_4(CuIMes)(AgIMes)$	$[Cu_3Fe_3(CO)_{12}]^{3-}$ + 3 $[Ag(IMes)_2]^+$	$[Ag_3Fe_3(CO)_{12}]^{3-}$ + 3 $[Cu(IMes)_2]^+$	-28.1
$3\ Fe(CO)_4(AgIMes)(AuIMes)$	$[Au_3Fe_3(CO)_{12}]^{3-}$ + 3 $[Ag(IMes)_2]^+$	$[Ag_3Fe_3(CO)_{12}]^{3-}$ + 3$[Au(IMes)_2]^+$	-46.7
$3\ Fe(CO)_4(CuIMes)(AuIMes)$	$[Au_3Fe_3(CO)_{12}]^{3-}$ + 3 $[Cu(IMes)_2]^+$	$[Cu_3Fe_3(CO)_{12}]^{3-}$ + 3 $[Au(IMes)_2]^+$	-18.7

Final Remarks

In this chapter a general strategy for the syntheses of new Fe-M (M = Ag, Cu) carbonyl clusters supported by N-Heterocyclic carbene ligands has been reported, starting from the Collman's reagent and M(NHC)Cl (M = Ag, Cu) complexes. The new species were fully characterised by means of IR, ^{1}H NMR and^{13}C{^{1}H} NMR spectroscopy, and their structures determined by X-ray analyses.

The synthetic protocol adopted in the previous chapter for the Au-containing compounds has been applied to the other two coinage metals, Ag and Cu. As in the case of Au, the result of the reactions strictly depends on the stoichiometry and the solvent employed. Indeed, the formation of $[Fe(CO)_4(MNHC)]^-$ (M = Cu, NHC = IMes, **1**; M = Cu, NHC = IPr, **2;** M = Ag, NHC = IMes, **3**; M = Ag, NHC = IPr, **4**) is favoured with 1:1 stoichiometry in polar solvent, such as dmso, while the neutral compounds $Fe(CO)_4(MNHC)_2$ (M = Cu, NHC = IMes, **11**; M = Cu, NHC = IPr, **12**; M = Ag, NHC = IMes, **13**; M = Ag, NHC = IPr, **14**) are easily obtained by reacting $Na_2[Fe(CO)_4]\cdot 2thf$ with two equivalents of M(NHC)Cl in a less polar solvent, such as thf.

In order to study the reactivity of these neutral species, they have been thermally treated in dmso at 130 °C. Compounds **11, 13** and **14** rapidly decomposed affording the triangular clusters $[M_3Fe_3(CO)_{12}]^{3-}$ (M = Cu, **17**; Ag, **7**), while **12** was thermally stable and displayed only limited dissociation of one $[CuIPr]^+$ group and resulted in a mixture of unreacted **12** (major) and **2** (minor).

It is important to notice that the thermal treatment of $Fe(CO)_4(MIMes)_2$ is the only way to obtain the triangular $[M_3Fe_3(CO)_{12}]^{3-}$ cluster for Au and Ag, while the square-in-a-square-type clusters $[\{MFe(CO)_4\}_4]^{4-}$ (M = Ag, **8**; Au, **19**) result from the reaction of the Collman's reagent with the M(I) salts (M = Ag, Au). As regards Cu, the $[\{CuFe(CO)_4\}_3]^{3-}$ triangular cluster is obtained independently of the synthetic strategy adopted.

Finally, the preparation of neutral trimetallic clusters of the general type $Fe(CO)_4(MNHC)(M'NHC)$ (NHC = IMes, IPr; M, M' = Cu, Ag, Au; M ≠ M') has been explored. The reactions between mono-anions $[Fe(CO)_4(MNHC)]^-$ (**1**-**6**) and one equivalent of M'(NHC)Cl were performed, but only with NHC = IPr it was possible to isolate in satisfactory yields all the new three species $Fe(CO)_4(CuIPr)(AgIPr)$ (**20**), $Fe(CO)_4(CuIPr)(AuIPr)$ (**21**) and $Fe(CO)_4(AgIPr)(AuIPr)$ (**22**). The reactions with NHC = IMes did not allow to isolate any $Fe(CO)_4(MIMes)(M'IMes)$, although in some cases there was the *in-situ* spectroscopic evidence of

the trimetallic cluster. Lastly, the new species $Fe(CO)_4(CH_2IMes)$ (**23**) has been obtained from the reaction of $Na_2[Fe(CO)_4]\cdot 2thf$ with Cu(IMes)Cl and Ag(IMes)Cl in thf.

CHAPTER 4

$[M_xM'_{5-x}Fe_4(CO)_{16}]^{3-}$

(M, M' = Cu, Ag, Au; M ≠ M'; x = 0-5)

2-D Alloy Carbonyl Clusters

4.1 Introduction

In the previous chapter, we noticed that several reactions led to the formation of $[M_3Fe_3(CO)_{12}]^{3-}$ and $[M_4Fe_4(CO)_{16}]^{4-}$ (M = Ag, Au), as a consequence of the loss of the ancillary ligands. For this reason, we investigated new reaction paths for the synthesis of new iron bimetallic carbonyl clusters (M = Ag, Cu, Au) devoid of ancillary ligands.

Species such as $[M_3Fe_3(CO)_{12}]^{3-}$ (M = Cu, Ag, Au), $[M_4Fe_4(CO)_{16}]^{4-}$ (M = Ag, Au) and $[M_5Fe_4(CO)_{16}]^{3-}$ (M = Cu, Ag, Au) may be viewed as 2-D molecular clusters, consisting of triangular M_3, square M_4 or centred rectangular M_5 2-D cores stabilised by $Fe(CO)_4$ fragments. During the attempts, we found out that it was possible to synthesise $[M_xM'_{5-x}Fe_4(CO)_{16}]^{3-}$ (M, M' = Cu, Ag, Au; M ≠ M'; x = 0-5) 2-D alloy molecular clusters by a combination of oxidation, condensation and substitution reactions.

In the literature, many Fe-M homoleptic carbonyl clusters are known. Under equimolar condition of Fe/M, the tetramer of $[MFe(CO)_4]^-$ was formed in the case of Au and Ag, that is $[Au_4Fe_4(CO)_{16}]^{4-}$ and $[Ag_4Fe_4(CO)_{16}]^{4-}$. These $[M_4Fe_4(CO)_{16}]^{4-}$ are composed of a M_4^{4+} square surrounded by four bridging $[Fe(CO)_4]^{2-}$ groups (Figure 4.1).[41,42] These crystal structures have been described in Chapter 3.

In the case of Cu, it is noteworthy that with a stoichiometric ratio Fe/Cu = 1 the species $[Cu_3Fe_3(CO)_{12}]^{3-}$ is formed. This cluster may be viewed as the trimer of $[MFe(CO)_4]^-$. It is composed of a Cu_3^{3+} triangle, with the three edges capped by a $[Fe(CO)_4]^{2-}$ fragment, that acts as a double bridging ligand (Figure 4.2).

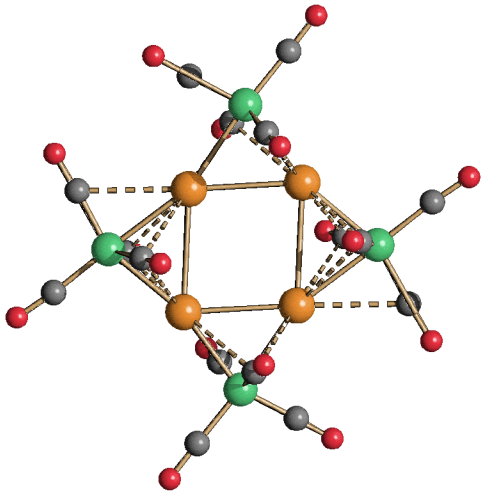

Figure 4.1 Molecular structure of $[M_4Fe_4(CO)_{16}]^{4-}$ (M= Ag, Au). M-C(O) contacts are represented as fragmented lines (orange, M; green, Fe; grey, C; red, O).[46]

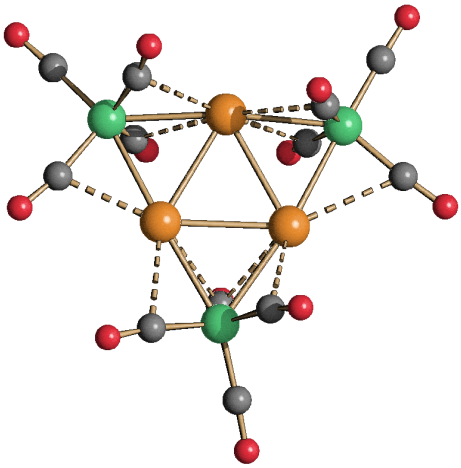

Figure 4.2 Molecular structure of $[Cu_3Fe_3(CO)_{12}]^{3-}$. M-C(O) contacts are represented as fragmented lines (orange, Cu; green, Fe; grey, C; red, O).[46]

The tendency of Cu(I) to form the trimer can be ascribed to its smaller size compared to Au and Ag. While the species $[Au_3Fe_3(CO)_{12}]^{3-}$ and $[Ag_3Fe_3(CO)_{12}]^{3-}$ are known and derive from the thermal decomposition of the neutral $Fe(CO)_4(MIMes)_2$ (M = Ag, Au; IMes = $C_3N_2H_2(C_6H_2Me_3)_2$) as described in Chapter 3, the compound $[Cu_4Fe_4(CO)_{16}]^{4-}$ has never been observed.[32]

With increasing amount of the monovalent cations Cu(I), Ag(I) and Au(I), iron bimetallic carbonyl clusters such as $[M_5Fe_4(CO)_{16}]^{3-}$ and $[M_6Fe_4(CO)_{16}]^{2-}$ are formed. The species $[M_5Fe_4(CO)_{16}]^{3-}$ is constituted by a M_5^{5+} centred rectangle capped by four $[Fe(CO)_4]^{2-}$ units and it may be viewed as a $[M_4Fe_4(CO)_{16}]^{4-}$ with an additional centred M^+. The $[M_6Fe_4(CO)_{16}]^{2-}$ cluster (at least for Ag and Au) can be considered as an oligomeric form that precipitates as an amorphous solid as its ammonium salt (Figure 4.3).

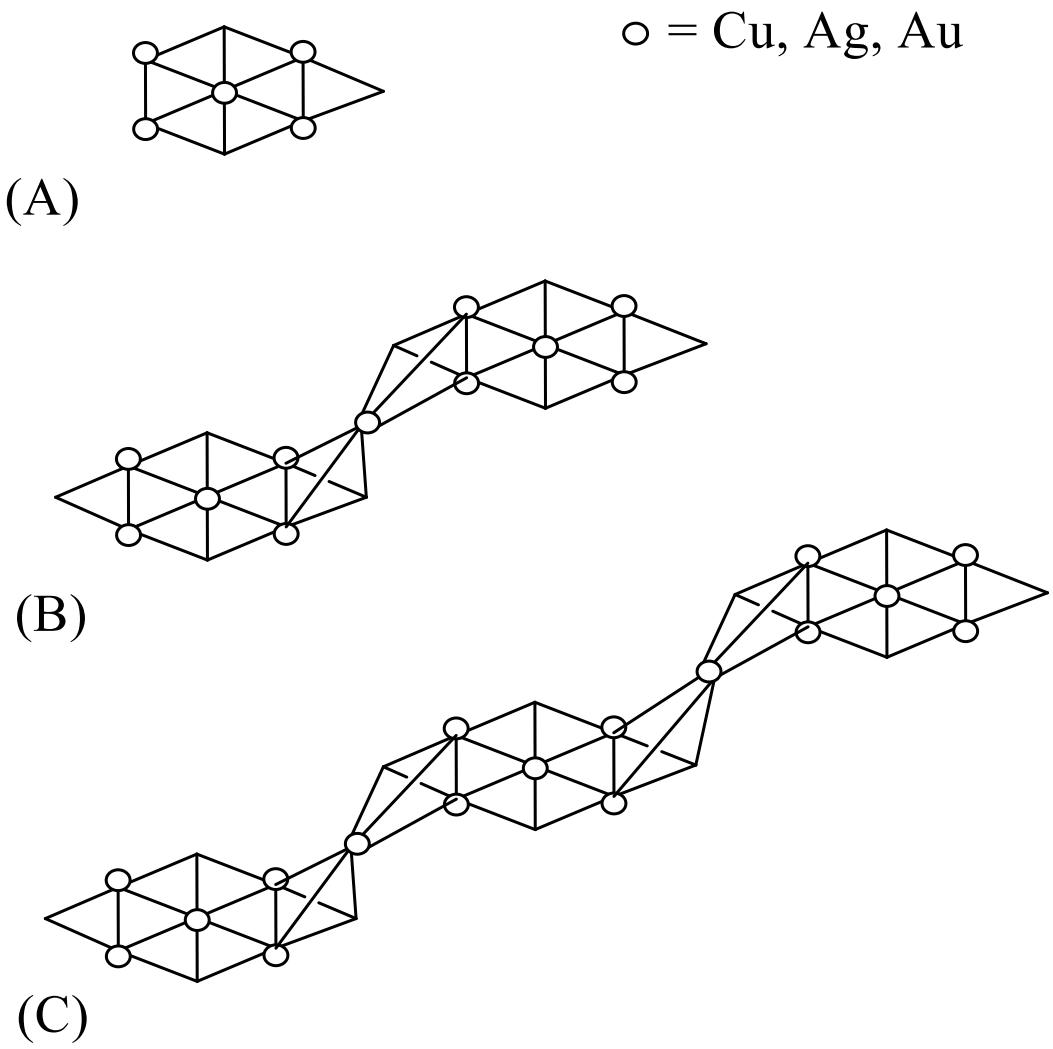

Figure 4.3 Growth scheme of $[M_6Fe_4(CO)_{16}]^{2-}$ cluster in the oligomeric form: (a) $[M_5Fe_4(CO)_{16}]^{3-}$ unit; (b) $[M\{M_5Fe_4(CO)_{16}\}_2]^{5-}$ dimer; (c) $[M_2\{M_5Fe_4(CO)_{16}\}_3]^{7-}$ trimer.[46]

This compound retains the $[M_5Fe_4(CO)_{16}]^{3-}$ planar structure with two additional M^+ cations that act as bridging group between two $[M_5Fe_4(CO)_{16}]^{3-}$ units. The possible resulting species are: $[M\{M_5Fe_4(CO)_{16}\}_2]^{5-}$, $[M_2\{M_5Fe_4(CO)_{16}\}_3]^{7-}$, $[M_3\{M_5Fe_4(CO)_{16}\}_4]^{9-}$, and so on.[38,41] Although these species are very interesting, they present a practical problem: the higher their negative charge is, the less soluble they are. For this reason, nowadays their characterisation is not complete. Conversely, thanks to its good solubility, the monomeric $[Cu_6Fe_4(CO)_{16}]^{2-}$ has been fully characterised (Figure 4.4). At difference compared to Ag and Au, this compound is constituted by a Cu_6^{6+} octahedron in which four of the eight triangular faces are capped by $[Fe(CO)_4]^{2-}$ fragments.

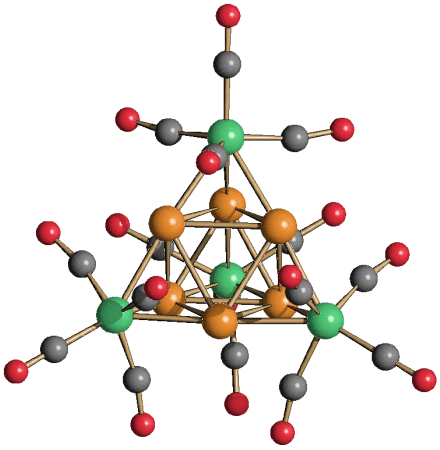

Figure 4.4 Molecular structure of $[Cu_6Fe_4(CO)_{16}]^{2-}$ (orange, Cu; green, Fe; grey, C; red, O).

By increasing the amount of M^+, depending on the nature of the metal, different products may be observed. In the case of Ag, the addition of one Ag^+ leads to the condensation of two $[Ag_6Fe_4(CO)_{16}]^{2-}$ units, with the formation of $[Ag_{13}Fe_8(CO)_{32}]^{n-}$ (n= 3, 4, 5).[47,48]

A different reactivity is observed in the case of Au. Indeed, further addition of Au(I) results in mixtures of *gold browns* such as $[Au_{21}\{Fe(CO)_4\}_{10}]^{5-}$, $[Au_{22}\{Fe(CO)_4\}_{12}]^{6-}$, $[Au_{28}\{Fe(CO)_3\}_4\{Fe(CO)_4\}_{10}]^{8-}$ and $[Au_{34}\{Fe(CO)_3\}_6\{Fe(CO)_4\}_8]^{10-}$ (Figure 4.5).[49]

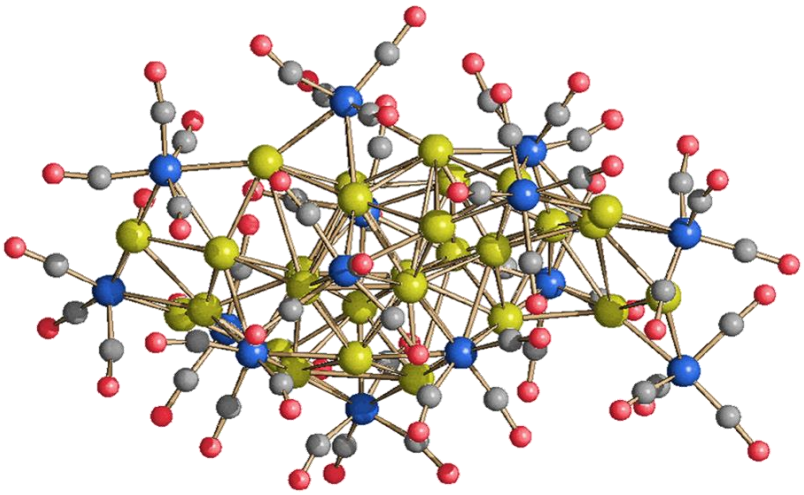

Figure 4.5 Molecular structure of $[Au_{28}\{Fe(CO)_3\}_4\{Fe(CO)_4\}_{10}]^{8-}$ (yellow, Au; blue, Fe; grey, C; red, O).[49]

Further addition of Au(I) leads to the oxidation of the $[Fe(CO)_4]^{2-}$ fragments and to gold disproportion, from which $[AuFe_4(CO)_{16}]^-$ is obtained.

4.2 General results

In this chapter, the synthesis and the characterisation of trimetallic $[M_xM'_{5-x}Fe_4(CO)_{16}]^{3-}$ (M, M' = Cu, Ag, Au; M ≠ M'; x = 0-5) clusters are reported. These new compounds resulted from a combination of oxidation, condensation and substitution reactions. The reactions of $[Cu_3Fe_3(CO)_{12}]^{3-}$ with increasing amounts of M(I) (M = Ag, Au) salts led to the formation in sequence of $[Cu_5Fe_4(CO)_{16}]^{3-}$, $[M_xCu_{5-x}Fe_4(CO)_{16}]^{3-}$ (x = 0-5), $[M_5Fe_4(CO)_{16}]^{3-}$ and $[M_6Fe_4(CO)_{16}]^{2-}$. Then, in the case of M = Ag, further addition of M(I) resulted in the formation of $[Ag_{13}Fe_8(CO)_{32}]^{3-}$, whereas *gold browns* and, eventually, $[AuFe_4(CO)_{16}]^-$ were formed when M = Au.

The molecular structures of these clusters have been determined by means of single crystal X-ray diffraction. In order to complete their characterisation, they have been also investigated by a combination of electron spray ionisation mass spectrometry (ESI-MS), IR and UV-visible spectroscopy.

4.3 Synthesis of trimetallic clusters $[Ag_xCu_{5-x}Fe_4(CO)_{16}]^{3-}$ (x = 0-5)

Reactions between Cu-Fe carbonyl clusters and Ag(I) salts

The reactions of $[Cu_3Fe_3(CO)_{12}]^{3-}$ with increasing amounts of $AgNO_3$ in CH_3CN resulted in the formation of the trimetallic clusters $[Ag_xCu_{5-x}Fe_4(CO)_{16}]^{3-}$ (x = 0-5), in accord with Scheme 4.1.

Scheme 4.1. Synthesis of $[Ag_xCu_{5-x}Fe_4(CO)_{16}]^{3-}$ (x = 0-5).

$[Cu_3Fe_3(CO)_{12}]^{3-}$ or $[Cu_5Fe_4(CO)_{16}]^{3-}$

+ Ag(I) ↓

$[Ag_xCu_{5-x}Fe_4(CO)_{16}]^{3-}$

+ Ag(I) ↓

$[Ag_6Fe_4(CO)_{16}]^{2-}$

+ Ag(I) ↓

$[Ag_{13}Fe_8(CO)_{32}]^{3-}$

At the end of each reaction, the work-up was performed by removing the solvent *in vacuo*, washing the solid residue with water and toluene, and extracting the product and by-products in solvents with increasing polarity. The progress of the reaction was monitored by IR spectroscopy that showed firstly the replacement of the ν_{CO} bands of $[Cu_3Fe_3(CO)_{12}]^{3-}$ (1921 and 1843 cm^{-1}) by two intense ν_{CO} bands comprised between those of $[Cu_5Fe_4(CO)_{16}]^{3-}$ (1937 and 1880 cm^{-1}) and $[Ag_5Fe_4(CO)_{16}]^{3-}$ (1948 and 1880 cm^{-1}), depending on the Ag content. By performing several reactions with different stoichiometry, it was possible to isolate a large number of $[Ag_xCu_{5-x}Fe_4(CO)_{16}]^{3-}$ (x = 0-5) clusters with various compositions. What we have noticed is that by increasing the amount of Ag(I) salt (up to 1 equivalent), the stoichiometric coefficient "x" increased.

An interesting aspect of these new compounds was the mechanism behind their formation, that could be explained by considering a combination of oxidation (equation (4.1)), condensation (equation (4.2)) and substitution (equations (4.3-4.7)) reactions. This last one was confirmed by reacting preformed $[Cu_5Fe_4(CO)_{16}]^{3-}$ with increasing amounts of $AgNO_3$. Also in these cases, formation of $[Ag_xCu_{5-x}Fe_4(CO)_{16}]^{3-}$ (x = 0-5) was observed.

Oxidation

$$5[Cu_3Fe_3(CO)_{12}]^{3-} + 6Ag^+ \rightarrow 3[Cu_5Fe_4(CO)_{16}]^{3-} + 6Ag + 3Fe + 12CO \quad (4.1)$$

Condensation

$$4[Cu_3Fe_3(CO)_{12}]^{3-} + 3Ag^+ \rightarrow 3[AgCu_4Fe_4(CO)_{16}]^{3-} \quad (4.2)$$

Substitution

$$[Cu_5Fe_4(CO)_{16}]^{3-} + Ag^+ \rightleftarrows [AgCu_4Fe_4(CO)_{16}]^{3-} + Cu^+ \quad (4.3)$$

$$[AgCu_4Fe_4(CO)_{16}]^{3-} + Ag^+ \rightleftarrows [Ag_2Cu_3Fe_4(CO)_{16}]^{3-} + Cu^+ \quad (4.4)$$

$$[Ag_2Cu_3Fe_4(CO)_{16}]^{3-} + Ag^+ \rightleftarrows [Ag_3Cu_2Fe_4(CO)_{16}]^{3-} + Cu^+ \quad (4.5)$$

$$[Ag_3Cu_2Fe_4(CO)_{16}]^{3-} + Ag^+ \rightleftarrows [Ag_4CuFe_4(CO)_{16}]^{3-} + Cu^+ \quad (4.6)$$

$$[Ag_4CuFe_4(CO)_{16}]^{3-} + Ag^+ \rightleftarrows [Ag_5Fe_4(CO)_{16}]^{3-} + Cu^+ \quad (4.7)$$

By pushing the reaction with an excess of $AgNO_3$ (> 1 equivalent per $[Cu_3Fe_3(CO)_{12}]^{3-}$), two new ν_{CO} bands at 1970 and 1895 cm^{-1}, attributable to $[Ag_6Fe_4(CO)_{16}]^{2-}$, appeared besides those of $[Ag_xCu_{5-x}Fe_4(CO)_{16}]^{3-}$ (x = 0-5), and rapidly became the major ones (equation (4.8)). Formation of $[Ag_6Fe_4(CO)_{16}]^{2-}$ was accompanied by the precipitation of an amorphous solid. Indeed, it was previously reported in the literature that $[Ag_6Fe_4(CO)_{16}]^{2-}$ was actually a mixture of almost non-

soluble polymeric species. Their formation was due to different equilibria; some representative ones were depicted in equations (4.9-4.11). Because of such equilibria, it was possible during the work-up of these reaction mixtures, to extract in polar solvents and then, crystallise Ag-rich $[Ag_xCu_{5-x}Fe_4(CO)_{16}]^{3-}$ (x = 0-5) species.

$$[Ag_5Fe_4(CO)_{16}]^{3-} + Ag^+ \rightleftarrows [Ag_6Fe_4(CO)_{16}]^{2-} \quad (4.8)$$

$$2[Ag_5Fe_4(CO)_{16}]^{3-} + Ag^+ \rightleftarrows [Ag\{Ag_5Fe_4(CO)_{16}\}_2]^{5-} \quad (4.9)$$

$$3[Ag_5Fe_4(CO)_{16}]^{3-} + 2Ag^+ \rightleftarrows [\{Ag\}_2\{Ag_5Fe_4(CO)_{16}\}_3]^{7-} \quad (4.10)$$

$$2[Ag\{Ag_5Fe_4(CO)_{16}\}_2]^{5-} + Ag^+ \rightleftarrows [\{Ag\}_3\{Ag_5Fe_4(CO)_{16}\}_4]^{9-} \quad (4.11)$$

Eventually, by employing 2.5 or more equivalents of $AgNO_3$ per mole of $[Cu_3Fe_3(CO)_{12}]^{3-}$, $[Ag_{13}Fe_8(CO)_{32}]^{3-}$ was obtained as the final product (equation (4.12)).

$$2[Ag_6Fe_4(CO)_{16}]^{2-} + Ag^+ \rightarrow [Ag_{13}Fe_8(CO)_{32}]^{3-} \quad (4.12)$$

Similar results were obtained by employing $[Cu_5Fe_4(CO)_{16}]^{3-}$ instead of $[Cu_3Fe_3(CO)_{12}]^{3-}$. Moreover, the investigation about the synthesis of $[Ag_xCu_{5-x}Fe_4(CO)_{16}]^{3-}$ was extended to other two Ag(I) salts, that is $Ag(dppe)(NO_3)$ and $Ag_2(dppm)(NO_3)_2$ (dppe = $Ph_2PCH_2CH_2PPh_2$; dppm = $Ph_2PCH_2PPh_2$). In these cases, the reactions were conducted in acetone by adding the Ag(I)-complexes as solids, resulting in $[Ag_xCu_{5-x}Fe_4(CO)_{16}]^{3-}$ as in the case of $AgNO_3$. In general, the presence of the phosphine stabilises Ag(I), by making it less reactive. The aim of this approach was to facilitate the crystallisation of any eventual instable product, but the results obtained were very similar to those achieved from the reactions performed with $AgNO_3$. The only two differences were:

- A major amount of the Ag(I)-phosphine complex was necessary to reach the same IR spectrum obtained with $AgNO_3$. This was due to the fact that the Ag(I)-phosphine complex is less reactive than $AgNO_3$.
- The formation of cationic by-products containing phosphines when the complexes were used in excess. In particular, crystals of $[Ag_3(dppm)_3(OH)][NO_3]_2$, $[Cu_3Br_3(dppe)_3]$ and $[Cu(dppe)_2]_3[Ag_{13}Fe_8(CO)_{16}]$ have been isolated.

The species $[Cu(dppe)_2]_3[Ag_{13}Fe_8(CO)_{16}]$ attracted mostly our interest; it derived from the complete substitution of Cu(I) with Ag(I) in $[Ag_xCu_{5-x}Fe_4(CO)_{16}]^{3-}$ (x = 0-5) while the free phosphines complexed Cu(I), by forming the $[Cu(dppe)_2]^+$ cation. The molecular structure of $[Ag_{13}Fe_8(CO)_{32}]^{3-}$ was already known in the literature and it may be viewed as an Ag(I) hosted in a

12 Ag(I) cuboctahedron, whose triangular faces were capped with eight $[Fe(CO)_4]^{2-}$ fragments (Figure 4.6).

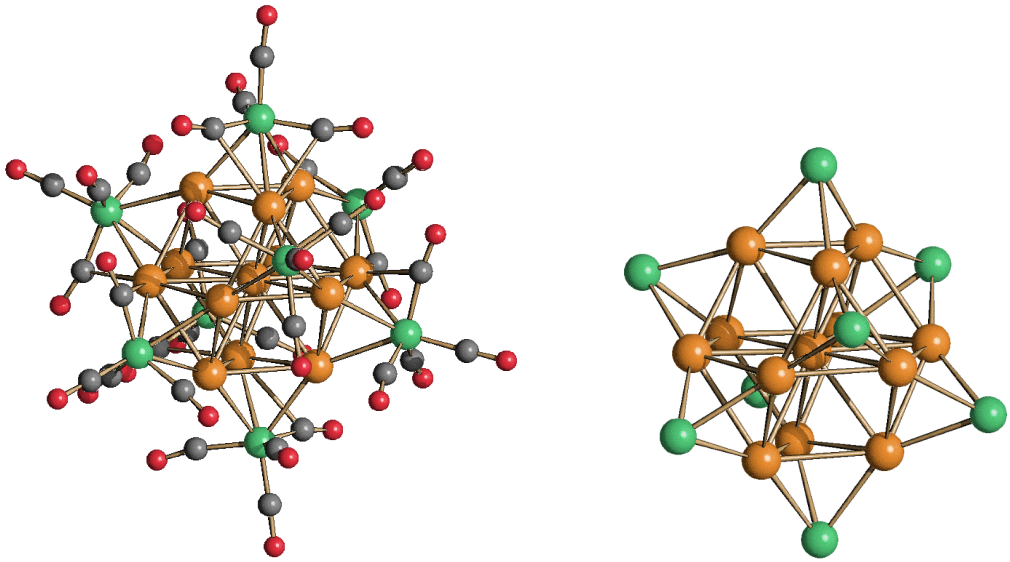

(a) (b)

Figure 4.6 (a) Molecular structure of $[Ag_{13}Fe_8(CO)_{32}]^{3-}$ and (b) its $Ag_{13}Fe_8$ metal cage (orange, Ag; green, Fe; grey, C; red, O).

The molecular structures of $[Ag_3(dppm)_3(OH)][NO_3]_2$ and $[Cu_3Br_3(dppe)_3]$ are shown in Figure 4.7 and Figure 4.8, respectively.

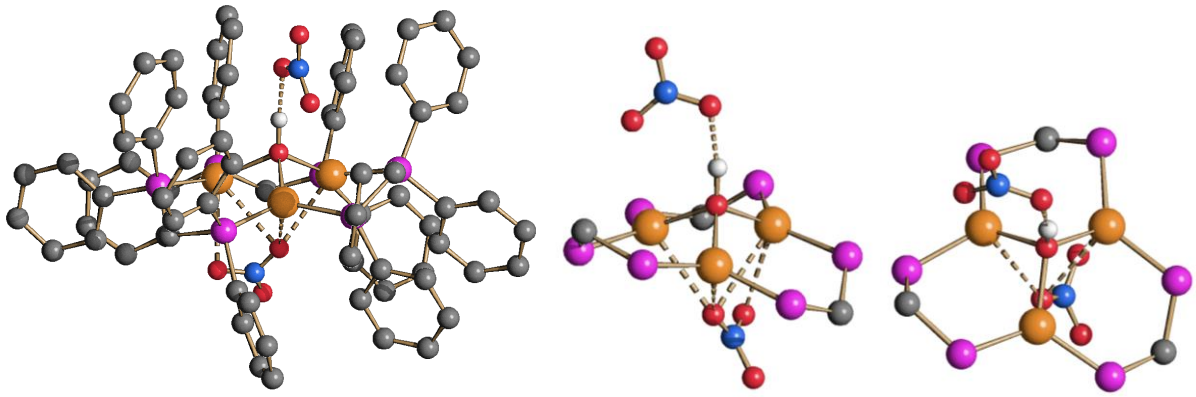

(a) (b) (c)

Figure 4.7 (a) Molecular structures of $[Ag_3(dppm)_3(OH)][NO_3]_2$ and (b, c) its metal cage (orange, Ag; purple, P; grey, C; red, O; blue, N; white, H). Hydrogen atoms, except the O-H group, have been omitted for clarity. The contacts between Ag(I)-NO_3^- and the hydrogen bond between OH^--NO_3^- are represented as fragmented lines.

The cation $[Ag_3(dppm)_3(OH)]^{2+}$ was constituted by three Ag(I), three dppm and a triple bridging OH^-. In this structure, each Ag(I) presented a trigonal planar coordination, since the metal was bonded to two P atoms and one hydroxyl group. This last one derived most likely from traces of humidity in the solvent.

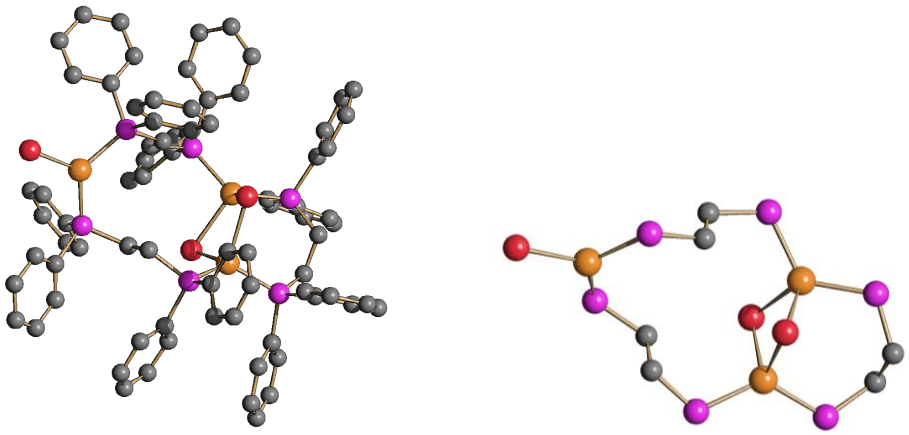

(a) (b)

Figure 4.8 (a) Molecular structure of $[Cu_3Br_3(dppe)_3]$ and (b) its metal cage (orange, Cu; purple, P; grey, C; red, Br). Hydrogen atoms have been omitted for clarity.

The structure of $[Cu_3Br_3(dppe)_3]$ was composed of three Cu(I), three dppe and three Br^-, one terminal and two double-bridging. Because of the bonds with two P and one Br^- atoms, one Cu(I) presented a trigonal planar coordination, while the other two Cu(I) ions played a tetrahedral coordination, since they were bonded to two P and two Br^-.

In general, during the work-up of all these reactions it was possible to separate and crystallise several salts of the type $[NEt_4]_3[Ag_xCu_{5-x}Fe_4(CO)_{16}]$ (x = 0-5). As evidenced in Table 4.1, Ag very rapidly substituted Cu in such clusters, which were always richer in Ag than the reagents. These were the only trimetallic clusters obtained. As shown before (see p. 82), by reacting $[Cu_5Fe_4(CO)_{16}]^{3-}$ with three equivalents of $Ag(dppe)(NO_3)$, crystals of $[Cu(dppe)_2]_3[Ag_{13}Fe_8(CO)_{32}]$ were obtained, that contained a bimetallic Ag-Fe cluster.

Table 4.1 Experimental conditions for the synthesis of $[NEt_4]_3[Ag_xCu_{5-x}Fe_4(CO)_{16}]$ (x = 0-5). Compositions have been determined by SC-XRD analysis.

Entry		Crystallisation solvent	Composition of the reagents		Composition of the products	
			Ag	Cu	Ag	Cu
	$[Cu_3Fe_3(CO)_{12}]^{3-}$ + n $AgNO_3$					
1	n = 0.8	CH_3CN	1.05	3.95	1.02	3.98
2	n = 1.3	CH_3CN	1.51	3.49	5.00	0.00
3		dmf			4.25	0.75
4	n = 2.1	CH_3CN	2.06	2.94	4.88	0.12
5	n = 2.3	dmf	2.17	2.83	4.92	0.08
	$[Cu_5Fe_4(CO)_{16}]^{3-}$ + 2.5 $AgNO_3$					
6		CH_3CN	1.67	3.33	5.00	0.00
7		dmf			4.81	0.19
	$[Ag_4Fe_4(CO)_{16}]^{4-}$ + 1.06 $[Cu(CH_3CN)_4][BF_4]$					
8		CH_3CN	3.95	1.05	4.37	0.63
	$[Ag_5Fe_4(CO)_{16}]^{3-}$ + 3 Cu(IMes)Cl					
9		dmf	3.12	1.88	4.90	0.10
	$[Ag_5Fe_4(CO)_{16}]^{3-}$ +$[Cu_3Fe_3(CO)_{12}]^{3-}$					
10		acetone	3.12	1.88	3.30	1.70
11		CH_3CN			3.45	1.55

Reactions between Ag-Fe carbonyl clusters and Cu(I) salts

Trimetallic $[Ag_xCu_{5-x}Fe_4(CO)_{16}]^{3-}$ (x = 0-5) clusters could also be obtained from the reactions of $[Ag_4Fe_4(CO)_{16}]^{4-}$ or $[Ag_5Fe_4(CO)_{16}]^{3-}$ with Cu(I) salts, or by mixing together $[Cu_3Fe_3(CO)_{12}]^{3-}$ and $[Ag_5Fe_4(CO)_{16}]^{3-}$. Some representative examples were reported in Table 4.1.

It must be remarked that the fractionary indices of $[Ag_xCu_{5-x}Fe_4(CO)_{16}]^{3-}$ (x = 0-5) indicated that they were actually mixtures of species differing for a few Ag/Cu atoms. Indeed, in some cases it was possible to separate, by extraction with solvents of different polarities during work-up of the same reaction, species with slightly different compositions (entries 2-3, 6-7 and 10-11 in Table 4.1).

4.4 Synthesis of trimetallic clusters $[Au_xCu_{5-x}Fe_4(CO)_{16}]^{3-}$ (x = 0-5)

The reactions between $[Cu_3Fe_3(CO)_{12}]^{3-}$ and Au(I) salts in acetonitrile were carried out and the results obtained were very similar to those employing Ag(I) salts, as shown in Scheme 4.2. By adding 0.5 equivalents of Au(I), the oxidation of $[Cu_3Fe_3(CO)_{12}]^{3-}$ to $[Cu_5Fe_4(CO)_{16}]^{3-}$ occurred. Then, by increasing the amount of Au(I), trimetallic $[Au_xCu_{5-x}Fe_4(CO)_{16}]^{3-}$ (x = 0-5) clusters were formed, followed by $[Au_6Fe_4(CO)_{16}]^{2-}$ with 1.5-2.0 equivalents of gold. Then, further addition of Au(I) resulted in mixtures of *gold browns* such as $[Au_{21}\{Fe(CO)_4\}_{10}]^{5-}$, $[Au_{22}\{Fe(CO)_4\}_{12}]^{6-}$, $[Au_{28}\{Fe(CO)_3\}_4\{Fe(CO)_4\}_{10}]^{8-}$, $[Au_{34}\{Fe(CO)_3\}_6\{Fe(CO)_4\}_8]^{10-}$,[49] and, eventually, $[AuFe_4(CO)_{16}]^-$ or $Fe(CO)_4(AuPPh_3)_2$, depending on the fact that an excess of $Au(Et_2S)Cl$ or $Au(PPh_3)Cl$ was used. Also in this case, $[Au_xCu_{5-x}Fe_4(CO)_{16}]^{3-}$ (x = 0-5) were the only trimetallic species isolated.

Scheme 4.2 Synthesis of $[Au_xCu_{5-x}Fe_4(CO)_{16}]^{3-}$ (x = 0-5).

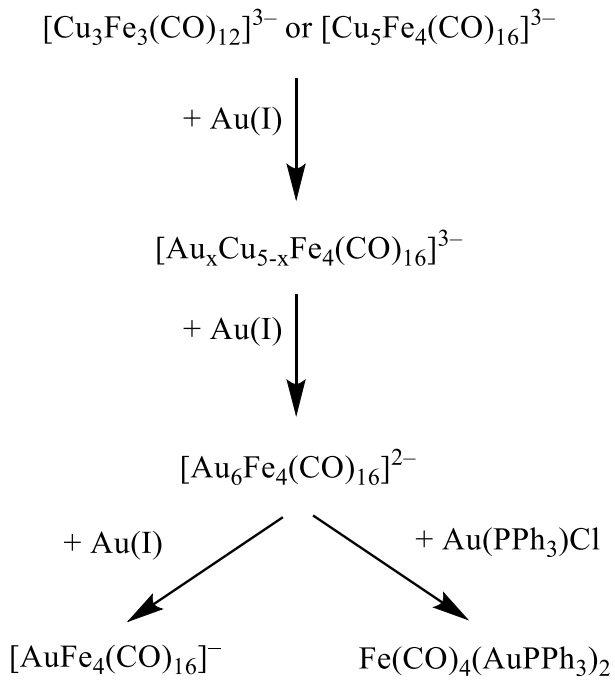

By comparing the results obtained, we found out that the replacement of Cu with Au in $[Au_xCu_{5-x}Fe_4(CO)_{16}]^{3-}$ (x = 0-5) was more gradual than in the related Ag-Cu-Fe clusters. As a consequence, it was possible to obtain species with a more continuous distribution of the two metals (Table 4.2). Moreover, Cu-substitution was favoured by using $Au(Et_2S)Cl$ compared to $Au(PPh_3)Cl$. This might be due to the fact that the phosphine complex was less reactive. Indeed, as in the case of Ag(I)-phosphines, to form $[Au_xCu_{5-x}Fe_4(CO)_{16}]^{3-}$, more Au(I) was requested.

Table 4.2 Experimental conditions for the synthesis of $[NEt_4]_3[Au_xCu_{5-x}Fe_4(CO)_{16}]$ (x = 0-5).

Entry		Crystallisation solvent	Composition of the reagents		Composition of the products	
			Au	Cu	Au	Cu
	$[Cu_3Fe_3(CO)_{12}]^{3-}$ + n $Au(PPh_3)Cl$					
12	n = 1.4	acetone	1.59	3.41	1.15	3.85
13	n = 1.5	acetone	1.67	3.33	1.31	3.69
14		dmf			1.67	3.33
15	n = 3.0	dmf	2.5	2.5	2.48	2.52
	$[Cu_3Fe_3(CO)_{12}]^{3-}$ + n $Au(Et_2S)Cl$					
16	n = 0.7	CH_3CN	0.95	4.05	2.18	2.82
17					2.73	2.27
18	n = 1.9	CH_3CN	1.94	3.06	4.59	0.41
19					4.61	0.39
	$[Cu_5Fe_4(CO)_{16}]^{3-}$ + 1.2 $Au(Et_2S)Cl$					
20		acetone	0.97	4.03	1.09	3.91

4.5 Synthesis of trimetallic clusters $[Au_xAg_{5-x}Fe_4(CO)_{16}]^{3-}$ (x = 0-5)

In order to complete the possible combinations between the three coinage metals, further attempts were made by reacting $[Ag_4Fe_4(CO)_{16}]^{4-}$ with $Au(Et_2S)Cl$. The trimetallic $[Au_xAg_{5-x}Fe_4(CO)_{16}]^{3-}$ (x = 0-5) clusters were, then, obtained and fully characterised as the previous ones (Table 4.3).

Table 4.3 Experimental conditions for the synthesis of $[NEt_4]_3[Au_xAg_{5-x}Fe_4(CO)_{16}]$ (x = 0-5).

Entry		Crystallisation solvent	Composition of the reagents		Composition of the products	
			Au	Ag	Au	Ag
	$[Ag_4Fe_4(CO)_{16}]^{4-}$ + 0.8$Au(Et_2S)Cl$					
21		CH_3CN	0.83	4.17	0.64	4.36
22		acetone			0.81	4.19

4.6 Molecular structures of $[M_xM'_{5-x}Fe_4(CO)_{16}]^{3-}$ (M, M' = Cu, Ag, Au; M ≠ M'; x = 0-5)

Crystals of $[NEt_4]_3[M_xM'_{5-x}Fe_4(CO)_{16}]$ (x = 0-5; M, M' = Cu, Ag, Au; M ≠ M') suitable for X-ray diffractometry have been obtained mainly from acetone, CH_3CN and dmf solutions. The molecular structure common to all trimetallic $[M_xM'_{5-x}Fe_4(CO)_{16}]^{3-}$ (x = 0-5; M, M' = Cu, Ag, Au; M ≠ M') clusters is represented in Figure 4.9.

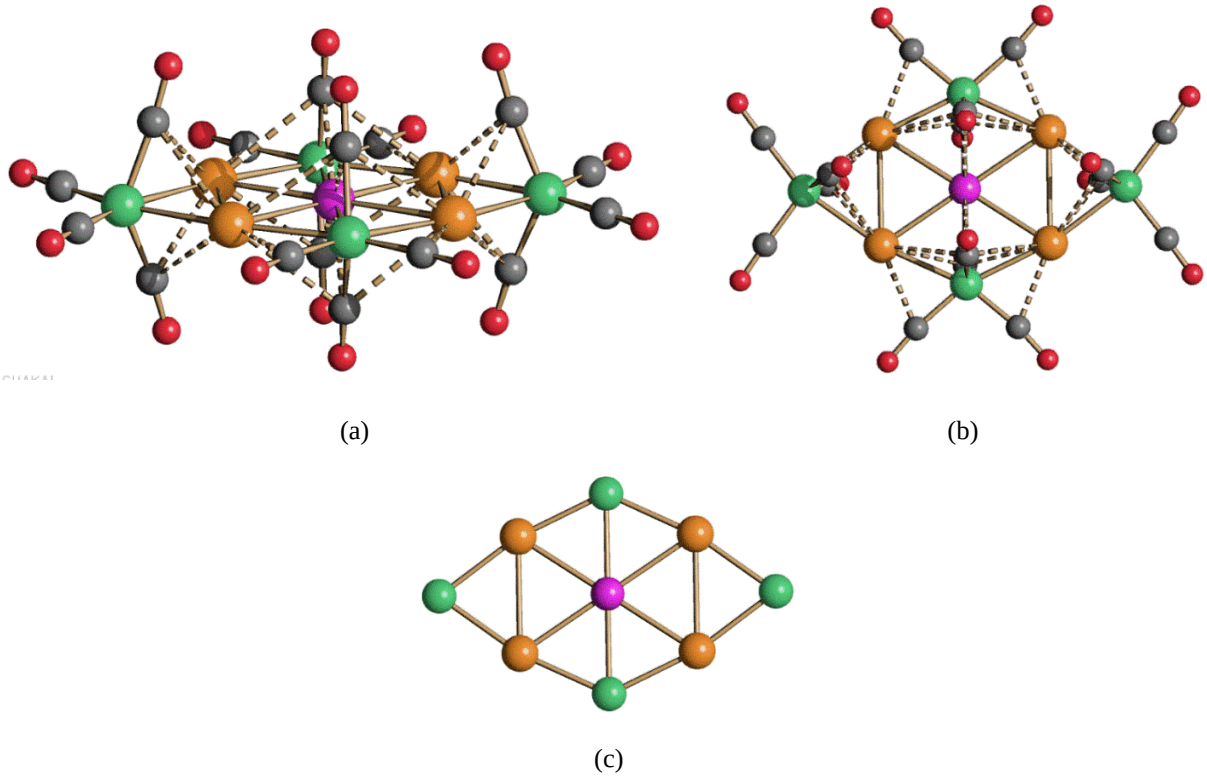

(a) (b)

(c)

Figure 4.9 Molecular structure of the $[M_xM'_{5-x}Fe_4(CO)_{16}]^{3-}$ (x = 0-5; M, M' = Cu, Ag, Au; M ≠ M') clusters (purple, M in the centre; orange, M in the corner positions; green, Fe; grey, C; red, O). M-C(O) contacts are represented as fragmented lines. Two different views are reported (a, b), as well as the metal core (c).[46]

The molecular structure of these mixed $[M_xM'_{5-x}Fe_4(CO)_{16}]^{3-}$ clusters was based on a centred M_5 rectangle, as previously found also in the bimetallic $[M_5Fe_4(CO)_{16}]^{3-}$ (M = Cu, Ag, Au) clusters. The positions occupied by the five coinage metals could be grouped into two sites: a) the unique central position; b) the four equivalent corner positions. This M_5 core was bonded to two μ-$Fe(CO)_4$ and two μ_3-$Fe(CO)_4$ groups on the shorter and longer edges of the rectangle, respectively. Overall, the M atom at the centre formed four M_{centre}-M_{corner} and two M-Fe bonds, whereas M atoms at the corner sites formed one M_{centre}-M_{corner}, one M_{corner}-M_{corner} and two M-Fe bonds. The Fe-M_{corner}-Fe coordination was almost linear, as expected for a d^{10} M(I) ion. Some sub van der Waals M-C(O) contacts were also present, but their nature was still debated.[31,40] They are more likely

forced by steric requirements of the ligands, than a real bonding or van der Waals attraction between M(I) and CO.

The structural analysis of these $[M_xM'_{5-x}Fe_4(CO)_{16}]^{3-}$ clusters highlighted two interesting features:

- The compositional disorder: the crystals obtained contained mixtures of species, and this fact was reflected in the fractional indices present in the formulas of $[M_xM'_{5-x}Fe_4(CO)_{16}]^{3-}$ (x = 0-5; M, M' = Cu, Ag, Au; M ≠ M'). For instance, $[Ag_{4.25}Cu_{0.75}Fe_4(CO)_{16}]^{3-}$ corresponded to a mixture of $[Ag_4CuFe_4(CO)_{16}]^{3-}$ (75%) and $[Ag_5Fe_4(CO)_{16}]^{3-}$ (25%), whereas $[Au_{2.48}Cu_{2.52}Fe_4(CO)_{16}]^{3-}$ contained $[Au_2Cu_3Fe_4(CO)_{16}]^{3-}$ (52%) and $[Au_3Cu_2Fe_4(CO)_{16}]^{3-}$ (48%).
- The substitutional disorder: M and M' were (not equivalently) disordered over the central and corner positions (Tables 4.4-4.6). In the case of Au-Cu clusters, Au strongly preferred the corner sites, and Cu the central position. This trend was observed, even if to a less extent, also in Ag-Cu clusters. In the case of Au-Ag clusters, even if the number of entries was very limited, it was possible to notice a preference of Au for the corner sites. These tendency was corroborated by theoretical studies conducted at the University of Venice.

The preference of Cu for the central position may be, at least partially, explained on the basis of the different ionic radii of the M(I) cations: Cu(I) 77 pm, Ag(I) 115 pm and Au(I) 137 pm. Thus, the smallest Cu(I) ion preferred the central site. Moreover, corner positions displayed two strong M-Fe bonds with an almost linear Fe-M-Fe arrangement. This was the typical coordination found in M(I) complexes. The strong affinity of Au for these corner sites indicated a stronger stability of such interactions in the case of Au compared to Cu and Ag.

Table 4.4 Composition of $[NEt_4]_3[Ag_xCu_{5-x}Fe_4(CO)_{16}]$ (x = 0-5).

Entry*	TOTAL		CENTRE		CORNER	
	Ag	Cu	Ag	Cu	Ag	Cu
1	1.02	3.98	0.02	0.98	1.00	3.00
10	3.30	1.70	0.60	0.40	2.70	1.30
11	3.45	1.55	0.59	0.41	2.86	1.14
3	4.25	0.75	0.83	0.17	3.42	0.58
8	4.37	0.63	0.85	0.15	3.52	0.48
7	4.81	0.19	0.97	0.03	3.84	0.16
4	4.88	0.12	0.97	0.03	3.92	0.08
9	4.90	0.10	0.98	0.02	3.92	0.08
5	4.92	0.08	1.00	0.00	3.92	0.08
2,6	5.00	0.00	1.00	0.00	4.00	0.00

* See Table 4.1. Entries are listed in order of increasing Ag content.

Table 4.5 Composition of $[NEt_4]_3[Au_xCu_{5-x}Fe_4(CO)_{16}]$ (x = 0-5).

Entry*	TOTAL		CENTRE		CORNER	
	Au	Cu	Au	Cu	Au	Cu
20	1.09	3.91	0.00	1.00	1.09	2.91
12	1.15	3.85	0.00	1.00	1.15	2.85
13	1.31	3.69	0.00	1.00	1.31	2.69
14	1.67	3.33	0.00	1.00	1.67	2.33
16	2.18	2.82	0.00	1.00	2.18	1.82
15	2.48	2.52	0.00	1.00	2.48	1.52
17	2.73	2.27	0.00	1.00	2.73	1.27
18	4.59	0.41	0.59	0.41	4.00	0.00
19	4.61	0.39	0.61	0.39	4.00	0.00

* See Table 4.2. Entries are listed in order of increasing Au content.

Table 4.6 Composition of $[NEt_4]_3[Au_xAg_{5-x}Fe_4(CO)_{16}]$ (x = 0-5).

Entry*	TOTAL		CENTRE		CORNER	
	Au	Ag	Au	Ag	Au	Ag
21	0.64	4.36	0.04	0.96	0.60	3.40
22	0.81	4.19	0.05	0.95	0.76	3.24

* See Table 4.3. Entries are listed in order of increasing Au content.

As expected, M_{centre}-M_{corner}, M_{corner}-M_{corner} and M-Fe distances steadily increased moving from Cu-rich to Ag or Au-rich clusters (Tables 4.7-4.9 and Scheme 4.3). This was well exemplified by comparing the M-M and M-Fe distances of trimetallic $[M_xM'_{5-x}Fe_4(CO)_{16}]^{3-}$ (x = 0-5; M, M' = Cu, Ag, Au; M ≠ M') with bimetallic $[M_5Fe_4(CO)_{16}]^{3-}$ (M = Cu, Ag, Au). Indeed, $[Cu_5Fe_4(CO)_{16}]^{3-}$ displayed considerably shorter distances, whereas these were almost identical in $[Ag_5Fe_4(CO)_{16}]^{3-}$ and $[Au_5Fe_4(CO)_{16}]^{3-}$.

Table 4.7 M-M and M-Fe distances of $[NEt_4]_3[Ag_xCu_{5-x}Fe_4(CO)_{16}]$ (x = 0-5).

Entry*	Composition		Distances				
	Ag	Cu	M(1)-M(2)	M(2)-M(2)	M(1)-Fe(1)	M(2)-Fe(1)	M(2)-Fe(2)
**	0.00	5.00	2.53	2.69	2.49	2.43	2.39
1	1.02	3.98	2.61	2.78	2.50	2.47	2.44
10	3.30	1.70	2.73	2.96	2.64	2.57	2.53
11	3.45	1.55	2.73	2.96	2.64	2.58	2.53
3	4.25	0.75	2.77	2.99	2.68	2.61	2.56
8	4.37	0.63	2.77	3.00	2.69	2.62	2.56
7	4.81	0.19	2.79	3.01	2.70	2.64	2.58
4	4.88	0.12	2.79	3.01	2.70	2.64	2.58
9	4.90	0.10	2.80	3.01	2.71	2.64	2.58
5	4.92	0.08	2.79	3.01	2.70	2.64	2.58
2,6	5.00	0.00	2.79	3.01	2.70	2.64	2.58

* See Table 4.1. Entries are listed in order of increasing Ag content.

Table 4.8 M-M and M-Fe distances of $[NEt_4]_3[Au_xCu_{5-x}Fe_4(CO)_{16}]$ (x = 0-5).

Entry*	Composition		Distances				
	Au	Cu	M(1)-M(2)	M(2)-M(2)	M(1)-Fe(1)	M(2)-Fe(1)	M(2)-Fe(2)
**	0.00	5.00	2.53	2.69	2.49	2.43	2.39
20	1.09	3.91	2.60	2.79	2.51	2.46	2.44
12	1.15	3.85	2.61	2.80	2.51	2.46	2.45
13	1.31	3.69	2.61	2.81	2.51	2.47	2.46
14	1.67	3.33	2.63	2.82	2.52	2.48	2.48
16	2.18	2.82	2.65	2.83	2.55	2.50	2.50
15	2.48	2.52	2.66	2.85	2.56	2.52	2.51
17	2.73	2.27	2.66	2.85	2.57	2.52	2.52
18	4.59	0.41	2.75	2.96	2.64	2.59	2.56
19	4.61	0.39	2.76	2.96	2.64	2.60	2.56
***	5.00	0.00	2.78	3.02	2.69	2.61	2.56

* See Table 4.2. Entries are listed in order of increasing Au content.

Table 4.9 M-M and M-Fe distances of $[NEt_4]_3[Au_xAg_{5-x}Fe_4(CO)_{16}]$ (x = 0-5).

Entry*	Composition		Distances				
	Au	Ag	M(1)-M(2)	M(2)-M(2)	M(1)-Fe(1)	M(2)-Fe(1)	M(2)-Fe(2)
**	0.00	5.00	2.79	3.01	2.70	2.64	2.58
21	0.64	4.36	2.79	3.00	2.70	2.64	2.57
22	0.81	4.19	2.78	3.00	2.70	2.63	2.56
***	5.00	0.00	2.78	3.02	2.69	2.61	2.56

* See Table 4.3. Entries are listed in order of increasing Au content.

Scheme 4.3 Labelling of the atoms used in Tables 4.7-4.9.

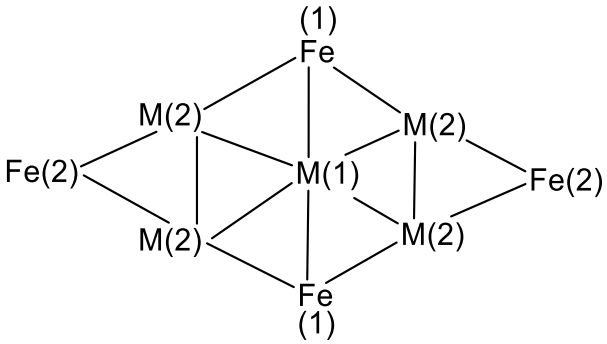

4.7 ESI-MS studies of $[M_xM'_{5-x}Fe_4(CO)_{16}]^{3-}$ (M, M' = Cu, Ag, Au; M ≠ M'; x = 0-5)

In order to further elucidate the composition of the $[M_xM'_{5-x}Fe_4(CO)_{16}]^{3-}$ clusters, ESI-MS studies have been carried out on some of their $[NEt_4]_3[M_xM'_{5-x}Fe_4(CO)_{16}]$ crystals. The ESI-MS spectra recorded on CH_3CN solutions of $[NEt_4]_3[Au_{2.48}Cu_{2.52}Fe_4(CO)_{16}]$, $[NEt_4]_3[Au_{4.62}Cu_{0.38}Fe_4(CO)_{16}]$, $[NEt_4]_3[Ag_{1.02}Cu_{3.98}Fe_4(CO)_{16}]$, $[NEt_4]_3[Au_{1.32}Cu_{3.68}Fe_4(CO)_{16}]$, $[NEt_4]_3[Au_{0.82}Ag_{4.18}Fe_4(CO)_{16}]$ are reported in Figures 4.10-4.14, and peak assignments are summarised in Tables 4.10-4.14.

Under ESI-MS conditions, $[M_xM'_{5-x}Fe_4(CO)_{16}]^{3-}$ clusters were oxidised to the $[M_xM'_{5-x}Fe_4(CO)_{16}]^{2-}$ di-anions and, in some cases, also their $\{[M_xM'_{5-x}Fe_4(CO)_{16}][NEt_4]\}^{2-}$ adducts were present in the spectra. The di-anionic nature of all these ions was confirmed by the systematic loss of m/z 14 units from the molecular ions, that corresponded to a CO ligand (m = 28 uma) assuming z = 2.

The ESI-MS spectrum (ES–) of $[NEt_4]_3[Au_{2.48}Cu_{2.52}Fe_4(CO)_{16}]$ displayed two sets of peaks at m/z (relative intensities in parentheses): 759(*30*), 694(*60*), 680(*10*), 666(*5*), 652(*10*), 638(*100*) and 626(*10*) (**set-1-Au_3Cu_2**); 692(*35*), 628(*60*), 614(*5*), 600(*30*), 586(*60*), 572(*80*) and 558(*15*) (**set-2-Au_2Cu_3**) (Figure 4.10 and Table 4.10). The peaks of **set-1-Au_3Cu_2** originated from the $[Au_3Cu_2Fe_4(CO)_{16}]^{2-}$ ion (m/z = 694) by the stepwise loss of 1-5 CO ligands (m/z = 680, 666, 652, 638, 626) whereas the peak at m/z 759 corresponded to the $\{[Au_3Cu_2Fe_4(CO)_{16}][NEt_4]\}^{2-}$ adduct. Similarly, the peaks of **set-2-Au_2Cu_3** originated from the $[Au_2Cu_3Fe_4(CO)_{16}]^{2-}$ ion (m/z = 628) by the stepwise loss of 1-5 CO ligands (m/z = 614, 600, 586, 572, 558) whereas the peak at m/z 692 corresponded to the $\{[Au_2Cu_3Fe_4(CO)_{16}][NEt_4]\}^{2-}$ adduct. Overall, the ESI-MS analysis indicated that two species of composition Au_3Cu_2 and Au_2Cu_3 were present in similar amounts, in agreement with the X-ray data which suggested that $[NEt_4]_3[Au_{2.48}Cu_{2.52}Fe_4(CO)_{16}]$ contained 48% of $[Au_3Cu_2Fe_4(CO)_{16}]^{3-}$ and 52% of $[Au_2Cu_3Fe_4(CO)_{16}]^{3-}$.

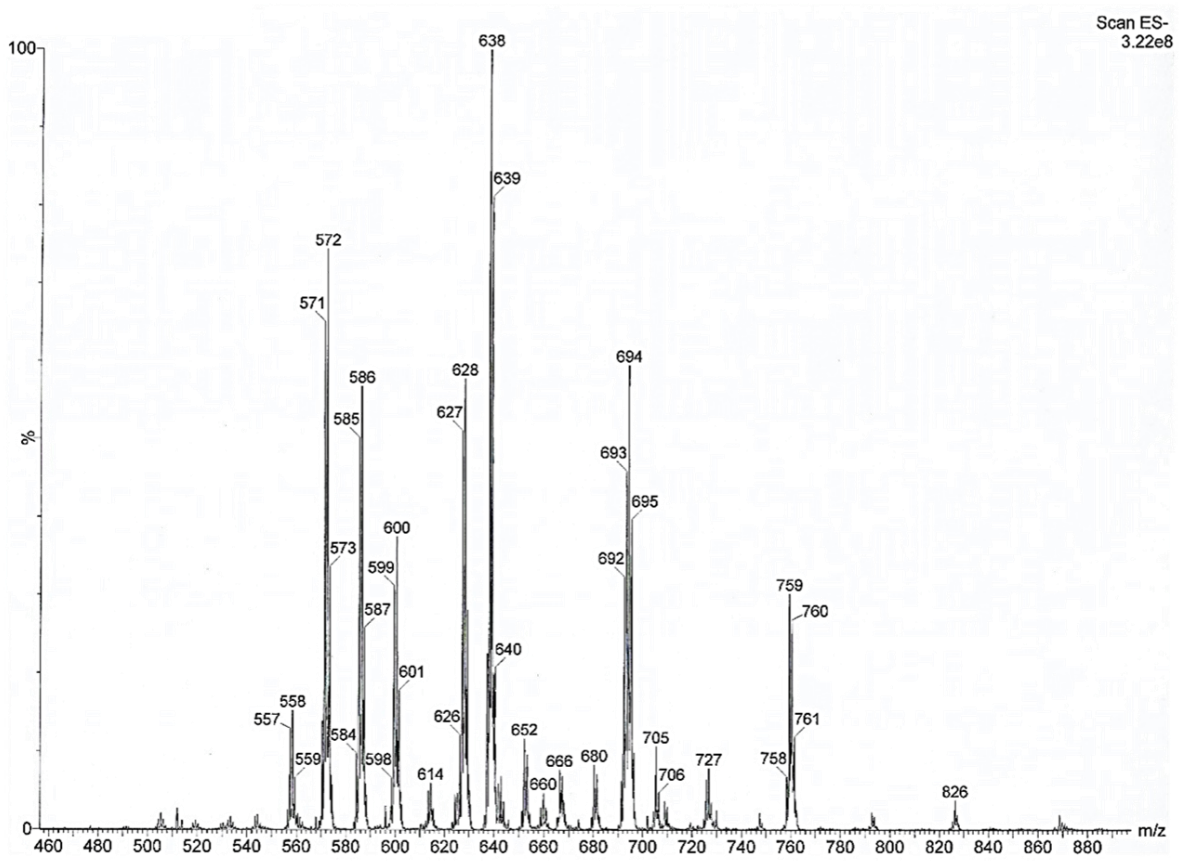

Figure 4.10 ESI-MS spectrum in CH_3CN (ES–) of $[NEt_4]_3[Au_{2.48}Cu_{2.52}Fe_4(CO)_{16}]$.

Table 4.10 Peak assignment of the ESI-MS spectrum (ES–) of $[NEt_4]_3[Au_{2.48}Cu_{2.52}Fe_4(CO)_{16}]$.

m/z	Relative intensity	Ion	Code
759	30	$\{[Au_3Cu_2Fe_4(CO)_{16}][NEt_4]\}^{2-}$	Au_3Cu_2+NEt_4
694	60	$[Au_3Cu_2Fe_4(CO)_{16}]^{2-}$	Au_3Cu_2
692	35	$\{[Au_2Cu_3Fe_4(CO)_{16}][NEt_4]\}^{2-}$	Au_2Cu_3+NEt_4
680	10	$[Au_3Cu_2Fe_4(CO)_{15}]^{2-}$	Au_3Cu_2(-1CO)
666	5	$[Au_3Cu_2Fe_4(CO)_{14}]^{2-}$	Au_3Cu_2(-2CO)
652	10	$[Au_3Cu_2Fe_4(CO)_{13}]^{2-}$	Au_3Cu_2(-3CO)
638	100	$[Au_3Cu_2Fe_4(CO)_{12}]^{2-}$	Au_3Cu_2(-4CO)
628	60	$[Au_2Cu_3Fe_4(CO)_{16}]^{2-}$	Au_2Cu_3
626	10	$[Au_3Cu_2Fe_4(CO)_{11}]^{2-}$	Au_3Cu_2(-5CO)
614	5	$[Au_2Cu_3Fe_4(CO)_{15}]^{2-}$	Au_2Cu_3(-1CO)
600	30	$[Au_2Cu_3Fe_4(CO)_{14}]^{2-}$	Au_2Cu_3(-2CO)
586	60	$[Au_2Cu_3Fe_4(CO)_{13}]^{2-}$	Au_2Cu_3(-3CO)
572	80	$[Au_2Cu_3Fe_4(CO)_{12}]^{2-}$	Au_2Cu_3(-4CO)
558	15	$[Au_2Cu_3Fe_4(CO)_{11}]^{2-}$	Au_2Cu_3(-5CO)

Similar considerations applied to $[NEt_4]_3[Au_{4.62}Cu_{0.38}Fe_4(CO)_{16}]$, for which the X-ray data suggested a mixture of 62% of $[Au_5Fe_4(CO)_{16}]^{3-}$ and 38% of $[Au_4CuFe_4(CO)_{16}]^{3-}$. Indeed, the ESI-MS spectrum showed two sets of peaks attributable to Au_5 (**set-1-Au$_5$**) and Au_4Cu (**set-2-Au$_4$Cu**) species (Figure 4.11 and Table 4.11). The first set (**set-1-Au$_5$**) displayed peaks at m/z 893(*30*), 828(*30*), 814(*45*), 800(*2*) and 772(*80*) attributable to the $\{[Au_5Fe_4(CO)_{16}][NEt_4]\}^{2-}$ adduct, the $[Au_5Fe_4(CO)_{16}]^{2-}$ parent ion and the stepwise loss of 1-4 CO ligands. It must be remarked that the peak corresponding to the loss of 3 carbonyls was probably too weak to be detected. Conversely, the second set (**set-2-Au$_4$Cu**) showed peaks at m/z 826(*30*), 761(*40*), 747(*20*), 730(*70*), 719(*10*) and 705(*100*) attributable to $\{[Au_4CuFe_4(CO)_{16}][NEt_4]\}^{2-}$, $[Au_4CuFe_4(CO)_{16}]^{2-}$ and the stepwise loss of 1-4 CO ligands.

The ESI-MS spectra of $[NEt_4]_3[Ag_{1.02}Cu_{3.98}Fe_4(CO)_{16}]$, $[NEt_4]_3[Au_{1.32}Cu_{3.68}Fe_4(CO)_{16}]$ and $[NEt_4]_3[Au_{0.82}Ag_{4.18}Fe_4(CO)_{16}]$ contained three sets of peaks instead of two sets as above, and suggested a slightly more complicated disorder (compositional) model (Figure 4.12 and Table 4.12). For instance, $[NEt_4]_3[Ag_{1.02}Cu_{3.98}Fe_4(CO)_{16}]$ could have been interpreted as a mixture of 2% of $[Ag_2Cu_3Fe_4(CO)_{16}]^{3-}$ and 98% of $[AgCu_4Fe_4(CO)_{16}]^{3-}$. Conversely, its ESI-MS spectrum displayed three sets of peaks (**set-1-Ag$_2$Cu$_3$**, **set-2-AgCu$_4$** and **set-3-Cu$_5$**) attributable the ionisation of these two species as well as an additional $[Cu_5Fe_4(CO)_{16}]^{3-}$ cluster. Indeed, **set-1-Ag$_2$Cu$_3$** included peaks at m/z 604(*40*), 539(*60*), 525(*10*), 510(*50*) and 497(*30*) attributable to $\{[Ag_2Cu_3Fe_4(CO)_{16}][NEt_4]\}^{2-}$, $[Ag_2Cu_3Fe_4(CO)_{16}]^{2-}$ and the stepwise loss of 1-3 carbonyls. **Set-2-AgCu$_4$** showed peaks at m/z 582(*60*), 517(*90*), 503(*10*), 488(*100*), 474(*65*), 460(*5*) and 447*(70)* attributable to $\{[AgCu_4Fe_4(CO)_{16}][NEt_4]\}^{2-}$, $[AgCu_4Fe_4(CO)_{16}]^{2-}$ and the stepwise loss of 1-5 CO ligands. Then, **set-3-Cu$_5$** comprised peaks at m/z 560(*35*), 495(*50*), 482(*15*), 466(*75*) and 452(*60*) attributable to $\{[Cu_5Fe_4(CO)_{16}][NEt_4]\}^{2-}$, $[Cu_5Fe_4(CO)_{16}]^{2-}$ and the stepwise loss of 1-3 carbonyls.

Similarly, the ESI-MS spectrum of $[NEt_4]_3[Au_{1.32}Cu_{3.68}Fe_4(CO)_{16}]$ suggested the presence of the three species $[Au_2Cu_3Fe_4(CO)_{16}]^{3-}$, $[AuCu_4Fe_4(CO)_{16}]^{3-}$ and $[Cu_5Fe_4(CO)_{16}]^{3-}$, as indicated by the presence of three sets of peaks (Figure 4.13 and Table 4.13).

Three sets of peaks were also present in the case of $[NEt_4]_3[Au_{0.82}Ag_{4.18}Fe_4(CO)_{16}]$ (Figure 4.14 and Table 4.14) suggesting a mixture of $[Au_2Ag_3Fe_4(CO)_{16}]^{3-}$, $[AuAg_4Fe_4(CO)_{16}]^{3-}$ and $[Ag_5Fe_4(CO)_{16}]^{3-}$.

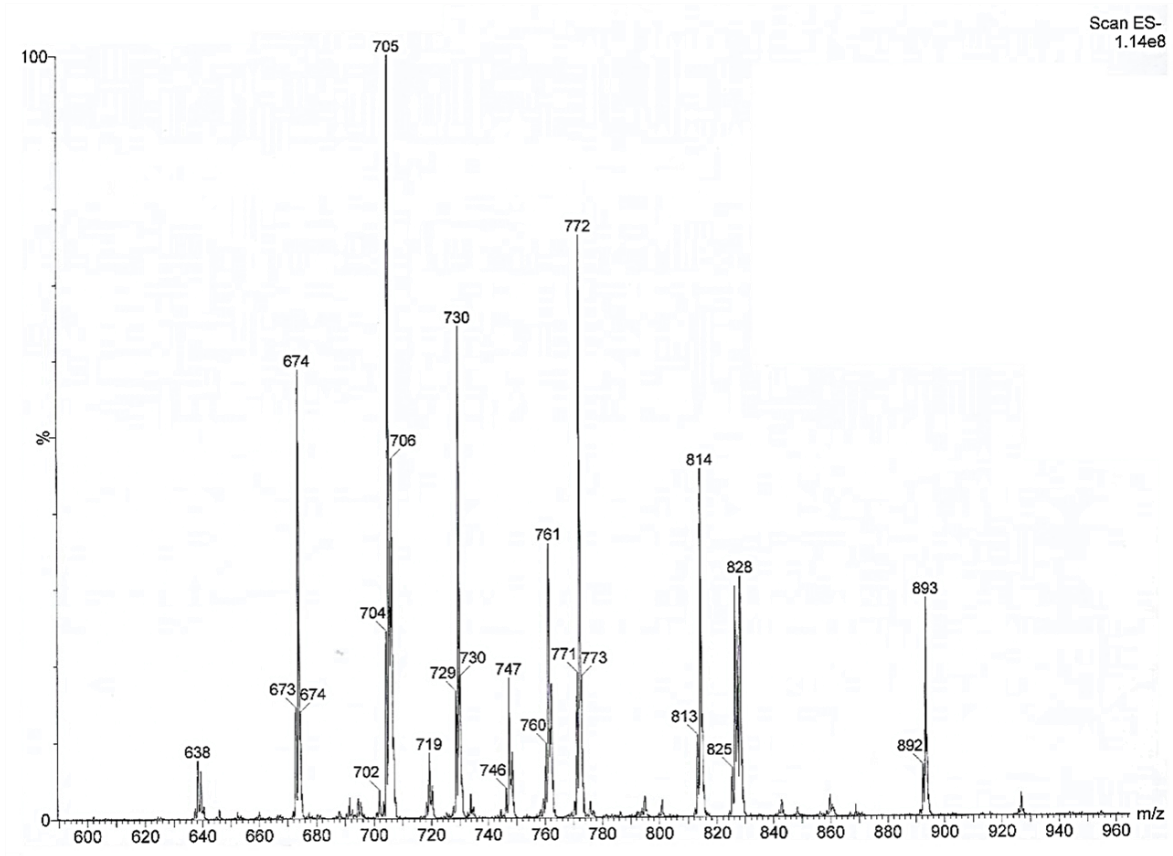

Figure 4.11 ESI-MS spectrum in CH_3CN (ES–) of $[NEt_4]_3[Au_{4.62}Cu_{0.38}Fe_4(CO)_{16}]$.

Table 4.11 Peak assignment of the ESI-MS spectrum (ES–) of $[NEt_4]_3[Au_{4.62}Cu_{0.38}Fe_4(CO)_{16}]$.

m/z	Relative intensity	Ion	Code
893	30	$\{[Au_5Fe_4(CO)_{16}][NEt_4]\}^{2-}$	Au_5+NEt_4
828	30	$[Au_5Fe_4(CO)_{16}]^{2-}$	Au_5
826	30	$\{[Au_4CuFe_4(CO)_{16}][NEt_4]\}^{2-}$	$Au_4Cu+NEt_4$
814	45	$[Au_5Fe_4(CO)_{15}]^{2-}$	$Au_5(-1CO)$
800	2	$[Au_5Fe_4(CO)_{14}]^{2-}$	$Au_5(-2CO)$
772	80	$[Au_5Fe_4(CO)_{12}]^{2-}$	$Au_5(-4CO)$
761	40	$[Au_4CuFe_4(CO)_{16}]^{2-}$	Au_4Cu
747	20	$[Au_4CuFe_4(CO)_{15}]^{2-}$	$Au_4Cu(-1CO)$
730	70	$[Au_4CuFe_4(CO)_{14}]^{2-}$	$Au_4Cu(-2CO)$
719	10	$[Au_4CuFe_4(CO)_{13}]^{2-}$	$Au_4Cu(-3CO)$
705	100	$[Au_4CuFe_4(CO)_{12}]^{2-}$	$Au_4Cu(-4CO)$

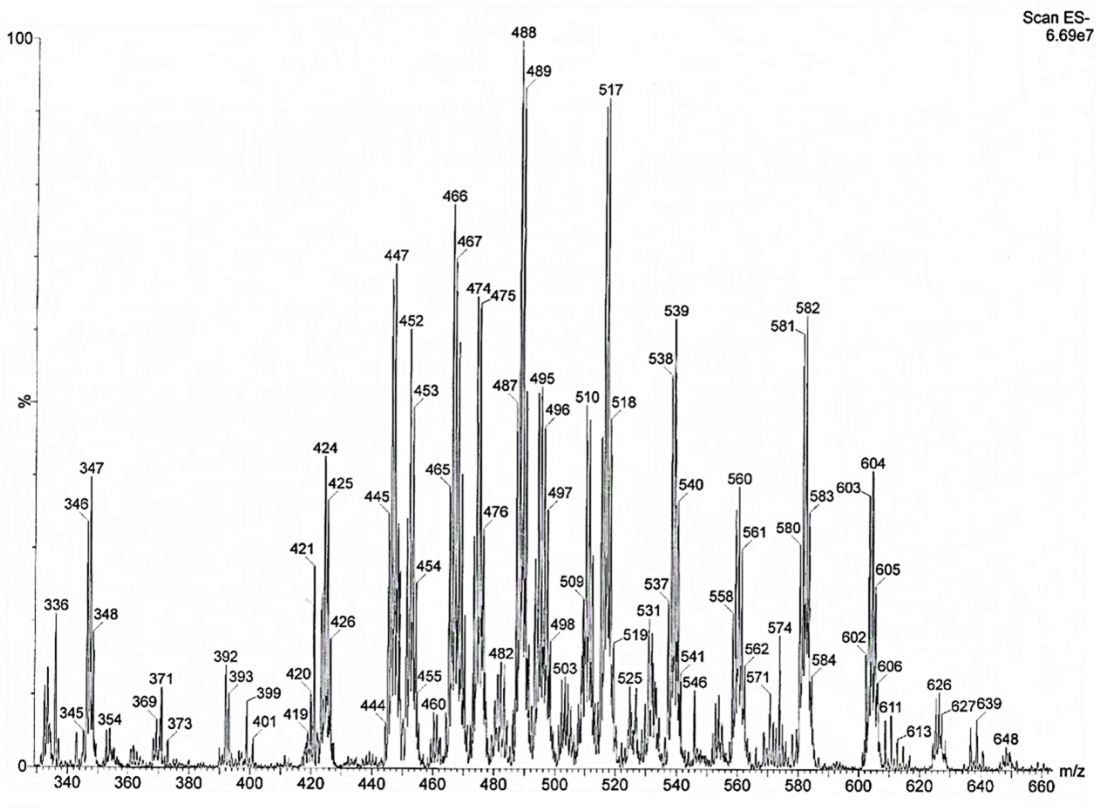

Figure 4.12 ESI-MS spectrum in CH_3CN (ES–) of $[NEt_4]_3[Ag_{1.02}Cu_{3.98}Fe_4(CO)_{16}]$.

Table 4.12 Peak assignment of the ESI-MS spectrum (ES–) of $[NEt_4]_3[Ag_{1.02}Cu_{3.98}Fe_4(CO)_{16}]$.

m/z	Relative intensity	Ion	Code
604	40	$\{[Ag_2Cu_3Fe_4(CO)_{16}][NEt_4]\}^{2-}$	Ag_2Cu_3+NEt_4
582	60	$\{[AgCu_4Fe_4(CO)_{16}][NEt_4]\}^{2-}$	$AgCu_4$+NEt_4
560	35	$\{[Cu_5Fe_4(CO)_{16}][NEt_4]\}^{2-}$	Cu_5+NEt_4
539	60	$[Ag_2Cu_3Fe_4(CO)_{16}]^{2-}$	Ag_2Cu_3
525	10	$[Ag_2Cu_3Fe_4(CO)_{15}]^{2-}$	Ag_2Cu_3(-1CO)
517	90	$[AgCu_4Fe_4(CO)_{16}]^{2-}$	$AgCu_4$
510	50	$[Ag_2Cu_3Fe_4(CO)_{14}]^{2-}$	Ag_2Cu_3(-2CO)
503	10	$[AgCu_4Fe_4(CO)_{15}]^{2-}$	$AgCu_4$(-1CO)
497	30	$[Ag_2Cu_3Fe_4(CO)_{13}]^{2-}$	Ag_2Cu_3(-3CO)
495	50	$[Cu_5Fe_4(CO)_{16}]^{2-}$	Cu_5
488	100	$[AgCu_4Fe_4(CO)_{14}]^{2-}$	$AgCu_4$(-2CO)
482	15	$[Cu_5Fe_4(CO)_{15}]^{2-}$	Cu_5(-1CO)
474	65	$[AgCu_4Fe_4(CO)_{13}]^{2-}$	$AgCu_4$(-3CO)
466	75	$[Cu_5Fe_4(CO)_{14}]^{2-}$	Cu_5(-2CO)
460	5	$[AgCu_4Fe_4(CO)_{12}]^{2-}$	$AgCu_4$(-4CO)
452	60	$[Cu_5Fe_4(CO)_{13}]^{2-}$	Cu_5(-3CO)
447	70	$[AgCu_4Fe_4(CO)_{11}]^{2-}$	$AgCu_4$(-5CO)

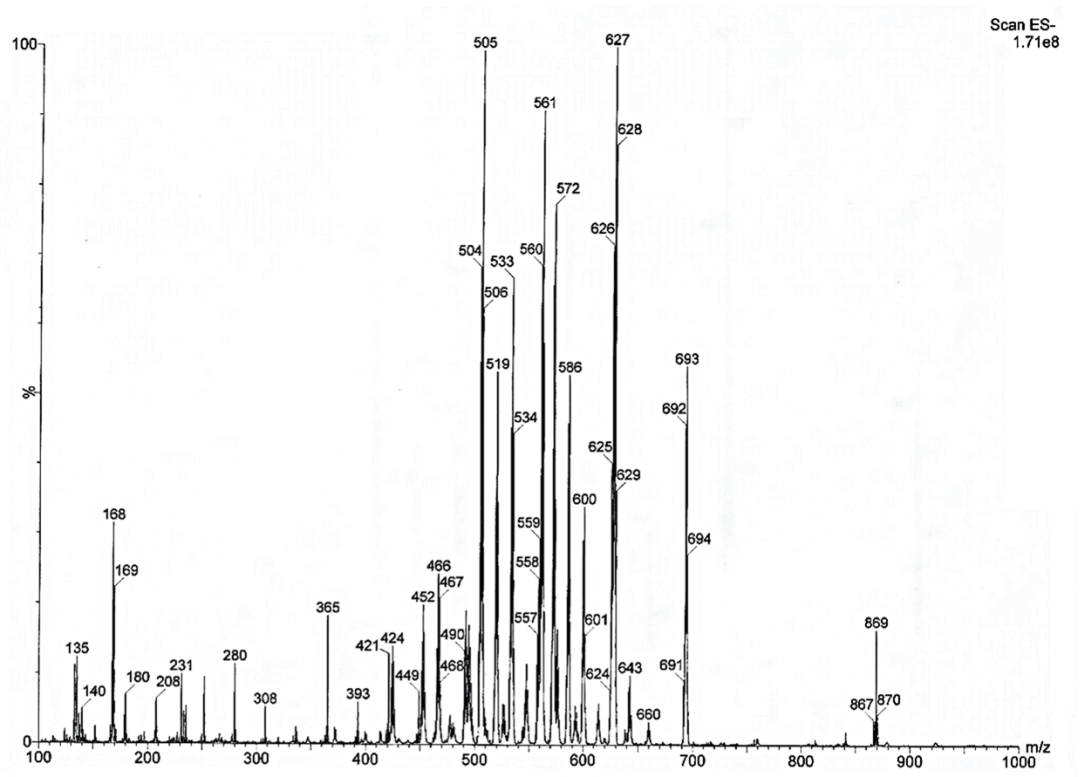

Figure 4.13 ESI-MS spectrum in CH_3CN (ES–) of $[NEt_4]_3[Au_{1.32}Cu_{3.68}Fe_4(CO)_{16}]$.

Table 4.13 Peak assignment of the ESI-MS spectrum (ES–) of $[NEt_4]_3[Au_{1.32}Cu_{3.68}Fe_4(CO)_{16}]$.

m/z	Relative intensity	Ion	Code
693	55	$\{[Au_2Cu_3Fe_4(CO)_{16}][NEt_4]\}^{2-}$	Au_2Cu_3+NEt_4
629	40	$[Au_2Cu_3Fe_4(CO)_{16}]^{2-}$	Au_2Cu_3
627	100	$\{[AuCu_4Fe_4(CO)_{16}][NEt_4]\}^{2-}$	$AuCu_4$+NEt_4
614	5	$[Au_2Cu_3Fe_4(CO)_{15}]^{2-}$	Au_2Cu_3(-1CO)
600	30	$[Au_2Cu_3Fe_4(CO)_{14}]^{2-}$	Au_2Cu_3(-2CO)
586	50	$[Au_2Cu_3Fe_4(CO)_{13}]^{2-}$	Au_2Cu_3(-3CO)
572	80	$[Au_2Cu_3Fe_4(CO)_{12}]^{2-}$	Au_2Cu_3(-4CO)
561	90	$[AuCu_4Fe_4(CO)_{16}]^{2-}$	$AuCu_4$
558	20	$[Au_2Cu_3Fe_4(CO)_{11}]^{2-}$	Au_2Cu_3(-5CO)
547	10	$[AuCu_4Fe_4(CO)_{15}]^{2-}$	$AuCu_4$(-1CO)
533	65	$[AuCu_4Fe_4(CO)_{14}]^{2-}$	$AuCu_4$(-2CO)
519	50	$[AuCu_4Fe_4(CO)_{13}]^{2-}$	$AuCu_4$(-3CO)
505	100	$[AuCu_4Fe_4(CO)_{12}]^{2-}$	$AuCu_4$(-4CO)
495	15	$[Cu_5Fe_4(CO)_{16}]^{2-}$	Cu_5
491	20	$[AuCu_4Fe_4(CO)_{11}]^{2-}$	$AuCu_4$(-5CO)
466	75	$[Cu_5Fe_4(CO)_{14}]^{2-}$	Cu_5(-2CO)
452	60	$[Cu_5Fe_4(CO)_{13}]^{2-}$	Cu_5(-3CO)

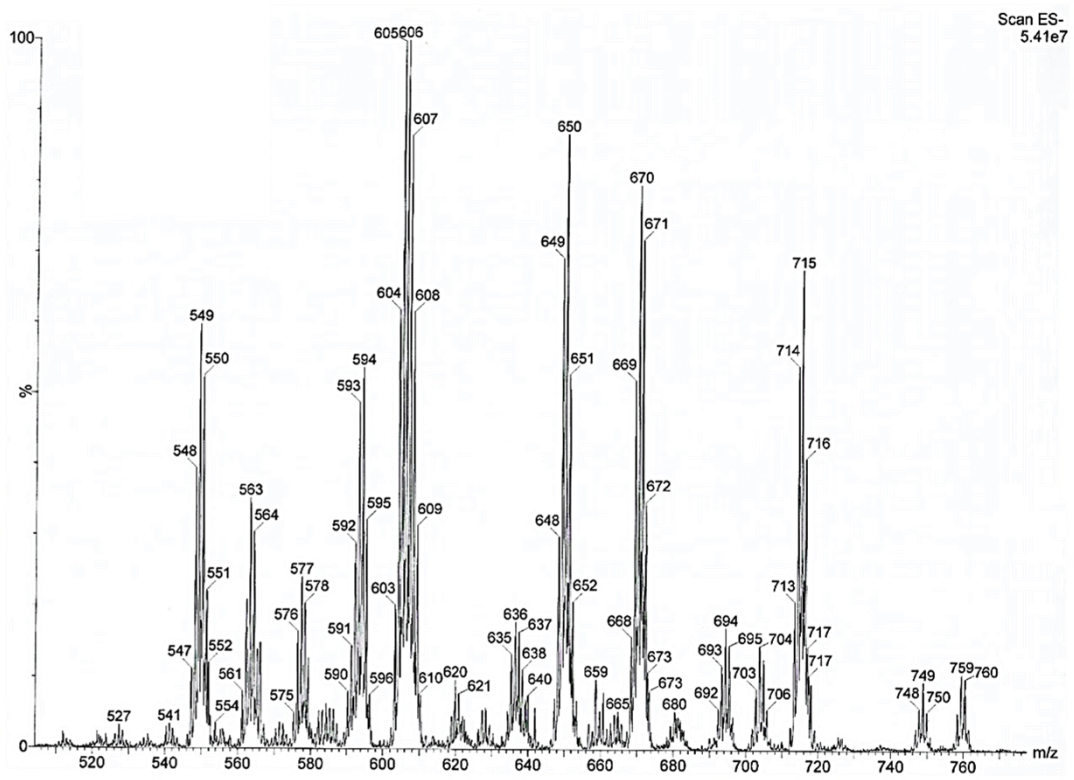

Figure 4.14 ESI-MS spectrum in CH_3CN (ES–) of $[NEt_4]_3[Au_{0.82}Ag_{4.18}Fe_4(CO)_{16}]$.

Table 4.14 Peak assignment of the ESI-MS spectrum (ES–) of $[NEt_4]_3[Au_{0.82}Ag_{4.18}Fe_4(CO)_{16}]$.

m/z	Relative intensity	Ion	Code
759	10	$\{[Au_2Ag_3Fe_4(CO)_{16}][NEt_4]\}^{2-}$	Au_2Ag_3+NEt_4
715	70	$\{[AuAg_4Fe_4(CO)_{16}][NEt_4]\}^{2-}$	$AuAg_4$+NEt_4
694	15	$[Au_2Ag_3Fe_4(CO)_{16}]^{2-}$	Au_2Ag_3
680	5	$[Au_2Ag_3Fe_4(CO)_{15}]^{2-}$	Au_2Ag_3(-1CO)
670	80	$\{[Ag_5Fe_4(CO)_{16}][NEt_4]\}^{2-}$	Ag_5+NEt_4
668	15	$[Au_2Ag_3Fe_4(CO)_{14}]^{2-}$	Au_2Ag_3(-2CO)
650	90	$[AuAg_4Fe_4(CO)_{16}]^{2-}$	$AuAg_4$
636	20	$[AuAg_4Fe_4(CO)_{15}]^{2-}$	$AuAg_4$(-1CO)
620	10	$[AuAg_4Fe_4(CO)_{14}]^{2-}$	$AuAg_4$(-2CO)
608	60	$[AuAg_4Fe_4(CO)_{13}]^{2-}$	$AuAg_4$(-3CO)
606	100	$[Ag_5Fe_4(CO)_{16}]^{2-}$	Ag_5
595	30	$[AuAg_4Fe_4(CO)_{12}]^{2-}$	$AuAg_4$(-4CO)
594	50	$[Ag_5Fe_4(CO)_{15}]^{2-}$	Ag_5(-1CO)
577	25	$[Ag_5Fe_4(CO)_{14}]^{2-}$	Ag_5(-2CO)
563	35	$[Ag_5Fe_4(CO)_{13}]^{2-}$	Ag_5(-3CO)
549	60	$[Ag_5Fe_4(CO)_{12}]^{2-}$	Ag_5(-4CO)

For sake of comparison, the ESI-MS spectra of the bimetallic $[M_5Fe_4(CO)_{16}]^{3-}$ (M = Ag, Cu) clusters are reported (Figures 4.15-4.16 and Tables 4.15-4.16). $[Au_5Fe_4(CO)_{16}]^{3-}$ was not investigated, since it decomposed under ESI-MS conditions.

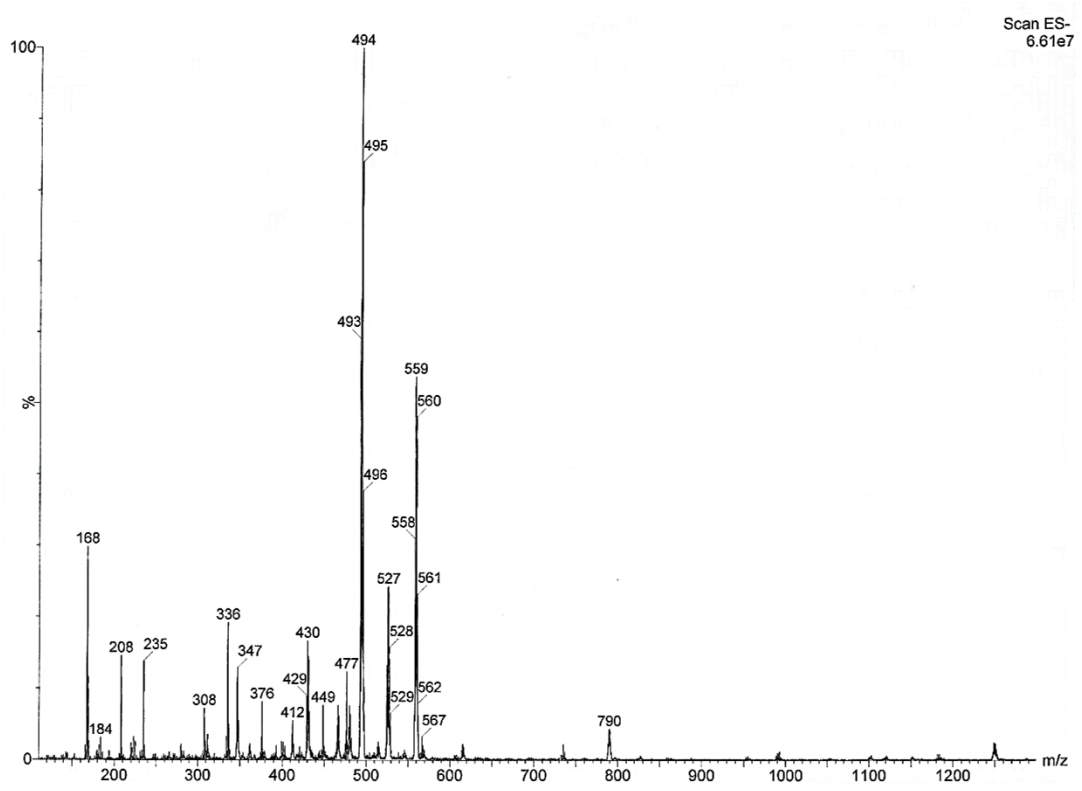

Figure 4.15 ESI-MS spectrum in CH_3CN (ES–) of $[NEt_4]_3[Cu_5Fe_4(CO)_{16}]$.

Table 4.15 Peak assignment of the ESI-MS spectrum (ES–) of $[NEt_4]_3[Cu_5Fe_4(CO)_{16}]$.

m/z	Relative intensity	Ion	Code
559	60	$\{[Cu_5Fe_4(CO)_{16}][NEt_4]\}^{2-}$	Cu_5+NEt_4
494	100	$[Cu_5Fe_4(CO)_{16}]^{2-}$	Cu_5
481	8	$[Cu_5Fe_4(CO)_{15}]^{2-}$	Cu_5(-1CO)
467	10	$[Cu_5Fe_4(CO)_{14}]^{2-}$	Cu_5(-2CO)

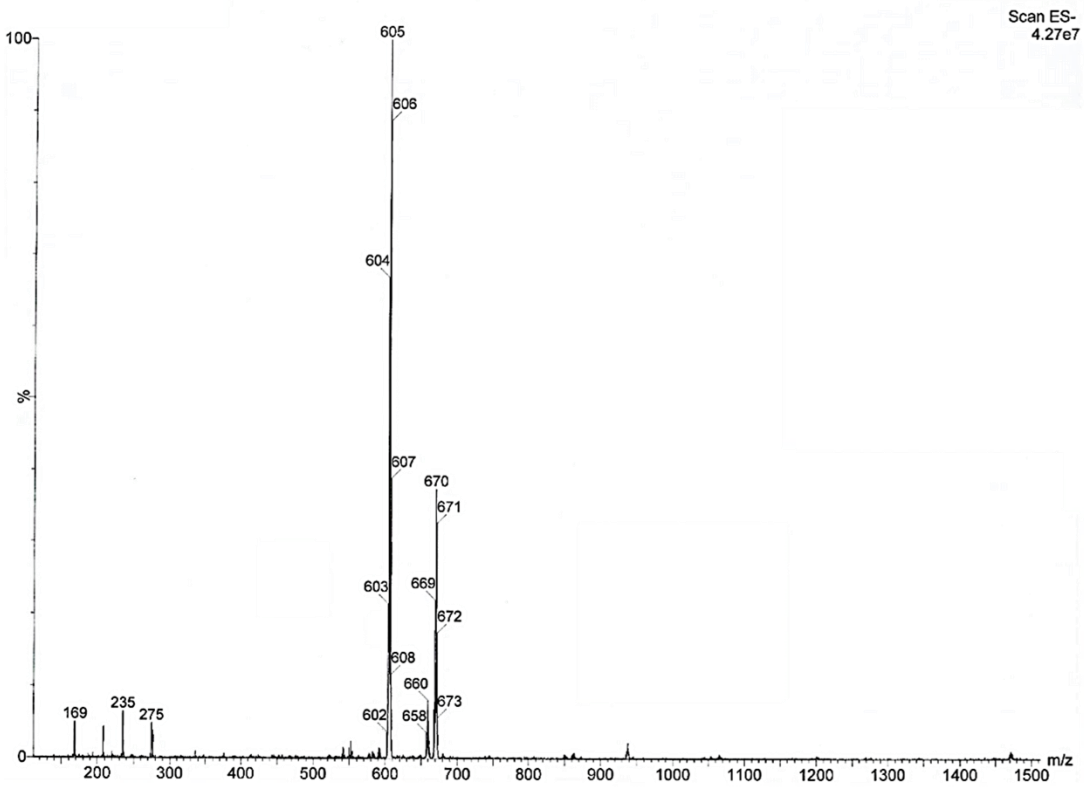

Figure 4.16 ESI-MS spectrum in CH_3CN (ES–) of $[NEt_4]_3[Ag_5Fe_4(CO)_{16}]$.

Table 4.16 Peak assignment of the ESI-MS spectrum (ES–) of $[NEt_4]_3[Ag_5Fe_4(CO)_{16}]$.

m/z	Relative intensity	Ion	Code
670	40	$\{[Ag_5Fe_4(CO)_{16}][NEt_4]\}^{2-}$	Ag_5+NEt_4
605	100	$[Ag_5Fe_4(CO)_{16}]^{2-}$	Ag_5

On the basis of both SC-XRD and ESI-MS data it was possible to conclude that the solid state structures of $[M_xM'_{5-x}Fe_4(CO)_{16}]^{3-}$ consisted of mixtures of two or three species differing for 1-2 coinage metal in the metal core of the cluster.

It is also noteworthy that the $[M_xM'_{5-x}Fe_4(CO)_{16}]^{3-}$ clusters under ESI-MS conditions showed a high tendency to lose 1-4 CO ligands, sometimes even 5 carbonyls. This suggested that in the gas phase their $M_xM'_{5-x}$ cores could be stabilised by both $Fe(CO)_4$ and $Fe(CO)_3$ groups, whereas in the solid state only the former was observed.

4.8 UV-visible studies of $[M_xM'_{5-x}Fe_4(CO)_{16}]^{3-}$ (M, M' = Cu, Ag, Au; M ≠ M'; x = 0-5)

$[M_xM'_{5-x}Fe_4(CO)_{16}]^{3-}$ clusters have been studied by means of UV-visible spectroscopy in CH_3CN solution, Figures 4.17-4.19. The spectra of the bimetallic $[M_5Fe_4(CO)_{16}]^{3-}$ clusters have been recorded as references.

$[Cu_5Fe_4(CO)_{16}]^{3-}$ displays three weak features at 266, 331 and 408 nm; that at 331 nm is very weak.

$[Ag_5Fe_4(CO)_{16}]^{3-}$ displays a strong absorption at 326 nm accompanied by two weak shoulders at 283 and 399 nm. The strong feature at 326 nm seems to be predictive of the presence of Ag in the cluster (see below).

$[Au_5Fe_4(CO)_{16}]^{3-}$ is readily oxidised to $[AuFe_4(CO)_{16}]^{-}$ after the dilution necessary for UV-vis spectroscopy and, therefore, its spectrum has not been recorded.

In the case of trimetallic $[Au_xCu_{5-x}Fe_4(CO)_{16}]^{3-}$ clusters (Table 4.17, Figure 4.17), the UV-visible spectra show only weak features. As a general trend, the weak absorption at *ca*. 269 nm increases by increasing the Cu content, whereas that at 347-367 nm increases by increasing the Au content. A weak absorption at 428-435 nm is present when significant amounts of Cu are present (compositions from $Cu_{3.91}Au_{1.09}$ to $Cu_{2.52}Au_{2.48}$) whereas is absent in the case of $Cu_{0.38}Au_{4.62}$. It must be remarked that all these features are very weak and, therefore, sometimes it is not easy to clearly detect them.

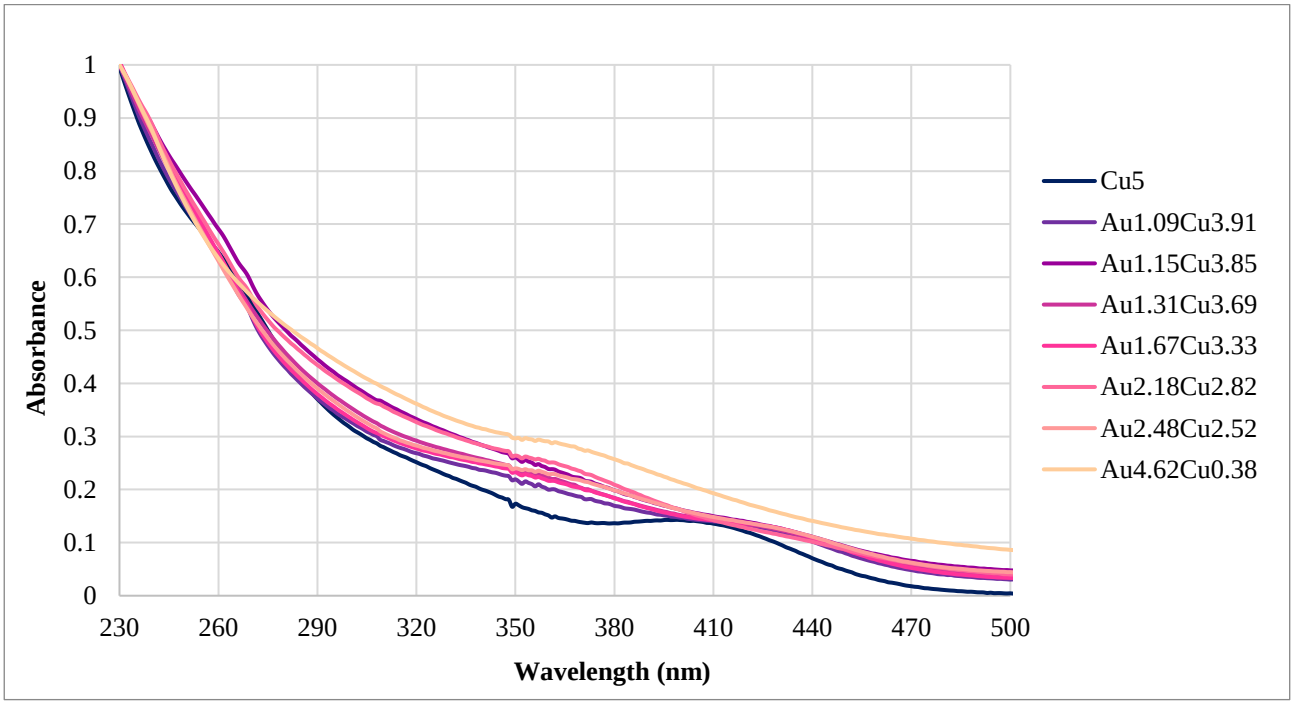

Figure 4.17 UV-visible absorption spectra of $[NEt_4]_3[Au_xCu_{5-x}Fe_4(CO)_{16}]$ in CH_3CN at 298 K.[46]

Table 4.17 UV-visible absorptions of $[NEt_4]_3[Au_xCu_{5-x}Fe_4(CO)_{16}]$ (x = 0-5) in CH_3CN solution. Weaker absorptions are given in parentheses.

Entry*	**Composition**		**Main absorption bands or shoulders (nm)**		
	Au	*Cu*			
**	0.00	5.00	266	(331)	408
20	1.09	3.91	269	-	428
12	1.15	3.85	269	(348)	430
13	1.31	3.69	-	(347)	430
14	1.67	3.33	(268)	355	430
16	2.18	2.82	(268)	365	-
15	2.48	2.52	-	364	(435)
19	4.61	0.39	(269)	367	428
***	5.00	0.00	-	-	-

* See Table 4.2. Entries are listed in order of increasing Au content.

** $[NEt_4]_3[Au_5Fe_4(CO)_{16}]$ is irreversibly oxidised after dilution and, therefore, its UV-vis spectrum has not been recorded.

In the case of $[Ag_xCu'_{5-x}Fe_4(CO)_{16}]^{3-}$ clusters (Table 4.18, Figure 4.18), there is a strong absorption at 326-337 nm whose intensity decreases by decreasing the Ag content, accompanied by two weaker features at lower and higher wavelengths. The strong feature at 326-337 nm is indicative of the presence of Ag in the clusters, as also indicated by the UV-visible spectra of $[Au_xAg_{5-x}Fe_4(CO)_{16}]^{3-}$ clusters (Table 4.19, Figure 4.19), whereas it is completely absent in those of $[Au_xCu_{5-x}Fe_4(CO)_{16}]^{3-}$.

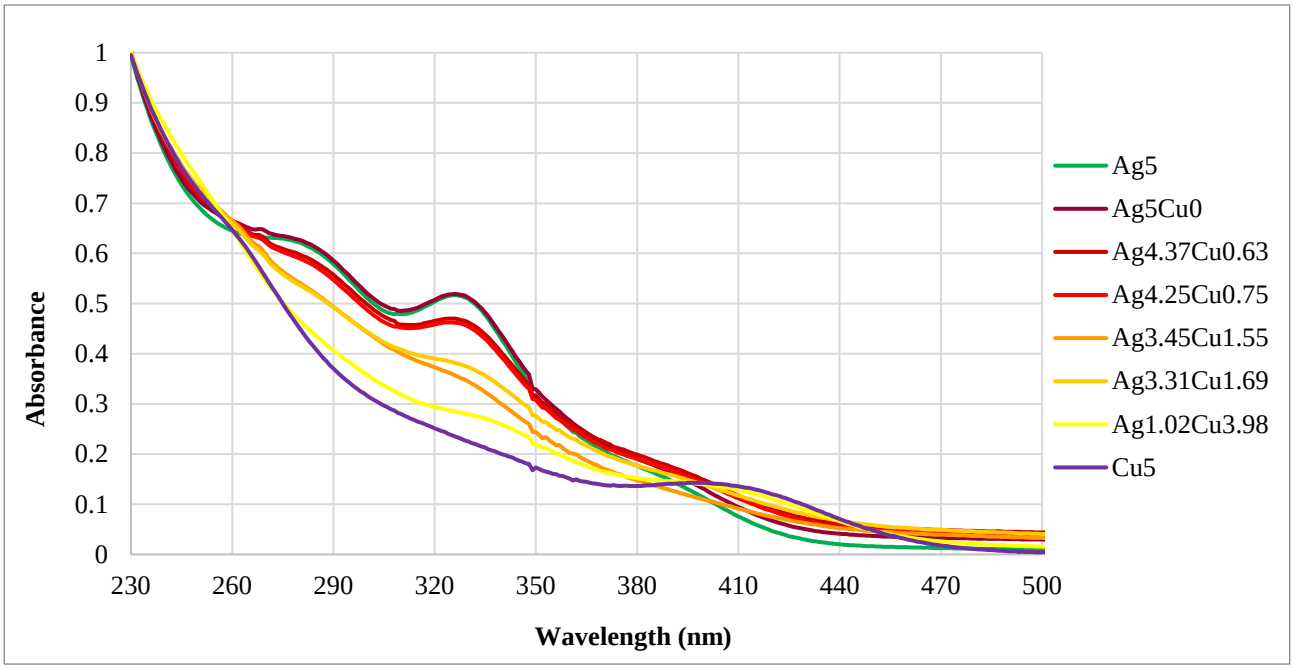

Figure 4.18 UV-visible absorption spectra of $[NEt_4]_3[Ag_xCu_{5-x}Fe_4(CO)_{16}]$ in CH_3CN at 298 K.[46]

Table 4.18 UV-visible absorptions of $[NEt_4]_3[Ag_xCu_{5-x}Fe_4(CO)_{16}]$ (x = 0-5) in CH_3CN solution.

Entry*	**Composition**		**Main absorption bands or shoulders (nm)**		
	Ag	*Cu*			
**	0.00	5.00	266	(331)	408
1	1.02	3.98	-	377	407
10	3.31	1.69	(286)	333	399
11	3.45	1.55	(290)	331	-
3	4.25	0.75	287	328	(399)
8	4.37	0.63	287	330	(401)
2,6	5.00	0.00	283	326	(399)

* See Table 4.1. Entries are listed in order of increasing Ag content.

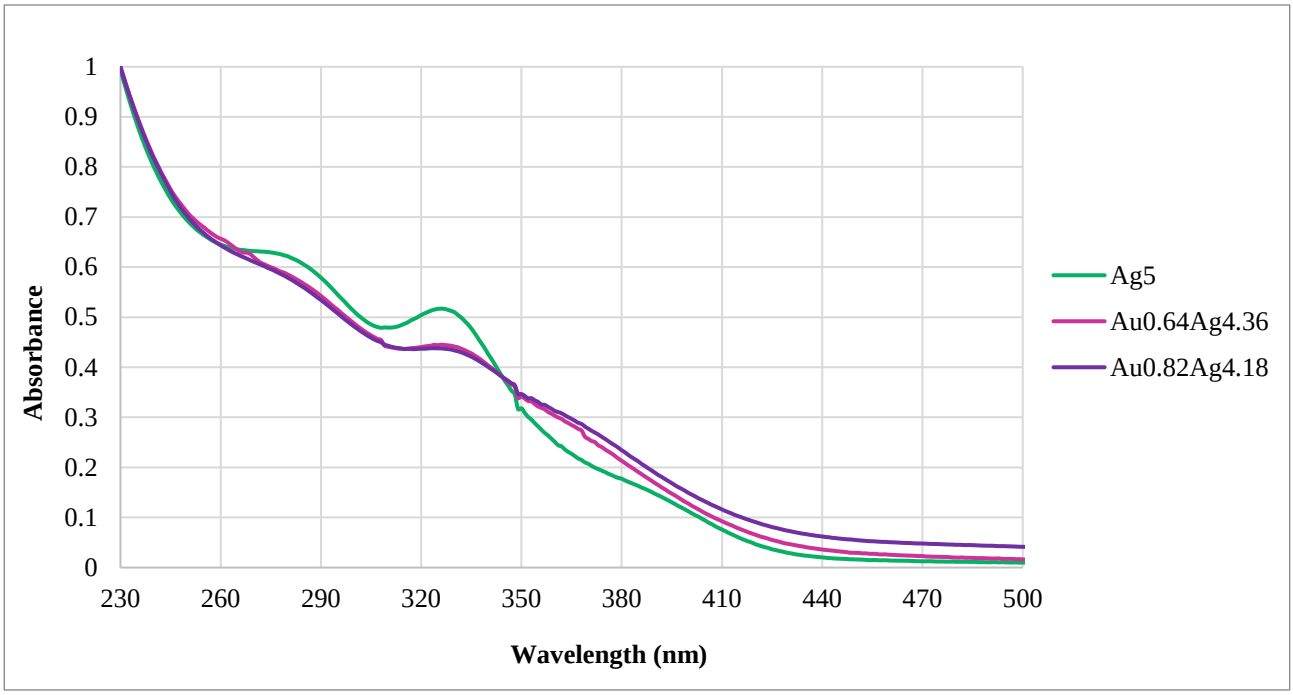

Figure 4.19 UV-visible absorption spectra of $[NEt_4]_3[Au_xAg_{5-x}Fe_4(CO)_{16}]$ in CH_3CN at 298 K.[46]

Table 4.19 UV-visible absorptions of $[NEt_4]_3[Au_xAg_{5-x}Fe_4(CO)_{16}]$ (x = 0-5) in CH_3CN solution.

Entry*	**Composition**		**Main absorption bands or shoulders (nm)**		
	Au	*Ag*			
2,6	0.00	5.00	283	326	(399)
21	0.64	4.36	290	328	-
22	0.82	4.18	284	330	-
**	5.00	0.00	-	-	-

* See Table 4.3. Entries are listed in order of increasing Au content.

** $[NEt_4]_3[Au_5Fe_4(CO)_{16}]$ is irreversibly oxidised after dilution and, therefore, its UV-vis spectrum has not been recorded.

Final Remarks

In this chapter the chemistry of the new mixed $[M_xM'_{5-x}Fe_4(CO)_{16}]^{3-}$ clusters has been explored, by employing a systematic approach for their synthesis and by studying their molecular structure and chemical/physical properties by means of IR, UV-visible spectroscopy, ESI-MS analysis and SC-XRD. This work started with the reactions between $[Cu_3Fe_3(CO)_{12}]^{3-}$ and $AgNO_3$, that led to the formation of the new $[Ag_xCu_{5-x}Fe_4(CO)_{16}]^{3-}$ (x = 0-5) clusters. In order to shed some light on the reaction mechanism, more attempts have been made by employing the oxidised form of the previous Cu-Fe cluster, $[Cu_5Fe_4(CO)_{16}]^{3-}$. More information has been collected by widening the reagents choice. Indeed, other M(I) salts such as $Ag(dppe)(NO_3)$, $Ag_2(dppm)(NO_3)_2$, $Au(Et_2S)Cl$ and $Au(PPh_3)Cl$ have been used. For sake of completeness, more combinations between $[M_5Fe_4(CO)_{16}]^{3-}$ clusters (M = Ag, Au) and M'(I) salts (M' = Cu, Ag) have been tested, as described in Sections 4.3 and 4.5.

The first product formed during the reaction of $[Cu_3Fe_3(CO)_{12}]^{3-}$ with M(I) (M = Ag, Au) salts was the $[Cu_5Fe_4(CO)_{16}]^{3-}$ species, followed by a progressive substitution of Cu by the other coinage metal, to give the mixed M_5 species $[Ag_xCu_{5-x}Fe_4(CO)_{16}]^{3-}$ or $[Au_xCu_{5-x}Fe_4(CO)_{16}]^{3-}$. This first step was faster in case of Ag, which firstly tended to substitute Cu in the 4 corner positions, and lastly in the central one. From a kinetic point of view, the 4 corner sites were more exposed and available to the M(I) than the central position. This tendency of the M(I) to occupy firstly the external positions of the clusters was also related to thermodynamic factors. Indeed, in those positions, M(I) forms Fe-M-Fe bonds with an almost linear coordination while the smaller dimension of Cu stabilised its occupancy at the centre of the cluster. After the formation of bimetallic $[Ag_5Fe_4(CO)_{16}]^{3-}$ and $[Au_5Fe_4(CO)_{16}]^{3-}$, further addition of M(I) resulted in $[M_6Fe_4(CO)_{16}]^{2-}$. From this point, depending on the combination of metals (Cu-Fe or Cu-Au) employed, different products have been isolated:

- When M(I) = Ag(I), crystals of $[Ag_3(dppm)_3(OH)][NO_3]_2$, $[Cu_3Br_3(dppe)_3]$ and $[Cu(dppe)_2]_3[Ag_{13}Fe_8(CO)_{16}]$ have been isolated after reacting Cu-Fe clusters with Ag(I) bidentate phosphines complexes.
- When M(I) = Au(I), *gold browns* were obtained and, eventually, $[AuFe_4(CO)_{16}]^-$ was formed. Finally, the attempts made with $Au(PPh_3)Cl$ led to the isolation of the already known neutral compound $Fe(CO)_4(AuPPh_3)_2$.

ESI-MS analysis corroborated the compositional disorder present in the $[M_xM'_{5-x}Fe_4(CO)_{16}]^{3-}$ (M, M' = Cu, Ag, Au; M ≠ M'; x = 0-5) clusters and finally, the UV-visible studies correlated the different absorption of these $[M_xM'_{5-x}Fe_4(CO)_{16}]^{3-}$ clusters with their composition.

CHAPTER 5

Co-M (M = Cu, Ag, Au) Carbonyl Clusters Stabilised by N-Heterocyclic Carbene Ligands

In this chapter the synthesis and characterisation of new Co-M (M = Cu, Ag, Au) carbonyl clusters containing N-Heterocyclic carbene ligands are reported. The compounds presented in this section are listed in Table 5.1.

Table 5.1 Clusters described in this chapter.

Compound	Compound number
$Co(CO)_4(CuIPr)$	**1**
$Co(CO)_4(AgIPr)$	**2**
$Co(CO)_4(AuIPr)$	**3**
$[Ag(IPr)_2][Ag\{Co(CO)_4\}_2]$	**4**
$Co(CO)_4(CuIMes)$	**5**
$Co(CO)_4(AgIMes)$	**6**
$Co(CO)_4(AuIMes)$	**7**
$[Cu(IMes)_2][Cu\{Co(CO)_4\}_2]$	**8**
$[Ag(IMes)_2][Ag\{Co(CO)_4\}_2]$	**9**
$[Au(IMes)_2][Au\{Co(CO)_4\}_2]$	**10**
$[HIPr]_2[Ag_2\{Co(CO)_4\}_4]$	**11**
$[Co_4(CO)_8(\mu\text{-}\eta^7\text{-IMes})]$	**12**

5.1 Introduction

This journey throughout the fascinating organometallic chemistry continues by investigating another class of compounds: cobalt carbonyl clusters. Cobalt tetracarbonyl $Co(CO)_4$ is not stable because Co possesses 9 valence electrons and cannot satisfy the 18 electron rule without making M-M bonds. For this reason, in the literature di- and tetra-nuclear species such as $Co_2(CO)_8$ and $Co_4(CO)_{12}$ are known.[50] $Co_4(CO)_{12}$ derives from the thermal condensation of the dimeric compound as shown in Scheme 5.1. Moreover, the reduction of $Co_2(CO)_8$ affords $[Co(CO)_4]^-$, that is a very important reagent in Co-CO chemistry.

Scheme 5.1 Relation amongst $[Co(CO)_4]^-$, $Co_2(CO)_8$ and $Co_4(CO)_{12}$.

$$4[Co(CO)_4]^- \xleftarrow{Na/Hg} 2Co_2(CO)_8 \longrightarrow Co_4(CO)_{12} + 4CO$$

Two isomers of $Co_2(CO)_8$ are known (Figure 5.1). The isomer (a) contains six terminal and two edge bridging CO ligands, whereas the isomer (b) presents only eight terminal carbonyls.

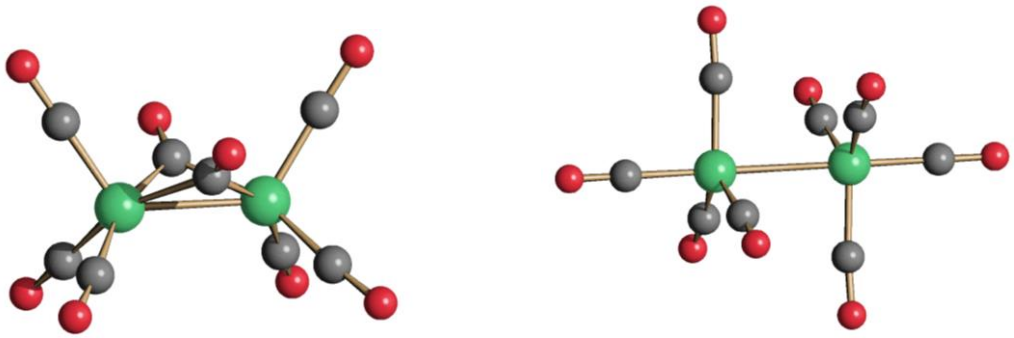

(a) (b)

Figure 5.1 Molecular structures of $Co_2(CO)_8$: (a) isomer with two bridging CO and (b) isomer with only terminal CO (green, Co; grey, C; red, O).

$Co_4(CO)_{12}$ is obtained from the condensation of two $Co_2(CO)_8$ and consequent loss of four carbonyl groups (Figure 5.2). From a structural point of view, $Co_4(CO)_{12}$ is composed by a Co_4 tetrahedron in which the apical Co is bonded to three terminal CO, while in the triangular base there are three double bridging and six terminal CO ligands.[50]

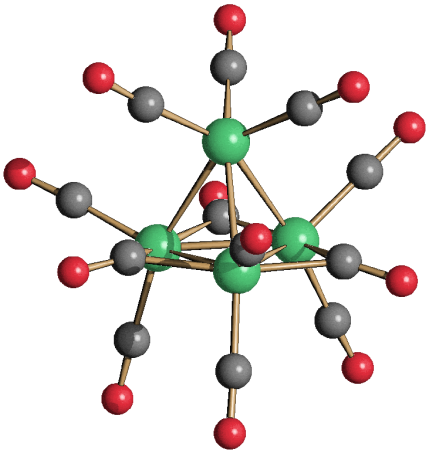

Figure 5.2 Molecular structure of $Co_4(CO)_{12}$ (green, Co; grey, C; red, O).

The *leitmotiv* of the first part of this Thesis regards the employment of coinage metals in the coordination chemistry of metal carbonyl clusters. In the literature, the anionic $[M\{Co(CO)_4\}_2]^-$ (M = Cu, Ag, Au) species have been reported (Figure 5.3),[51,52] and result from the reaction between M(I) salts and two equivalents of $[Co(CO)_4]^-$.

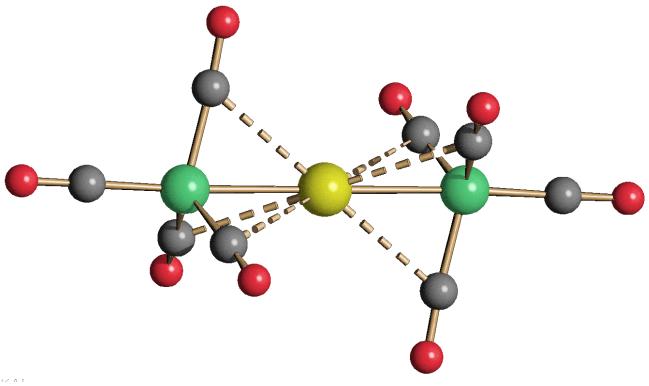

Figure 5.3 Molecular structure of $[Au\{Co(CO)_4\}_2]^-$ (yellow, Au; green, Co; grey, C; red, O). Au···C(O) contacts are represented as fragmented lines.

In order to study new Co-M (M = Cu, Ag, Au) carbonyl clusters, an approach similar to that described in the previous chapters has been adopted. For this purpose, M(NHC)Cl complexes have been used, by following the indications provided by Banerjee S. et al.,[53] that isolated for the first time the bimetallic $Co(CO)_4$(CuIPr) compound and inspired the work herein reported.

5.2 General results

The present chapter regards the synthesis and the characterisation of new bimetallic carbonyl clusters $Co(CO)_4$(MNHC) (M = Cu, NHC = IPr, **1**; IMes, **5**; M = Ag, NHC =IPr, **2**; IMes, **6**; M = Au, NHC =IPr, **3**; IMes, **7**). In particular, the species $Co(CO)_4$(CuIPr) (**1**),

$[Cu(IMes)_2][Cu\{Co(CO)_4\}]$ (**8**), $[Ag(IMes)_2][Ag\{Co(CO)_4\}]$ (**9**), $Co(CO)_4(AgIPr)$ (**2**), $Co(CO)_4(AuIPr)$ (**3**), $Co(CO)_4(AuIMes)$ (**7**) and $[Au(IMes_2)][Au\{Co(CO)_4\}]$ (**10**) have been spectroscopically identified (IR). Moreover, **1**, **2**, **3** and **9** have been isolated and characterised by means of spectroscopic (IR, ^1H and ^{13}C NMR) and structural (single crystal X-ray diffraction) methods. Thermal decomposition in the presence of $Co_2(CO)_8$ was performed and led to the isolation (even if in traces) of $[HIPr]_2[Ag_2\{Co(CO)_4\}_4]$ (**11**) and $[Co_4(CO)_8(\mu\text{-}\eta^7\text{-IMes})]$ (**12**), that have been structurally characterised.

5.3 General aspects

This project was explored by reacting $Na[Co(CO)_4]$ with M(NHC)Cl (M = Cu, Ag, Au; NHC = IMes, IPr) in thf with stoichiometric ratios. Depending on the nature of M, different results were achieved. The equilibria that control the reactions are shown in Scheme 5.2 and play a fundamental role for the outcome of the reaction.

Scheme 5.2 Syntheses of the complexes.

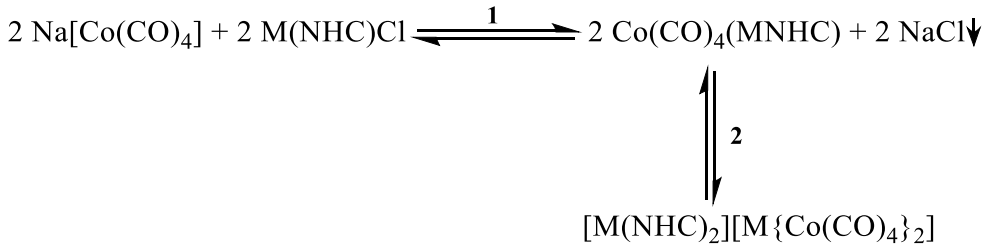

As shown in Scheme 5.2, the reaction between $Na[Co(CO)_4]$ and M(NHC)Cl leads to the formation of the neutral compound $Co(CO)_4(MNHC)$ followed by NaCl precipitation, in accord to the first equilibrium. This first step is favoured by the salt precipitation in low polar solvents, such as dichloromethane and thf. Precipitation of NaCl seems to be the driving force of the first equilibrium. Thus, by using $[PPN][Co(CO)_4]$ instead of $Na[Co(CO)_4]$, no reaction was observed. More polar solvents such as CH_3CN and dmso lead to the dissociation of the Co-M adducts and formation of the starting $[Co(CO)_4]^-$ anion. Equilibrium (2) involves the self-ionisation of $Co(CO)_4(MNHC)$ to $[M(NHC)_2]^+$ and $[M\{Co(CO)_4\}_2]^-$. This second equilibrium is strongly influenced by the nature of NHC and M. Indeed, during these reactions, the neutral and ionic products seemed to be in competition and their relative amount strictly depends on several aspects, such as the Co-M bond strength, the steric effect of the carbene ligand and the solvent polarity.

5.4 Synthesis and characterisation of $Co(CO)_4(MIPr)$ (M = Cu, 1; Ag, 2; Au, 3)

The reaction between $Na[Co(CO)_4]$ and M(IPr)Cl (M = Cu, Ag, Au) in thf in equimolar amounts resulted in the neutral species $Co(CO)_4(MIPr)$ (M = Cu, **1**; Ag, **2**; Au, **3**). The reactions were monitored by means of IR spectroscopy. After 20 minutes, the IR spectra showed the unique presence of the neutral compounds. At the end of the reaction, the solvent was removed *in vacuum*. The solid residue was extracted in toluene and crystals of $Co(CO)_4(MIPr)$ (M = Cu, **1**; Ag, **2**; Au, **3**) suitable for X-ray diffraction were obtained by slow diffusion of *n*-pentane on the toluene solution.

It is interesting to notice that **1** and **3** are the only products obtained in thf when Cu(IPr)Cl and Au(IPr)Cl were employed. Indeed, there was no evidence for ionic compounds such as $[Cu(IPr)_2][Cu\{Co(CO)_4\}_2]$ and $[Au(IPr)_2][Au\{Co(CO)_4\}_2]$.

The IR spectrum of **1** in CH_2Cl_2 displays ν_{CO} bands at 2041(s), 1960(s), 1935(s), 1913(sh) cm^{-1} as previously reported in the literature.[53] In more polar solvents such as CH_3CN and dmso, the intensities of these bands decrease and a strong band at 1889 cm^{-1} typical of $[Co(CO)_4]^-$ appears. This indicates that, accordingly to equilibrium (1), in polar solvents **1** dissociates into $[Co(CO)_4]^-$ and $[Cu(IPr)(solv)]^+$.

Similarly, **3** displays ν_{CO} bands in CH_2Cl_2 solution at 2047(s), 1968(s), 1951(s) cm^{-1}, and dissociation is observed in more polar solvents, even if to a lower extent compared to **1**. This is in agreement with the fact that Co-Au bonds are expected to be stronger than Co-Cu ones. The nature of **3** has been further corroborated by means of SC-XRD, ^1H and $^{13}C\{^1H\}$ NMR analyses.

In the case of M = Ag, the reaction was more complicated and led to the formation of **2** accompanied by traces of $[Ag(IPr)_2][Ag\{Co(CO)_4\}_2]$ (**4**) and $[Co(CO)_4]^-$, as clearly evidenced by IR spectroscopy.

Compounds **1-3** have been also characterised by means of ^1H and $^{13}C\{^1H\}$ NMR spectroscopy. Data recorded for **1** are in accord to that reported in the literature.[53] The $^{13}C\{^1H\}$ NMR spectra of **2** and **3** show a broad resonance at 205.8 and 207.6 ppm attributable to the CO ligands, in view of the high quadrupole moment of cobalt. This explains why the carbonyl resonance was not observed in the case of **1**. The carbene carbon appears as a singlet at δ_C 187.2 ppm in the $^{13}C\{^1H\}$ NMR spectrum of **3**, whereas two doublets with $^1J_{C\text{-}109Ag}$ = 234 and $^1J_{C\text{-}107Ag}$ = 202 Hz centred at δ_C 185.3 ppm are present in the case of **2**.

Crystal structures

Molecular structures of **1-3** have been determined by means of X-ray crystallography (Figures 5.4-5.5). The molecular structure of **1** is not reported since it was already published by Banerjee et al.[53]

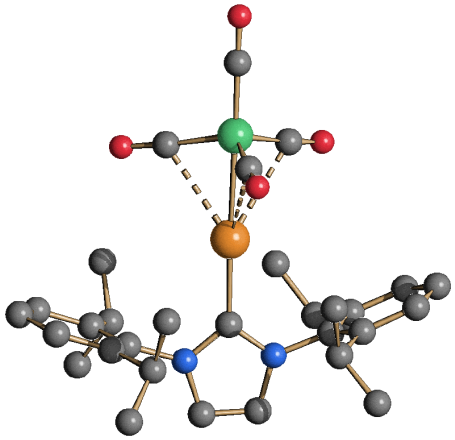

Figure 5.4 Molecular structure of $Co(CO)_4(AgIPr)$ (**2**). Au···C(O) contacts [2.71-2.85 Å] are represented as fragmented lines. Hydrogen atoms have been omitted for clarity (green, Fe; orange, Ag; blue, N; red, O; grey, C). Main bond distances (Å) and angles (°): Co-Ag 2.5344(3), Ag-$C_{carbene}$ 2.1062(19), Co-C(O) 1.774(3)-1.781(2), Co-Ag-$C_{carbene}$ 177.49(6).

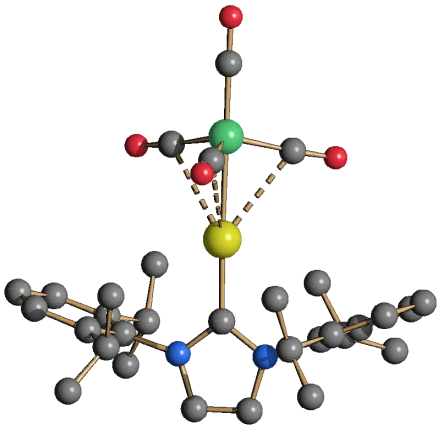

Figure 5.5 Molecular structure of $Co(CO)_4(AuIPr)$ (**3**). Au···C(O) contacts [2.67-2.86 Å] are represented as fragmented lines. Hydrogen atoms have been omitted for clarity (green, Fe; yellow, Au; blue, N; red, O; grey, C). Main bond distances (Å) and angles (°): Co-Au 2.5132(5), Au-$C_{carbene}$ 2.007(4), Co-C(O) 1.775(5)-1.781(4), Co-Au-$C_{carbene}$ 178.21(12).

The molecular structures of **2** and **3** are very similar to that previously reported for **1**, as well as $Co(CO)_4(AuPPh_3)$ and the mono-anions $[Fe(CO)_4(MNHC)]^-$. **1-3** adopt a trigonal bipyramidal structure, with the M(NHC) fragment in an axial position. They contain strong M-Co, Co-C(O) and M-$C_{carbene}$ interactions as well as some weak M···C(O) contacts. The nature of the latter contacts is rather debated in the literature, since they could be merely due to steric requirements of the CO

ligands, rather than any real attraction (even van der Waals) between the carbonyls and the coinage metal.

5.5 Reactions between Na[Co(CO)$_4$] and M(IMes)Cl (M = Cu, Ag, Au)

As mentioned above, the outcome of these reactions depends on few factors such as the nature of the carbene ligand. In particular, the reactions performed with M(IMes)Cl (M = Cu, Ag, Au) resulted in a mixture of products: the neutral species Co(CO)$_4$(MIMes) (M = Cu, **5**; Ag, **6**; Au, **7**) and the ionic complexes [M(IMes)$_2$][M{Co(CO)$_4$}$_2$] (M = Cu, **8**; Ag, **9**; Au, **10**). Their relative abundance was also related to the nature of M, and in particular:

- When M = Cu, Ag: the ionic species **8** and **9** are the major products observed by IR spectroscopy, and only traces of **5** and **6** are detected.
- When M = Au: the neutral species **10** is the major product formed, whereas only traces of the ionic compound **7** have been detected.

This complex distribution of products was reflected in the IR spectra, in which all of these species show two strong and broad ν_{CO} bands in the 1930-1968 cm^{-1} region. In addition to these bands, the ionic species [M(NHC)$_2$][M{Co(CO)$_4$}$_2$] present a sharp band at 2022-2026 cm^{-1}, that moves to 2038-2047 cm^{-1} for the neutral compounds Co(CO)$_4$(MNHC).

As far as the reaction conducted with Cu(IMes)Cl in thf is concerned, the IR spectrum reveals the presence of both the neutral and ionic compounds. After removing the solvent *in vacuum*, the solid residue was extracted in CH_2Cl_2 and from the slow diffusion of *n*-hexane on the CH_2Cl_2 solution crystals of [Cu(IMes)$_2$][Co(CO)$_4$] suitable for SC-XRD were obtained.

When Ag(IMes)Cl was used, the reaction mixture obtained was similar to that observed with Cu(IMes)Cl. Indeed, a simultaneous presence of [Co(CO)$_4$]$^-$, Co(CO)$_4$(AgIMes) (**6**) (2037 cm^{-1}) and [Ag(IMes)$_2$][Ag{Co(CO)$_4$}$_2$] (**9**) (2025 cm^{-1}) was exhibited in the IR spectrum. After workup, **9** was isolated and its molecular structure determined by X-ray diffraction. The nature of **9** was also corroborated by NMR analysis.

The ^{1}H NMR spectrum of [Ag(IMes)$_2$][Ag{Co(CO)$_4$}$_2$] (**9**) displays the typical resonances due to the presence of the IMes ligand. Nonetheless, the spectrum shows additional resonances attributable to traces of impurities. The ^{13}C{^{1}H} NMR spectrum shows the characteristic signals of the aromatic and aliphatic substituents of the IMes ligand and a multiplet at 206.0 ppm attributable to the $C_{carbene}$-Ag ($^1J_{C\text{-}Ag}$ = 207 and 180 Hz). The NMR analysis was conducted in deuterated

acetone, and for this reason is not possible to distinguish at 182.5 ppm the peculiar singlet of the CO ligands.

Finally, when Au(IMes)Cl was employed, the equilibrium between $Co(CO)_4$(AuIMes) (**7**) (2044 cm^{-1}) and the $[Au(IMes)_2][Au\{Co(CO)_4\}_2]$ (**10**) ionic product (2023 cm^{-1}) was observed.

Crystal structures

The molecular structure of $[Cu(IMes)_2][Co(CO)_4]$ was determined by means of SC-XRD analysis (Figure 5.6).

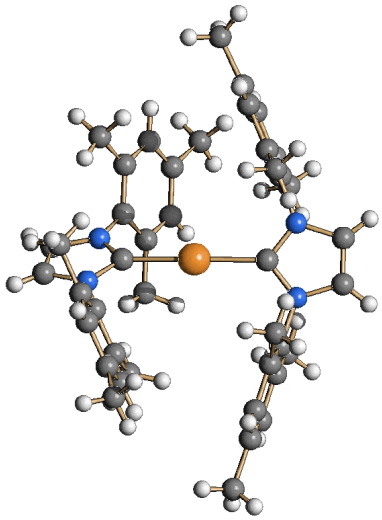

Figure 5.6 Molecular structure of $[Cu(IMes)_2]^+$ present in $[Cu(IMes)_2][Co(CO)_4]$ salt (orange, Cu; blue, N; grey, C; white, H).

The formation of $[Cu(IMes)_2][Co(CO)_4]$ was due to the decomposition of $[Cu\{Co(CO)_4\}_2]^-$ anion during the crystallisation process.

9 was structurally characterised as $[Ag(IMes)_2][Ag\{Co(CO)_4\}_2]$ salt by SC-XRD (Figure 5.7). **9** consists of an ionic packing of $[Ag(IMes)_2]^+$ cations and $[Ag\{Co(CO)_4\}_2]^-$ anions. This represents the first structural determination of the $[Ag\{Co(CO)_4\}_2]^-$ anion, even if its synthesis was previously reported.[51] It closely resembles to the related $[Cu\{Co(CO)_4\}_2]^-$ and $[Au\{Co(CO)_4\}_2]^-$ species. The Ag-Co distances [2.5375(4) and 2.5500(4) Å] are similar to that of **2** [2.5344(3) Å] and slightly shorter than in the neutral tetramer $[Ag_4\{Co(CO)_4\}_4]$ [2.59 Å]. The Ag(I) ion displays a linear coordination and the two Co-centres adopt both a trigonal bipyramidal (TBP) geometry as previously found also in $[Au\{Co(CO)_4\}_2]^-$. Regarding $[Cu\{Co(CO)_4\}_2]^-$, four crystal structures have been previously reported in the literature with miscellaneous cations, comprising that of **8** (Space Group $P2_1/n$). During this work, a second polymorph of **8** has been isolated (Space Group

*C*2/*c*). In all of these salts, the two Co-centres of $[Cu\{Co(CO)_4\}_2]^-$ adopt a TBP coordination, apart in $[N(PPh_3)_2][Cu\{Co(CO)_4\}_2]$, where a Co centre is TBP and the second one displays a tetrahedral coordination of the four CO ligands, with Ag capping one edge of the $Co(CO)_4$ tetrahedron.

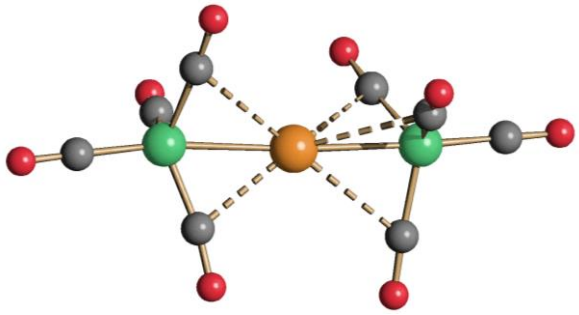

Figure 5.7 Molecular structure of the $[Ag\{Co(CO)_4\}_2]^-$ anion present in $[Ag(IMes)_2][Ag\{Co(CO)_4\}_2]$ (**9**). Ag···C(O) contacts [2.42-2.83 Å] are represented as fragmented lines (green, Co; orange, Ag; red, O; grey, C). Main bond distances (Å) and angles (°): Co-Ag 2.5375(4) and 2.5500(4), Co-C(O) 1.763(3)- 1.783(3), Co-Ag-Co 175.082(17).

5.6 Thermal treatment

Compounds **1-3** and **7-9** are thermally stable, and they do not react with oxidising or reducing agents. The only two exceptions are the thermal reactions of **2** and **8** with $Co_2(CO)_8$ which afforded traces of $[HIPr]_2[Ag_2\{Co(CO)_4\}_4]$ (**11**) (Figure 5.8) and $[Co_4(CO)_8(\mu\text{-}\eta^7\text{-IMes})]$ (**12**) (Figure 5.9), respectively.

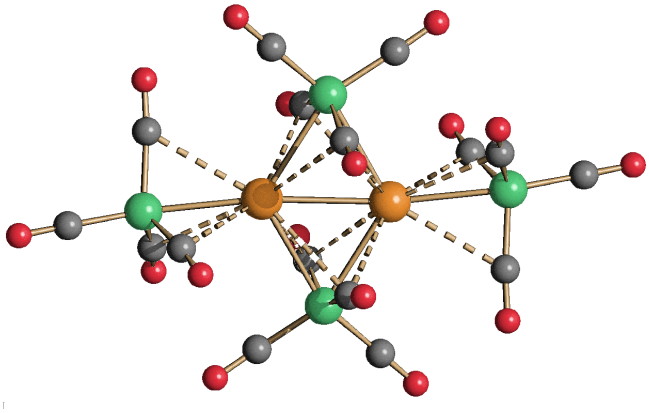

Figure 5.8 Molecular structure of the $[Ag_2\{Co(CO)_4\}_4]^{2-}$ anion present in $[HIPr]_2[Ag_2\{Co(CO)_4\}_4]$ (**11**). Ag···C(O) contacts [2.60-2.99 Å] are represented as fragmented lines (green, Co; orange, Ag; red, O; grey, C). Main bond distances (Å) and angles (°): Ag-Ag 2.8631(3), Co_t-Ag 2.6451(3), Co_b-Ag 2.7510(3) and 2.8494(3), Co_t-C(O) 1.757(2)-1.782(2), Co_b-C(O) 1.784(2)-1.789(2), Co_t-Ag-Ag 171.812(10), Ag-Co_b-Ag 61.462(8).

11 consists of an ionic packing of $[HIPr]^+$ cations and $[Ag_2\{Co(CO)_4\}_4]^{2-}$ anions. The latter anions are also unprecedented for Cu and Au. They may be viewed as dimers of $[Ag\{Co(CO)_4\}_2]^-$, indicating a possible equilibrium in solution between $[M\{Co(CO)_4\}_2]^-$ and $[M_2\{Co(CO)_4\}_4]^{2-}$

species. The Ag-Ag contact [2.8631(3) Å] is indicative of an argentophilic interaction as found in other Ag clusters stabilised by organometallic carbonyl fragments. $[Ag_2\{Co(CO)_4\}_4]^{2-}$ contains two types of $Co(CO)_4$ group, indicated as Co_t (terminal) and Co_b (bringing). As expected, the Co_t-Ag contact [2.6451(3)Å] is shorter than Co_b-Ag [2.7510(3) and 2.8494(3) Å]. Moreover, the Co_t-Ag distance of $[Ag_2\{Co(CO)_4\}_4]^{2-}$ is longer than in **2** and **9**, in view of the fact that Ag displays coordination number two in **2** and **9**, and three (four considering also the Ag-Ag contact) in **11**. Indeed, the Ag-Co contact [2.75 Å] in the mononuclear complex $Co(CO)_4\{AgAs_3(CH_3)_5(C_6H_4)_2\}$, that contains an Ag centre strongly bonded to three As atom (Ag coordination number 4), is even longer than in **11**.[54]

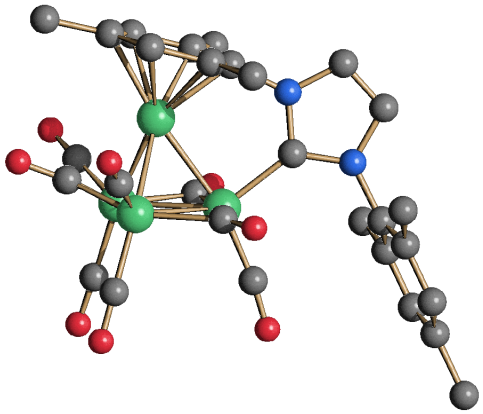

Figure 5.9 Molecular structure of $[Co_4(CO)_8(\mu\text{-}\eta^7\text{-IMes})]$ (**12**). Hydrogen atoms have been omitted for clarity (green, Fe; blue, N; red, O; grey, C).

The neutral cluster **12** may be viewed as a derivative of $Co_4(CO)_{12}$, in which four CO ligands have been replaced by a $\mu\text{-}\eta^7$-IMes ligand. **12** possesses a tetrahedral Co_4 core with three μ-CO ligands on the basal Co_3 triangle. Within this triangle, two Co atoms are bonded to one axial and one equatorial terminal CO, whereas the third Co is bonded to one axial CO and the $C_{carbene}$ of IMes in the equatorial position. One aromatic ring of IMes is η^7-bonded to the fourth Co atom. The $\mu\text{-}\eta^7$-coordination is unprecedented for IMes, but it has been previously reported for other NHC ligands possessing aromatic substituents, including the $HRu_7(CO)_{17}(\mu\text{-}\eta^7\text{-NHC})$ cluster [NHC = $C_3H_2(Me)(Ph)$].[55]

It is well known that $Co_2(CO)_4$ can be thermally transformed into $Co_4(CO)_{12}$. In the presence of IMes, the latter may lose four further CO ligands, resulting in **12**.

5.7 Ammonia-Borane Dehydrogenation

In addition to the chemical characterisation of these new Co-M carbonyl clusters, we decided to extend the boundaries of this study by investigating the possibility to employ them in catalysis. In particular, we focused our attention on a very interesting and promising topic, which is the hydrogen storage by using ammonia-borane (AB) as substrate (Figure 5.10). This process requires an active species presenting both acid and base sites. Heterometallic systems containing a coinage metal and a metal carbonyl fragment, such as Co-M carbonyl clusters, may be described as metal-only Lewis pairs, since they contain a transition metal Lewis acid (coinage metal) and a transition metal Lewis base (metal carbonyl fragment). In this respect, they resemble main group frustrated Lewis pairs (FLPs). As far as AB is concerned, it contains both hydridic (B-H) and protic (N-H) hydrogens, which could be activated by interaction with the Lewis acid site and the Lewis base site, respectively, of a heterometallic metal-only Lewis pair. Moreover, AB is a leading candidate for the hydrogen storage, because of its low molecular weight (30.9 g/mol) and high chemical weight percent hydrogen (19.6 wt % H_2).

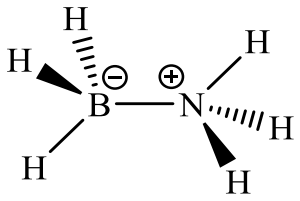

Figure 5.10 Ammonia-borane (AB).

This research has been carried out in collaboration with Prof. Rita Mazzoni (University of Bologna) and Dr. Carlo Lucarelli (University of Como). Moreover, a relevant support has been given by Prof. Ivan Rivalta (University of Bologna) through theoretical studies, that are currently in progress.

Both neutral and ionic compounds have been tested as catalysts for the dehydrogenation of AB in thf as solvent. In particular, **1-3** and **7** are present in thf mainly (or solely) as neutral species $Co(CO)_4(MNHC)$, whereas **8** and **9** as ionic species $[M(NHC)_2][M\{Co(CO)_4\}_2]$. For comparison, also bimetallic Fe-M-NHC complexes have been tested, that is $Fe(CO)_4(MNHC)_2$. Moreover, in order to verify the relevance of the bimetallic nature of these species in catalysis, also related homometallic species have been tested under similar experimental conditions, that is M(NHC)Cl and $Na[Co(CO)_4]$. All these catalysts have been preliminarily tested by NMR at 25 °C and 50 °C. In a typical test, AB, the catalyst and thf were mixed in an oven-dried NMR tube containing a capillary with a $BF_3{\cdot}Et_2O$ reference and the sample maintained at 25 °C or 50 °C. The

disappearance of AB with time has been monitored by ^{11}B NMR comparing the integral of the resonance of AB with that of the standard. The results are summarised in Tables 5.2-5.3.

Table 5.2 Catalytic dehydrogenation of AB at 298 K monitored by ^{11}B NMR spectroscopy. Catalyst load 5% mol/mol.

		AB conversion by ^{11} B NMR		
Catalyst	**Solvent**	**1 h**	**4 h**	**24 h**
$[Co(CO)_4\{Cu(IPr)\}]$	thf	60.2	94	100
$[Co(CO)_4\{Cu(IPr)\}]$	diglyme	65.8	-	100
$[Co(CO)_4\{Ag(IPr)\}]$	thf	0	0	3
$[Co(CO)_4\{Au(IPr)\}]$	thf	0	0	33.2
$[Co(CO)_4\{Cu(IMes)\}]$	thf	1.1	0.5	0.9
$[Co(CO)_4\{Au(IMes)\}]$	thf	0	0	8.7
$[Ag(IMes)_2][Ag\{Co(CO)_4\}_2]$	thf	0	5.0	7.4
$[Fe(CO)_4\{Cu(IPr)\}_2]$	thf	38.7	42.7	79.8
$[Fe(CO)_4\{Au(IPr)\}_2]$	thf	27.9	34.6	42.8
$[Fe(CO)_4\{Cu(IMes)\}_2]$	thf	17.2	27.6	38.6
$[Fe(CO)_4\{Au(IMes)\}_2]$	thf	33.2	28.5	31.9
Cu(IPr)Cl	thf	32.2	26.9	26.1
Cu(IMes)Cl	thf	13.3	23.1	17.5
$Na[Co(CO)_4]$	thf	0	0	0

Table 5.3 Catalytic dehydrogenation of AB at 323 K monitored by ^{11}B NMR spectroscopy. Catalyst load 5% mol/mol.

		AB conversion by ^{11} B NMR		
Catalyst	**Solvent**	**1 h**	**4 h**	**24 h**
$[Co(CO)_4\{Cu(IPr)\}]$	thf	44.7	48.8	70.1
$[Co(CO)_4\{Ag(IPr)\}]$	thf	0	0	0
$[Co(CO)_4\{Au(IPr)\}]$	thf	0	7.4	78.5
$[Co(CO)_4\{Cu(IMes)\}]$	thf	7.1	18.4	53.6
$[Co(CO)_4\{Au(IMes)\}]$	thf	3.5	17.7	51.8
$[Ag(IMes)_2][Ag\{Co(CO)_4\}_2]$	thf	49.2	49.5	47.1
$[Fe(CO)_4\{Cu(IPr)\}_2]$	thf	17.9	42.6	100.0
$[Fe(CO)_4\{Au(IPr)\}_2]$	thf	22.6	24.0	69.4
$[Fe(CO)_4\{Cu(IMes)\}_2]$	thf	21.2	32.5	69.9
$[Fe(CO)_4\{Au(IMes)\}_2]$	thf	23.2	22.3	30.9
$Na[Co(CO)_4]$	thf	14.1	12.7	34.6

The best catalytic performance was obtained when $Co(CO)_4(CuIPr)$ was used as catalyst at room temperature. Indeed, $Co(CO)_4(CuIPr)$ displays the complete conversion of AB after 24 h at 298 K and, already after 4 h, the conversion is 94% (Figure 5.11).

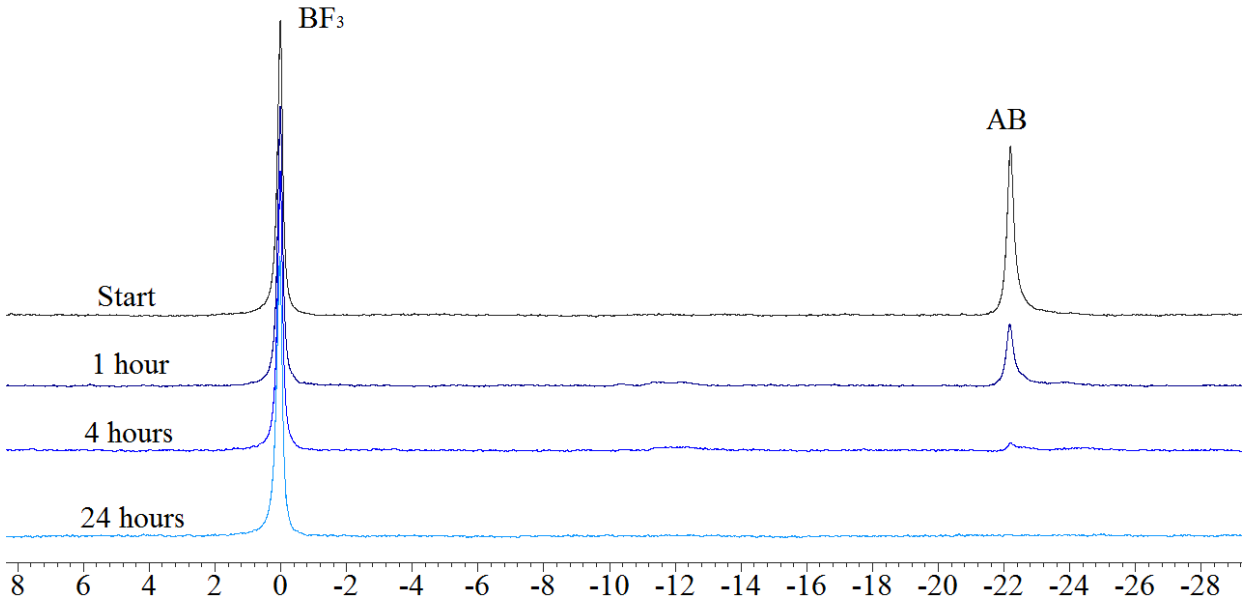

Figure 5.11 ^{11}B NMR spectra acquired during the catalytic dehydrogenation of AB with $Co(CO)_4(CuIPr)$ in thf at 298 K. Catalyst load 5% mol/mol.

As shown in Figure 5.11, the integral of AB decreased from 62.5 to 24.9 after 1 hour, to 3.8 after 4 hours and reached the zero after one day, involving the total conversion of AB and the end of the reaction. The same catalytic reaction was performed at 323 K but did not reach the same results. Indeed, the catalytic performance of $Co(CO)_4(CuIPr)$ significantly decreases at 323 K. Conversely, $Fe(CO)_4(CuIPr)_2$ displays an opposite trend: the conversion is 79.8% after 24 h at 298 K, that increases up to 100.0% at 323 K. Related homometallic species are almost inactive. Bimetallic Co-Ag complexes such as $Co(CO)_4(AgIPr)$ and $[Ag(IMes)_2][Ag\{Co(CO)_4\}_2]$ are inactive at 298 K, and only the latter displays 47.1% conversion after 24 h at 323 K. Co-Au and Fe-Au are less active compared to Co-Cu and Fe-Cu complexes. Moreover, their catalytic performances increase significantly with temperature.

With respect to the characterisation of the final products, the dehydrogenation of AB led to the evolution of H_2 with the precipitation of a white solid composed by N, B and H atoms, known as polyborazylene (BNH_x; $0 < x < 2$) (Figure 5.12).[56] IR analysis of the remaining solution detected the presence of the catalyst and in some cases the species deriving from its decomposition. According to these preliminary studies, the best catalyst seems to be **1**.

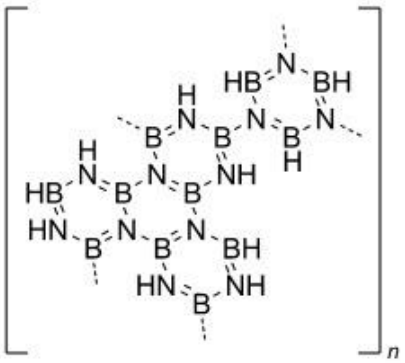

Figure 5.12 Proposed structure of polyborazylene.[56]

In order to obtain some information about the role of $Co(CO)_4(CuIPr)$ during the AB dehydrogenation, the reaction was monitored by IR spectroscopy. The experiments were conducted in a FT-IR cell in CaF_2 and in a reactor by employing the same concentration of reagents employed in the NMR tube experiments.

In Figure 5.13, the IR spectrum of the substrate and the catalyst before the reaction is reported. As far as AB is concerned, its spectrum presents three bands at 3310, 3239 and 3180 cm^{-1} due to the N—H stretchings and four bands at 2356, 2317, 2275 and 2220 cm^{-1} referred to the B—H stretchings. In the ν_{CO} region it is possible to observe the four bands belonging to the catalyst (2046, 1966, 1943, and 1924 cm^{-1}).

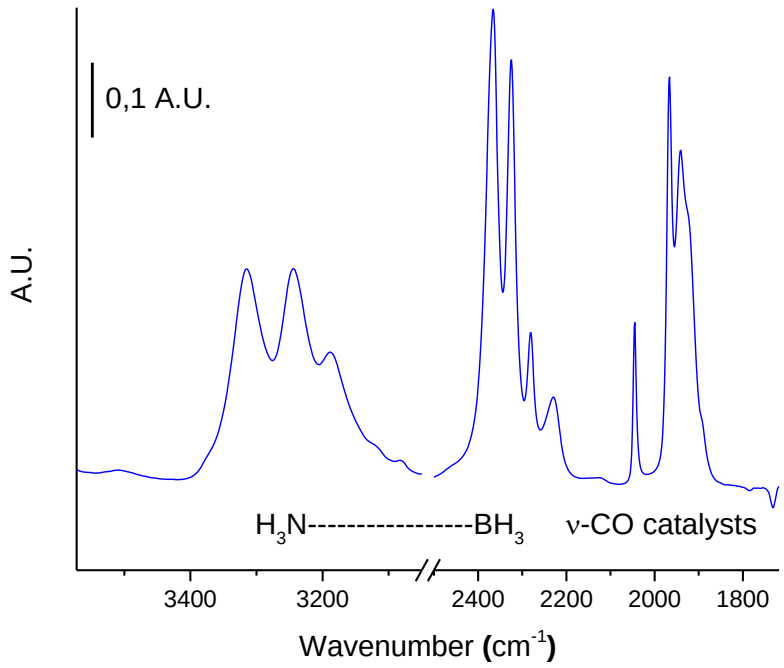

Figure 5.13 FT-IR spectrum of NH_3BH_3 and $Co(CO)_4(CuIPr)$ after subtraction of the THF spectrum.

During the reaction, the consumption of AB is followed by the decrease in intensity of the bands relative to the N—H and B—H stretchings in the region of 3400-3100 and 2400-2200 cm^{-1}, respectively. The dehydrogenation of the substrate is promoted by the catalyst, that during the reaction evolves in a deactivated form. This transformation is accompanied by the disappearance of the four ν_{CO} bands of $Co(CO)_4$(CuIPr) and the growth of a band centred at 1892 cm^{-1}, attributable to the mono-anion $[Co(CO)_4]^-$ (Figure 5.14). This trend was observed in both two reaction systems, that is the IR cell and the reactor. The reaction progress in the IR cell is represented by the light blue line (start of reaction) and blue line (end of reaction), whereas in the reactor it is highlighted with purple (start of reaction) and red (end of reaction) lines.

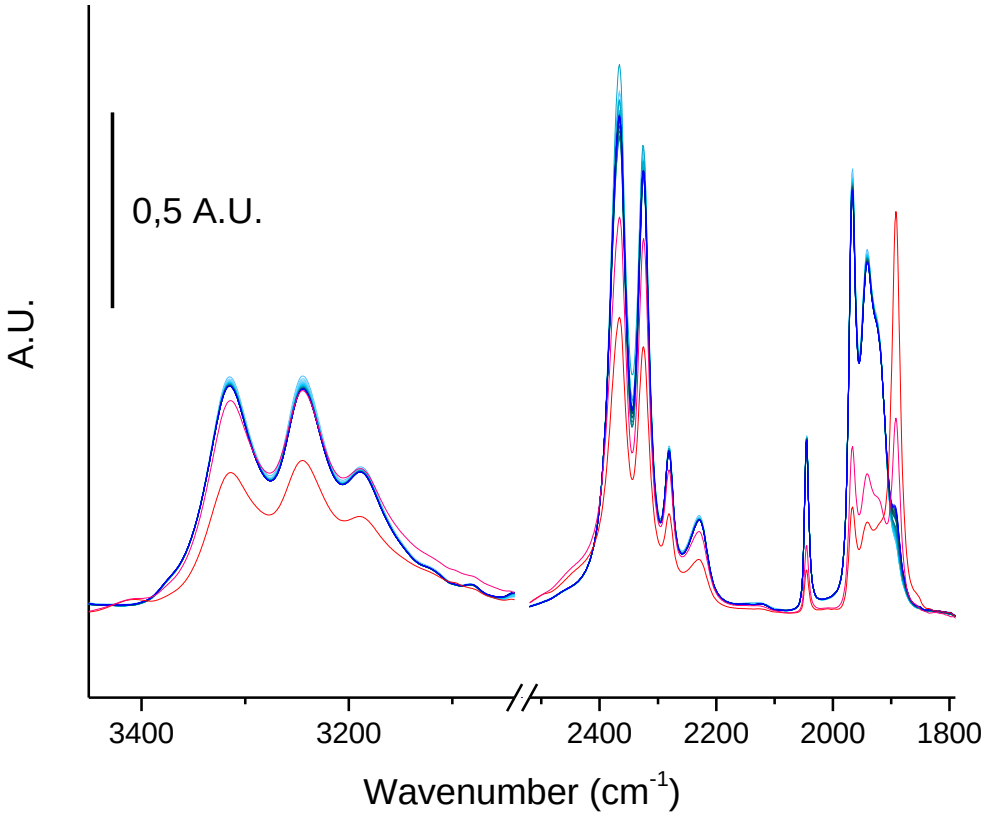

Figure 5.14 FT-IR spectra after subtraction of the first spectrum at the beginning of reaction. The IR spectra were recorded by monitoring the dehydrogenation of AB with $Co(CO)_4$(CuIPr). From light blue to blue lines: spectra recorded during time in the IR cell. Purple line: spectrum recorded after 5 h of reaction in the reactor. Red line: spectrum recorded after 10 h of reaction in the reactor.

The negative bands at 2046, 1966, 1943, 1924 cm^{-1} and the concomitant growth of the band at 1892 cm^{-1} confirm the transformation of the catalyst in $[Co(CO)_4]^-$ (Figure 5.15). Unfortunately, no bands attributable to any other decomposition product were observed.

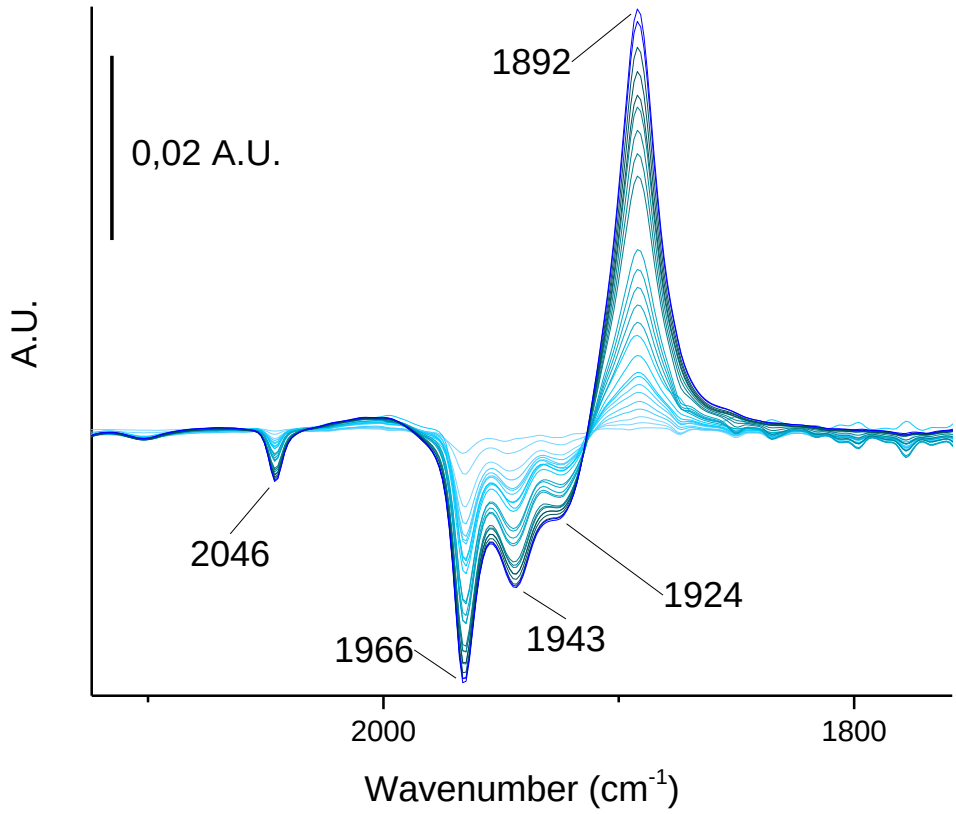

Figure 5.15 FT-IR spectra after subtraction of THF spectrum. The IR spectra were recorded by monitoring the dehydrogenation of AB in presence of $Co(CO)_4$(CuIPr). From light blue to blue lines: spectra recorded during time in the IR cell.

Another important information was obtained by performing frequent gas analyses during the reaction conducted in the reactor. These analyses allowed the quantification of H_2 evolved during the dehydrogenation of AB. As displayed in Figure 5.16 with the blue line, after 300 minutes of reaction, 0.63 equivalent of H_2 referred to the initial moles of AB were formed. The production of hydrogen during time was not constant, as shown by the red line (Figure 5.16). Unfortunately, the reason of such trend is not yet clear, but it will be further investigated in the future.

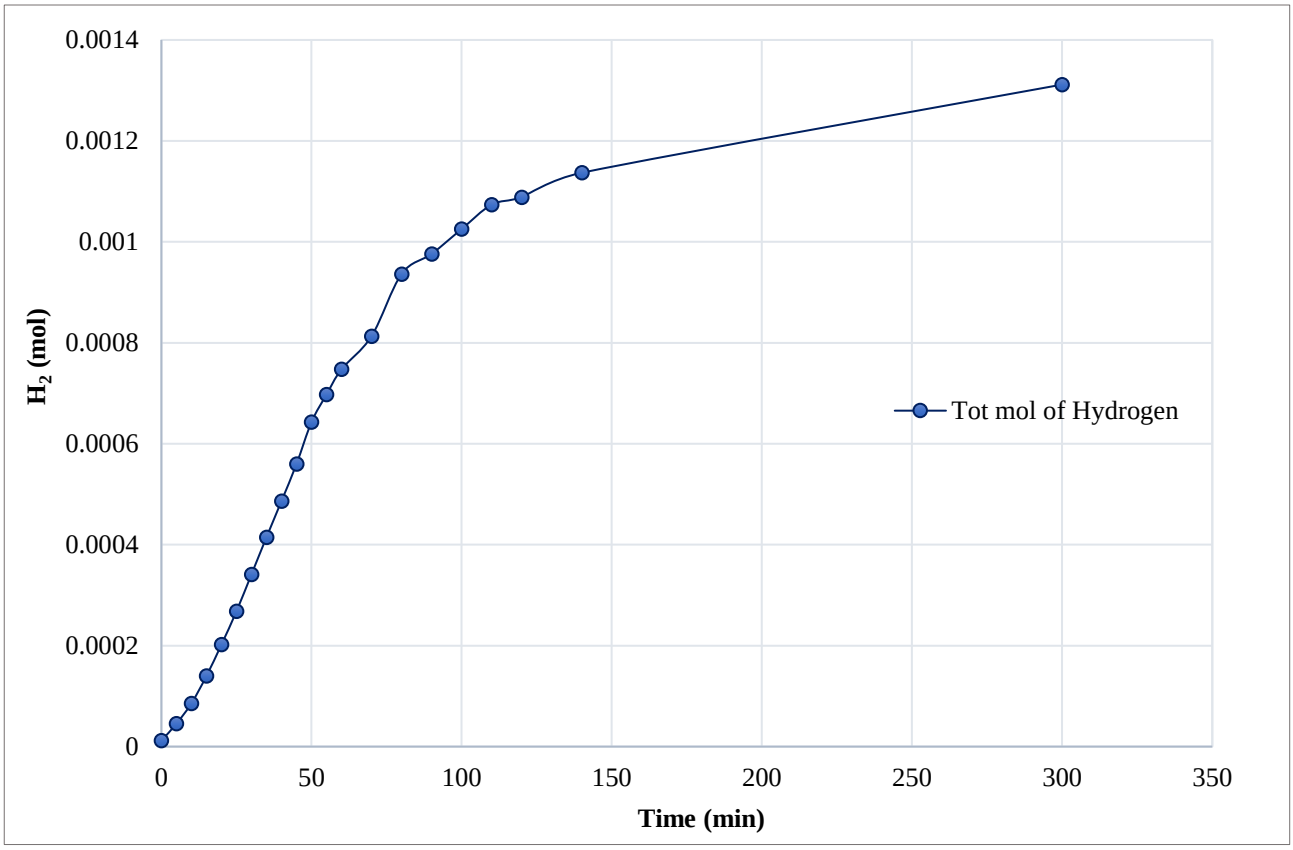

Figure 5.16 Moles of H_2 produced by reacting AB with $Co(CO)_4(CuIPr)$ in the reactor (blue line) and moles of H_2 formed per minute (red line).

Final Remarks

In this chapter the synthesis and the characterisation of new bimetallic Co-M carbonyl clusters have been reported. The investigation of the reactions between $Na[Co(CO)_4]$ and M(NHC)Cl (M = Cu, Ag, Au; NHC = IMes, IPr) led to the formation of $Co(CO)_4(MNHC)$ and $[M(NHC)_2][M\{Co(CO)_4\}_2]$. The presence of these clusters is regulated by equilibria, that can be controlled by changing the reaction conditions, such as solvent and the nature of the carbene ligand. Indeed, bulky ligands and low polar solvents promote the formation of the neutral $Co(CO)_4(MNHC)$ species, whereas smaller carbene ligands in more polar solvents favour the ionic $[M(NHC)_2][M\{Co(CO)_4\}_2]$ compounds. The nature of M is crucial as well, since it influences the bond strength with Co, conditioning the competition between the neutral and the ionic species. The reactions conducted during this research resulted in the isolation of the new $Co(CO)_4(MIPr)$ (M = Cu, **1**; Ag, **2**; Au, **3**) and $[Ag(IMes)_2][Ag\{Co(CO)_4\}_2]$ (**9**). Furthermore, the presence of $[Ag(IPr)_2][Ag\{Co(CO)_4\}_2]$ (**4**), $Co(CO)_4(MIMes)$ (M = Cu, **5**; Ag, **6**; Au, **7**) and $[M(IMes)_2][M\{Co(CO)_4\}_2]$ (M = Cu, **8**; Au, **10**) was evidenced by spectroscopic analyses.

This study sheds some light on the Co-M(NHC) chemistry and the importance of the nature of M and NHC. Indeed, in case of M = Cu, the neutral compound was favoured by IPr ligands, while the presence of the less bulky IMes established an equilibrium between the neutral and the ionic cluster, shifted toward the latter.

The reactions performed with Au(NHC)Cl revealed a stronger Co-M bond that allowed the persistent and unique presence of the neutral compounds, even in high polar solvents.

An opposite behaviour was registered with Ag(NHC)Cl. The Co-Ag bond is weaker than Co-Cu and Co-Au, and for this reason both the neutral and ionic species were present in solution. In this case the result of the reaction was not affected by the size of the carbene.

In order to study their reactivity, thermal treatment of these new Co-M complexes has been performed. Compounds **1-3** and **7-9** were thermally stable, whereas the thermal decomposition of **2** and **8** with $Co_2(CO)_8$ afforded traces of $[HIPr]_2[Ag_2\{Co(CO)_4\}_4]$ (**11**) and $[Co_4(CO)_8(\mu\text{-}\eta^7\text{-IMes})]$ (**12**), respectively.

Finally, a systematic study concerning the dehydrogenation of ammonia-borane (AB) has been explored. For this purpose, the new Co-M(NHC) clusters, the analogous Fe-M(NHC) and the related homometallic complexes have been employed as catalysts. After several tests, $Co(CO)_4(CuIPr)$ appeared as the most promising catalyst, letting to achieve the 94% conversion of AB after 4h of reaction.

CHAPTER 6

Homoleptic and Heteroleptic Platinum Carbonyl Clusters

This chapter describes the synthesis and characterisation of new homoleptic and heteroleptic platinum carbonyl clusters. The compounds presented in this chapter are summarised in Table 6.1.

Table 6.1 Clusters described in this chapter.

Compound	Compound number
$[Pt_6(CO)_{10}(dppm)]^{2-}$	**1**
$[Pt_{12}(CO)_{20}(dppm)_2]^{2-}$	**2**
$[Pt_{18}(CO)_{30}(dppm)_3]^{2-}$	**3**
$[Pt_{24}(CO)_{40}(dppm)_4]^{2-}$	**4**
$[Pt_{12}(CO)_{20}(PTA)_4]^{2-}$	**5**
$[Pt_{15}(CO)_{25}(PTA)_5]^{2-}$	**6**
$[NEt_4][Pt_9(CO)_{18}]\cdot py$	**7**
$[Pt_{12}(CO)_{22}(PPh_2py)_2]^{2-}$	**8**
$Pt_5(XylNC)_{10}$	**9**
$Pt_9(XylNC)_{13}(CO)$	**10**
$[Pt_{27}(CO)_{31}]^{4-}$	**11**
$[Pt_{26}(CO)_{32}]^{-}$	**12**
$[Pt_{12}(CO)_{10}(SnCl)_2(SnCl_2)_4\{Cl_2Sn(\mu\text{-}OH)SnCl_2\}_2]^{2-}$	**13**
$[Pt_7(CO)_6(SnBr_2)_4\{Br_2Sn(\mu\text{-}OH)SnBr_2\}\{Br_2Sn(\mu\text{-}Br)SnBr_2\}]^{2-}$	**14**
$[Pt(CO)(Br)(SnBr_3)_2]^{-}$	**15**
$[Pt_2(CO)_2(Br)_4(SnBr_2)]^{2-}$	**16**

6.1 Introduction

The present chapter provides an overview of the work on homoleptic and heteroleptic platinum carbonyl clusters conducted during the last three years. As in the best stories, everything started with a discovery, in this case by Booth and Chatt, who formulated the first platinum dicarbonyl, known as $[Pt(CO)_2]_n$.[57] Because of its low solubility, this compound has never been characterised. The story carried on with Chini and Longoni, two scientists whose contribution to the inorganic and cluster chemistry has been fundamental. Indeed, they demonstrated that the platinum dicarbonyl readily reacted with alkali under CO atmosphere affording a series of oligomeric di-anions with general formula $[Pt_{3n}(CO)_{6n}]^{2-}$ (n = 2-6),[58,59] named "Chini clusters". These clusters may be viewed as oligomers composed of stacks of $Pt_3(CO)_3(\mu\text{-}CO)_3$ units arranged in a trigonal prismatic fashion along a *pseudo*-C_3 axis. On the basis of this work and elemental analysis, it was possible to re-formulate the platinum dicarbonyl as a higher oligomer in the Chini series of formula $[Pt_{\sim 30}(CO)_{\sim 60}]^{2-}$. More recently, it was possible to structurally characterise also the $[Pt_{3n}(CO)_{6n}]^{2-}$ (n = 4, 6, 7, 8) oligomers, almost completing the whole series and showing that the largest oligomers ($n \geq 5$) self-assembly in the solid state affording infinite (conductive) molecular Pt-wires.[60]

Over the years, homoleptic Chini anions have been employed for the synthesis of globular platinum molecular nanoclusters (*platinum browns*) and bimetallic clusters, as precursors of platinum nanoparticles and nanowires, for the preparation of conductive materials and catalysts.

Regarding the synthesis of the Chini clusters $[Pt_{3n}(CO)_{6n}]^{2-}$ (n = 1-10), three methods are reported in the literature, but amongst these the best way is the reductive carbonylation of Na_2PtCl_6 in methanol in the presence of CO and a base. As shown in Scheme 6.1, it is possible to control the dimension of the cluster (which means the subscript *n*) by modulating the amount and/or the strength of the base.[61] The Na^+ cation can be, then, exchanged by metathesis with organo-ammonium or phosphonium salts.

An interesting property of the $[Pt_{3n}(CO)_{6n}]^{2-}$ (n = 1-10) clusters is the possibility to be easily inter-converted by means of redox reactions under CO atmosphere (Figure 6.1). It is important to underline that the more reduced the clusters are (lower nuclearity), the more prone to oxidation and, thus, air sensitive they are. Because of this, $[Pt_3(CO)_6]^{2-}$, which represents the most reduced Chini cluster, has been only spectroscopically characterised.[62] As indicated by the blue arrow in Figure 6.1, the oxidation process allows to increase the dimensions of the Chini clusters, by means of the addition of $Pt_3(CO)_6$ units.

Scheme 6.1 Reaction pathways for the synthesis of $[Pt_{3n}(CO)_{6n}]^{2-}$ (n = 2-10).

Scheme I

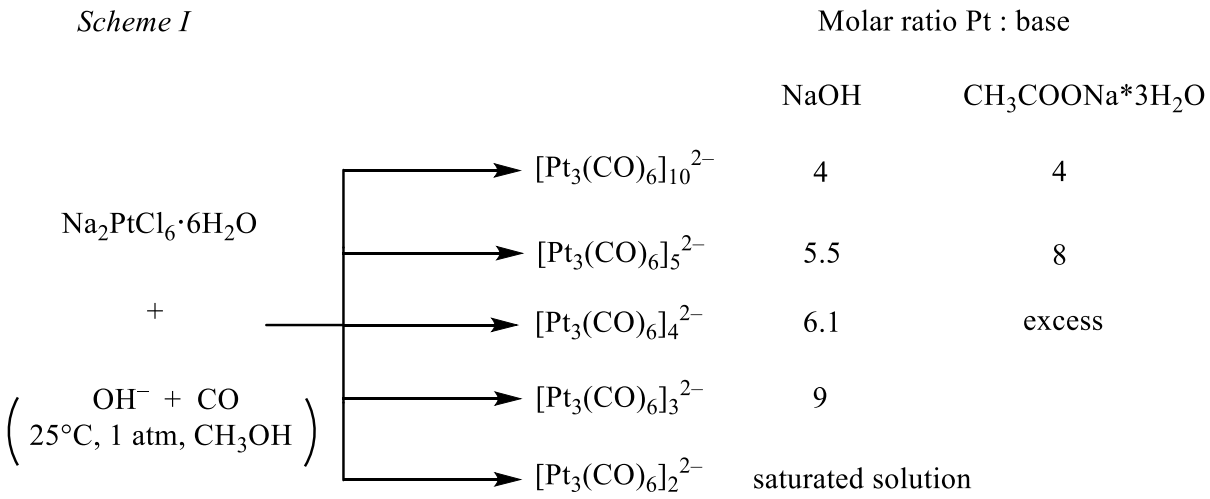

Scheme II

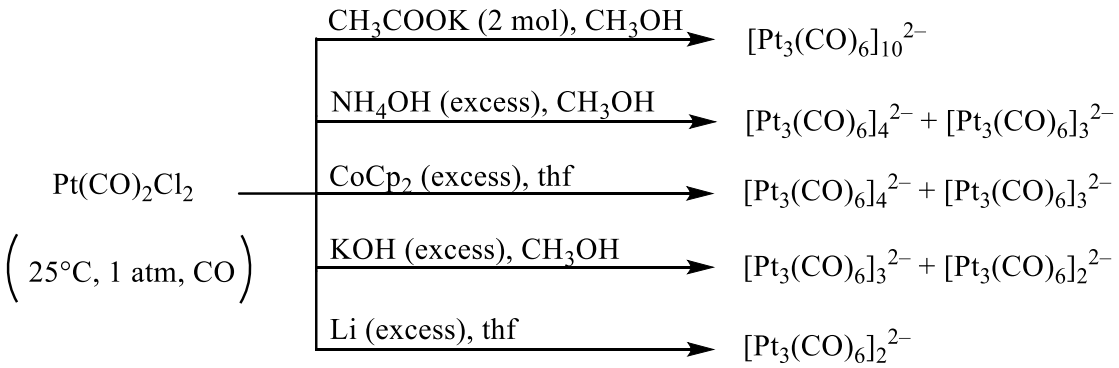

Scheme III

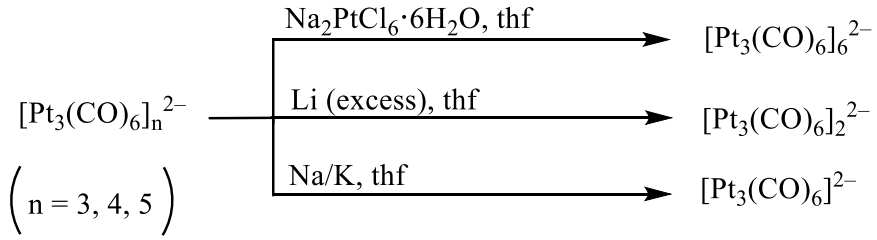

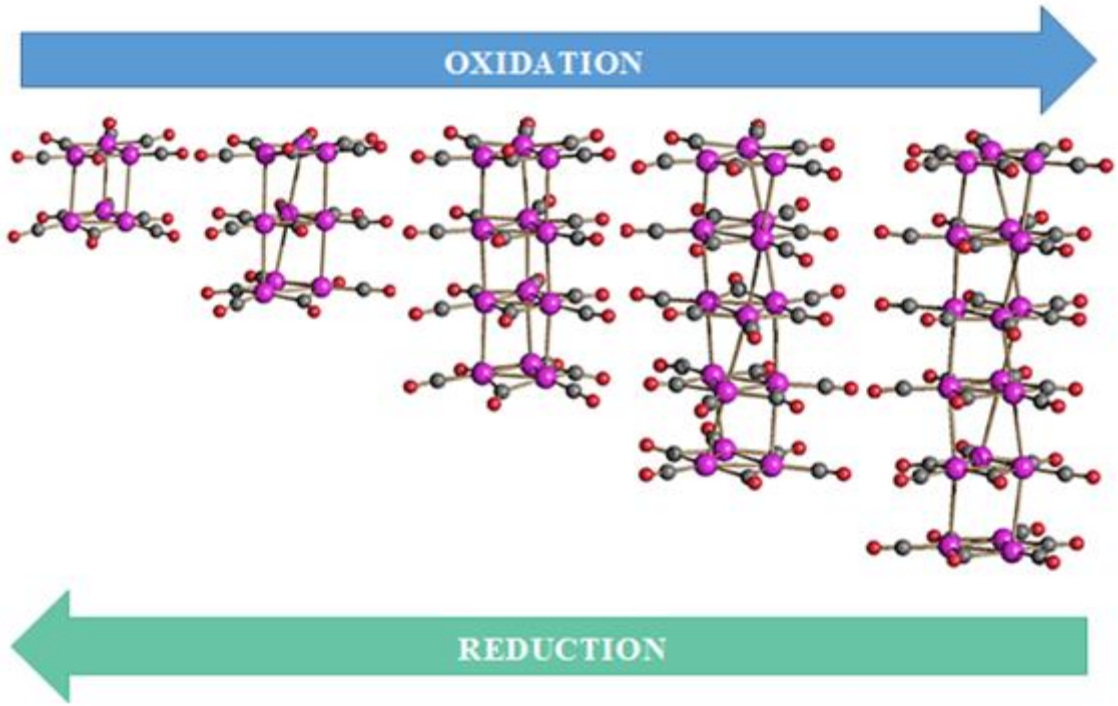

Figure 6.1 Molecular structures and redox inter-conversion of the $[Pt_{3n}(CO)_{6n}]^{2-}$ (n = 2-6) clusters (purple, Pt; red, O; grey, C).[61]

Except $[Pt_3(CO)_6]^{2-}$, the other Chini clusters $[Pt_6(CO)_{12}]^{2-}$, $[Pt_9(CO)_{18}]^{2-}$, $[Pt_{12}(CO)_{24}]^{2-}$, $[Pt_{15}(CO)_{30}]^{2-}$ and, to a less extent, $[Pt_{18}(CO)_{36}]^{2-}$ lend themselves well as starting reagents for further reactions in organic solvents. Larger clusters are usually less soluble and $[Pt_{21}(CO)_{42}]^{2-}$ and $[Pt_{24}(CO)_{48}]^{2-}$ have been only characterised in the solid state.[63–65]

Platinum browns are another category of homometallic platinum carbonyl clusters, characterised by Pt/CO $\leq$ 1.25. This name reflects their brownish colour in solution. In Figure 6.2 some examples of *platinum browns* are reported. Their nature may be controlled by experimental conditions employed during their synthesis (i.e. stoichiometry, temperature and solvent).

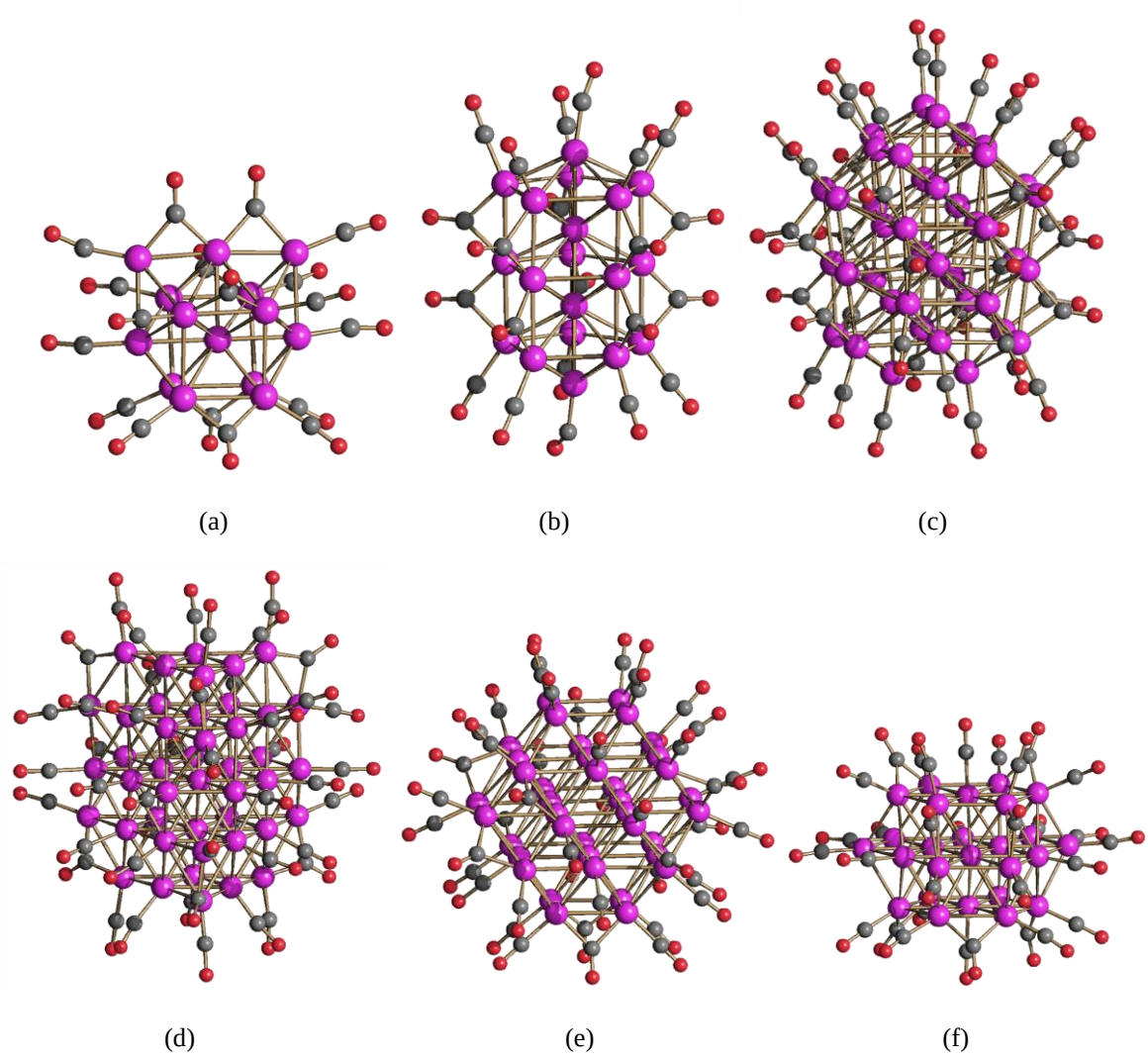

Figure 6.2 Molecular structures of (a) $[Pt_{14}(CO)_{18}]^{4-}$, (b) $[Pt_{19}(CO)_{22}]^{4-}$, (c) $[Pt_{40}(CO)_{40}]^{6-}$, (d) $[Pt_{44}(CO)_{45}]^{n-}$, (e) $[Pt_{38}(CO)_{44}]^{2-}$ and (f) $[Pt_{26}(CO)_{32}]^{-}$ (purple, Pt; red, O; grey, C).[61]

As introduced in the title of this chapter, Pt carbonyl clusters can be divided into two categories, that is the homoleptic and the heteroleptic clusters. The preparation of the latter involves CO substitution, which is a general strategy in order to functionalise metal carbonyl clusters. During this reaction, retention of the cluster structure, cluster rearrangement and/or cluster breakdown may be observed.[66,67] A recent study on the functionalisation of Chini clusters with phosphine ligands clarify this process.[68] In particular, a competition between the non-redox substitution with retention of the nuclearity of the cluster and the redox fragmentation is observed in the case of the reactions of homoleptic Chini clusters with monodentate and bidentate phosphines (Figure 6.3). The non-redox substitution results in $[Pt_{3n}(CO)_{6n-x}(L)_x]^{2-}$ (n = 2-5; x = 1-n) heteroleptic analogues of anionic Chini clusters. Conversely, redox fragmentation (elimination) reactions lead to lower nuclearity homoleptic species $[Pt_{3(n-1)}(CO)_{6(n-1)}]^{2-}$ as well as miscellaneous neutral complexes, $Pt_x(CO)_y(L)_z$.

The outcome of these reactions depends on (a) the nuclearity of the cluster, (b) the nature of the ligand and (c) the stoichiometry of the reaction.

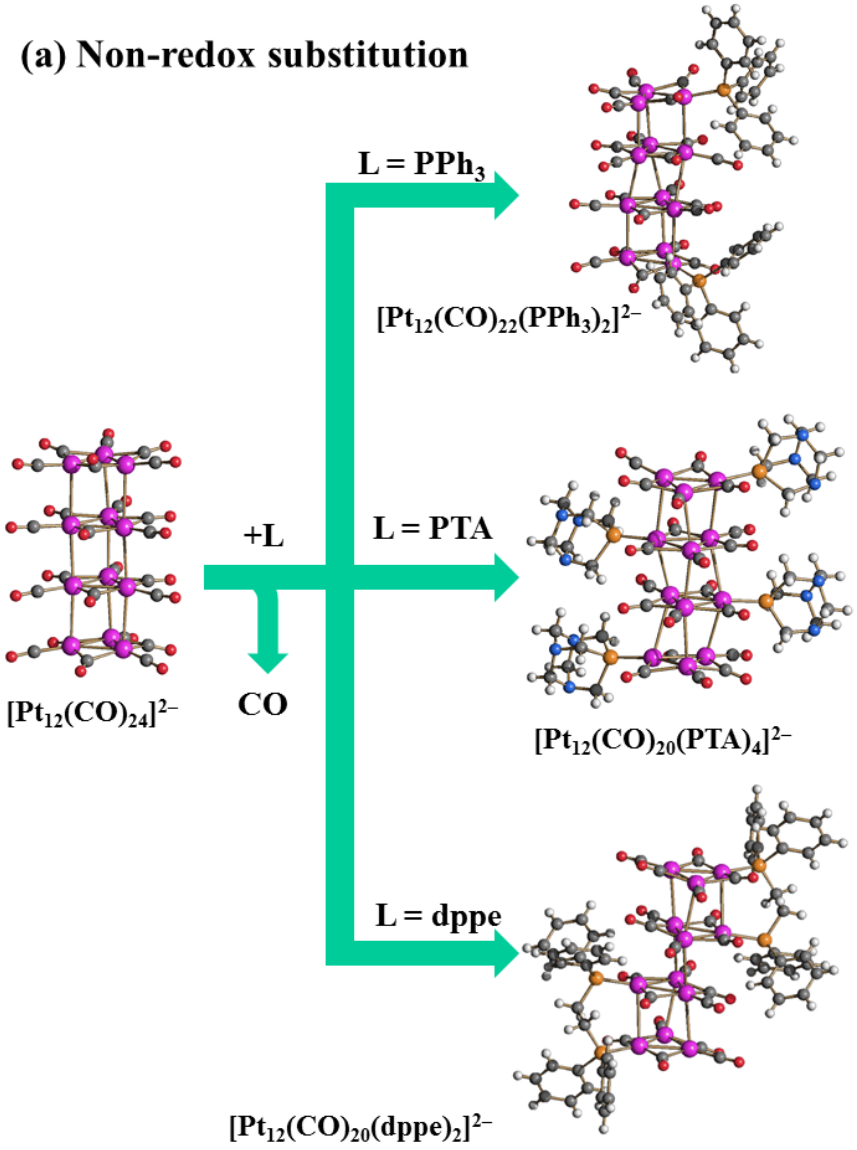

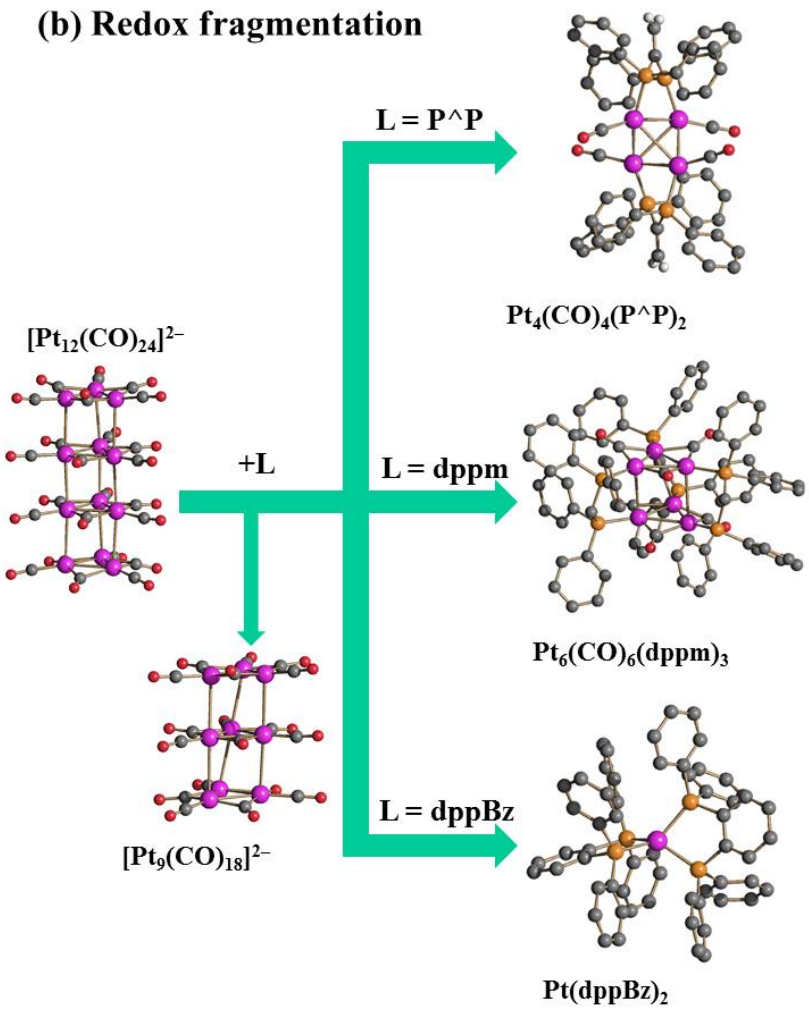

Figure 6.3 Some examples of the reactions of $[Pt_{12}(CO)_{24}]^{2-}$ homoleptic anionic Chini cluster with phosphines: (a) non-redox substitution and (b) redox fragmentation (purple, Pt; orange, P; red, O; grey, C).[69]

The non-redox substitution is favoured by lower nuclearity clusters, whereas larger clusters usually prefer redox fragmentation. Moreover, monodentate and flexible bidentate phosphines promote the non-redox substitution, whereas more rigid bidentate ligands often result in redox fragmentation affording neutral Pt complexes. Furthermore, the non-redox substitution is favoured by the use of stoichiometric amounts of the ligands, whereas an excess of phosphine leads to redox fragmentation. Thus, by employing stoichiometric amounts of PPh_3, PTA, dppe and R-dppp, heteroleptic anionic Chini type clusters can be obtained through non-redox substitution. Conversely, when used in excess, redox fragmentation occurs affording mixtures of lower nuclearity anionic clusters and zero-valent species such as $Pt_3(CO)_3(PPh_3)$, $Pt_6(CO)_6(dppe)_3$, $Pt_4(CO)_4(dppe)_2$ and $Pt(dppe)_2$.[70]

6.2 General results

This Chapter reports some further advances in the chemistry of platinum carbonyl clusters. In the first part, the synthesis, and the characterisation of new phosphines-derivatives of $[Pt_{3n}(CO)_{6n}]^{2-}$ (n = 2-4) are reported. In particular, the reaction between $[Pt_6(CO)_{12}]^{2-}$ and $CH(PPh_2)_2$ (dppm) afforded $[Pt_6(CO)_{10}(dppm)]^{2-}$ (**1**). The oxidation of **1** resulted in the oligomerisation of the starting compounds leading to the isolation of the larger clusters $[Pt_{12}(CO)_{20}(dppm)_2]^{2-}$ (**2**), $[Pt_{18}(CO)_{30}(dppm)_3]^{2-}$ (**3**) and $[Pt_{24}(CO)_{40}(dppm)_4]^{2-}$ (**4**).

By reacting $[Pt_{3n}(CO)_{6n}]^{2-}$ (n = 2-5) with increasing amounts of 1,3,5-triaza-7-phosphaadamantane (PTA) it was possible to isolate $[Pt_{12}(CO)_{20}(PTA)_4]^{2-}$ (**5**) and $[Pt_{15}(CO)_{25}(PTA)_5]^{2-}$ (**6**). The PTA ligands confer solubility in water to **5** and **6**, and their cytotoxicity towards human ovarian (A2780) cancer cells and their cisplatin-resistant strain (A2780cisR) has been evaluated.

Since the substitution reactions on $[Pt_{3n}(CO)_{6n}]^{2-}$ clusters are supposed to proceed *via* an associative mechanism, some attempts have been made in order to trap in the solid state species of the type $[Pt_{3n}(CO)_{6n}(L)]^{2-}$. Thus, $[NEt_4]_2[Pt_9(CO)_{18}]\cdot py$ (**7**) co-crystals containing a N-donor solvent molecule were obtained, but unfortunately no interaction was present between pyridine and the Chini cluster. Then, by performing the reaction between $[Pt_{12}(CO)_{24}]^{2-}$ and two equivalents of PPh_2py, the substitution product $[Pt_{12}(CO)_{22}(PPh_2py)_2]^{2-}$ (**8**) occurred. Also in this case there was no interaction between Pt and N.

The reactivity of Chini clusters was, then, also extended to isonitriles. The reaction of $[Pt_6(CO)_{12}]^{2-}$ with XylNC afforded $Pt_5(XylNC)_{10}$ (**9**), whereas $Pt_9(XylNC)_{13}(CO)$ (**10**) was obtained from the reaction of $[Pt_{15}(CO)_{30}]^{2-}$ with XylNC.

The study of higher nuclearity platinum carbonyl clusters led to the synthesis and structural characterisation of $[Pt_{27}(CO)_{31}]^{4-}$ (**11**) which, in turn, can be oxidised to $[Pt_{26}(CO)_{32}]^{-}$ (**12**).

Finally, new bimetallic Pt-Sn clusters were investigated. The reactions of $[Pt_6(CO)_6(SnX_2)_2(SnX_3)_4]^{4-}$ (X = Cl; Br) with an excess of $HBF_4\cdot Et_2O$ afforded the new heterometallic $[Pt_{12}(CO)_{10}(SnCl)_2(SnCl_2)_4\{Cl_2Sn(\mu\text{-}OH)SnCl_2\}_2]^{2-}$ (**13**) and $[Pt_7(CO)_6(SnBr_2)_4\{Br_2Sn(\mu\text{-}OH)SnBr_2\}\{Br_2Sn(\mu\text{-}Br)SnBr_2\}]^{2-}$ (**14**) clusters. The latter was accompanied by crystals of $[PPh_4][Pt(CO)(Br)(SnBr_3)_2]$ (**15**) and $[PPh_4]_2[Pt_2(CO)_2(Br)_4(SnBr_2)]$ (**16**) as side-products.

The new species described in this chapter have been characterised by means of IR and NMR spectroscopy, ESI-MS analysis and single crystal X-ray diffraction (SC-XRD)

6.3 Synthesis and characterisation of $[Pt_6(CO)_{10}(dppm)]^{2-}$ (1)

The reaction of $[Pt_6(CO)_{12}]^{2-}$ with a slight excess of dppm in CH_3CN afforded the new di-anionic cluster $[Pt_6(CO)_{10}(dppm)]^{2-}$ (**1**) in high yields, in agreement with equation (6.1). The reaction was monitored by IR spectroscopy and the reaction was completed after ca. 2 hours.

$$[Pt_6(CO)_{12}]^{2-} + dppm \rightarrow [Pt_6(CO)_{10}(dppm)]^{2-} + 2CO \quad (6.1)$$

In agreement with equation (6.1), during the reaction the solution was periodically evacuated in order to remove the CO and push the reaction toward the substitution product. **1** was characterised by means of ESI-MS, IR and $^{31}P\{^1H\}$ NMR spectroscopy, and its molecular structure determined *via* SC-XRD.

The carbonyl stretchings decreased during the reaction, from ν_{CO} 2000(vs), 1800(s) cm^{-1} typical of $[Pt_6(CO)_{12}]^{2-}$, to ν_{CO} 2006(s), 1980(vs), 1780(s), 1770(s) cm^{-1} of **1**. This frequencies decrease can be ascribed to the greater σ basicity of the phosphine ligand compared to CO.

The ESI-MS spectrum in CH_3CN solution showed a main peak in the negative mode at m/z 917, corresponding to the molecular ion $[Pt_6(CO)_{10}(dppm)]^{2-}$. Moreover, a minor peak was observed at m/z 1833, which was assigned to its oxidation product $[Pt_{12}(CO)_{20}(dppm)_2]^{2-}$.

In keeping with the solid state structure, the $^{31}P\{^1H\}$ NMR spectrum of $[Pt_6(CO)_{10}(dppm)]^{2-}$ recorded in CD_3CN at 298 K displayed a resonance centred at δ_P 51.0 ppm, in view of the equivalence of the two P atoms of the unique dppm ligand (Figure 6.4). This resonance showed a large $^1J_{PtP}$ coupling to one Pt atom (4960 Hz) as well as a second-order $^2J_{PP}$ (88 Hz). In addition, two very different $^2J_{PtP}$ coupling constants were observed, the larger one (602 Hz) to two equivalent Pt atoms, and the smaller one (15 Hz) to a single Pt atom. Based on the crystal structure, the larger $^2J_{PtP}$ value corresponds to coupling to the two Pt atoms of the triangle to which the P atom is directly bonded, whereas the smaller $^2J_{PtP}$ value corresponds to inter-triangle coupling to the Pt atom bonded to the other P of the same dppm ligand. The assignment of the $^{31}P\{^1H\}$ NMR spectrum was fully corroborated by simulation with gNMR 5.0.6.0.

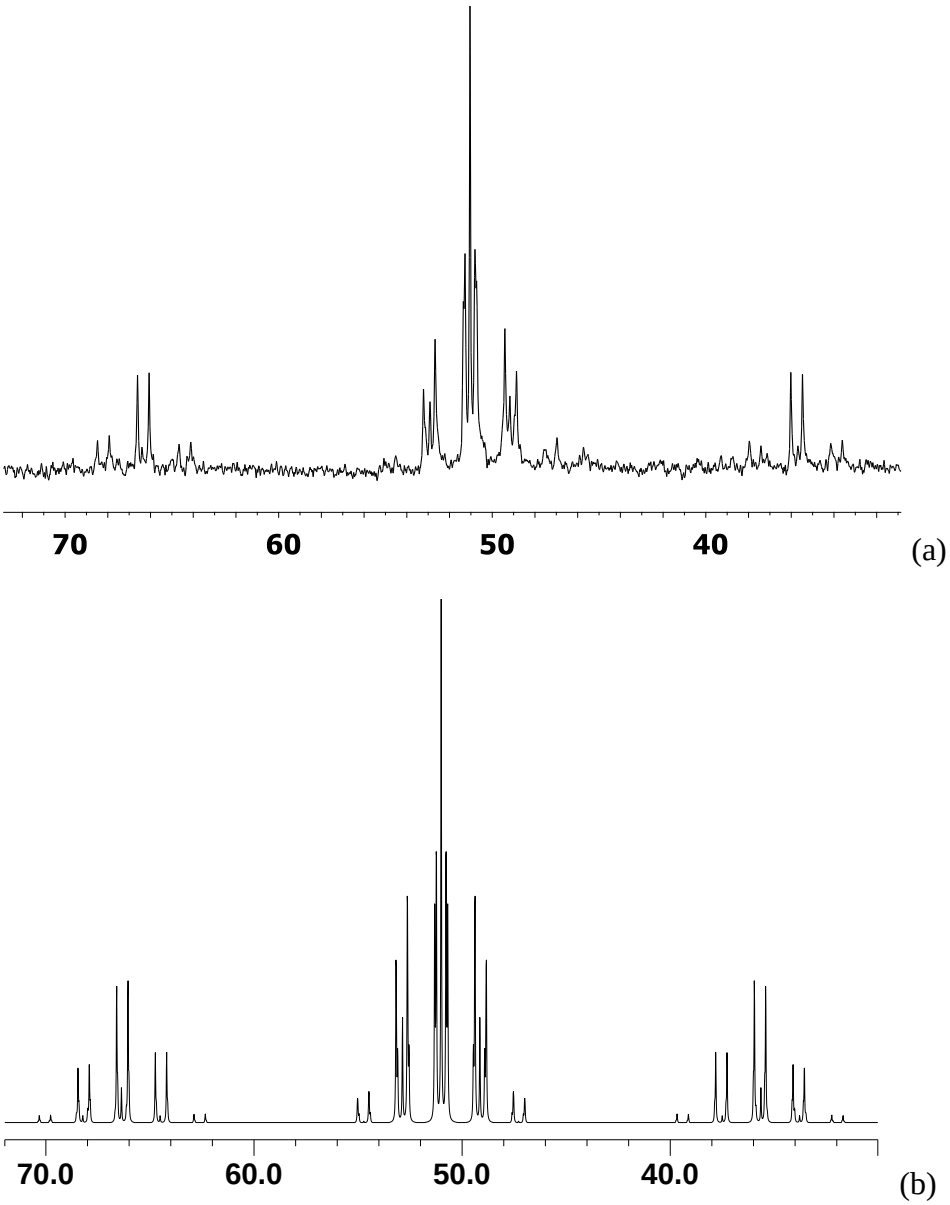

Figure 6.4 $^{31}P\{^{1}H\}$ NMR spectra of $[Pt_6(CO)_{10}(dppm)]^{2-}$ (**1**) in CD_3CN at 298 K: (a) experimental; (b) simulated. δ (ppm): 51.0 ($^{1}J_{PtP}$ = 4960 Hz (1Pt), $^{2}J_{PtP}$ = 602 Hz (2Pt) and 15 Hz (1Pt), $^{2}J_{PP}$ = 88 Hz).[69]

Crystal structures

The molecular structure of **1** has been determined by means of X-ray crystallography as $[NEt_4]_2$[**1**]·CH_3CN salt (Figure 6.5).

The structure of the heteroleptic anion **1** can be formally derived from that of $[Pt_6(CO)_{12}]^{2-}$, after replacing two terminal CO ligands, one per Pt_3-triangular unit, with dppm. The Pt_6-cage of the cluster retained the trigonal prismatic structure of the parent homoleptic Chini cluster. This can be ascribed to the presence of a single -CH_2- group in the dppm ligand that hampered the rotation of

the Pt_3-triangle. Indeed, $[Pt_6(CO)_{10}(PPh_3)_2]^{2-}$ displayed an octahedral structure, in view of the presence of monodentate phosphine ligands.[71]

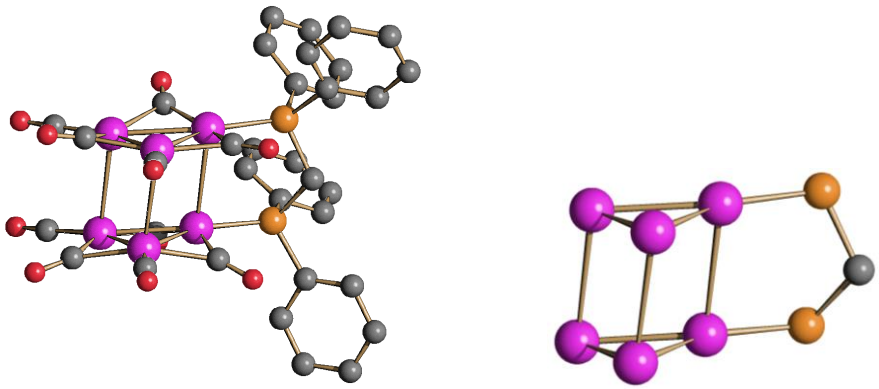

(a) (b)

Figure 6.5 (a) Molecular structure of $[Pt_6(CO)_{10}(dppm)]^{2-}$ (**1**) and (b) its Pt-P core (purple, Pt; orange, P; red, O; grey, C). Hydrogen atoms have been omitted for clarity.[69]

6.4 Syntheses and characterisation of $[Pt_{12}(CO)_{20}(dppm)_2]^{2-}$ (2) and $[Pt_{18}(CO)_{30}(dppm)_3]^{2-}$ (3)

The oxidation of **1** with $HBF_4{\cdot}Et_2O$ in CH_3CN afforded the higher nuclearity cluster $[Pt_{12}(CO)_{20}(dppm)_2]^{2-}$ (**2**), in accord to equation (6.2). The reaction was reversed by adding $[NBu_4][OH]$ under CO to a solution of $[Pt_{12}(CO)_{20}(dppm)_2]^{2-}$ in dmf, in agreement with equation (6.3).

$$2[Pt_6(CO)_{10}(dppm)]^{2-} + 2H^+ \rightarrow [Pt_{12}(CO)_{20}(dppm)_2]^{2-} + H_2 \quad (6.2)$$

$$[Pt_{12}(CO)_{20}(dppm)_2]^{2-} + 2OH^- + CO \rightarrow 2[Pt_6(CO)_{10}(dppm)]^{2-} + CO_2 + H_2O \quad (6.3)$$

It is likely that, in the presence of a bidentate ligand, the oxidation of $[Pt_6(CO)_{10}(dppm)]^{2-}$ proceeds through a $[Pt_6(CO)_{10}(dppm)]^-$ radical mono-anion which immediately dimerises resulting in $[Pt_{12}(CO)_{20}(dppm)_2]^{2-}$ (Scheme 6.2).

The reaction of **2** in dmf with a slight excess of $HBF_4{\cdot}Et_2O$ in the presence of air afforded $[Pt_{18}(CO)_{30}(dppm)_3]^{2-}$ (**3**) (Scheme 6.3) as indicated by the shift of the ν_{CO} bands in the IR spectrum towards higher wavenumbers. As previously shown in equation (6.3), **3** can be reversibly reduced to **2** in the presence of a strong base, under CO atmosphere in dmf.

Scheme 6.2 Proposed mechanism for the oxidation of $[Pt_6(CO)_{10}(dppm)]^{2-}$ (**1**) to $[Pt_{12}(CO)_{20}(dppm)_2]^{2-}$ (**2**).

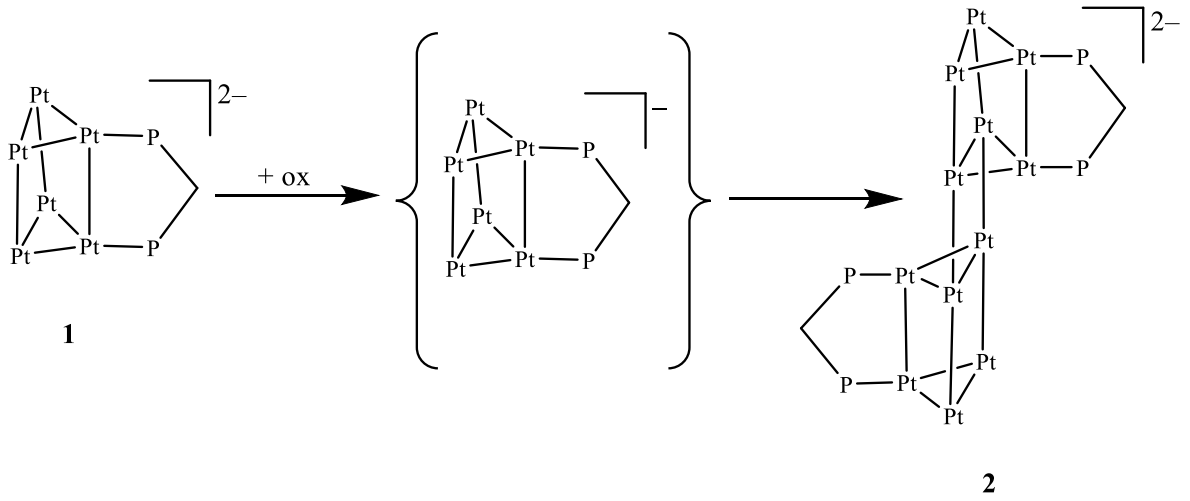

Scheme 6.3 Oxidation of $[Pt_6(CO)_{10}(dppm)]^{2-}$ (**1**) resulting in $[Pt_{12}(CO)_{20}(dppm)_2]^{2-}$ (**2**) and $[Pt_{18}(CO)_{30}(dppm)_3]^{2-}$ (**3**) (ox = H^+ and/or air; red = CO/OH^-).

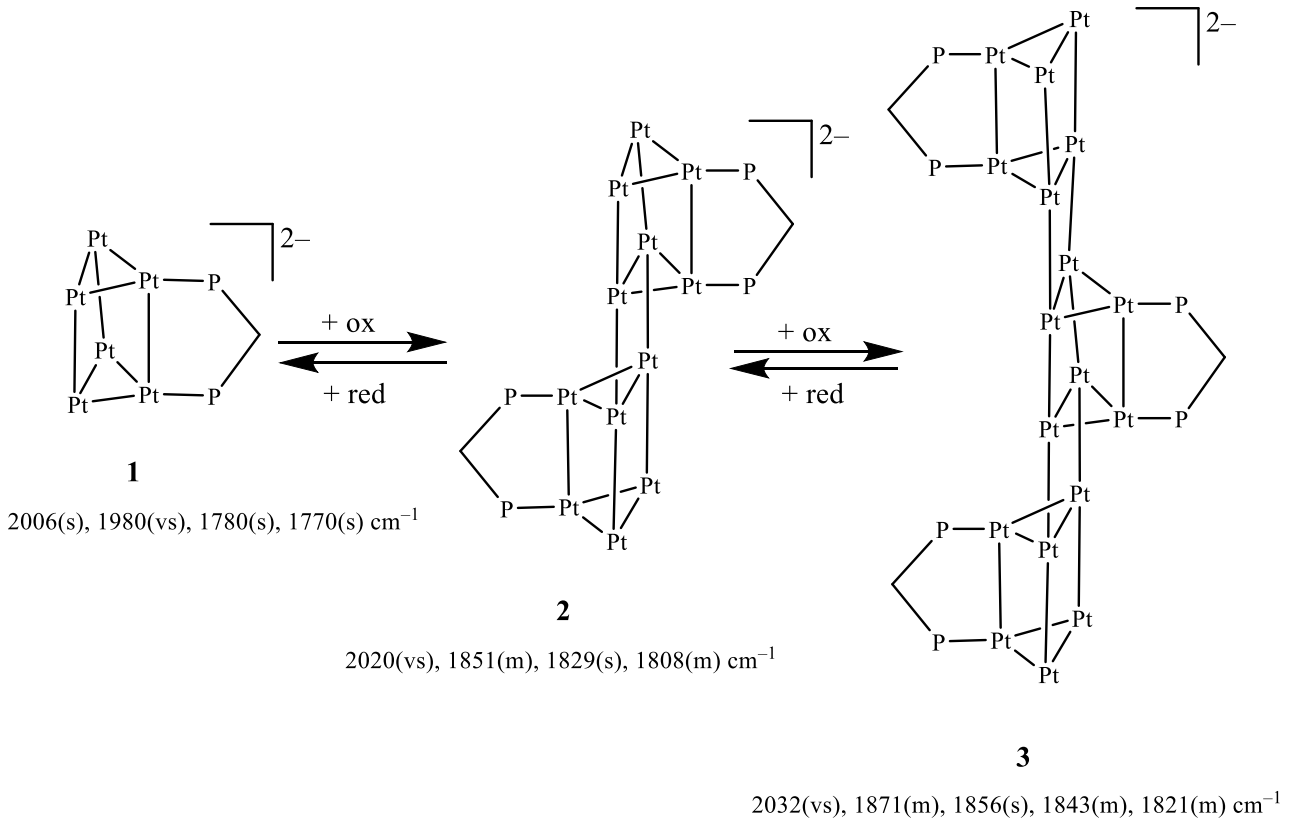

In order to further increase the nuclearity of the clusters, **3** was treated in air with an excess of $HBF_4{\cdot}Et_2O$. The IR spectrum of the resulting species displayed ν_{CO} bands at 2045(vs), 1859(s)

and 1826(m) cm^{-1}. This new compound was too instable to be fully characterised. Nonetheless, on the basis of its IR spectrum, we can tentatively formulate it as $[Pt_{24}(CO)_{40}(dppm)_4]^{2-}$ (**4**). It is clear that the oxidation of heteroleptic Chini clusters containing bidentate ligands allows to grow the dimension of the compound by the sequential addition of $\{Pt_6(CO)_{10}(dppm)\}$ units, resulting in $[\{Pt_6(CO)_{10}(dppm)\}_x]^{2-}$ (x = 1-4) molecular clusters. This should be contrasted with the "normal" growing mode of homoleptic Chini clusters, which involve the addition of $\{Pt_3(CO)_6\}$ triangular units.

2 and **3** were fully characterised through IR, ESI-MS and $^{31}P\{^1H\}$ NMR spectroscopy. Unfortunately, the molecular structure of **3** was not determined, because all the attempts to crystallise it failed, whereas crystals of **2** suitable for SC-XRD have been obtained.

As far as the spectroscopic characterisation is concerned, **2** displayed ν_{CO} bands in the IR spectrum at 2020(vs), 1851(m), 1829(s), 1808(m) cm^{-1} in CH_3CN solution, whereas **3** displayed ν_{CO} bands at 2032(vs), 1871(m), 1856(s), 1843(m), 1821(m) cm^{-1}, considerably moved towards higher wavenumbers compared to the parent **2**.

The ESI-MS spectra showed the expected peak of the **2** molecular ion at m/z 1834 and a main peak at m/z 2752 attributable to the **3** molecular ion.

The $^{31}P\{^1H\}$ NMR spectrum of **2** showed the presence of two non-equivalent P atoms in a 1:1 ratio. Thus, it displayed two resonances at δ_P 46.2 and 38.7 ppm. Both resonances presented $^1J_{PtP}$ coupling to one Pt atom (4962 and 5144 Hz, respectively), a $^2J_{PtP}$ coupling constant to two Pt atoms (546 and 626 Hz, respectively), and a smaller $^2J_{PP}$ (83 Hz). The $^{31}P\{^1H\}$ NMR spectrum of **3** displayed three resonances attributable to the three non-equivalent types of P atoms present within the structure, each type consisting of two P atoms (see Experimental Section for further details).

Crystal structure

2 was structurally characterised throughout SC-XRD as $[NEt_4]_2$[**2**]·$2CH_3CN$·2dmf and $[NEt_4]_2$[**2**]·4dmf solvated salts (Figure 6.6).

The cluster may be viewed as composed of two trigonal prismatic $[Pt_6(CO)_{10}(dppm)]$ units rotated of 180° and joined by two symmetry equivalent Pt-Pt bonds [2.9798(6) and 2.986(5) Å, for the two salts, respectively]. As a consequence, there is one μ-CO ligand per $[Pt_6(CO)_{10}(dppm)]$ unit which weakly interacts with one Pt atom of the second $[Pt_6(CO)_{10}(dppm)]$ unit [Pt···C(O) 3.226(12) and 3.285(18) Å, for the two salts, respectively].

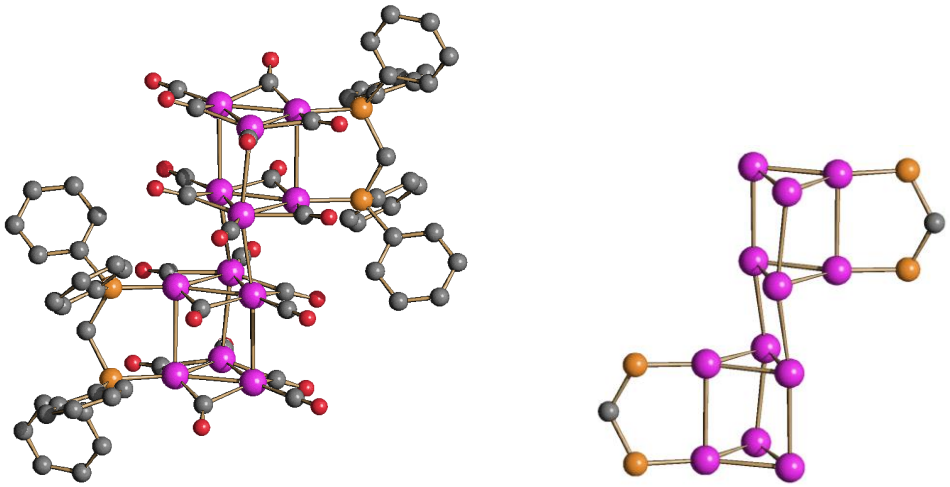

(a) (b)

Figure 6.6 (a) Molecular structure of $[Pt_{12}(CO)_{20}(dppm)_2]^{2-}$ (**2**) and (b) its Pt-P core. (purple, Pt; orange, P; red, O; grey, C). Hydrogen atoms have been omitted for clarity.[69]

6.5 Syntheses and characterisation of $[Pt_{12}(CO)_{20}(PTA)_4]^{2-}$ (5) and $[Pt_{15}(CO)_{25}(PTA)_5]^{2-}$ (6)

The reaction of $[Pt_9(CO)_{18}]^{2-}$ in CH_3CN with three equivalents of PTA afforded the substitution product $[Pt_9(CO)_{15}(PTA)_3]^{2-}$ with the retention of the nuclearity, as shown in Scheme 6.4.

Scheme 6.4. Reaction of $[Pt_9(CO)_{18}]^{2-}$ with PTA.

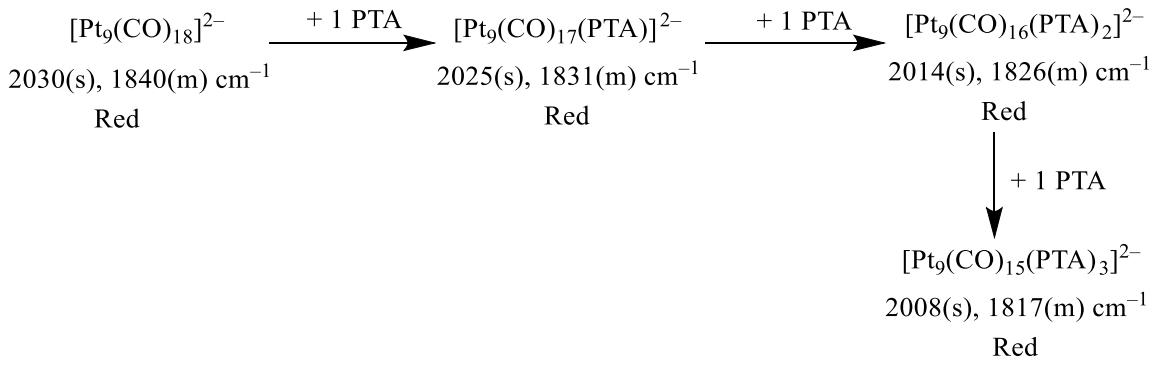

The red solution of $[Pt_9(CO)_{15}(PTA)_3]^{2-}$ under oxidising condition (air or stoichiometric amount of $HBF_4{\cdot}Et_2O$) became green, resulting in the higher nuclearity $[Pt_{12}(CO)_{20}(PTA)_4]^{2-}$ (**5**) cluster. Further oxidation of **5** afforded the di-anionic $[Pt_{15}(CO)_{25}(PTA)_5]^{2-}$ (**6**) compound (Scheme 6.5).

Scheme 6.5 Syntheses of $[Pt_{15}(CO)_{25}(PTA)_5]^{2-}$ (**6**) and $[Pt_{12}(CO)_{20}(PTA)_4]^{2-}$ (**5**) by oxidation of $[Pt_9(CO)_{15}(PTA)_3]^{2-}$ (ox = air or $HBF_4 \cdot Et_2O$).

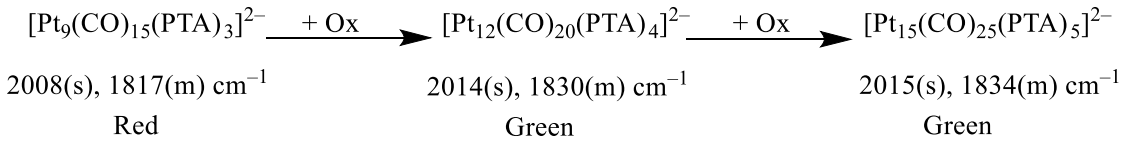

The compounds **5** and **6** have been characterised by IR and $^{31}P\{^1H\}$ NMR spectroscopy, and their molecular structures fully determined *via* X-ray crystallography.

The $^{31}P\{^1H\}$ NMR spectra of **5** and **6** recorded in CD_3COCD_3 at 298 K exhibited two resonances at δ_P (ppm) -42.6 (2P, $^1J_{PtP}$ = 4571 Hz, $^2J_{PtP}$ = 502 Hz) and -43.8 (2P, $^1J_{PtP}$ = 4588 Hz, $^2J_{PtP}$ = 511 Hz), and three resonances at -46.2 (2P, $^1J_{PtP}$ = 4560 Hz, $^2J_{PtP}$ = 480 Hz), -47.1 (2P, $^1J_{PtP}$ = 4544 Hz, $^2J_{PtP}$ = 540 Hz) and -54.1 (1P, $^1J_{PtP}$ = 4694 Hz, $^2J_{PtP}$ = 470 Hz), respectively. These data confirm the molecular structures identified by SC-XRD analysis.

The presence of some peaks in the $^{31}P\{^1H\}$ NMR spectrum not attributed to $[Pt_{12}(CO)_{20}(PTA)_4]^{2-}$, indicated the presence of some minor impurities, as corroborated by ESI-MS.

Thus, the ESI mass spectrum of **5** recorded in CH_3CN (negative mode) showed an intense peak at *m/z* (relative intensity in parentheses) 1765(*100*) attributable to the parent molecular ion. Lower intensity peaks observed at 1701(*19*) and 1830(*30*) can be assigned to $[Pt_{12}(CO)_{21}(PTA)_3]^{2-}$ and $[Pt_{12}(CO)_{19}(PTA)_5]^{2-}$, and those at 1259(*10*) and 1323(*40*) corresponded to the reduced species $[Pt_9(CO)_{16}(PTA)_2]^{2-}$ and $[Pt_9(CO)_{15}(PTA)_3]^{2-}$, respectively.

Crystal structures

The nature of **5** and **6** has been fully corroborated by SC-XRD as their $[NEt_4]_2$[**5**]$\cdot 1.5CH_3COCH_3$ (Figure 6.7) and $[NMe_3(CH_2Ph)]_2$[**6**]$\cdot CH_3COCH_3$ salts (Figure 6.8).

The molecular structure of **5** can be formally obtained from that of $[Pt_{12}(CO)_{24}]^{2-}$, after replacing four terminal CO ligands by PTA, one in each of the four Pt_3-triangular units. Overall, $[Pt_{12}(CO)_{20}(PTA)_4]^{2-}$ retains the trigonal prismatic structure of the parent homoleptic Chini cluster. It may be viewed as being composed of a stacking of four $Pt_3(\mu\text{-}CO)_3(CO)_2(PTA)$ units. The four PTA ligands are placed on alternate sides of the cluster, in order to minimise steric repulsion.

6 is composed of five $Pt_3(\mu\text{-}CO)_3(CO)_2(PTA)$ units and closely resembles to the parent **5**. The molecular structures of **5** and **6** indicate that it is possible to substitute one terminal CO ligand per Pt_3-unit in Chini clusters by PTA with retention of their trigonal prismatic structures.[72]

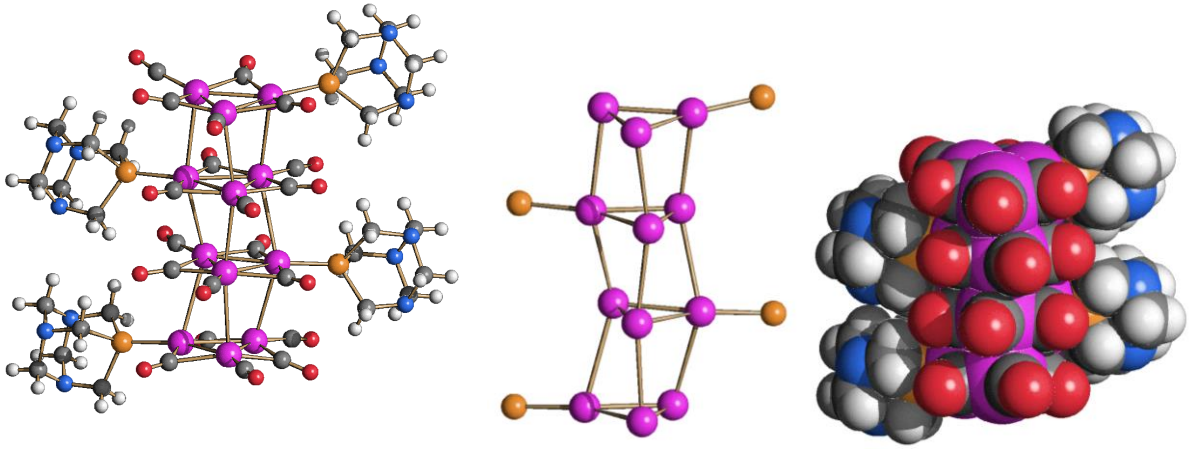

(a) (b) (c)

Figure 6.7 (a) The molecular structure of $[Pt_{12}(CO)_{20}(PTA)_4]^{2-}$ (**5**), (b) the $Pt_{12}P_4$ core, and (c) a space-filling model (purple, Pt; orange, P; blue, N; red, O; grey, C; white, H).[72]

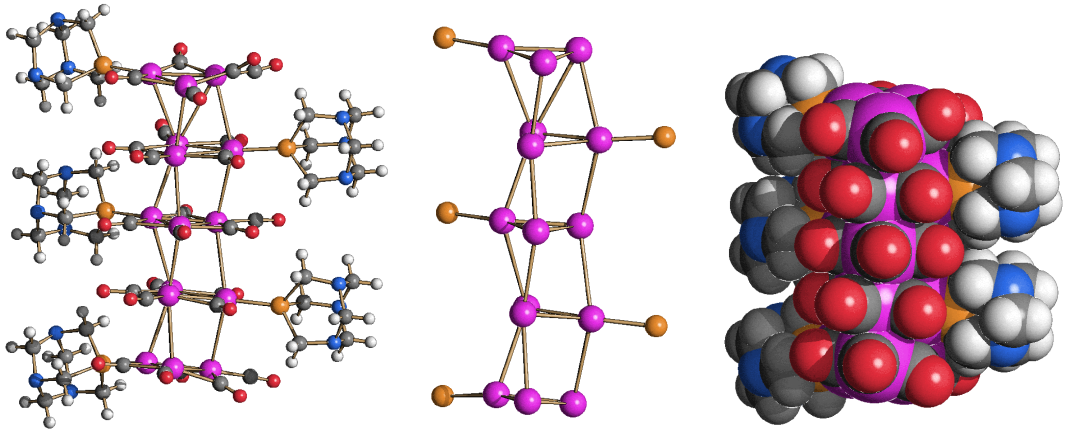

(a) (b) (c)

Figure 6.8 (a) The molecular structure of $[Pt_{15}(CO)_{25}(PTA)_5]^{2-}$ (**6**), (b) the $Pt_{15}P_5$ core, and (c) a space-filling model (purple, Pt; orange, P; blue, N; red, O; grey, C; white, H).[72]

Water solubility

The ability of PTA to confer water solubility was qualitatively assessed by dissolving **5** as $[NEt_4]^+$ salt in CH_2Cl_2 (green solution) and then, adding a similar volume of water. After a while, the lower organic layer becomes almost colourless, whereas the top aqueous layer becomes coloured. Conversely, with $[NEt_4]_2[Pt_{12}(CO)_{24}]$, the cluster remains in the organic layer. The solubility in water of $[NEt_4]_2$[**5**], as determined by atomic absorption, is 1.20 mg/mL.

Cytotoxicity studies

Thanks to their water solubility, it was possible to evaluate **5** and **6** against a human ovarian cancer cell line (A2780) and its cisplatin-resistant strain (A2780cisR). The data presented in Table 6.2 have been collected during preliminary tests conducted by Dr. Silvia Ruggieri (University of Bologna) at the Institut des Sciences et Ingénierie Chimiques, Ecole Polytechnique Fédérale de Lausanne, in collaboration with Prof. P. J. Dyson.[72] As shown in Table 6.2, compared to cisplatin, **5** and **6** are considerably less cytotoxic to the A2780 cell line, whereas they are both slightly more cytotoxic to A2780cisR cells.

Table 6.2 Cytotoxicity of $[Pt_{12}(CO)_{20}(PTA)_4]^{2-}$ (**5**), $[Pt_{15}(CO)_{25}(PTA)_5]^{2-}$ (**6**) and cisplatin reference towards human ovarian cancer cells.

Compound	IC_{50}(A2780) [μM]	IC_{50} (A2780cisR) [μM]
$[Pt_{12}(CO)_{20}(PTA)_4]^{2-}$	22.3 ± 1.4	12.2 ± 1.5
$[Pt_{15}(CO)_{25}(PTA)_5]^{2-}$	12.3 ± 1.1	6.13 ± 0.7
cisplatin	1.9 ± 0.7	23 ± 3

6.6 Syntheses and characterisation of $[NEt_4]_2[Pt_9(CO)_{18}]\cdot py$ (7) and $[Pt_{12}(CO)_{22}(PPh_2py)_2]^{2-}$ (8)

In order to trap in the solid state a species of the type $[Pt_{3n}(CO)_{6n}(L)]^{2-}$, that is supposed to be an intermediate/transition state in the substitution reactions of Chini clusters, two different approaches have been used. First, $[NEt_4]_2[Pt_9(CO)_{18}]$ has been crystallised from a solution of pyridine by slow diffusion of isopropanol. The aim was to obtain a solid state structure where the pyridine molecule approached a Pt atom of the Chini cluster with its N-donor atom. As a result, crystals of $[NEt_4]_2[Pt_9(CO)_{18}]\cdot py$ (**7**) were obtained, but the pyridine molecule was not interacting with the cluster.[73]

Regarding the second approach, the reaction of $[Pt_{12}(CO)_{24}]^{2-}$ with two equivalents of PPh_2py in acetone resulted in the substitution product $[Pt_{12}(CO)_{22}(PPh_2py)_2]^{2-}$ (**8**).[73] Crystals of $[NEt_4]_2$[**8**] suitable for X-ray analyses were obtained by slow diffusion of *n*-hexane on the acetone solution. In this case the aim was to force an interaction between the N-atom of the bidentate PPh_2py ligand and the cluster. Also this approach was not successful, since the crystals of $[NEt_4]_2$[**8**] (Figure 6.9) were isomorphous and isostructural with $[NEt_4]_2[Pt_{12}(CO)_{22}(PPh_3)_2]$, and showed no Pt···N interaction.

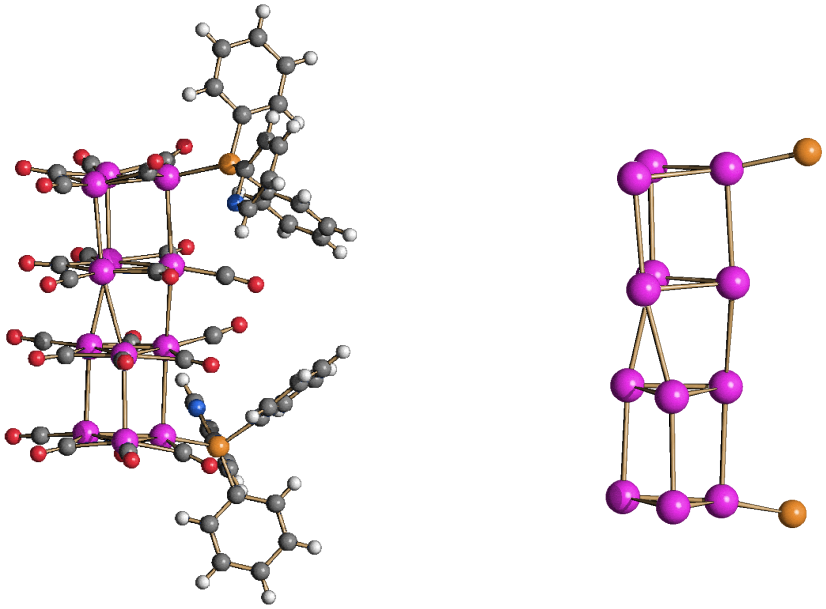

(a) (b)

Figure 6.9 Molecular structure of (a) $[Pt_{12}(CO)_{22}(PPh_2py)_2]^{2-}$ (**8**) and (b) its $Pt_{12}P_2$ skeleton (purple, Pt; orange, P; red, O; grey, C; white, H).[73]

6.7 Syntheses and characterisation of $Pt_5(XylNC)_{10}$ (9) and $Pt_9(XylNC)_{13}(CO)$ (10)

The reactions of $[Pt_6(CO)_{12}]^{2-}$ and $[Pt_{15}(CO)_{30}]^{2-}$ in CH_3CN solutions with XylNC afforded $Pt_5(XylNC)_{10}$ (**9**) and $Pt_9(XylNC)_{13}(CO)$ (**10**), respectively.[73] Crystals of $Pt_5(XylNC)_{10}$·2toluene and $Pt_9(XylNC)_{13}(CO)$·solv suitable for X-ray diffraction were obtained by slow diffusion of *n*-pentane on the toluene solutions (Figures 6.10-6.11).

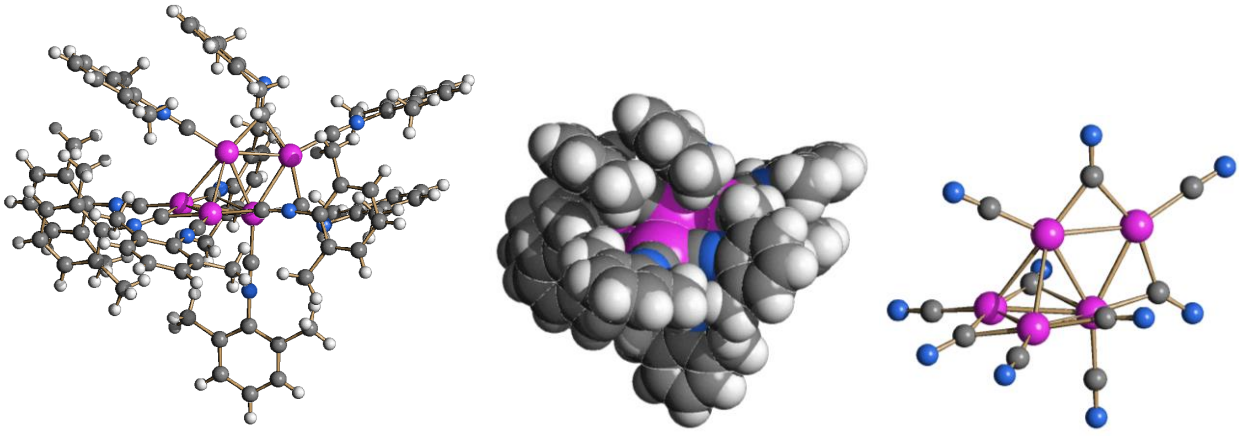

(a) (b) (c)

Figure 6.10 Molecular structure of (a) $Pt_5(XylNC)_{10}$ (**9**), (b) space filling model and (c) a simplified view of the metal skeleton and stereochemistry of the ligands (purple, Pt; blue, N; grey, C; white, H).[73]

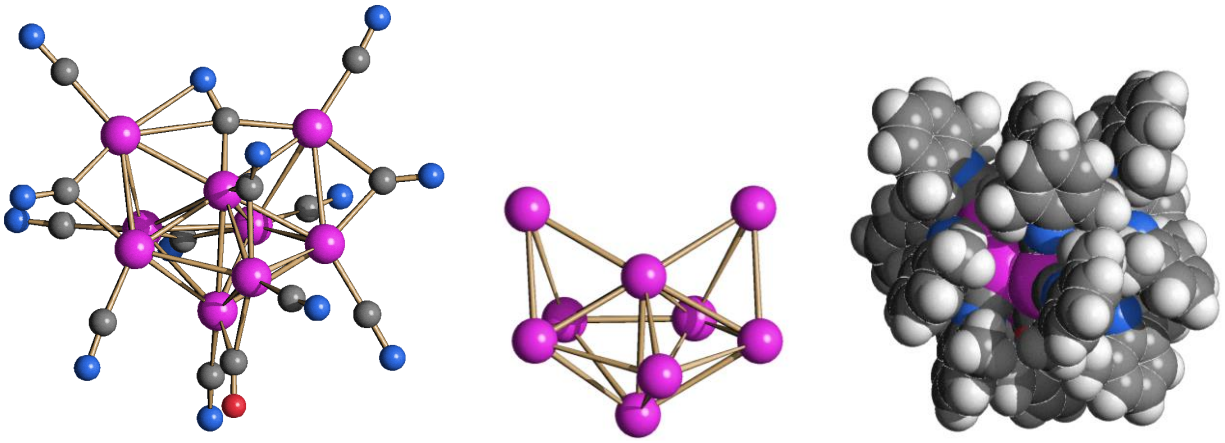

(a) (b) (c)

Figure 6.11 (a) A simplified view of the metal skeleton and stereochemistry of the ligands of $Pt_9(XylNC)_{13}(CO)$ (**10**), (b) the Pt_5 skeleton and (c) space filling model (purple, Pt; blue, N; red, O; grey, C; white, H).[73]

The molecular structure of **9** consists of an edge-bridged Pt_5 tetrahedron bonded to five μ-CNXyl and five terminal CNXyl ligands. The metal core and stereochemistry of the ligands is the same found in related $Pt_5(CO)_6(PR_3)$ (R = Ph, Cy, $CH_2C(O)Ph$) and $Pt_5(CO)_7(IMes)_3$ clusters.[74–76]

The metal framework of **10** may be viewed as a Pt_7 pentagonal bipyramid (PBP) with two further Pt atoms capping two non-adjacent triangular faces which share a common vertex.

6.8 Synthesis and characterisation of $[Pt_{27}(CO)_{31}]^{4-}$ (11)

A thf solution of $[PPh_4]_2[Pt_{15}(CO)_{30}]$ was heated at 65 °C under H_2 atmosphere for 8 hours, affording a solution of $[Pt_{24}(CO)_{30}]^{2-}$ and an oily precipitate of $[Pt_{27}(CO)_{31}]^{4-}$ (**11**). Then, the solvent was removed under reduced pressure and the residue washed with H_2O, isopropanol, toluene, thf and extracted in acetone. Crystals of $[PPh_4]_4[Pt_{27}(CO)_{31}]$ suitable for X-ray diffraction have been obtained by slow diffusion of isopropanol on the acetone solution (Figure 6.12).

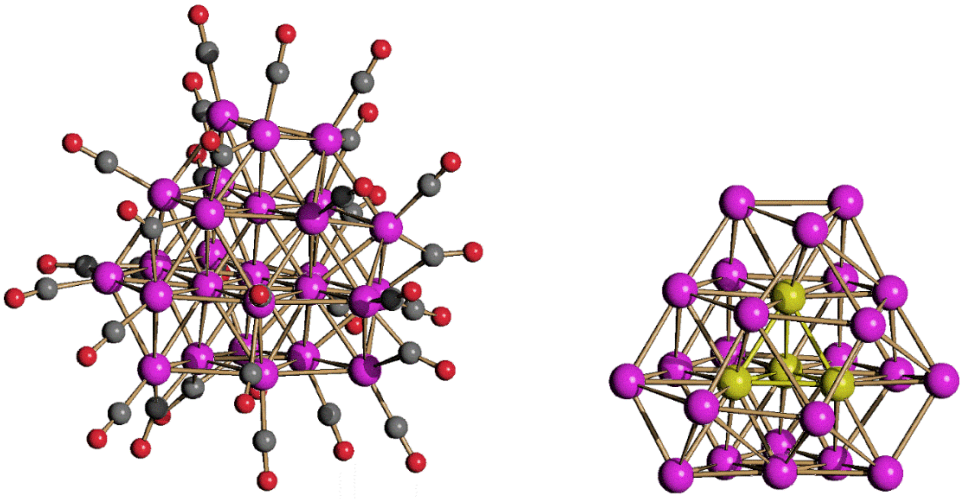

(a) (b)

Figure 6.12 Molecular structure of (a) $[Pt_{27}(CO)_{31}]^{4-}$ (**11**) and (b) its Pt_{27} metal core containing a fully interstitial Pt_4 tetrahedron (purple, superficial Pt; yellow, interstitial Pt; red, O; grey, C).

The molecular structure of **11** is composed of a *ccp* M_{27} framework generated by the overlapping of four ABCA layers, consisting of 3, 7, 12 and 6 atoms, respectively. As shown in Figure 6.12, this structure encapsulates a fully interstitial Pt_4 tetrahedron. The structure is completed by 31 CO ligands, 18 of which are terminal and 13 edge bridging.

The UV-visible spectrum of **11** as $[NBu_4]^+$ salt in CH_3CN solution shows a featureless spectrum with a broad, continuous electronic absorption characteristic of interband transitions. Thus, the UV-visible spectrum of **11** shown in Figure 6.13 is very similar to those of small metal nanoparticles, as reported in the literature.[77]

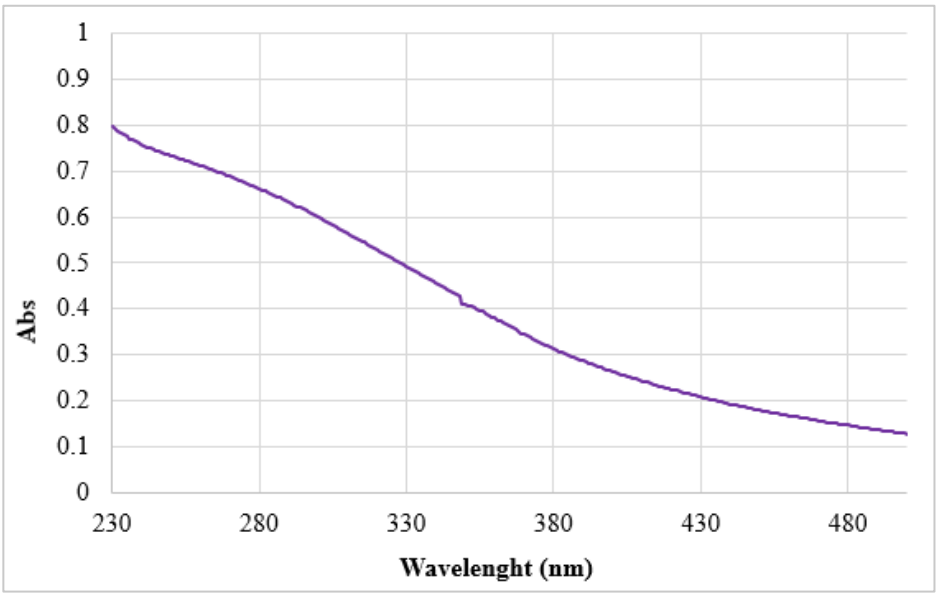

Figure 6.13 UV-visible absorption spectrum of $[NBu_4]_4[Pt_{27}(CO)_{31}]$ (**11**) in CH_3CN at 298 K.

*Reactivity of **11***

$[Pt_{40}(CO)_{40}]^{6-}$ was obtained during the synthesis of **11** in dmso at 150 °C. The IR spectroscopy of the crude mixture revealed the characteristic frequencies of **11**, but after work-up only $[Pt_{40}(CO)_{40}]^{6-}$ was extracted. Interestingly, in the literature it is reported that the latter derives from the decomposition of $[Pt_{19}(CO)_{22}]^{4-}$.[78] We can suppose that after the thermal treatment, **11** decomposed into $[Pt_{19}(CO)_{22}]^{4-}$, that in turn was transformed into $[Pt_{40}(CO)_{40}]^{6-}$ during the work-up.

Then, **11** was treated in acetone with $HBF_4{\cdot}Et_2O$, affording at first $[Pt_{26}(CO)_{32}]^{2-}$. By pushing the oxidation further, it was possible to obtain quantitatively $[Pt_{26}(CO)_{32}]^{-}$ (**12**) (Figure 6.14), as shown in Scheme 6.6. This mono-anion can be alternatively formulated as $[HPt_{26}(CO)_{32}]^{-}$. On the basis of the data available at the moment it is not possible to distinguish between these two formulations. Further oxidation of **12** led to a purported neutral $[Pt_{26}(CO)_{30}]$ as indicated by IR spectroscopy. Because of its scarce stability, all the attempts to crystallise the neutral cluster failed.

Scheme 6.6 Synthesis of $[Pt_{26}(CO)_{32}]^{n}$ (n =-2-0).

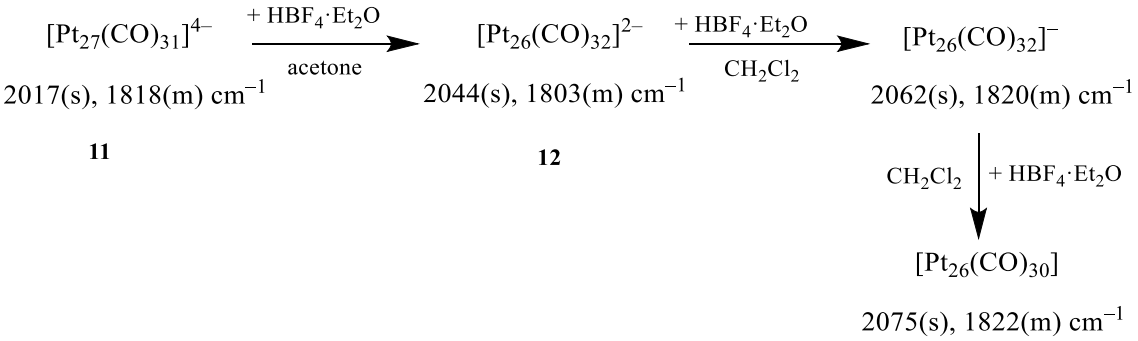

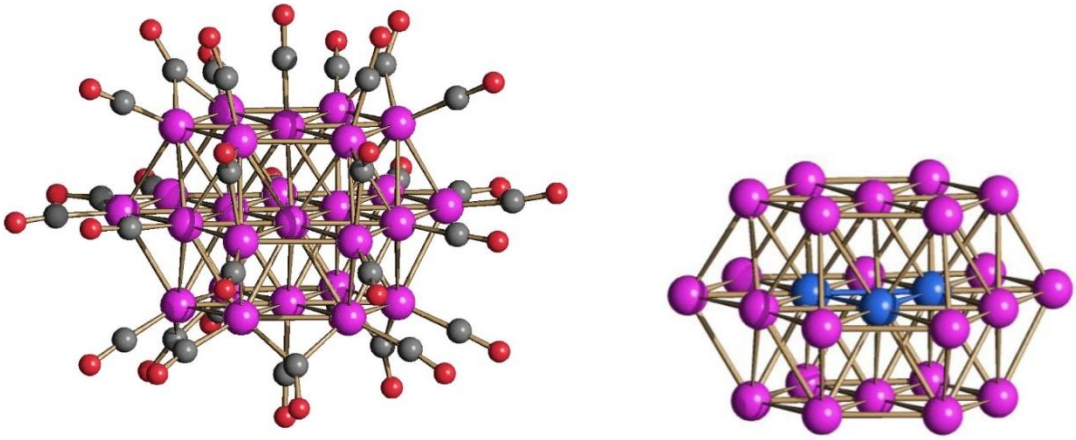

Figure 6.14 Molecular structure of (a) $[Pt_{26}(CO)_{32}]^{-}$ (**12**) and (b) its *hcp* Pt_{26} core (purple, Pt; red, O; grey, C). Fully interstitial Pt atoms in (b) are represented in blue.

12 reveals a hexagonal ABA closest packed (*hcp*) structure, composed of three layers of 7, 12 and 7 Pt atoms, respectively. The metal core of the cluster displays a pseudo D_{3h} symmetry. Three Pt atoms, which form a triangle, are completely encapsulated within the cluster core, while there are two 9-coordinate and three 8-coordinate "terrace-like" surface atoms which bind a single terminal carbonyl. Inclusion of the 23 terminal and 9 edge bridging carbonyl ligands lowers the pseudo D_{3h} Pt_{26} core symmetry to mirror-plane C_s. The fact that the bonding parameters and structures of $[Pt_{26}(CO)_{30}]^{-}$ and $[Pt_{26}(CO)_{30}]^{2-}$ are almost identical suggests that their Pt_{26} kernel is very stable and not affected by the addition/removal of a single electron.

6.9 Syntheses and characterisation of $[Pt_{12}(CO)_{10}(SnCl)_2(SnCl_2)_4\{Cl_2Sn(\mu\text{-}OH)SnCl_2\}_2]^{2-}$ (13) and $[Pt_7(CO)_6(SnBr_2)_4\{Br_2Sn(\mu\text{-}OH)SnBr_2\}\{Br_2Sn(\mu\text{-}Br)SnBr_2\}]^{2-}$ (14)

The oxidation of $[Pt_6(CO)_6(SnX_2)_2(SnX_3)_4]^{4-}$ (X = Cl, Br) in CH_3CN with an excess of $HBF_4{\cdot}Et_2O$, followed by removal of the solvent *in vacuo* and dissolving the residue in CH_2Cl_2 led to the isolation of $[Pt_{12}(CO)_{10}(SnCl)_2(SnCl_2)_4\{Cl_2Sn(\mu\text{-}OH)SnCl_2\}_2]^{2-}$ (**13**) and $[Pt_7(CO)_6(SnBr_2)_4\{Br_2Sn(\mu\text{-}OH)SnBr_2\}\{Br_2Sn(\mu\text{-}Br)SnBr_2\}]^{2-}$ (**14**), as shown in Scheme 6.7.[79]

Scheme 6.7 Syntheses of **13** and **14**.

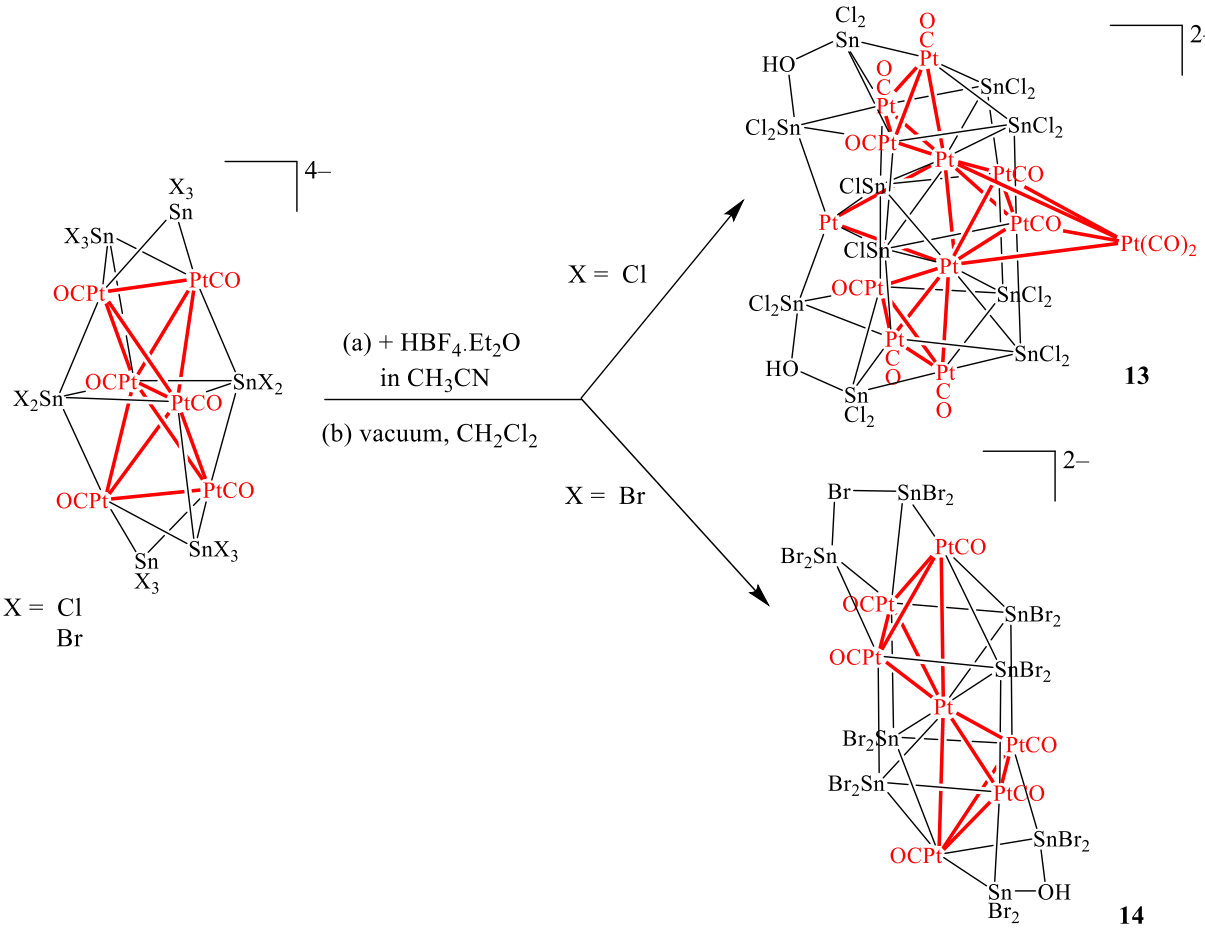

Crystals of $[PPh_4]_2[Pt_{12}(CO)_{10}(SnCl)_2(SnCl_2)_4\{Cl_2Sn(\mu\text{-}OH)SnCl_2\}_2]$ ($[PPh_4]_2$[**13**]) and $[PPh_4]_2[Pt_7(CO)_6(SnBr_2)_4\{Br_2Sn(\mu\text{-}OH)SnBr_2\}\{Br_2Sn(\mu\text{-}Br)SnBr_2\}]$ ($[PPh_4]_2$[**14**]) suitable for X-ray analyses were obtained from slow diffusion of *n*-hexane on the CH_2Cl_2 solutions. The formation of orange ($[PPh_4]_2$[**14**]) crystals was accompanied by minor amounts of a few yellow crystals, that revealed to be a mixture of $[PPh_4][Pt(CO)(Br)(SnBr_3)_2]$ (**15**) and $[PPh_4]_2[Pt_2(CO)_2(Br)_4(SnBr_2)]$ (**16**). These were side-products of the synthesis of **14**, which were formed from the partial oxidation of the anionic cluster in the presence of an excess of strong acid.

The ^{1}H NMR spectra of $[PPh_4]_2$[**13**] and $[PPh_4]_2$[**14**] in CD_2Cl_2 displayed a common resonances at δ_H 7.64-7.96 ppm (40H) due to the $[PPh_4]^+$ cation, a broad resonance at δ_H 6.93 ppm (2H) attributable to the OH groups for $[PPh_4]_2$[**13**] and a broad resonance at δ_H 3.14 ppm that integrated 1.4H for $[PPh_4]_2$[**14**]. This resonance might be assigned to the OH group of **14** or to some adventitious water.

Crystal structures

The molecular structures of **13** and **14** were determined as $[PPh_4]_2$[**13**] and $[PPh_4]_2$[**14**] salts (Figures 6.15-6.18 and Table 6.3).

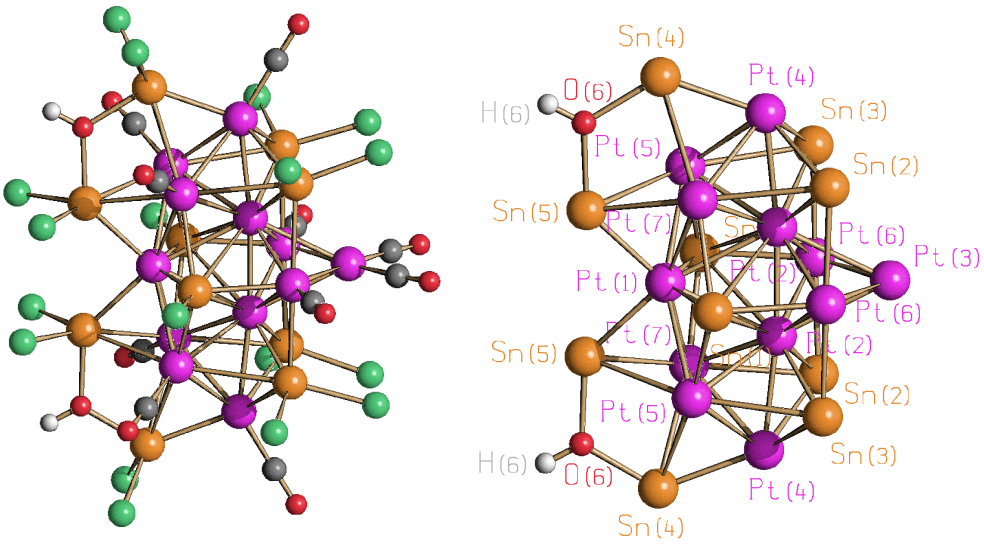

(a) (b)

Figure 6.15 (a) Molecular structure of $[Pt_{12}(CO)_{10}(SnCl)_2(SnCl_2)_4\{Cl_2Sn(\mu\text{-}OH)SnCl_2\}_2]^{2-}$ (**13**) and (b) its $Pt_{12}Sn_{10}$ metal core with labelling (purple, Pt; orange, Sn; green, Cl; red, O; grey, C).[79]

Table 6.3 Comparison of the most relevant bond lengths (Å) of $[Pt_{12}(CO)_{10}(SnCl)_2(SnCl_2)_4\{Cl_2Sn(\mu\text{-}OH)SnCl_2\}_2]^{2-}$ (**13**) and $[Pt_7(CO)_6(SnBr_2)_4\{Br_2Sn(\mu\text{-}OH)SnBr_2\}\{Br_2Sn(\mu\text{-}Br)SnBr_2\}]^{2-}$ (**14**).

Compound number	Pt-Pt	Pt-Sn	Sn-X
13	2.5837(7)-2.9883(6)	2.5854(8)-3.3505(7)	2.331(3)-2.380(3)
	Average 2.7970(19)	Average 2.840(4)	Average 2.359(9)
14	2.6947(5)-3.2450(5)	2.6256(9)-3.2991(9)	2.4669(18)-2.789(3)
	Average 2.8434(12)	Average 2.792(3)	Average 2.546(6)

The cluster anion **13** is located on a 2-fold axis and the H atom bonded to O(6) was initially located on the Fourier map and then, refined by a riding model. An inter-molecular H-bond involving O(6)-H(6) and Cl(5)#1 [O(6)-H(6) 0.95 Å, H(6)···Cl(5)#1 2.14 Å, O(6)···Cl(5)#1 3.063(8) Å, <O(6)H(6)Cl(5)#1 164.9°; symmetry operation #1 –x+1/2, y-1/2, -z+1/2] is present corroborating the location of H(6) (Figure 6.16).[80,81] Because of the 2-fold symmetry, each cluster anion contains two O(6)-H(6) hydrogen-bond donors and two Cl(5) acceptor groups. This produces extended planes perpendicular to the crystallographic *c* axis of H-bonded cluster anions, with the $[PPh_4]^+$ cations occupying the inter-layer positions. This represents a rare case of a supramolecular arrangement of anionic metal carbonyl clusters *via* H-bonds.[82,83]

Regarding the molecular anion, **13** consists of three Pt_5 trigonal bipyramids (TBP) sharing three vertices and originating a common Pt_3 triangle (in blue in Figure 6.17). The resulting Pt_{12} framework displays idealised C_{2v} and crystallographic C_2 symmetry. Each of the two (symmetry related) $\{Cl_2Sn(\mu\text{-}OH)SnCl_2\}^-$ ligands is η^2-μ_4-bonded to two adjacent triangular faces of a TBP, as previously found in $[Pt_5(CO)_5\{Cl_2Sn(OR)SnCl_2\}_3]^{3-}$ (R = H, Me, Et, ^{i}Pr). The four $SnCl_2$ stannylene ligands are μ_4-bonded to open butterfly surfaces, whereas the two $[SnCl]^+$ ligands are μ_6-bonded to "triangular crown" Pt_6 frames, where the central triangular unit is represented by the three Pt atoms shared by the three Pt_5TBPs [Pt(1), Pt(2), Pt(2)] and the wingtips are Pt(5), Pt(6) and Pt(7). The former three Pt atoms are not bonded to any CO, whereas the remaining nine Pt atoms are bonded to one terminal CO each, a part Pt(3) which is bonded to two terminal carbonyls.[79]

The Pt_7 core of **14** is composed of two Pt_4 tetrahedra that share a common vertex located on a crystallographic inversion centre (Figure 6.18). The four $SnBr_2$ stannylene ligands are μ_4-bonded to the Pt_7 core resulting in a bicapped centred pseudo-cubic Pt_7Sn_4 framework. The $\{Br_2Sn(\mu\text{-}OH)SnBr_2\}^-$ and $\{Br_2Sn(\mu\text{-}Br)SnBr_2\}^-$ ligands are η^2-μ_3-bonded to two opposite (related by the inversion centre) triangular faces of the Pt_7 core. The cluster contains a fully interstitial Pt atom. The remaining six Pt atoms are bonded to one terminal CO ligand each. The OH group of the

$\{Br_2Sn(\mu\text{-}OH)SnBr_2\}^-$ ligand is involved in a weak O-H···π interaction with one Ph ring of a $[PPh_4]^+$ cation [O-H···C_t 2.96 Å, < O-H···C_t 153°; C_t centroid of the Ph ring].[79]

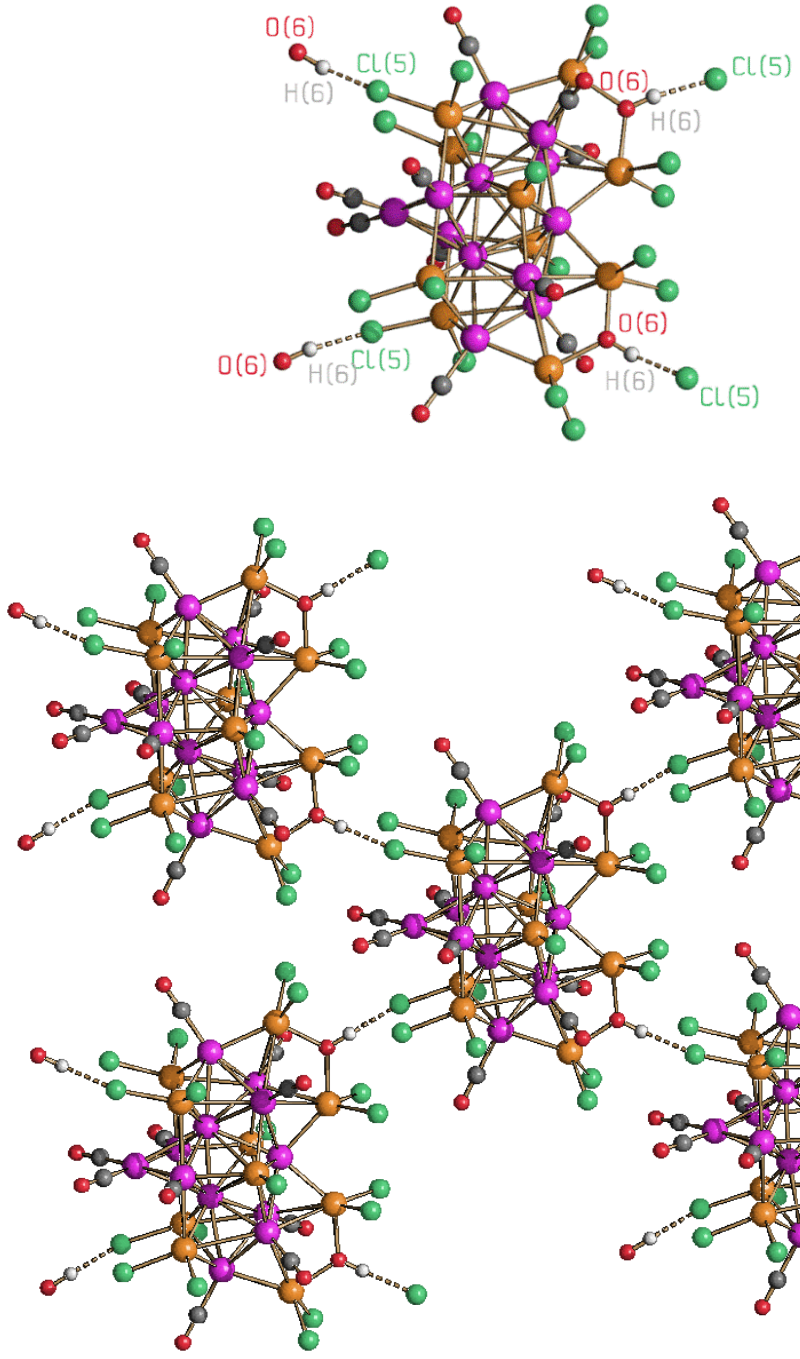

(a)

(b)

Figure 6.16 H-bonds involving the $[Pt_{12}(CO)_{10}(SnCl)_2(SnCl_2)_4\{Cl_2Sn(\mu\text{-}OH)SnCl_2\}_2]^{2-}$ (**13**) anion. (a) A single molecule is reported with its two OH-donors and Cl-acceptor groups with labelling. (b) Five molecules are represented (purple, Pt; orange, Sn; green, Cl; grey, C; red, O; white, H; H-bonds as dashed lines).[79]

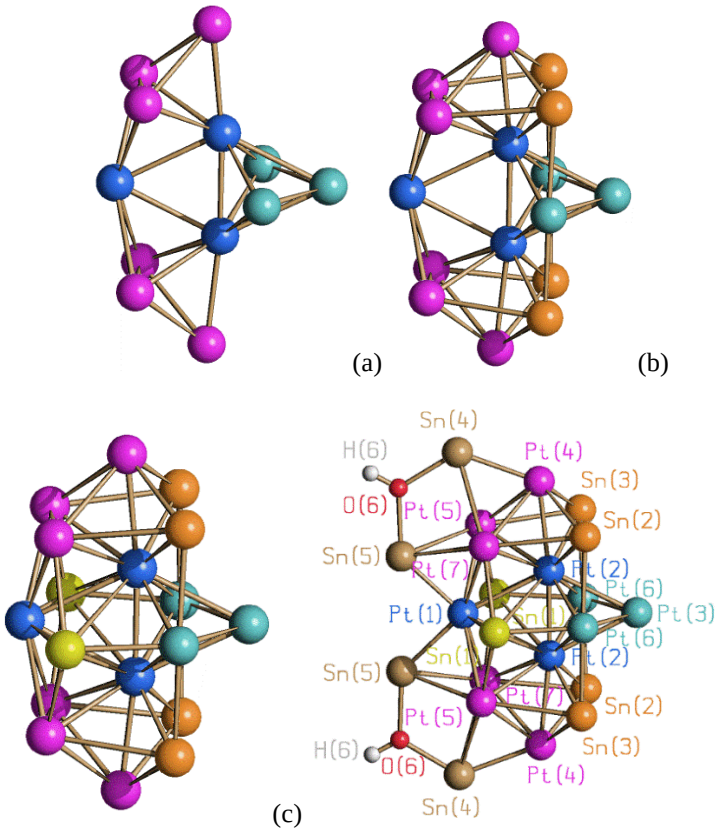

Figure 6.17 (a) The Pt_{12} core of $[Pt_{12}(CO)_{10}(SnCl)_2(SnCl_2)_4\{Cl_2Sn(\mu\text{-}OH)SnCl_2\}_2]^{2-}$ (**13**) composed of three trigonal bipyramids (two related by C_2 in purple, the third in cyan) sharing three vertices (in blue the common triangle). (b) The $Pt_{12}Sn_4$ framework obtained by addition of four $[SnCl_2]$ ligands to (a) (Sn in orange). (c) The $Pt_{12}Sn_6$ framework resulting from the addition of two $[SnCl]^+$ (yellow) ligands to (b). (d) The final $Pt_{12}Sn_{10}$ framework including the two $[Cl_2Sn(OH)SnCl_2]^-$ bidentate ligands (Sn in brown) with labelling.[79]

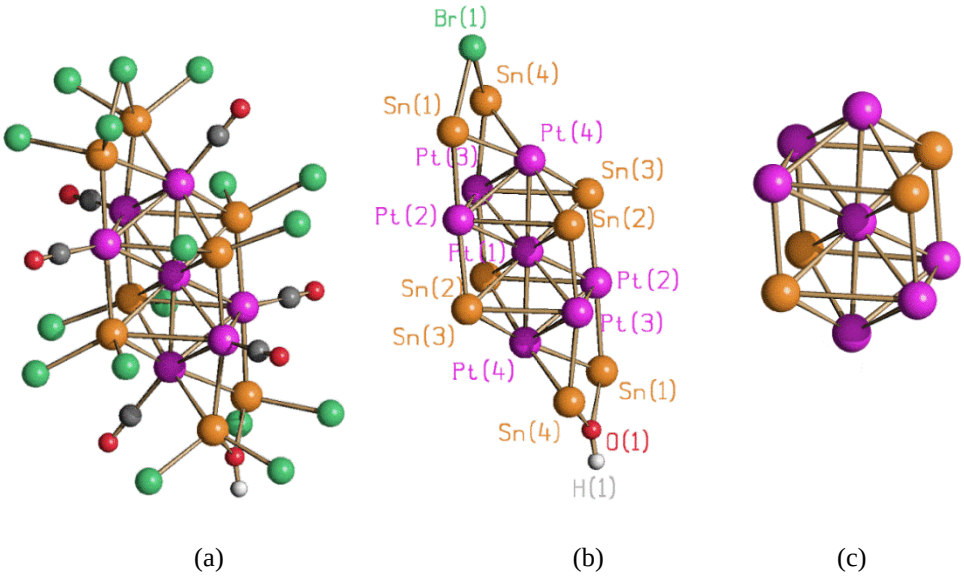

Figure 6.18 (a) Molecular structure of $[Pt_7(CO)_6(SnBr_2)_4\{Br_2Sn(\mu\text{-}OH)SnBr_2\}\{Br_2Sn(\mu\text{-}Br)SnBr_2\}]^{2-}$ (**14**), (b) its Pt_7Sn_8 metal core (the μ-OH and μ-Br groups are represented for sake of clarity) with labelling, and (c) its bicapped centred pseudo-cubic Pt_7Sn_4 framework (purple, Pt; orange, Sn; green, Br; grey, C; red, O; white, H).[79]

Crystals of $[PPh_4][Pt(CO)(Br)(SnBr_3)_2]$ ($[PPh_4]$[**15**]) and $[PPh_4]_2[Pt_2(CO)_2(Br)_4(SnBr_2)]$ ($[PPh_4]_2$[**16**]) were found as side-products of the synthesis of **14** and contained the new anionic $[Pt(CO)(Br)(SnBr_3)_2]^-$ (**15**) and $[Pt_2(CO)_2(Br)_4(SnBr_2)]^{2-}$ (**16**) complexes (Figure 6.19).

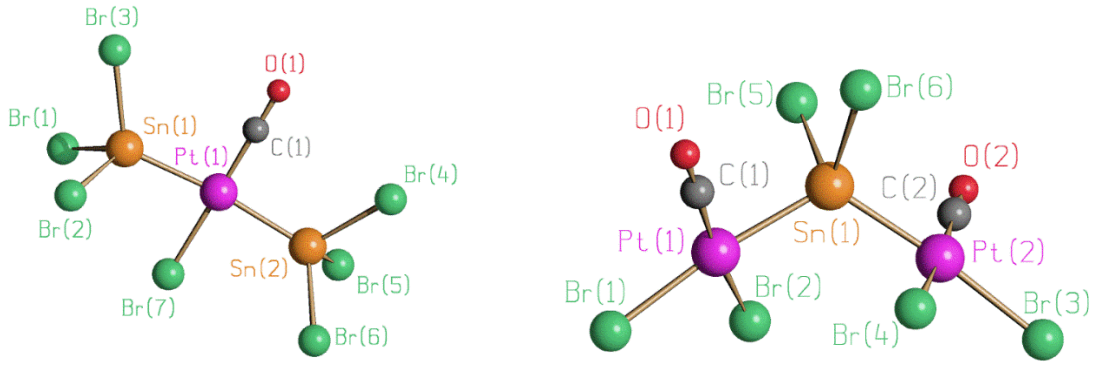

(a) (b)

Figure 6.19 Molecular structures of (a) $[Pt(CO)(Br)(SnBr_3)_2]^-$ (**15**) and (b) $[Pt_2(CO)_2(Br)_4(SnBr_2)]^{2-}$ (**16**) with labelling (purple, Pt; orange, Sn; green, Br; red, O; grey, C).[79]

15 is a square-planar Pt(II) complex with two $[SnBr_3]^-$ ligands in relative *trans*-position, one bromide and one carbonyl. Such CO-complex is unprecedented, whereas related square planar Pt-complexes containing two $[SnX_3]^-$ and one X^- ligands have been previously reported.[84,85] **16** contains two square planar *cis*-$PtBr_2(CO)$ moieties joined by a bridging $SnBr_2$ group, as found in $[Pt_2(CO)_2(I)_2(PR_3)_2(SnCl_2)]$ (R = cyclo-hexyl) and related species.

Final Remarks

This chapter presented the synthesis and the characterisation of new homoleptic and heteroleptic Pt carbonyl clusters. The possibility to gradually substitute CO with other ligands was investigated, leading to the isolation and characterisation of the dianion $[Pt_6(CO)_{10}(dppm)]^{2-}$ (**1**). The oxidative oligomerisation of this new species resulted in higher nuclearity clusters, such as $[Pt_{12}(CO)_{20}(dppm)_2]^{2-}$ (**2**), $[Pt_{18}(CO)_{30}(dppm)_3]^{2-}$ (**3**) and $[Pt_{24}(CO)_{40}(dppm)_4]^{2-}$ (**4**). This represents a new growing mode of Chini clusters that proceeds *via* the addition of Pt_6 rather Pt_3 units.

Secondly, the reactions between homoleptic Chini clusters and PTA were performed, affording the new water soluble $[Pt_{12}(CO)_{20}(PTA)_4]^{2-}$ (**5**) and $[Pt_{15}(CO)_{25}(PTA)_5]^{2-}$ (**6**) compounds. Their solubility in water might be exploited for applications in catalysis and/or medicine. At this regard, some preliminary tests on the anti-cancer activity of **5** and **6** have been performed.

The reactions of Chini clusters have been, then, extended to other soft nucleophiles, and in particular isonitriles. Contrary to what happened with PTA, the reactions of $[Pt_6(CO)_{12}]^{2-}$ and $[Pt_{15}(CO)_{30}]^{2-}$ with XylNC did not proceed *via* non-redox substitution, but resulted in redox fragmentation. Further studies should be devoted in the future in order to understand if this is a general trend with isonitriles, or it is due to the XylNC employed.

Thermal treatment of Chini clusters confirmed to be a general way in order to prepare globular platinum carbonyl clusters (*platinum browns*). Thus heating $[Pt_{15}(CO)_{30}]^{2-}$ in thf afforded the new $[Pt_{27}(CO)_{31}]^{4-}$ (**11**) cluster, whose oxidation resulted the well-known $[Pt_{26}(CO)_{32}]^{-}$ (**12**). Further oxidation of **12** led to the neutral and instable $[Pt_{26}(CO)_{32}]$ compound which escaped any crystallisation attempt. Nonetheless, these results point out that it might be possible to obtain neutral homoleptic platinum carbonyl clusters just by increasing their nuclearity. Indeed, it is well established that $Pt(CO)_4$ cannot be obtained.

Finally, by carrying on the work previously started by my research group on Pt-Sn carbonyl clusters, the reaction of $[Pt_6(CO)_6(SnX_2)_2(SnX_3)_4]^{4-}$ (X = Cl, Br) with an excess of $HBF_4{\cdot}Et_2O$ was performed, resulting in the new $[Pt_{12}(CO)_{10}(SnCl)_2(SnCl_2)_4\{Cl_2Sn(\mu\text{-}OH)SnCl_2\}_2]^{2-}$ (**13**) and $[Pt_7(CO)_6(SnBr_2)_4\{Br_2Sn(\mu\text{-}OH)SnBr_2\}\{Br_2Sn(\mu\text{-}Br)SnBr_2\}]^{2-}$ (**14**).

Overall, homoleptic Chini clusters further confirm to be very good starting materials for the preparation of heteroleptic clusters, higher nuclearity globular nanoclusters and heterometallic clusters.

CHAPTER 7

Bimetallic Ni-Pd and Ni-Pt Carbonyl Clusters

This chapter reports the synthesis and characterisation of new Ni-M (M = Pd, Pt) carbonyl clusters. The compounds presented in this section are listed in Table 7.1.

Table 7.1 Clusters presented in this chapter.

Compound	Compound number
$[Ni_{22-x}Pd_{20+x}(CO)_{48}]^{6-}$ (x = 0.62)	**1**
$[Ni_{29-x}Pd_{6+x}(CO)_{42}]^{6-}$ (x = 0.09)	**2**
$[Ni_{29+x}Pd_{6-x}(CO)_{42}]^{6-}$ (x = 0.27)	**3**
$[Ni_{36-x}Pd_{5+x}(CO)_{46}]^{6-}$ (x = 0.41)	**4**
$[Ni_{37-x}Pd_{7+x}(CO)_{48}]^{6-}$ (x = 0.69)	**5**
$[HNi_{37-x}Pd_{7+x}(CO)_{48}]^{5-}$ (x = 0.53)	**6**
$[Pt_{6-x}Ni_x(CO)_{12}]^{2-}$ (x = 1.25, 2.53,3.24, 4.15, 4.16, 4.41, 5.78, 5.90)	**7**
$[Pt_{12-x}Ni_x(CO)_{21}]^{4-}$ (x = 2.91, 5.82, 6.29, 6.41)	**8**
$[HPt_{14+x}Ni_{24-x}(CO)_{44}]^{5-}$ (x= 0.70)	**9**
$[Pt_{19-x}Ni_x(CO)_{22}]^{4-}$ (x = 2.27, 3.23)	**10**

7.1 Introduction

The last topic of this Thesis concerns the investigation of bimetallic Ni-Pd and Ni-Pt carbonyl clusters. Even if they are all Group 10 metals, their affinity towards carbonyl ligands is different, as well as their capacity to form carbonyl compounds. For this reason, analogies and differences between the Ni-Pd and Ni-Pt chemistry have been explored.

The first Ni carbonyl compound was obtained in 1890 when Ludwig Mond (1839-1909) and his staff casually discovered $Ni(CO)_4$ during the process aimed at synthesising Cl_2. The plant was equipped with Ni valves, that reacted with CO by forming a dark incrustation.[1] This discovery aroused enthusiasm amongst the scientific community, and generated interest about this particular class of compounds. Later on, Walter Otto Hieber (1895-1976) carried on the study about carbonyl compounds, and suggested a new representation of the structure of $Ni(CO)_4$ (Figure 7.1).[86]

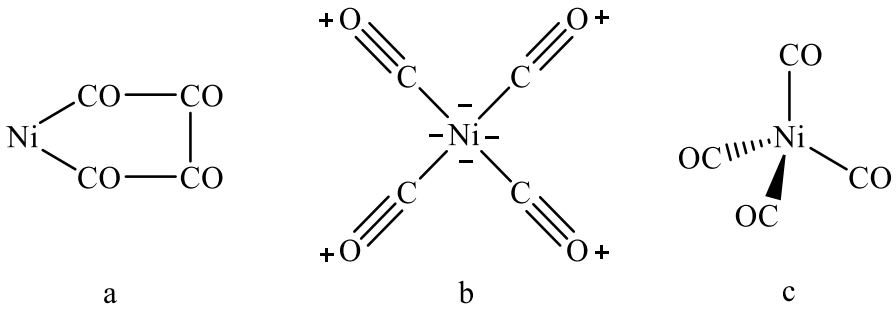

Figure 7.1 Representations of $Ni(CO)_4$ (a) with a cyclic structure by Mond, (b) with a planar square geometry by Werner-Hieber-Manchot and (c) with the actual tetrahedral model.

The formation of $Ni(CO)_4$ is thermodynamically spontaneous at room temperature. Conversely, this does not happen in case of Pd and Pt. Indeed, although they belong to the same group, they show a different affinity towards CO. It is known that the related $M(CO)_4$ (M = Pd, Pt) complexes are very unstable and subjected to rapid decomposition. These differences are due to their atomic properties, as shown in Table 7.2.

Table 7.2 Ionisation energy and electronic affinity of Ni, Pd and Pt.

	Electronic configuration	**Ionisation energy/eV**	**Electronic affinity/eV**
Ni(0)	d^{10}	1.72	1.2
Pd(0)	d^{10}	4.23	1.3
Pt(0)	d^{10}	3.28	2.4

As shown in Table 7.2, the IE of Ni(0) is lower than Pd(0) and Pt(0), whereas the EA of Ni(0) is similar to that of Pd(0) and lower than Pt(0). By analysing these values, the Ni-CO interaction is favoured by the back-donation capacity of Ni, the Pt-CO bond is essentially based on the fact that Pt is a good σ acceptor, whereas homoleptic Pd carbonyls are never favoured. As reported in the literature, different approaches for the synthesis of Pd carbonyl clusters are known. One of these consists in the use of phosphine ligands. Phosphines are greater σ donors than CO and, for this reason, they can favour the accumulation of electronic density on Pd, by enabling the back-donation towards CO and affording the heteroleptic species with the general formula $Pd_n(CO)_x(PR_3)_y$. These compounds contain only bridging CO ligands, whereas terminal positions are occupied by phosphines. Another approach to Pd carbonyl compounds is represented by the formation of bimetallic clusters with the employment of a second metal with a greater affinity to CO, such as Ni. Nickel tends to form Ni-CO bonds whereas Pd prefers Pd-Pd bonds. As a result, Ni-Pd carbonyl clusters usually display high nuclearity and compact structures composed of a metal core of Pd surrounded by Ni atoms bonded to terminal, double- and/or triple-bridging CO. For this reason, it is proper to say that in this chemistry these two metals are complementary. Pd tends to maximise the Pd-Pd interstitial interactions, whereas Ni ensures the stability by creating a CO shell. Some examples of Ni-Pd carbonyl compounds known in the literature are $[Ni_{13}Pd_{13}(CO)_{34}]^{4-}$, $[Ni_{16}Pd_{16}(CO)_{40}]^{4-}$ and $[Ni_{26}Pd_{20}(CO)_{54}]^{6-}$ (Figure 7.2).[87,88] In particular, these clusters were obtained by reacting $[Ni_6(CO)_{12}]^{2-}$ with Pd(II) salts or complexes, such as $PdCl_2(Et_2S)_2$ or $[PdCl_4]^{2-}$.[87–89]

As shown in Figure 7.2, the molecular structure of $[Ni_{13}Pd_{13}(CO)_{34}]^{4-}$ may be view as a stack of five Ni-Pd layers that generate a compact packing with tetrahedral and octahedral cavities. $[Ni_{16}Pd_{16}(CO)_{40}]^{4-}$ displays a compact structure as well, composed by 6 layers. The metal skeleton of $[Ni_{26}Pd_{20}(CO)_{54}]^{6-}$ derives from the latter after addition of an extra layer.

In some cases, the complete segregation of Pd in the inner core of the clusters is not observed. When this happens, substitutional and/or compositional disorder phenomena occur. When the first one is observed, the composition of the cluster is well defined, but some metal sites are Ni-Pd disordered. The second phenomenon regards the overall Ni-Pd composition of the cluster, which is the result of a mixture of a few isostructural species differing for few Ni/Pd atoms.

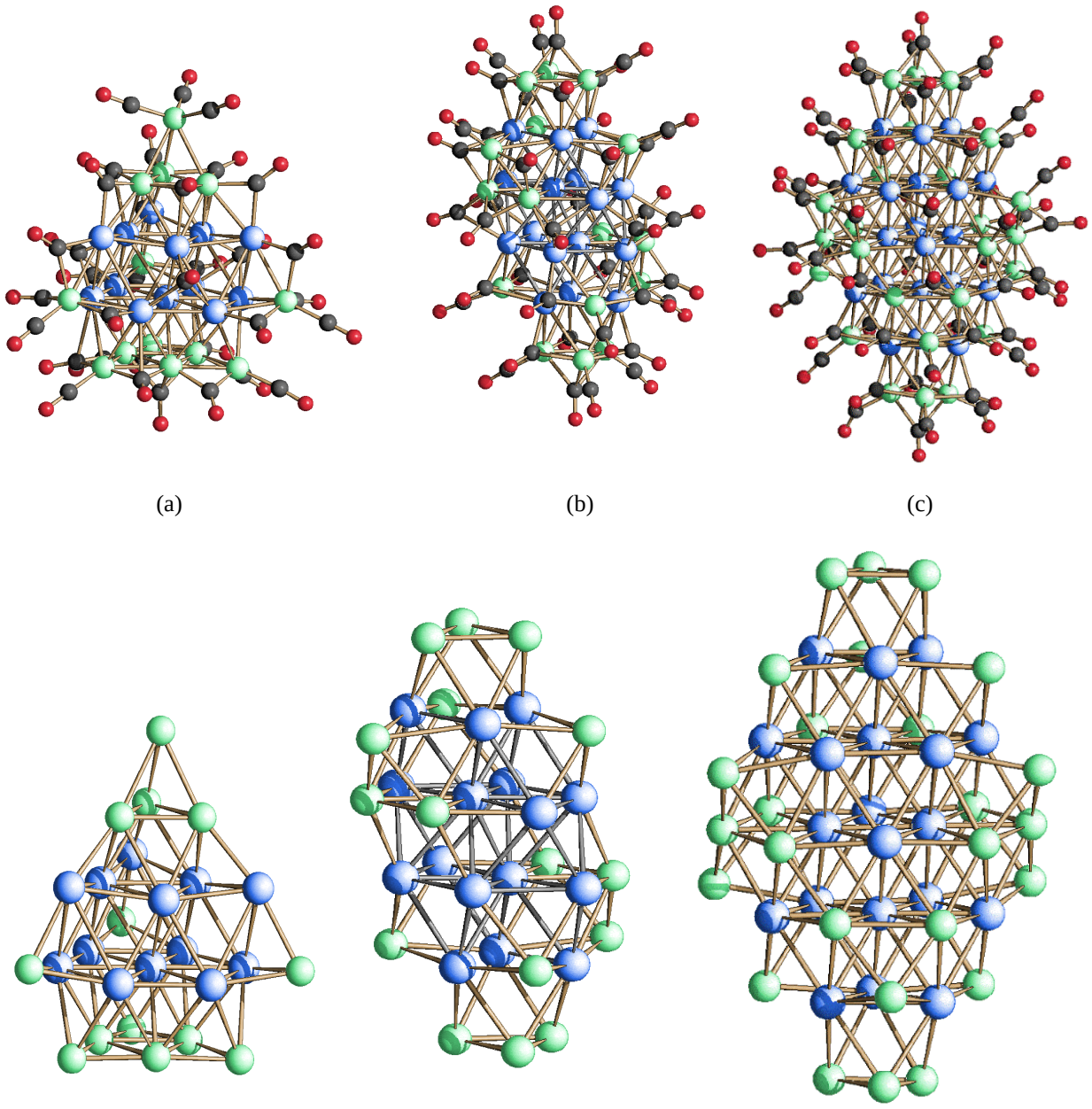

Figure 7.2 Molecular structures and metal cores of (a) $[Ni_{13}Pd_{13}(CO)_{34}]^{4-}$, (b) $[Ni_{16}Pd_{16}(CO)_{40}]^{4-}$ and (c) $[Ni_{26}Pd_{20}(CO)_{54}]^{6-}$ (blue, Pd; green, Ni; grey, C; red, O).[87,88]

Another interesting compound reported in the literature is the hexa-anion $[Ni_{36}Pd_8(CO)_{48}]^{6-}$ (Figure 7.3), which for the first time revealed some similarities between Ni-Pd and Ni-Pt carbonyl cluster chemistry, since it is isostructural with $[Ni_{38}Pt_6(CO)_{48}]^{6-}$ and $[Ni_{35}Pt_9(CO)_{48}]^{6-}$. $[Ni_{36}Pd_8(CO)_{48}]^{6-}$ presents a crystalline disorder, due to the substitution of Ni and Pd atoms, as indicated in the yellow positions in Figure 7.3.[90] The disordered sites are in the centre of the eight triangular faces of the Ni_{30} metal cage.

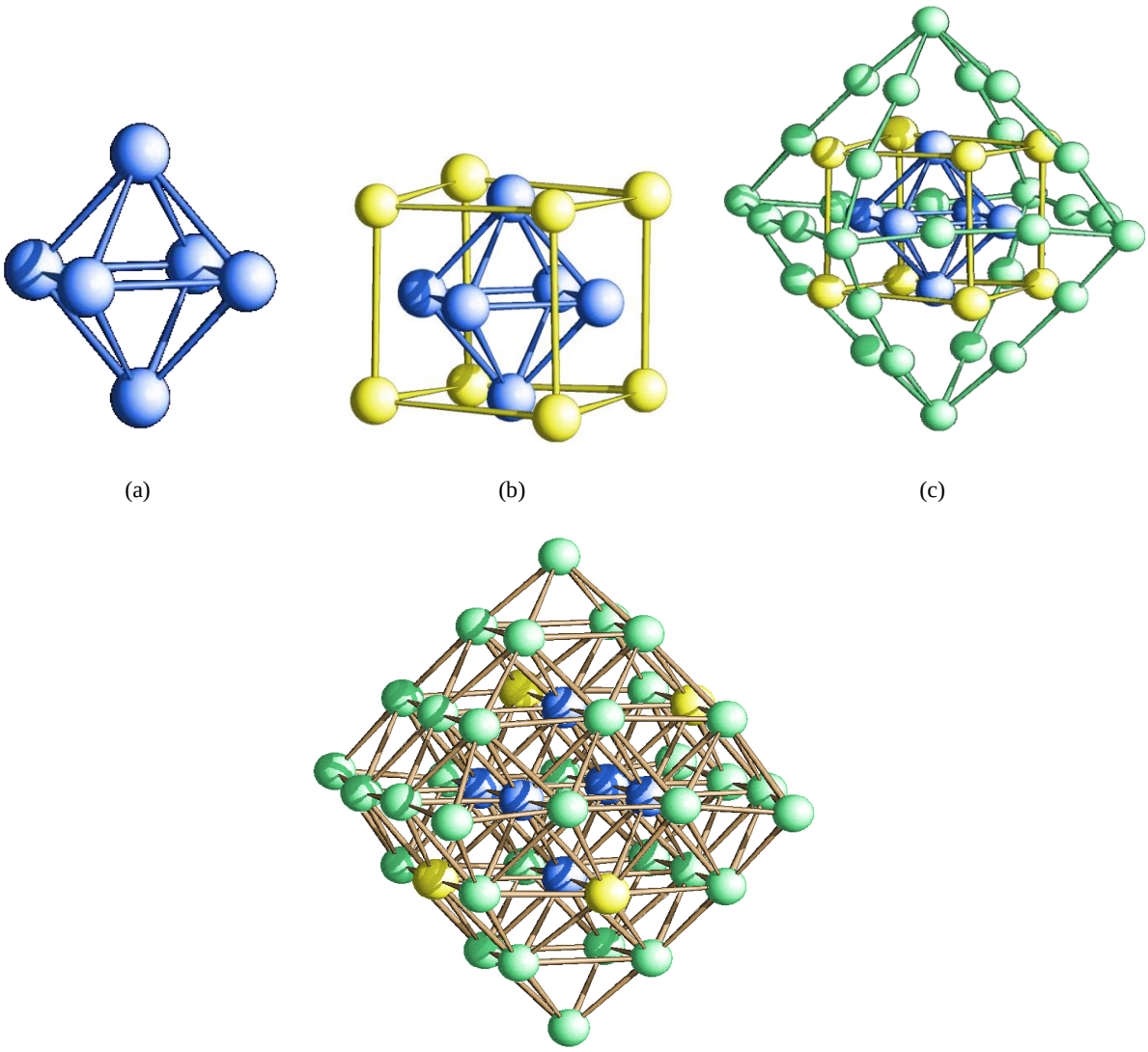

(a) (b) (c)

(d)

Figure 7.3 Metal core of $[Ni_{36}Pd_8(CO)_{48}]^{6-}$ constituted by a (a) Pd_6 octahedron encapsulated in a (b) disordered (Ni_6Pd_2) cube, (c) protected by a Ni_{30} metal cage. The resulting molecular structure of (d) $[Ni_{36}Pd_8(CO)_{48}]^{6-}$ (blue, Pd; yellow, Ni/Pd; green, Ni).[90]

The molecular structure of $[Ni_{36}Pd_8(CO)_{48}]^{6-}$ is similar to $[Ni_{38}Pt_6(CO)_{48}]^{6-}$ (Figure 7.4). The only difference between these two clusters is the fact that the 6 Pt atoms of $[Ni_{38}Pt_6(CO)_{48}]^{6-}$ are all located in the inner octahedron, with a perfect segregation of Ni and Pt, whereas the Pd atoms of $[Ni_{36}Pd_8(CO)_{48}]^{6-}$ are also present (and disordered) on the surface of the cluster. Beside the fully interstitial Pd_6 octahedron, there are two additional Pd atoms disordered over the eight triangular faces of the cluster.

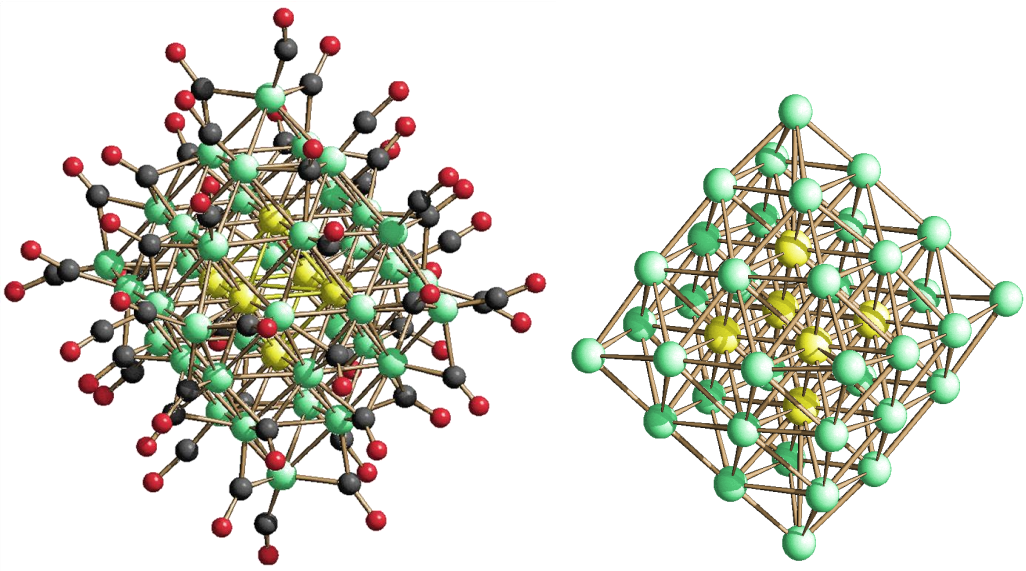

(a) (b)

Figure 7.4 (a) Molecular structure of $[Ni_{38}Pt_6(CO)_{48}]^{6-}$ and (b) its $Ni_{38}Pt_6$ metal core (yellow, Pt; green, Ni; black, C; red, O).

7.2 General results

In this Chapter, the synthesis and the characterisation of the new molecular alloy nanoclusters $[Ni_{22-x}Pd_{20+x}(CO)_{48}]^{6-}$ (x = 0.62) (**1**), $[Ni_{29-x}Pd_{6+x}(CO)_{42}]^{6-}$ (x = 0.09) (**2**), $[Ni_{29+x}Pd_{6-x}(CO)_{42}]^{6-}$ (x = 0.27) (**3**), $[Ni_{36-x}Pd_{5+x}(CO)_{46}]^{6-}$ (x = 0.41) (**4**), $[Ni_{37-x}Pd_{7+x}(CO)_{48}]^{6-}$ (x = 0.69) (**5**) and $[HNi_{37-x}Pd_{7+x}(CO)_{48}]^{5-}$ (x = 0.53) (**6**) will be described.

Then, a systematic study on the reactions of Chini clusters with $[Ni_6(CO)_{12}]^{2-}$ has been conducted, leading to the isolation and characterisation of the new $[Pt_{6-x}Ni_x(CO)_{12}]^{2-}$ (x = 1.25, 2.53, 3.24, 4.15, 4.16, 4.41, 5.78, 5.90) clusters (**7**). Their spontaneous CO loss afforded the new $[Pt_{12-x}Ni_x(CO)_{21}]^{4-}$ (x = 2.91, 5.82, 6.29, 6.41) (**8**) species. The oxidation of **8** resulted in the formation of $[HPt_{14+x}Ni_{24-x}(CO)_{44}]^{5-}$ (x = 0.70) (**9**). Finally, $[Pt_{19-x}Ni_x(CO)_{22}]^{4-}$ (x = 2.27, 3.23) (**10**) has been obtained after thermal decomposition in acetonitrile of a purported $[Pt_{9-x}Ni_x(CO)_{18}]^{2-}$ cluster.

The obtained compounds have been characterised by means of IR, ESI-MS and NMR spectroscopy, and their molecular structures have been determined by SC-XRD. Moreover, the Pt/Ni content of these new clusters has been corroborated by ICP analysis.

7.3 Synthesis and characterisation of $[Ni_{22-x}Pd_{20+x}(CO)_{48}]^{6-}$ (x = 0.62) (1)

The redox condensation of $[NBu_4]_2[Ni_6(CO)_{12}]$ with 0.7-0.8 equivalents of $PdCl_2(Et_2S)_2$ in CH_2Cl_2 led to the formation of $[Ni_{22-x}Pd_{20+x}(CO)_{48}]^{6-}$ (x = 0.62) (**1**). At the end of the reaction, the solvent was removed *in vacuo*, the solid residue washed with water, toluene, CH_2Cl_2, thf, and extracted with acetone. Crystals suitable for X-ray diffraction have been obtain after slow diffusion of *n*-hexane on the acetone solution. **1** has been characterised by means of IR spectroscopy and X-ray diffractometry. The IR spectrum showed ν_{CO} signals at 1999(vs), 1873(s), 1856(s) cm^{-1} in CH_3CN solution.

Crystal structure

The molecular structure of **1** has been determined by means of SC-XRD on its $[NBu_4]_6[\mathbf{1}]\cdot 4CH_3COCH_3$ (x = 0.62) crystals (Figure 7.5 and Table 7.3).

1 presented both compositional and substitutional disorders. The first one was evidenced by the mixture of $[Ni_{21}Pd_{21}(CO)_{48}]^{6-}$ (62%) and $[Ni_{22}Pd_{20}(CO)_{48}]^{6-}$ (38%) found in the crystals, whereas the substitutional disorder was indicated by the fact that there were some positions within the metal cage of the cluster which may be occupied by either Ni or Pd (sites coloured in blue and yellow in Figure 7.5).

From a structural point of view, **1** may be viewed as a five-layer close-packed stacking arrangement comprising 40 metal atoms capped by two additional metal atoms on two triangular faces related by an inversion centre (Figure 7.5). The close-packed layers adopted a *ccp* ABCAB configuration and contained 6, 9, 10, 9 and 6 metal atoms, respectively. The structure contained 12 terminal, 18 edge bridging and 18 face capping CO ligands. Ni-C and Pd-C contacts up to 2.31 and 2.50 Å, respectively, were considered as bonds on the basis of the reported covalent radii of C, Ni and Pd.[91] **1** contained 522 cluster valence electrons (CVE), that corresponded to 261 (6n+9) filled molecular orbitals, in keeping with other high nuclearity Ni-Pt and Ni-Pd carbonyl clusters.[88,90,92,93]

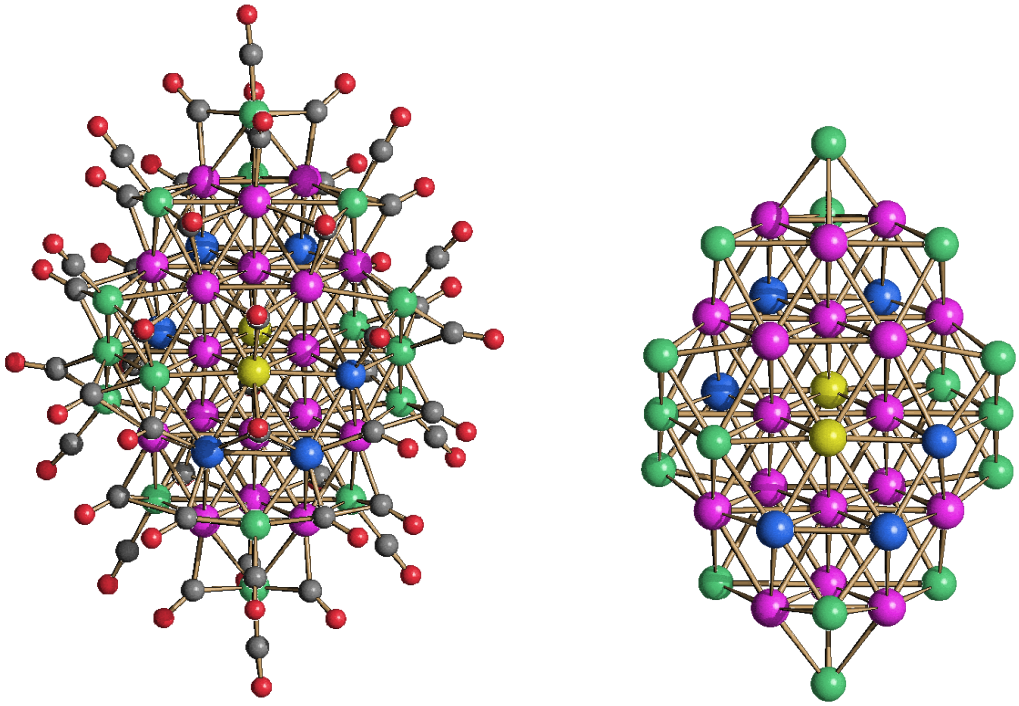

(a) (b)

Figure 7.5 (a) Molecular structure of (**1**) and (b) its M_{42} metal core (green, Ni; purple, Pd; yellow, Ni/Pd ≈ 16:84; blue, Ni/Pd ≈ 82,85,87:18,15,13; grey, C; red, O).[89]

Table 7.3 Main bond distances (Å) of $[Ni_{22-x}Pd_{20+x}(CO)_{48}]^{6-}$ (x = 0.62) (**1**), $[Ni_{29-x}Pd_{6+x}(CO)_{42}]^{6-}$ (x = 0.09) (**2**) and $[Ni_{29+x}Pd_{6-x}(CO)_{42}]^{6-}$ (x = 0.27) (**3**).

Compound	Ni-Ni	Ni-Pd	Pd-Pd
1	2.4696(10)-2.95(2) Average 2.56(4)	2.40(4)-2.82(3) Average 2.67(5)	2.59(3)-2.9053(6) Average 2.773(19)
2	2.444(3)-2.725(3) Average 2.58(4)	2.35(7)-2.68(7) Average 2.61(9)	2.618(2)-2.7689(15) Average 2.68(3)
3	2.437(5)-2.732(3) Average 2.58(2)	2.324(17)-2.889(17) Average 2.65(5)	2.6256(19)-2.7585(13) Average 2.704(3)

7.4 Syntheses and structures of $[Ni_{29-x}Pd_{6+x}(CO)_{42}]^{6-}$ (x = 0.09) (2) and $[Ni_{29+x}Pd_{6-x}(CO)_{42}]^{6-}$ (x = 0.27) (3).

2 and **3** were obtained from the reaction of $[NEt_4]_2[Ni_6(CO)_{12}]$ with 0.6-0.7 equivalents of $PdCl_2(Et_2S)_2$ in CH_3CN and extracted in CH_3CN after work-up (see Experimental for details). It must be noticed that the synthesis of **2** and **3** differed from that of **1** into three points: (1) the stoichiometry of the reaction (0.6-0.7 *vs* 0.7-0.8 moles of $Pd(Et_2S)_2Cl_2$ per mole of $[Ni_6(CO)_{12}]^{2-}$ for

2 and **3** *vs* **1**); (2) the solvent employed, that is CH_3CN (**2** and **3**) or CH_2Cl_2 (**1**); (3) the cation of $[Ni_6(CO)_{12}]^{2-}$, that is $[NEt_4]^+$ (**2** and **3**) or $[NBu_4]^+$ (**1**). Point (3) was closely related to (2), since $[NEt_4]_2[Ni_6(CO)_{12}]$ was not soluble in CH_2Cl_2 whereas $[NBu_4]_2[Ni_6(CO)_{12}]$ was completely soluble in the same solvent, and both salts were soluble in CH_3CN. Conversely, **2** and **3** were obtained under very similar experimental conditions, that is, the same cation and solvent, and only slightly differed for the stoichiometric ratio of the reagents (see Experimental Section). These differences are so minimal that it was not very easy to control them, and the reactions for the synthesis of **2** and **3** must be carried out in a very controlled way. Indeed, **2** and **3** displayed the same structures (see below) and only showed minor differences in the composition, that is, $Ni_{28.91}Pd_{6.09}$ for **2** and $Ni_{29.27}Pd_{5.73}$ for **3**.

Crystal structures

2 and **3** were structurally characterised by means of SC-XRD as their $[NEt_4]_6$[**2**]·$3CH_3CN$·solv and $[NEt_4]_6$[**3**]·$3CH_3CN$·solv salts (Figure 7.6).

These two compounds were isostructural, with a Ni/Pd disorder as indicated by the yellow sites in Figure 7.6 and presented a slight difference in Ni/Pd compositions, *ca.* 82:18 and 88:12 for **2** and **3**, respectively. In the case of **2**, this corresponded to a mixture of $[Ni_{29}Pd_6(CO)_{42}]^{6-}$ (91%) and $[Ni_{28}Pd_7(CO)_{42}]^{6-}$ (9%), which means it was an almost pure sample of $[Ni_{29}Pd_6(CO)_{42}]^{6-}$. Conversely, in the case of **3** the compositional disorder was greater, indeed significant amounts of both $[Ni_{29}Pd_6(CO)_{42}]^{6-}$ (73%) and $[Ni_{30}Pd_5(CO)_{42}]^{6-}$ (27%) were present.

The molecular structures of **2** and **3** were based on a *hcp* M_{35} metal core composed of three compact ABA layers consisting of 10, 15 and 10 metal atoms, respectively. Both structures contained 42 CO ligands, 9 in terminal positions, 18 edge bridging and 15 face capping. Pd atoms were not bonded to any CO or connected only to edge bridging or face capping CO ligands.

2 and **3** contained 440 CVE. Thus, they were isoelectronic with $[Cu_xNi_{35-x}(CO)_{40}]^{5-}$ (x = 3 or 5), assuming x = 5. This corresponded to 220 (6n+10) filled molecular orbitals.

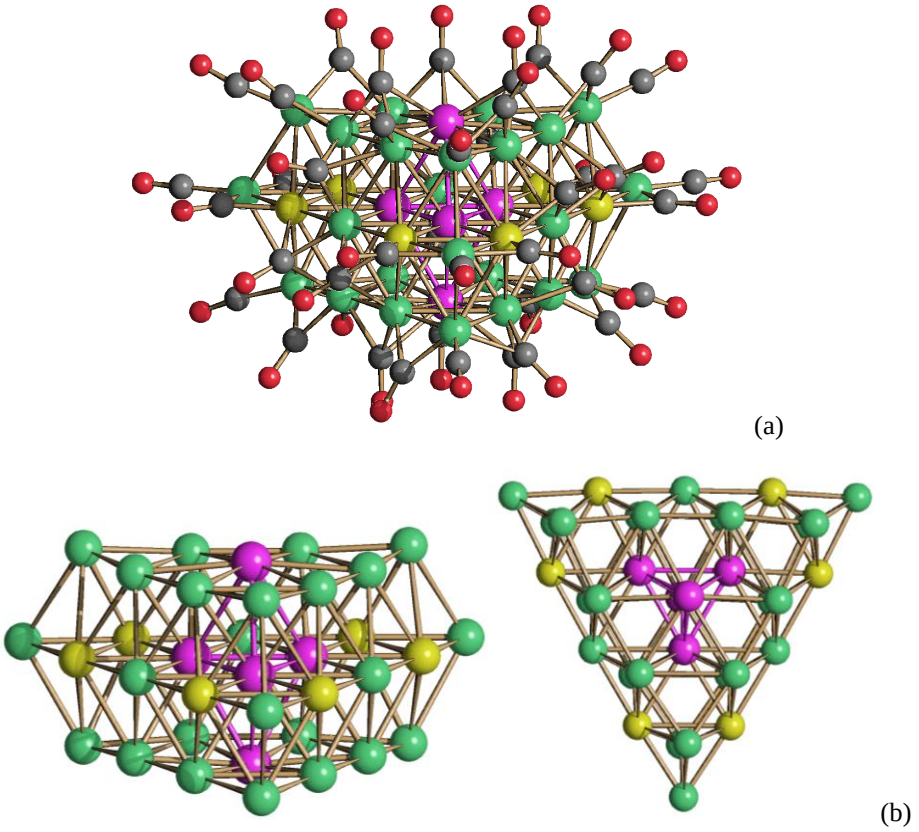

Figure 7.6 (a) Molecular structure of **2** and **3**, and (b) two views of their M_{35} metal core (green, Ni; purple, Pd; yellow, Ni/Pd ≈ 82:18 and 88:12; grey, C; red, O).[89]

Electrochemistry and Infrared Spectro-electrochemistry

The redox properties of **1** and **2** were determined by means of electrochemical and spectroelectrochemical methods. This represented the first detailed studies on the electrochemistry of large Ni-Pd carbonyl clusters.

The redox chemistry of **1** was studied by *in situ* infrared spectroelectrochemistry (IR SEC) in CH_3CN solution containing $[N^nBu_4][PF_6]$ as supporting electrolyte. The analysis revealed three chemically reversible redox (one oxidation and two reduction) processes. The IR spectra of the four oxidation states of **1** are reported in Figure 7.7, and the stretching frequencies of the terminal (ν^t_{CO}) and bridging (ν^b_{CO}) carbonyl groups for each species are summarised in Table 7.4. By observing the terminal carbonyl stretching values reported in Table 7.4, all processes were accompanied by a shift of 14 cm^{-1}, indicating one-electron transfer for each redox exchange.[94] Thus, the four long-lived species $[\mathbf{1}]^{5-/6-/7-/8-}$ were spectroscopically characterised, proving that the structure of $[\mathbf{1}]^{6-}$ was stable with a variable number of electrons.

Table 7.4 Infrared stretching frequencies (cm^{-1}) of the terminal (ν^{t}_{CO}) and bridging (ν^{b}_{CO}) carbonyl groups for [**1**]^{n} in CH_3CN as a function of the cluster charge *n*.

Cluster charge *n*	ν^{t}CO	ν^{b}CO
-5	2014	1883(sh), 1866
-6	1999	1873, 1856
-7	1985	1857
-8	1971	1852

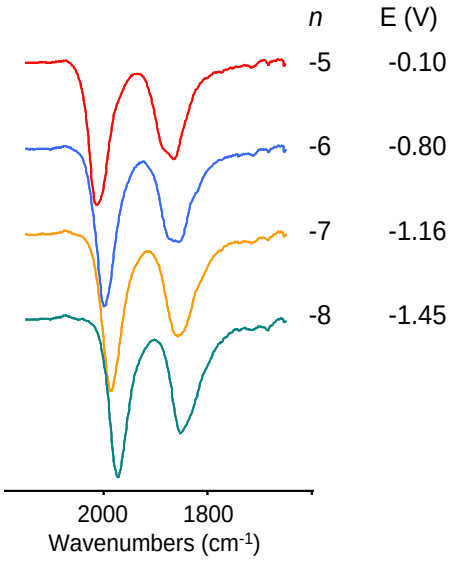

Figure 7.7 Selected infrared spectra of [**1**] ^{n} as a function of the cluster charge *n* and of the potential E (*vs.* Ag pseudo-reference electrode), in CH_3CN containing 0.1 M [N^{n}Bu$_4$][PF_6]. The absorptions of the solvent and the supporting electrolyte have been subtracted.[89]

The electrochemical properties of **2** were preliminarily investigated by cyclic voltammetry at a Pt electrode in CH_3CN/[N^{n}Bu$_4$][PF_6] solution. Overall, one oxidation and two reduction processes of the cluster were identified by the SEC, and the IR spectra of four oxidation states of [**2**]$^{n-}$ were selected (Figure 7.8). The stretching frequencies of the terminal (ν^{t}_{CO}) and bridging (ν^{b}_{CO}) carbonyl groups for each species were reported in Table 7.5. The charge of each species was assigned according to one-electron transfer for each redox exchange, as inferred by a near-uniform shift of 15 cm^{-1} of the stretching frequencies of terminal CO ligands for all the processes. By the joint electrochemical/spectroelectrochemical study of **2**, four redox couples chemically reversible in the timescale of CV were identified; the three long-lived species [**2**]$^{6-/7-/8-}$ and the relatively unstable [**2**]$^{5-}$ were spectroscopically characterised, proving that also the structure of [**2**]$^{6-}$ was stable with a variable number of electrons.

Table 7.5 Infrared stretching frequencies (cm^{-1}) of the terminal (ν^{t}_{CO}) and bridging (ν^{b}_{CO}) carbonyl groups for [**2**]^{n} in CH_3CN as a function of the cluster charge *n*.

Cluster charge *n*	ν^{t}CO	ν^{b}CO
-5	2010	1882, 1866
-6	1995	1873, 1854sh
-7	1980	1860, 1840sh
-8	1963	1841

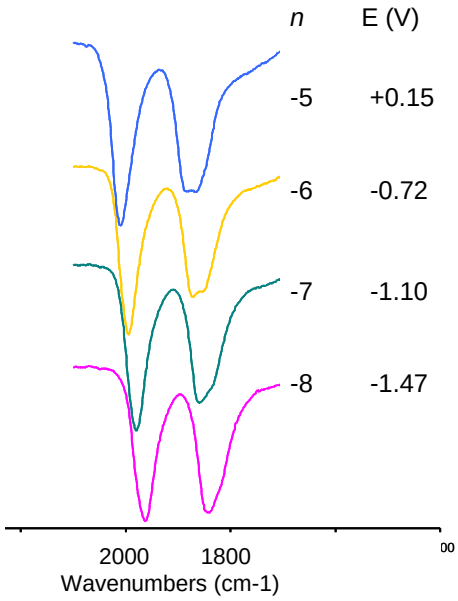

Figure 7.8 Selected infrared spectra of [**2**]^{n} as a function of the cluster charge *n* and of the potential E (*vs.* Ag pseudo-reference electrode), in CH_3CN containing 0.1 M [N^{n}Bu$_4$][PF_6]. The absorptions of the solvent and the supporting electrolyte have been subtracted.[89]

7.5 Synthesis and characterisation of $[Ni_{36-x}Pd_{5+x}(CO)_{46}]^{6-}$ (x = 0.41) (4)

By reacting $[NMe_3(CH_2Ph)]_2[Ni_6(CO)_{12}]$ with 0.8 equivalents of $[Pd(CH_3CN)_4][BF_4]_2$ in thf the new compound $[Ni_{36-x}Pd_{5+x}(CO)_{46}]^{6-}$ (x = 0.41) (**4**) was obtained. After 24 h at room temperature, the reaction was stopped, and the solvent removed *in vacuo*. The residue was washed with H_2O and extracted with acetone. A saturated solution of $[NMe_4]Cl$ in H_2O was added up to complete precipitation of the compound. The solid was recovered by filtration, washed with H_2O, toluene, thf, and extracted with CH_3CN. Crystals of $[NMe_4]_2[NMe_3CH_2Ph]_4$[**4**]·3CH_3CN·solv suitable for X-ray analyses were obtained by layering *n*-hexane and di-iso-propyl-ether on the CH_3CN solution.

Crystal structure

The molecular structure of **4** was studied by means of single crystal X-ray diffraction on its $[NMe_4]_2[NMe_3CH_2Ph]_4$[**4**]·$3CH_3CN$·solv salt (Figures 7.9-7.10).

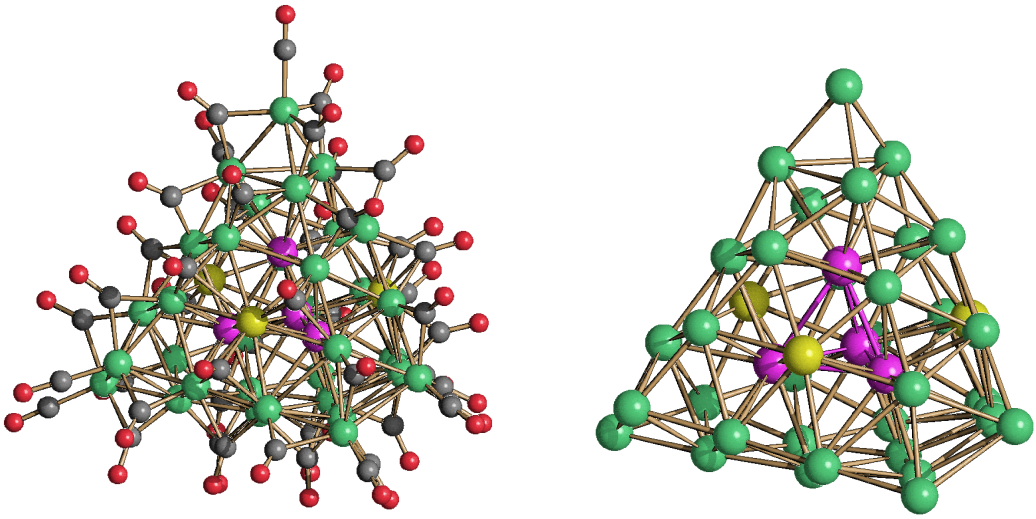

(a) (b)

Figure 7.9 (a) Molecular structure of $[Ni_{36-x}Pd_{5+x}(CO)_{46}]^{6-}$ (x = 0.41) (**4**) and (b) its M_{41} metal core (green, Ni; purple, Pd; yellow, Ni/Pd ≈ 53:47; grey, C; red, O).

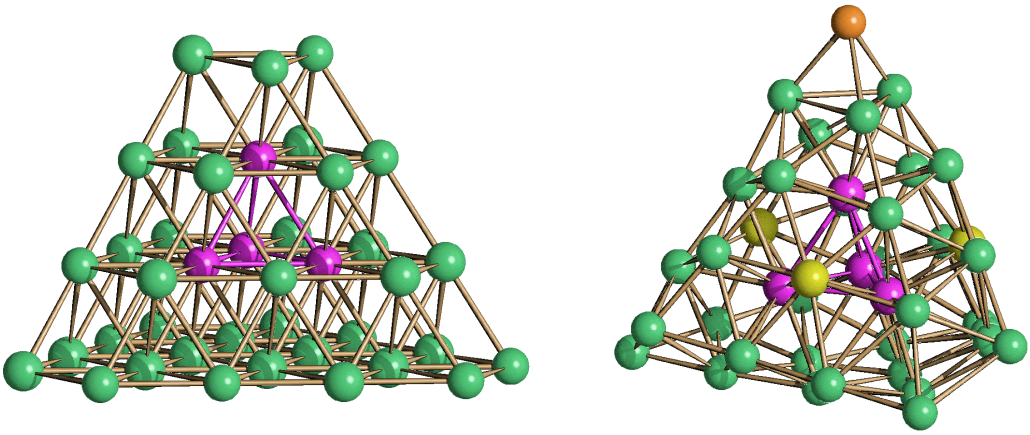

(a) (b)

Figure 7.10 (a) The idealised *ccp* M_{40} core of $[Ni_{36-x}Pd_{5+x}(CO)_{46}]^{6-}$ (x = 0.41) (**4**) (green, surface atoms; purple, the fully interstitial M_4 tetrahedron) and (b) its real M_{41} metal core obtained by adding a further Ni atom (orange) to the top triangular face (yellow, the three disordered Ni/Pd sites at the centre of the (111) faces).

The hexa-anion **4** adopted a *ccp* M_{40} framework composed of four ABCA layers consisting of 3, 7, 12 and 18 atoms, respectively (Figure 7.10). This M_{40} framework encapsulates a fully interstitial Pd_4 tetrahedron that generates a distortion of the idealised M_{40} model and is capped by an additional Ni atom. The structure is completed by 7 terminal, 27 edge bridging and 12 face capping

CO ligands. As for **1**, also in this case substitutional disorder was found in the three positions located at the centre of the three distorted (111) faces. Compositional disorder was detected by the presence of both $[Ni_{36}Pd_5(CO)_{46}]^{6-}$ (59%) and $[Ni_{35}Pd_6(CO)_{46}]^{6-}$ (41%) clusters in the crystals.

7.6 Syntheses and characterisation of $[Ni_{37-x}Pd_{7+x}(CO)_{48}]^{6-}$ (x = 0.69) (5) and $[HNi_{37-x}Pd_{7+x}(CO)_{48}]^{5-}$ (x = 0.53) (6)

The reactions between $[NBu_4]_2[Ni_6(CO)_{12}]$ and 0.9-1 equivalents of $[Pd(CH_3CN)_4][BF_4]_2$ in thf resulted in the formation of $[Ni_{37-x}Pd_{7+x}(CO)_{48}]^{6-}$ (x = 0.69) (**5**) and $[HNi_{37-x}Pd_{7+x}(CO)_{48}]^{5-}$ (x = 0.53) (**6**). The reactions were stirred at room temperature for one day and then the solvents were removed under low pressure. The solid residues were washed with water, toluene, thf and extracted in acetonitrile (**5**) or acetone (**6**). Crystals suitable for X-ray crystallography have been obtained after slow diffusion of *n*-hexane and di-iso-propyl-ether on the CH_3CN solution and *n*-hexane on the acetone solution, respectively. Compounds of type **5** and **6** may be viewed as an acid-base couple related by the protonation/deprotonation equilibrium depicted in Scheme 7.1. The slight difference in composition reflects the slight different stoichiometry of the reactions that led to the obtainment of the crystals.

Scheme 7.1 Protonation/deprotonation equilibrium between **5** and **6**.

$$\underset{\mathbf{6}}{[HNi_{37-x}Pd_{7+x}(CO)_{48}]^{5-}} \underset{+\,H^+}{\overset{-\,H^+}{\rightleftharpoons}} \underset{\mathbf{5}}{[Ni_{37-x}Pd_{7+x}(CO)_{48}]^{6-}}$$

Crystal structures

The nature of **5** and **6** has been corroborated by means of SC-XRD as their $[NBu_4]_6[\mathbf{5}]\cdot 6CH_3CN$ (x = 0.69) and $[NBu_4]_5[\mathbf{6}]\cdot 2CH_3COCH_3\cdot solv$ (x = 0.53) salts (Figures 7.11-7.13 and Table 7.6).

The molecular structures of **5** and **6** are rather similar to that of the related $[Ni_{36}Pd_8(CO)_{48}]^{6-}$ anion, that consists of a $Ni_{36}Pd_2$ ν_3 octahedron encapsulating a Pd_6 octahedron. The two additional Pd atoms on the surface are disordered showing a preference for the central position of the eight (111) faces. The metal cores of **5** and **6** contain 168 M-M bonds and are completed by 48 CO ligands, 18 terminal, 12 edge bridging and 18 face bridging.

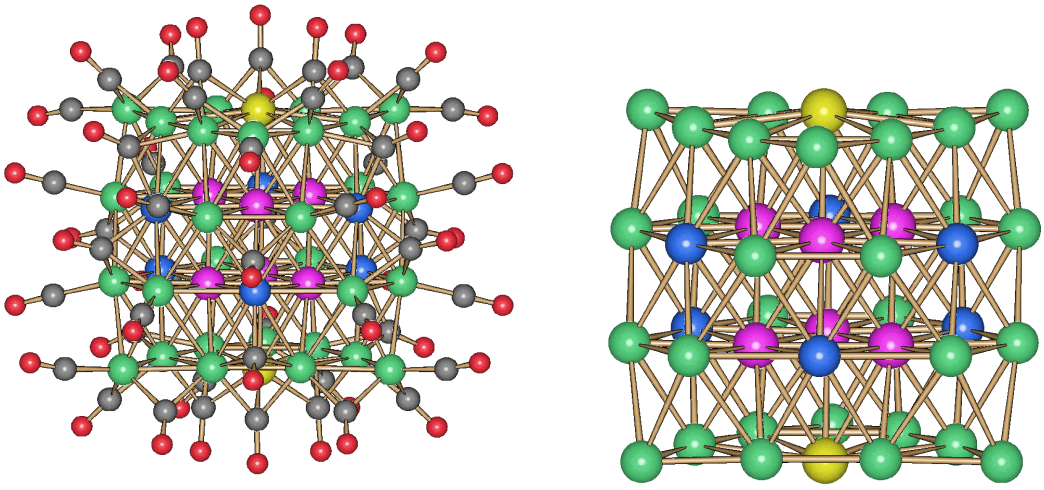

(a) (b)

Figure 7.11 (a) Molecular structure of $[Ni_{37-x}Pd_{7+x}(CO)_{48}]^{6-}$ (x = 0.69) (**5**) and (b) its M_{44} metal core (green, Ni; purple, Pd; yellow, Ni/Pd ≈ 33:67; blue, Ni/Pd ≈ 91:9; grey, C; red, O).

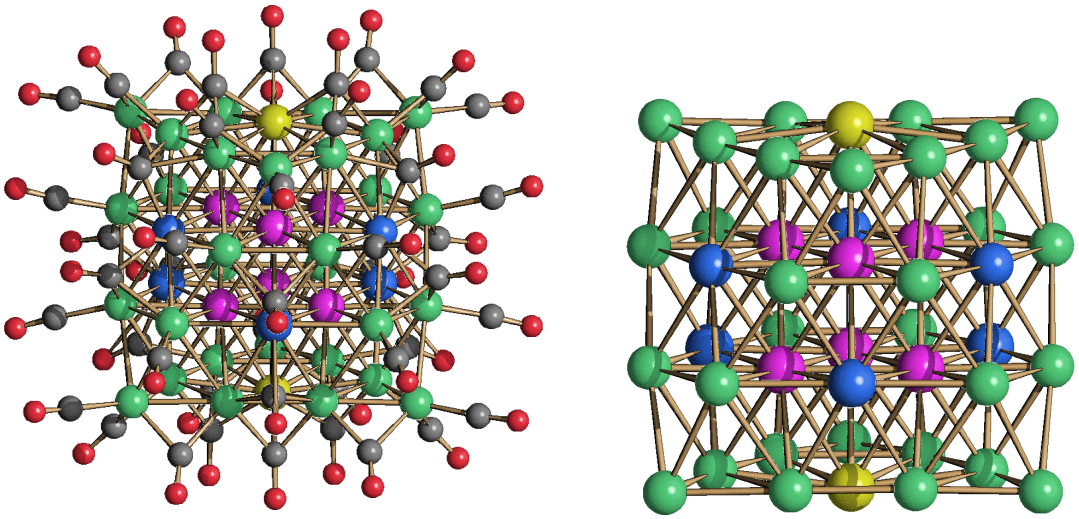

(a) (b)

Figure 7.12 (a) Molecular structure of the first independent molecule of $[HNi_{37-x}Pd_{7+x}(CO)_{48}]^{5-}$ (x = 0.53) (**6**) and (b) its M_{44} metal core (green, Ni; purple, Pd; yellow, Ni/Pd ≈ 42:58; blue, Ni/Pd ≈ 88,91,92:12,9,8; grey, C; red, O).

Table 7.6 Main bond distances (Å) of **4**-**6**.

Compound	Ni-Ni	Ni-Pd	Pd-Pd
4	2.401(3)-3.006(3) Average 2.57(2)	2.400(2)-2.796(2) Average 2.634(11)	2.695(2)-2.722(2) Average 2.713(5)
5	2.3754(17)-2.8280(17) Average 2.598(9)	2.4995(16)-2.8537(13) Average 2.634(7)	2.6412(13)-2.8537(13) Average 2.735(4)
6	2.373(4)-2.808(4) Average 2.57(3)	2.497(3)-2.844(3) Average 2.60(3)	2.618(3)-2.844(3) Average 2.696(18)

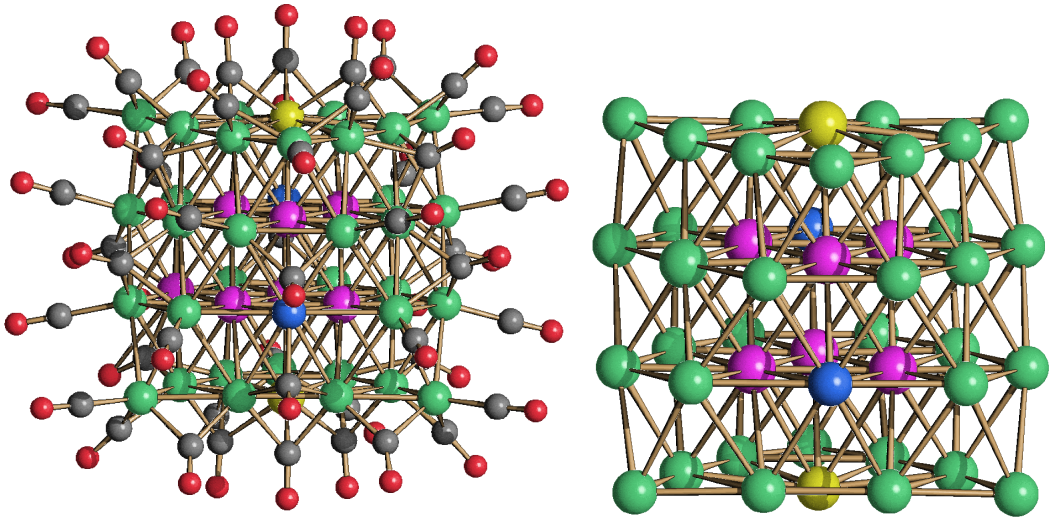

(a) (b)

Figure 7.13 (a) Molecular structure of the second independent molecule of $[HNi_{37-x}Pd_{7+x}(CO)_{48}]^{5-}$ (x = 0.53) (**6**) and (b) its M_{44} metal core (green, Ni; purple, Pt; yellow, Ni/Pd ≈ 51:49; blue, Ni/Pd ≈ 83:17; grey, C; red, O).

In addition to the metal frameworks, **5** and **6** display similar Ni/Pd substitutional and compositional disorder. Thus **5** is actually a mixture of $[Ni_{37}Pd_7(CO)_{48}]^{6-}$ (31%) and $[Ni_{36}Pd_8(CO)_{48}]^{6-}$ (69%), whereas **6** consists of $[HNi_{37}Pd_7(CO)_{48}]^{5-}$ (47%) and $[HNi_{38}Pd_6(CO)_{48}]^{5-}$ (53%). Furthermore, in the case of **6** two independent molecules are present within the unit cell, displaying some significant differences in their compositions. Thus, the first independent molecule consists of $[HNi_{37}Pd_7(CO)_{48}]^{5-}$ (26%) and $[HNi_{38}Pd_6(CO)_{48}]^{5-}$ (74%), whereas the second site contains $[HNi_{37}Pd_7(CO)_{48}]^{5-}$ (68%) and $[HNi_{38}Pd_6(CO)_{48}]^{5-}$ (32%).

7.7 Synthesis and characterisation of $[Pt_{6-x}Ni_x(CO)_{12}]^{2-}$ (x = 1.25, 2.53, 3.24, 4.15, 4.16, 4.41, 5.78, 5.90) (7)

The reactions between $[NBu_4]_2[Pt_6(CO)_{12}]$ and $[NBu_4]_2[Ni_6(CO)_{12}]$ in thf with different stoichiometric ratios led to the formation of a new series of compounds with general formula $[Pt_{6-x}Ni_x(CO)_{12}]^{2-}$ (**7**). By performing the reaction with different stoichiometric Pt/Ni ratio, several compounds of type **7** with different Pt/Ni contents were obtained, in accordance to equations (7.1-7.5). It must be remarked that compounds of type **7** are always obtained in mixtures (see below).

$$5[Ni_6(CO)_{12}]^{2-} + [Pt_6(CO)_{12}]^{2-} \rightarrow 6[Ni_5Pt(CO)_{12}]^{2-} \quad (7.1)$$

$$2\,[Ni_6(CO)_{12}]^{2-} + [Pt_6(CO)_{12}]^{2-} \rightarrow 3[Ni_4Pt_2(CO)_{12}]^{2-} \quad (7.2)$$

$$[Ni_6(CO)_{12}]^{2-} + [Pt_6(CO)_{12}]^{2-} \rightarrow 2[Ni_3Pt_3(CO)_{12}]^{2-} \quad (7.3)$$

$$[Ni_6(CO)_{12}]^{2-} + 2[Pt_6(CO)_{12}]^{2-} \rightarrow 3[Ni_2Pt_4\ (CO)_{12}]^{2-} \quad (7.4)$$

$$[Ni_6(CO)_{12}]^{2-} + 5[Pt_6(CO)_{12}]^{2-} \rightarrow 6[NiPt_5(CO)_{12}]^{2-} \quad (7.5)$$

Compound of type **7** richer in platinum can be more conveniently obtained from the reactions of $[NBu_4]_2[Pt_9(CO)_{18}]$ with $[NBu_4]_2[Ni_6(CO)_{12}]$ in accordance with equation (7.6).

$$2[Ni_6(CO)_{12}]^{2-} + 5[Pt_9(CO)_{18}]^{2-} \rightarrow 9[NiPt_5(CO)_{12}]^{2-} + 2Ni^{2+} + 2CO + Ni(CO)_4 \quad (7.6)$$

All of these reactions (7.1-7.6) are rather slow and require at least one day at room temperature. Then, the solvent was removed under reduced pressure, the residue washed with water and toluene, and extracted with thf. After slow diffusion of *n*-hexane, crystals of $[NBu_4]_2[Pt_{6-x}Ni_x(CO)_{12}]$ (x = 1.25, 3.24, 4.15, 4.16, 4.41, 5.78, 5.90) and $[NBu_4]_4[Pt_{6-x}Ni_x(CO)_{12}][Br]_2$ (x = 2.53) have been obtained. These crystals have been characterised by means of IR, NMR, ESI-MS spectroscopy, ICP analysis and SC-XRD. Comparison of ICP and SC-XRD analysis indicates that the single crystals used for the structural determination and the bulk of the sample have the same composition.

Compounds of type **7** richer in Pt displayed IR spectra similar to $[Pt_6(CO)_{12}]^{2-}$ (ν_{CO} 2000(vs) and 1808(m) cm^{-1}), whereas those richer in Ni showed IR spectra similar to $[Ni_6(CO)_{12}]^{2-}$ (ν_{CO} 1990(vs) and 1798(m) cm^{-1}).

In order to further elucidate the composition of these $[Pt_{6-x}Ni_x(CO)_{12}]^{2-}$ clusters, ESI-MS studies have been carried out on some of their $[NBu_4]_2[Pt_{6-x}Ni_x(CO)_{12}]$ crystals. The ESI-MS spectra recorded on CH_3CN solutions of $[NBu_4]_2[Pt_{4.75}Ni_{1.25}(CO)_{12}]$, $[NBu_4]_2[Pt_{2.76}Ni_{3.24}(CO)_{12}]$ and $[NBu_4]_2[Pt_{1.75}Ni_{4.15}(CO)_{12}]$ are reported in Figures 7.14-7.15, and peak assignments are summarised in Tables 7.7-7.8.

The di-anionic nature of all these ions was confirmed by the systematic loss of m/z 14 units from the molecular ions, that corresponded to a CO ligand (m = 28 uma) assuming z = 2.

The ESI-MS spectrum (ES–) of $[NBu_4]_2[Pt_{4.75}Ni_{1.25}(CO)_{12}]$ showed that the main species in the mixture is $[Pt_5Ni(CO)_{12}]^{2-}$ which is present in the gas phase as molecular ion (m/z = 683), as well as related ions obtained by the addition/loss of a few CO ligands (Figure 7.14, Table 7.7). Moreover, significant amounts of $[Pt_4Ni_2(CO)_{12}]^{2-}$ are present as well as traces of $[Pt_6(CO)_{12}]^{2-}$, $[Pt_3Ni_3(CO)_{12}]^{2-}$, $[Pt_2Ni_4(CO)_{12}]^{2-}$ and $[PtNi_5(CO)_{12}]^{2-}$. Thus, the crystals of $[NBu_4]_2[Pt_{4.75}Ni_{1.25}(CO)_{12}]$ are actually a complex mixture of clusters of the type **7**.

Similar results have been obtained by analysing other samples of clusters of type **7** with different Ni/Pt composition. As a further example, the ESI-MS spectrum of a mixture of $[NBu_4]_2[Pt_{2.76}Ni_{3.24}(CO)_{12}]$ and $[NBu_4]_2[Pt_{1.85}Ni_{4.15}(CO)_{12}]$ is shown in Figure 7.15 (Table 7.8). These crystals were obtained by reacting $[Pt_6(CO)_{12}]^{2-}$ with a sight excess of $[Ni_6(CO)_{12}]^{2-}$. The two species crystallised together from the same batch. In this case, the major species present was the unreacted $[Ni_6(CO)_{12}]^{2-}$ (m/z = 344), as well as detectable amounts of $[Pt_6(CO)_{12}]^{2-}$, $[Pt_5Ni(CO)_{12}]^{2-}$, $[Pt_4Ni_2(CO)_{12}]^{2-}$, $[Pt_3Ni_3(CO)_{12}]^{2-}$, $[Pt_2Ni_4(CO)_{12}]^{2-}$ and $[PtNi_5(CO)_{12}]^{2-}$. Therefore, all the compounds $[Pt_{6-x}Ni_x(CO)_{12}]^{2-}$ with x = 0-6 were present in different amounts within this sample. We can conclude that the reactions are not selective and lead to mixtures of compounds with the same structure but different Ni/Pt contents.

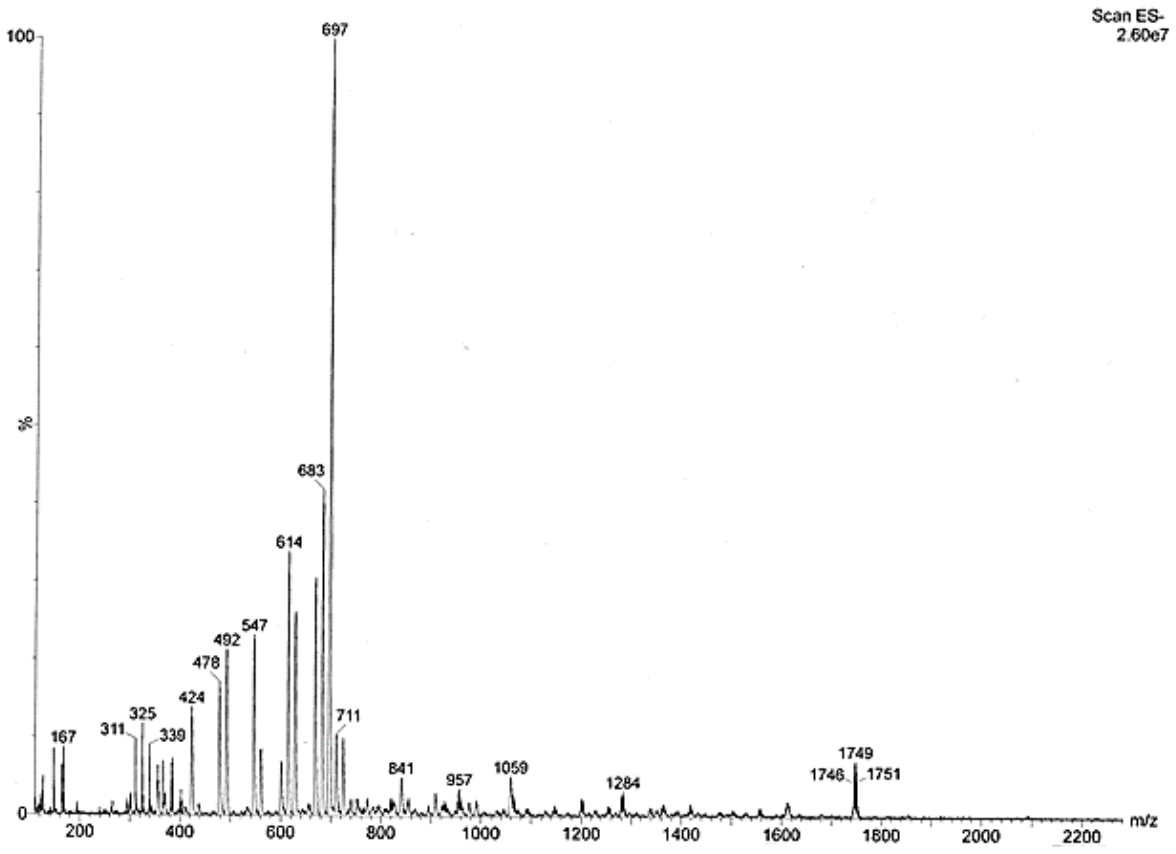

Figure 7.14 ESI-MS spectrum in CH_3CN (ES–) of $[NBu_4]_2[Pt_{6-x}Ni_x(CO)_{12}]$ (x = 1.25).

Table 7.7 Peak assignment of the ESI-MS spectrum (ES–) of $[NBu_4]_2[Pt_{6-x}Ni_x(CO)_{12}]$ (x = 1.25).

m/z	Relative intensity	Ion	Code
1749	10	$\{[Pt_6(CO)_{12}][NBut_4]\}^-$	Pt_6+NBu_4
1612	4	$\{[Pt_5Ni(CO)_{12}][NBut_4]\}^{2-}$	$Pt_5Ni+NBu_4$
725	10	$[Pt_5Ni(CO)_{15}]^{2-}$	$Pt_5Ni+3CO$
711	10	$[Pt_5Ni(CO)_{14}]^{2-}$	$Pt_5Ni+2CO$
697	100	$[Pt_5Ni(CO)_{13}]^{2-}$	$Pt_5Ni+1CO$
683	45	$[Pt_5Ni(CO)_{12}]^{2-}$	Pt_5Ni
669	30	$[Pt_5Ni(CO)_{11}]^{2-}$	$Pt_5Ni–1CO$
629	25	$[Pt_4Ni_2(CO)_{13}]^{2-}$	Pt_4Ni_2+1CO
614	35	$[Pt_4Ni_2(CO)_{12}]^{2-}$	Pt_4Ni_2
601	5	$[Pt_4Ni_2(CO)_{11}]^{2-}$	$Pt_4Ni_2–1CO$
561	8	$[Pt_3Ni_3(CO)_{13}]^{2-}$	Pt_3Ni_3+1CO
547	20	$[Pt_3Ni_3(CO)_{12}]^{2-}$	Pt_3Ni_3
492	20	$[Pt_2Ni_4(CO)_{13}]^{2-}$	Pt_2Ni_4+1CO
478	15	$[Pt_2Ni_4(CO)_{12}]^{2-}$	Pt_2Ni_4
424	15	$[PtNi_5(CO)_{13}]^{2-}$	$PtNi_5$

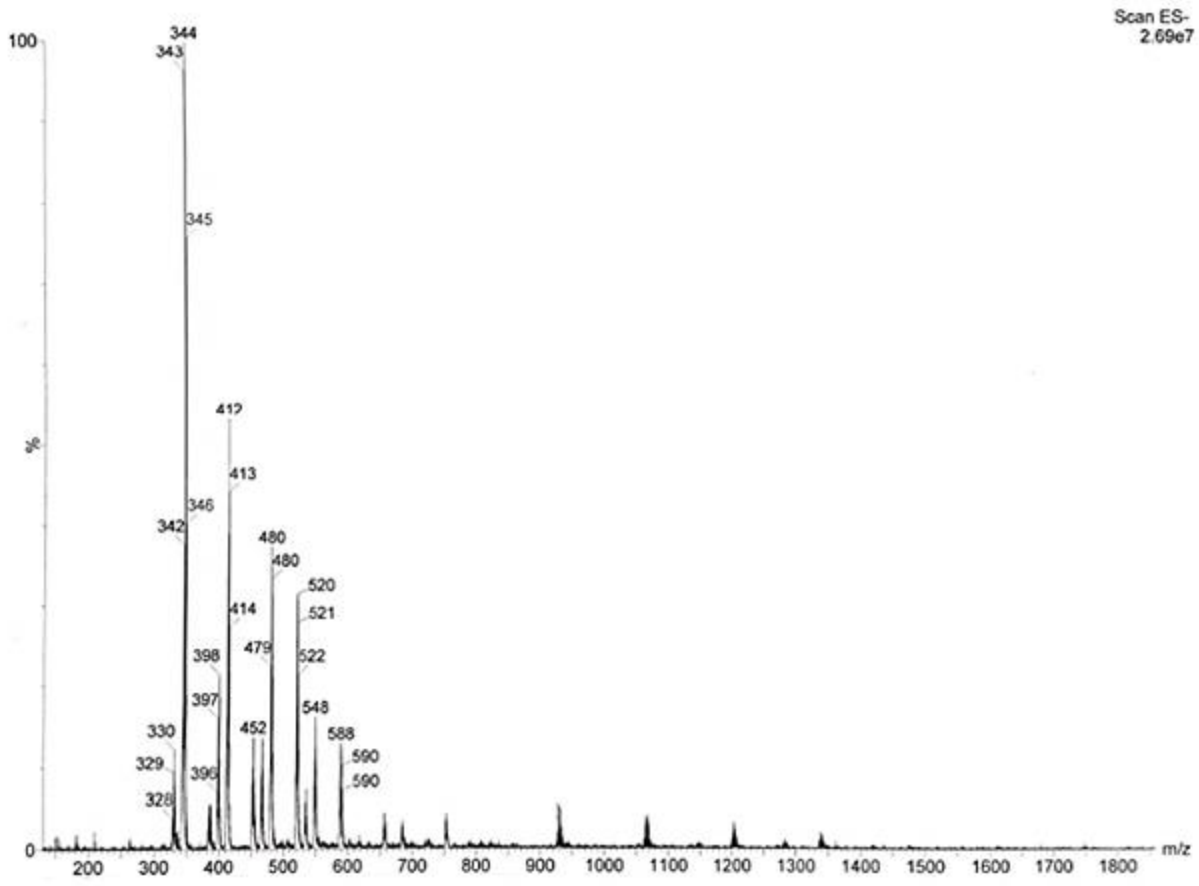

Figure 7.15 ESI-MS spectrum in CH_3CN (ES–) of $[NBu_4]_2[Pt_{6-x}Ni_x(CO)_{12}]$ (x = 3.24, 4.15).

Table 7.8 Peak assignment of the ESI-MS spectrum (ES–) of $[NBu_4]_2[Pt_{6-x}Ni_x(CO)_{12}]$ (x = 3.24, 4.15).

m/z	Relative intensity	Ion	Code
1338	2	$\{[Pt_3Ni_3(CO)_{12}][NBut_4]\}^-$	$Pt_3Ni_3+NBu_4$
1203	5	$\{[Pt_2Ni_4(CO)_{12}][NBut_4]\}^-$	$Pt_2Ni_4+NBu_4$
1068	8	$\{[PtNi_5(CO)_{12}][NBut_4]\}^-$	$PtNi_5+NBu_4$
928	10	$\{[Ni_6(CO)_{12}][NBut_4]\}^-$	Ni_6+NBu_4
753	8	$[Pt_6(CO)_{12}]^{2-}$	Pt_6
685	5	$[Pt_5Ni(CO)_{12}]^{2-}$	Pt_5Ni
657	8	$[Pt_5Ni(CO)_{10}]^{2-}$	$Pt_5Ni–2CO$
588	10	$[Pt_4Ni_2(CO)_{10}]^{2-}$	$Pt_4Ni_2–2CO$
548	12	$[Pt_3Ni_3(CO)_{12}]^{2-}$	Pt_3Ni_3
535	5	$[Pt_3Ni_3(CO)_{11}]^{2-}$	$Pt_3Ni_3–1CO$
520	30	$[Pt_3Ni_3(CO)_{10}]^{2-}$	$Pt_3Ni_3–2CO$
480	35	$[Pt_2Ni_4(CO)_{12}]^{2-}$	Pt_2Ni_4
466	12	$[Pt_2Ni_4(CO)_{11}]^{2-}$	$Pt_2Ni_4–1CO$
452	12	$[Pt_2Ni_4(CO)_{10}]^{2-}$	$Pt_2Ni_4–2CO$
412	50	$[PtNi_5(CO)_{12}]^{2-}$	$PtNi_5$
398	20	$[PtNi_5(CO)_{11}]^{2-}$	$PtNi_5–1CO$
385	5	$[PtNi_5(CO)_{10}]^{2-}$	$PtNi_5–2CO$
344	100	$[Ni_6(CO)_{12}]^{2-}$	Ni_6
330	14	$[Ni_6(CO)_{11}]^{2-}$	$Ni_6–1CO$

^{195}Pt NMR studies have been carried out aiming at better understanding the substitutional disorder of these M_6 compounds. The resulting NMR spectra presented several resonances in the region between -4400 and -5200 ppm. The complexity of such spectra suggested the presence of isomers of **7** (Figure 7.16), in addition to the presence of cluster with different Ni/Pt content. This investigation is actually in progress.

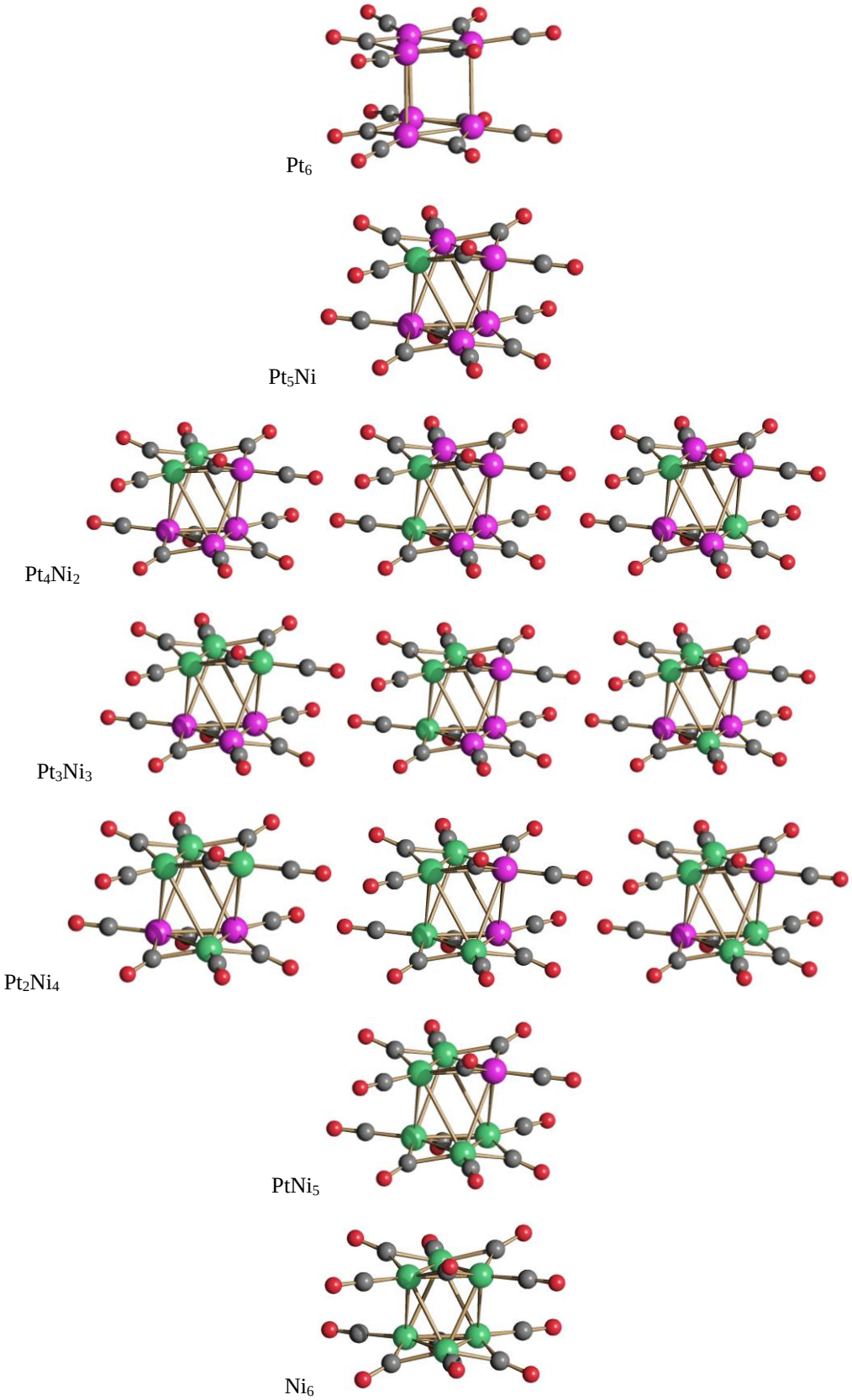

Figure 7.16 Possible constitutional isomers of $[Pt_{6-x}Ni_x(CO)_{12}]^{2-}$ (purple, Pt; green, Ni; red, O; grey, C).

Crystal structure

Bimetallic Chini clusters of type **7** have been structurally characterised by means of SC-XRD as $[NBu_4]_2[Pt_{6-x}Ni_x(CO)_{12}]$ (x = 1.25, 3.24, 4.15, 4.16, 4.41, 5.78, 5.90) and $[NBu_4]_4[Pt_{6-x}Ni_x(CO)_{12}][Br]_2$ (x = 2.53) salts. All of them contain the same octahedral $[Pt_{6-x}Ni_x(CO)_{12}]^{2-}$ anion. As an example, the structure of $[Pt_{1.85}Ni_{4.15}(CO)_{12}]^{2-}$ is reported in Figure 7.17.

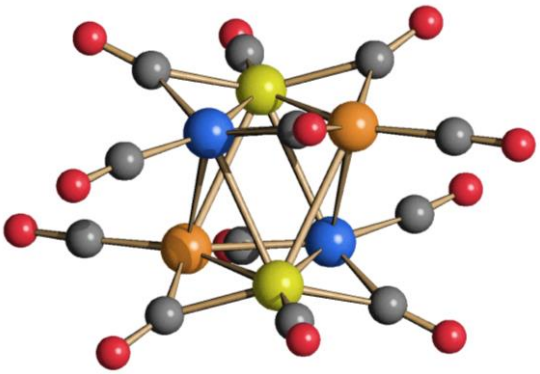

Figure 7.17 Molecular structure of $[NBu_4]_2[Pt_{6-x}Ni_x(CO)_{12}]$ (x = 4.15) (in blue Pt 0.3724, in yellow Pt 0.3563, in orange Pt 0.1972).

All these crystal structures display compositional disorder being mixtures of anions of type **7** with a different Pt/Ni composition. This disorder is represented in Figure 7.17 by using three colours for the six metal sites of the octahedron, being these positions two by two related by an inversion centre. The different crystals of **7** show a different Pt/Ni composition as evidenced by the different Pt/Ni occupancy factors in these six sites. The structures are completed by 12 carbonyls, 6 in terminal and 6 in edge bridging positions. All the anions of type **7** are, therefore, isostructural with $[Ni_6(CO)_{12}]^{2-}$. Conversely, $[Pt_6(CO)_{12}]^{2-}$ adopts a trigonal prismatic geometry in all its salts, due to electronic and steric reasons. It is noteworthy that it is enough to replace just a Pt atom with a Ni one in order to invert the structure from trigonal prismatic to octahedral.

Oxidation of $[Pt_{6-x}Ni_x(CO)_{12}]^{2-}$

In order to obtain higher nuclearity bimetallic Chini clusters, the oxidation of **7** with $HBF_4{\cdot}Et_2O$ has been studied. Unfortunately, this led to homometallic Chini clusters such as $[Pt_9(CO)_{18}]^{2-}$ and $[Pt_{12}(CO)_{24}]^{2-}$, with loss of Ni as $Ni(CO)_4$ or Ni^{2+}.

7.8 Synthesis and characterisation of $[Pt_{12-x}Ni_x(CO)_{21}]^{4-}$ (x = 2.91, 5.82, 6.29, 6.41) (8)

7 is not stable in solution for a prolonged time. Indeed, it spontaneously loses CO affording higher nuclearity clusters with general formula $[Pt_{12-x}Ni_x(CO)_{21}]^{4-}$ (**8**), in accordance to equation (7.7):

$$2[Pt_{6-x}Ni_x(CO)_{12}]^{2-} \rightleftarrows [Pt_{12-x}Ni_x(CO)_{24}]^{4-} \rightarrow [Pt_{12-x}Ni_x(CO)_{21}]^{4-} + 3CO \quad (7.7)$$

The transient $[Pt_{12-x}Ni_x(CO)_{24}]^{4-}$ species has not been detected, since it immediately loses 3 molecules of CO resulting in the more stable tetra-anion $[Pt_{12-x}Ni_x(CO)_{21}]^{4-}$ (**8**). This process can be accelerated by heating **7** in CH_3CN solution at 90 °C for 30 minutes under nitrogen atmosphere. During this thermal treatment, the red/orange solution of **7** becomes brownish. This colour indicates the formation of **8** as also corroborated by IR spectroscopy.

Crystal structure

8 has been isolated from several attempts, with different Pt/Ni contents and counterions. Crystallographic data have been recorded on crystals of $[NEt_4]_4[Pt_{9.09}Ni_{2.91}(CO)_{21}]$, $[NBu_4]_4[Pt_{6.18}Ni_{5.82}(CO)_{21}]$, $[NMe_4]_4[Pt_{5.71}Ni_{6.29}(CO)_{21}]\cdot 2CH_3CN$ and $[NEt_4]_4[Pt_{5.59}Ni_{6.41}(CO)_{21}]\cdot 2CH_3CN$ (Figure 7.18).

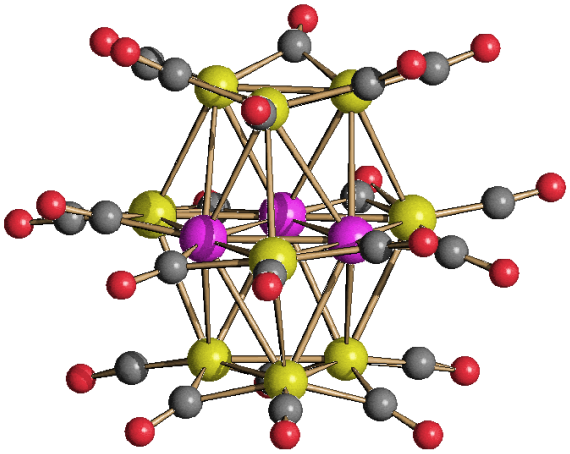

Figure 7.18 (a) Molecular structure of $[Pt_{12-x}Ni_x(CO)_{21}]^{4-}$ (x = 2.91, 5.82, 6.29, 6.41) (**8**) (purple, Pt; yellow, Pt/Ni; grey, C; red, O).

The molecular structures of all these clusters are similar to that of the previously reported $[Pt_3Ni_9(CO)_{21}]^{4-}$ and $[Ni_{12}(CO)_{21}]^{4-}$. The Pt/Ni content of **8** is controlled by the composition of the parent **7**. In both cases, **7** and **8** may be viewed as families of isostructural bimetallic clusters with a different metal composition. From a structural point of view, **8** is composed by 3 ABA layers, consisting of 3, 6 and 3 atoms, respectively. The inner sites of the framework are occupied by Pt

atoms (coloured in purple), whereas the other 9 positions are Pt-Ni disordered, as depicted in yellow in Figure 7.18. The molecular structure is completed by 9 terminal and 12 edge bridging CO groups.

It must be remarked that the isostructural $[Ni_{12}(CO)_{21}]^{4-}$ was easily protonated to afford the hydride clusters $[HNi_{12}(CO)_{21}]^{3-}$ and $[H_2Ni_{12}(CO)_{21}]^{2-}$. Indeed, these two hydrides were the more stable species, whereas the homometallic Ni tetra-anion was rather unstable. Conversely, in the case of **8**, as well as $[Pt_3Ni_9(CO)_{21}]^{4-}$, the tetra-anion is the most stable form and all attempt to protonate them failed. This may be explained on the basis of the greater electronegativity of Pt compared to Ni, that makes **8** a weaker base than $[Ni_{12}(CO)_{21}]^{4-}$.

Oxidation of $[Pt_{12-x}Ni_x(CO)_{21}]^{4-}$

Acetone solutions of **8** were treated with $HBF_4{\cdot}Et_2O$ aiming at obtaining the mono- and di-protonated forms of **8**. Even if there was spectroscopic evidence of the formation of $[HPt_{12-x}Ni_x(CO)_{21}]^{3-}$ and $[H_2Pt_{12-x}Ni_x(CO)_{21}]^{2-}$, it was not possible to isolate nor crystallise them. Indeed, these compounds rearranged over the time affording the penta-anion $[HPt_{14+x}Ni_{24-x}(CO)_{44}]^{5-}$ (x = 0.70) (**9**) (Figure 7.19), whose molecular structure is rather similar to the previously reported $[HPt_{14}Ni_{24}(CO)_{44}]^{5-}$.[95]

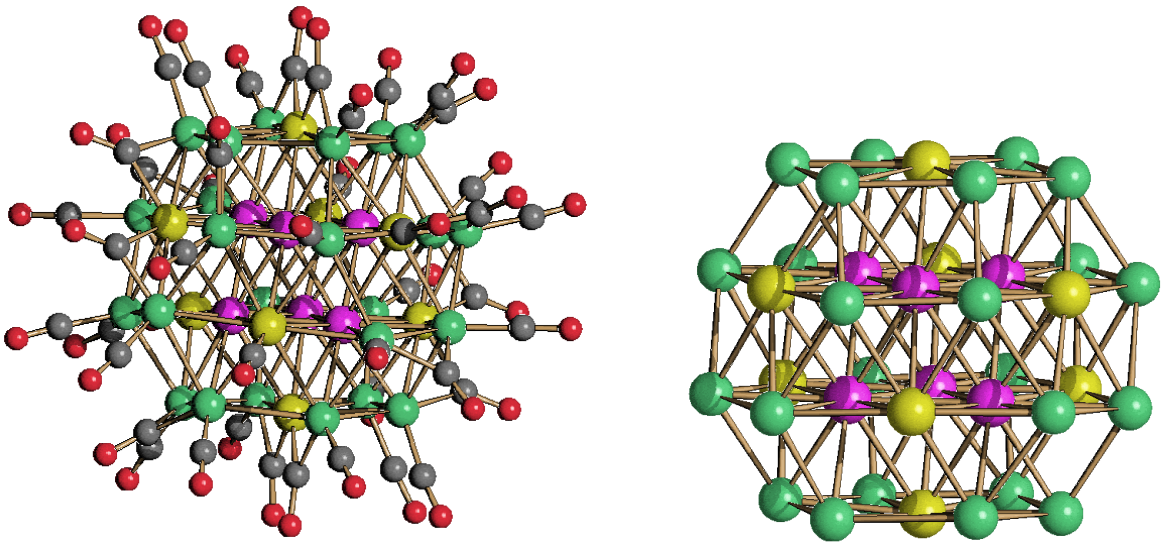

(a) (b)

Figure 7.19 (a) Molecular structure of $[HPt_{14+x}Ni_{24-x}(CO)_{44}]^{5-}$ (x = 0.70) (**9**) and (b) its M_{38} metal core (green, Ni; purple, Pt; yellow, Ni/Pt; grey, C; red, O).

9 presents a truncated-octahedron framework generated by 4 ABAB layers, constituted by 7, 12, 12 and 7 atoms, respectively. Analogously to $[HPt_{14}Ni_{24}(CO)_{44}]^{5-}$,[95] Pt atoms occupy the six

vertices of the interstitial octahedron, whereas the positions at the centres of the eight hexagonal faces are disordered Ni/Pt. The metal cage is completed by 44 CO ligands.

7.9 Synthesis and characterisation of $[Pt_{19-x}Ni_x(CO)_{22}]^{4-}$ (x = 2.27, 3.23) (10)

Aiming at synthesising high nuclearity Pt/Ni carbonyl clusters, an acetone solution of $[Pt_{12}(CO)_{24}]^{2-}$ was reacted with one equivalent of $[Ni_6(CO)_{12}]^{2-}$, resulting in a new species, whose IR spectrum was rather similar to that of $[Pt_9(CO)_{18}]^{2-}$. The new species might be formulated as $[Pt_{9-x}Ni_x(CO)_{18}]^{2-}$ but, unfortunately, it was not stable in solution and rearranged over the time affording a new $[Pt_{19-x}Ni_x(CO)_{22}]^{4-}$ (**10**) carbonyl cluster.

Analogously to **8**, the formation of **10** can be accelerated by heating the dark purple acetonitrile solution of $[Pt_{9-x}Ni_x(CO)_{18}]^{2-}$ at 90 °C for a few hours. Formation of **10** was evidenced by the change of the colour of the acetonitrile solution from dark purple to brown. The IR spectrum of **10** shows ν_{CO} bands at 2000(vs), 1987(sh), 1922(w), 1797(s) and 1754(w) cm^{-1}, very similar to those of $[Pt_{19}(CO)_{22}]^{4-}$.

Crystal structure

The molecular structure of **10** was determined by SC-XRD as its $[NEt_4]_4$[**10**]·CH_3COCH_3 (x = 2.27) and $[NBu_4]_4$[**10**]·$2CH_3CN$ (x = 3.23) salts (Figure 7.20).

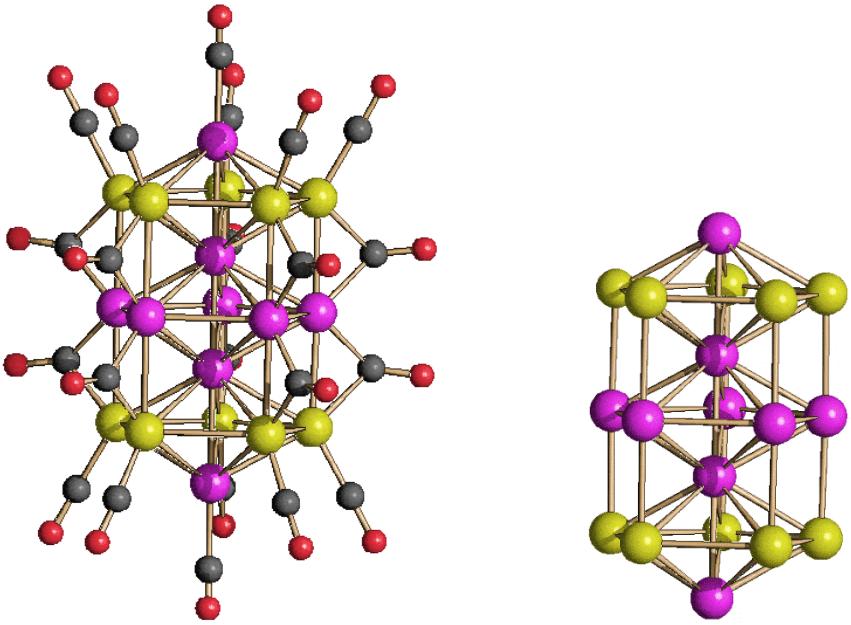

(a) (b)

Figure 7.20 (a) Molecular structure $[Pt_{19-x}Ni_x(CO)_{22}]^{4-}$ (x = 2.27, 3.23) (**10**) and (b) its M_{19} metal core (purple, Pt; yellow, Pt/Ni; grey, C; red, O).

10 may be view as two centred pentagonal prisms fused together by a common face and capped by 2 Pt atoms. Similar to **8**, this cluster presents substitutional and compositional disorder, as indicated by the yellow positions in Figure 7.20, whereas the inner pentagonal bipyramid and the two capping positions are fully occupied by Pt. 12 terminal and 10 edge bridging carbonyl ligands complete the metal cage.

As for **7** and **8**, the composition of **10** is controlled by the composition of the parent $[Pt_{9-x}Ni_x(CO)_{18}]^{2-}$ and, therefore, the amount of $[Pt_{12}(CO)_{24}]^{2-}$ and $[Ni_6(CO)_{12}]^{2-}$ employed. In all cases, **10** is always far richer in Pt than Ni, being the excess of Ni eliminated as $Ni(CO)_4$. This reflects the fact that the homometallic species $[Pt_{19}(CO)_{22}]^{4-}$ is well-known, whereas the related $[Ni_{19}(CO)_{22}]^{4-}$ does not exist. In turn, this may be explained on the basis of the fact that Pt-Pt bonds are stronger than Ni-Ni ones.

The isolation of **10** was an indirect evidence of the existence of the parent $[Pt_{9-x}Ni_x(CO)_{18}]^{2-}$.

Final Remarks

An interesting study regarding Ni-Pd and Ni-Pt carbonyl clusters has been carried out and the more relevant results have been described in this chapter. Analogies and differences amongst these two bimetallic systems emerged and helped the understanding of the role of Pt and Pd in Ni cluster chemistry. In particular, all the obtained results show the affinity of Ni towards carbonyl ligands, whereas Pt and Pd tend to maximise the M-M interactions by occupying the inner positions of the framework. Common features of the new bimetallic carbonyl clusters presented in this chapter are the compositional and/or substitutional disorders. The first one concerns the fact that in the same unit cell more species with different Ni/M (M = Pd, Pt) composition crystallised. The second phenomenon regards some metal sites of the metal cage which are Ni-M disordered. When this occurs, the complete segregation of M in the inner core of the clusters is not observed and a mixture of isostructural species differing for few Ni/M sites is formed. Compositional disorder is, thus, related to the presence of mixture of species with different composition, whereas substitutional disorder regards isomers of the same species.

The first part of this section reported the synthesis and the characterisation of new Ni-Pd carbonyl clusters obtained by reacting $[Ni_6(CO)_{12}]^{2-}$ with $PdCl_2(Et_2S)_2$. As results, new molecular alloy nanoclusters $[Ni_{22-x}Pd_{20+x}(CO)_{48}]^{6-}$ (x = 0.62) (**1**), $[Ni_{29-x}Pd_{6+x}(CO)_{42}]^{6-}$ (x = 0.09) (**2**) and $[Ni_{29+x}Pd_{6-x}(CO)_{42}]^{6-}$ (x = 0.27) (**3**) have been obtained. The reactions conducted between $[Ni_6(CO)_{12}]^{2-}$ and another Pd(II) salt, namely $[Pd(CH_3CN)_4][BF_4]_2$, led to the formation of $[Ni_{36-x}Pd_{5+x}(CO)_{46}]^{6-}$ (x = 0.41) (**4**), $[Ni_{37-x}Pd_{7+x}(CO)_{48}]^{6-}$ (x = 0.69) (**5**) and $[HNi_{37-x}Pd_{7+x}(CO)_{48}]^{5-}$ (x = 0.53) (**6**) species. From a structural point of view, all of these compounds display a compact framework with a good segregation of the two metals with partial substitutional and/or compositional disorders. Furthermore, electrochemical and spectroelectrochemical studies conducted on **1** and **2** revealed four redox couples chemically reversible in the timescale of CV and proved that both the hexa-anions were stable with a variable number of electrons.

Then, a systematic study involving Chini clusters and $[Ni_6(CO)_{12}]^{2-}$ has been explored, leading to the isolation and characterisation of the new $[Pt_{6-x}Ni_x(CO)_{12}]^{2-}$ (x = 1.25, 2.53, 3.24, 4.15, 4.16, 4.41, 5.78, 5.90) (**7**). CO elimination from **7** afforded $[Pt_{12-x}Ni_x(CO)_{21}]^{4-}$ (x = 2.91, 5.82, 6.29, 6.41) (**8**). The oxidation of these compounds resulted in the formation of a M_{38} species of formula $[HPt_{14+x}Ni_{24-x}(CO)_{44}]^{5-}$ (x = 0.70) (**9**). Finally, $[Pt_{19-x}Ni_x(CO)_{22}]^{4-}$ (x = 2.27, 3.23) (**10**) has been obtained after thermal decomposition in CH_3CN of the purported $[Pt_{9-x}Ni_x(CO)_{18}]^{2-}$.

CHAPTER 8

Final Remarks

During my PhD, several new metal carbonyl clusters (MCCs) have been synthesised. From a dimensional point of view, the nuclearity of such species ranges from 2 to 44 metal atoms. Lower nuclearity compounds may be viewed as polymetallic complexes, whereas higher nuclearity species can reach the nanocluster size, by resembling to ultrasmall nanoparticles (USNPs). All the new compounds have been structurally characterised by means of single crystal X-ray diffraction (SC-XRD), that turned to be the unique technique able to define the total structure of the clusters with atomic precision. Crystallographic analyses are of paramount importance in this chemistry. Nevertheless, further techniques are necessary for the complete characterisation of MCCs, such as IR and NMR spectroscopies, ESI-MS spectrometry, electrochemical and UV-visible studies, and elemental analyses (Inductively Coupled Plasma-Mass Spectrometry, ICP-MS).

This Thesis presents the new homometallic and heterometallic carbonyl clusters that have been investigated during my PhD. By exploring homometallic clusters, it was possible to study the chemistry of the different metals within carbonyl compounds, gaining insights into their tendency to form M-CO and M-M bonds, as well as their main structural motives. Conversely, the investigation of heterometallic systems highlighted two interesting aspects, that is the fact that (1) each metal maintains its own features leading to segregation phenomena, but at the same time (2) synergetic effects may be present resulting in larger heterometallic clusters compared to homometallic ones. These points may be observed, for examples, with the bimetallic Fe-M(NHC) and Co-M(NHC) (M = Cu, Ag, Au) systems (Chapters 2, 3 and 5), in which Fe and Co maintain the Fe-CO and Co-CO bonds, whereas the coinage metals preserve the M-NHC interactions. A further examples regards the bimetallic Ni-M (M = Pd, Pt) carbonyl compounds (Chapter 7), whose structural analyses brought to light a very strong segregation of the two metals within the metal cage. As described in Chapter 7, Ni tends to form strong M-CO bonds, while Pd and Pt are more prone to maximise the M-M interactions. For this reason, the crystallographic studies of these bimetallic compounds show a distribution of Ni on the surface of the cluster, whereas Pd and Pt are mainly located in the inner core of the metal cage.

As far as the synergic effects in bimetallic systems are concerned, the most interesting case regards Ni-Pd and Ni-Pt MCCs. Indeed, the nuclearity of homometallic Ni carbonyl clusters does not overcome 12 metal atoms. However, in the presence of Pd or Pt, the bimetallic Ni-M (M = Pd, Pt) compounds can achieve considerably higher nuclearity.

In addition to metal segregation, these heterometallic carbonyl clusters also display compositional and/or substitutional disorders. Several structural analyses performed on crystals of Ni-M (M = Pd, Pt) carbonyl clusters show a mixture of species with different compositions, as well as a blend of isomers (Chapters 6 and 7). Further investigations of such structures with equal composition, may provide a better insight of alloy nanoclusters. Substitutional and compositional disorder phenomena have been also detected in heterometallic $[M_xM'_{5-x}Fe_4(CO)_{16}]^{3-}$ (M, M' = Cu, Ag, Au; M ≠ M'; x = 0-5) carbonyl clusters (Chapter 4). The latter refers to the fact that $[M_xM'_{5-x}Fe_4(CO)_{16}]^{3-}$ are actually mixtures of clusters with slight different M/M' composition. Conversely, substitutional disorder indicates that also mixtures of clusters with the same composition but different distribution of M and M' (isomers) are present. Joined experimental and theoretical investigations clearly pointed out that these phenomena are the result of a subtle balance among Fe-Cu, Fe-Ag and Fe-Au interactions.

The presence of a second metal joining the metal cage may influence not only the molecular structure but also the catalytic activity. Indeed, catalytic studies conducted in collaboration with Prof. Rita Mazzoni (University of Bologna) regarding the dehydrogenation of ammonia-borane (AB) display great performances when neutral $Fe(CO)_4(CuIPr)_2$ or $Co(CO)_4(CuIPr)$ are used as catalysts. Conversely, the analogous homometallic species show a lower or no catalytic activity during the reaction. This collaboration highlighted a tangible synergic effect provided by the presence of both metals.

A significant part of my PhD was dedicated to the investigation of lower nuclearity MCCs stabilised by NHC ligands. Before this work, the literature was quite limited to Ru and Os carbonyl compounds with ancillary NHC ligands. We decided to extend this work to other two metallic systems, that is Fe and Co, by developing a general strategy for the synthesis of mono-anionic $[Fe(CO)_4(MNHC)]^-$ and neutral $Fe(CO)_4(MNHC)_2$, $Co(CO)_4(MNHC)$ (M = Cu, Ag, Au; NHC = IMes, IPr) species. During this investigation, further methods for the preparation of mixed neutral compounds have been fine-tuned. In particular, neutral trimetallic $Fe(CO)_4(MNHC)(M'NHC)$ (M, M' = Cu, Ag, Au; M ≠ M'; NHC = IPr) and neutral heteroleptic $Fe(CO)_4(MNHC)(MNHC')$ (M = Au; NHC = IMes, IPr) compounds have been isolated. The characterisation of these new species allows to link some of their properties to the nature of the NHC ligand employed. Indeed,

depending on the organic fragment of the carbene, some species seem to be more stable and catalytically active than others. For example, IMes-containing MCCs display poor catalytic performances for the dehydrogenation of AB, whereas IPr-containing species turn out to be more active and stable. The stability of these species is also influenced by the nature of the coinage metal. At this regard, DFT calculations confirm the fact that the species containing M-Au bonds are more stable than those presenting M-Cu or M-Ag bonds (M = Fe, Co). This can be explained on the basis of the M-M bond strength, that is higher with Au, medium with Cu and lower with Ag. As stated in the introduction of this Thesis (Chapter 1), thermal treatments represent an efficient method for the growth of the sizes of MCCs. Indeed, the thermal decompositions of the new Fe-M(NHC) carbonyl clusters led to the isolation of larger compounds with different composition. In future, this project might be extended by employing different NHC carbene ligands or by changing the nature of the starting carbonyl reagent.

In the second part of my PhD, the chemistry of the Chini clusters has been investigated. Several reactions with different phosphines have been performed, affording new heteroleptic Pt clusters, with higher dimension and different properties. As an example, by substituting one or more CO ligands with PTA, water solubility is conferred to the resulting clusters, by making them valid candidates for biological tests. At this regard, a collaboration with Prof. P. J. Dyson has been conducted and led to interesting findings (see Chapter 6). Moreover, the use of a bidentate phosphine such as dppm allowed the discovery of a new growing mode of heteroleptic Chini clusters. This consists in the growth of $[Pt_6(CO)_{10}(dppm)]^{2-}$ *via* the formal addition of one $[Pt_6(CO)_{10}(dppm)]$ fragment after each oxidation step and results in the formation of $[Pt_6(CO)_{10}(dppm)]_n^{2-}$ (n = 2-4) heteroleptic clusters. Further oxidation should afford infinite molecular wires, as already found whilst studying the oxidation of homoleptic Chini clusters. In addition, Chini clusters may also grow in a tridimensional way after thermal treatment under controlled conditions *via* CO loss and formation of new Pt-Pt bonds. This results in higher nuclearity globular molecular nanoclusters as demonstrated with the synthesis and structural characterisation of $[Pt_{27}(CO)_{31}]^{4-}$.

In addition to heteroleptic Pt carbonyl clusters, the bimetallic Pt-Sn system was investigated, in order to complete the previous work started by my research group. New Pt-Sn carbonyl clusters have been isolated and fully characterised. Furthermore, some of them were used as precursors for the preparation of nanostructured catalytic materials for the selective oxidation of hydroxymethylfurfural (HMF) to furandicarboxyl acid (FDCA), in collaboration with Prof. Stefania Albonetti (University of Bologna). In particular, $[Pt_{12}(CO)_{24}]^{2-}$, $[Pt_6(CO)_6(SnCl_2)_2(SnCl_3)_4]^{4-}$ and $[Pt_6(CO)_8(SnCl_2)(SnCl_3)_2(PPh_3)_2]^{2-}$ were used for the preparation of Pt and bimetallic Pt/Sn

nanoparticles deposited on TiO_2. The obtained materials were tested as catalysts in the aqueous phase oxidation of HMF to FDCA, by comparing their catalytic behaviour to that obtained with analogous systems prepared by TiO_2 impregnation with metal salt solutions using the same metal loading and Pt/Sn ratio.

Another interesting collaboration, currently in progress, is that regarding the use of Fe-Ag and homometallic Fe carbonyl clusters in catalysis, for the preparation of Cu open cell foams for the hydrogenation of HMF (in collaboration with Prof. Patricia Benito, University of Bologna). The results of these collaborations have not been discussed in detail within this Thesis mainly because, a part the synthesis of the clusters, most of the work was then carried out in the collaborating laboratories. Thus, I preferred to focus the core of the Thesis on the synthetic and characterisation work performed in my laboratory. Nonetheless, all these collaborations point out that MCCs are suitable precursors for the preparation of nanostructured materials and catalysts.

The very last part of my PhD was dedicated to the investigation of larger MCCs. At this regard, several new high nuclearity bimetallic carbonyl clusters have been obtained, by reacting $[Ni_6(CO)_{12}]^{2-}$ with Pd(II) species, such as $[Pd(CH_3CN)_4][BF_4]_2$ and $Pd(Et_2S)_2Cl_2$, and Chini clusters. This study offered the possibility to investigate mixing and alloying effects in large bimetallic molecular clusters, as well as to study their redox behaviour by means of electrochemical and spectroelectrochemical methods (in collaboration with Dr. Tiziana Funaioli, University of Pisa). Electrochemical studies conducted on some high nuclearity MCCs reveal their multivalent nature and detect reversible redox processes.

Finally, the work concerning Ni-Pt and Ni-Pd carbonyl clusters achieved significant results in the last months, but it is not currently concluded. It is reasonable to think that in the future, the nature and reactivity of these MCCs will be investigated further.

CHAPTER 9

Experimental Section

All reactions and sample manipulations were carried out using standard Schlenk techniques under nitrogen and in dried solvents. All the reagents were commercial products (Aldrich) of the highest purity available and used as received, except the following compounds which have been prepared according to the literature (Table 9.1).

Table 9.1. Clusters prepared according to literature methods. A = N or P; R = Me, Et, Bu, CH_2Ph and Ph.

Compound	Ref
$[AR_4]_3[Cu_3Fe_3(CO)_{12}]$	96
$[AR_4]_3[Cu_5Fe_4(CO)_{16}]$	96
$[AR_4]_4[Ag_4Fe_4(CO)_{16}]$	41
$[AR_4]_3[Ag_5Fe_4(CO)_{16}]$	41
$[AR_4]_2[Pt_{3n}(CO)_{6n}]$ (n = 2-6)	97
$[AR_4]_2[Ni_6(CO)_{12}]$	98

IR spectra were recorded on a Perkin Elmer Spectrum One interferometer in CaF_2 cells with 0.1 mm thickness.

Analyses of C, H and N were obtained with a Thermo Quest Flash EA 1112NC instrument.

^{1}H, $^{13}C\{^{1}H\}$, $^{31}P\{^{1}H\}$ and $^{11}B\{^{1}H\}$ NMR measurements were performed on a Varian Mercury Plus 400 MHz instrument. The proton and carbon chemical shifts were referenced to the non-deuterated aliquot of the solvent, whereas the phosphorous and boron chemical shifts were referenced to external H_3PO_4 (85% in D_2O) and internal $BF_3{\cdot}Et_2O$, respectively.

ESI mass spectra were recorded on a Waters Micromass ZQ4000 instrument and in all cases the solvent is acetonitrile.

Absorption spectra were recorded at 298 K using an Agilent Cary 100 UV-vis spectrometer.

Analyses of $[Pt_{6-x}Ni_x(CO)_{12}]^{2-}$, $[Pt_{12-x}Ni_x(CO)_{21}]^{4-}$ and $[Pt_{19-x}Ni_x(CO)_{22}]^{4-}$ species were performed by microwave plasma-atomic emission spectrometry on an Agilent 4210 MP-AES instrument.

The diffraction experiments were carried out on a Bruker APEX II diffractometer equipped with a PHOTON100 detector using Mo–Kα radiation. Data were corrected for Lorentz polarisation and absorption effects (numerical absorption correction SADABS). Structures were solved by direct methods and refined by full-matrix least-squares based on all data using F^2. Hydrogen atoms were fixed at calculated positions and refined by a riding model. All non-hydrogen atoms were refined with anisotropic displacement parameters.

Structure drawings have been performed with SCHAKAL99.

Theoretical DFT calculations have been carried out by Prof. Marco Bortoluzzi (University of Venezia), while the electrochemical studies have been carried out by Dr. Tiziana Funaioli (University of Pisa).

Synthesis of $[NEt_4][Fe(CO)_4(AuIMes)]$

$Na_2[Fe(CO)_4]\cdot 2thf$ (0.180 g, 0.500 mmol) and Au(IMes)Cl (0.270 g, 0.500 mmol) were charged in a Schlenk tube under a nitrogen atmosphere and dmso (15 mL) was added. The mixture was stirred for 2 h at room temperature and then, a saturated solution of $[NEt_4]Br$ in H_2O (40 mL) was added up to complete precipitation. The resulting yellow solid was recovered by filtration, washed with H_2O (3 × 15 mL), toluene (3 × 15 mL), and extracted with acetone (15 mL). Crystals of $[NEt_4][Fe(CO)_4(AuIMes)]$ suitable for X-ray crystallography were obtained by slow diffusion of *n*-hexane (35 mL) on the acetone solution (yield 0.232 g, 58 % based on Fe, 58 % based on Au).

$[NMe_4][Fe(CO)_4(AuIMes)]$ was obtained following a similar procedure and employing $[NMe_4]Cl$ instead of $[NEt_4]Br$.

$C_{33}H_{44}AuFeN_3O_4$ (799.53): calcd. (%): C 49.55, H 5.55, N 5.26; found: C 50.04, H 5.34, N 5.07. IR (nujol, 293 K) ν_{CO}: 1975(w), 1927(s), 1830(vs), 1790(vs) cm^{-1}. IR (dmso, 293 K) ν_{CO}: 1923(s), 1814(vs) cm^{-1}. IR (CH_3CN, 293 K) ν_{CO}: 1927(s), 1821(vs) cm^{-1}. IR (acetone, 293 K) ν_{CO}: 1924(s), 1820(vs) cm^{-1}. ^1H NMR (CD_3CN, 298 K): δ 7.20 (s, 2H, CH_{imid}), 7.05 (s, 4H, CH_{Ar}), 3.19 (q, $^2J_{HH}$ = 7.2 Hz, 8H, $NC\mathit{H}_2CH_3$), 2.35 (s, 6H, CH_3), 2.18 (s, 12H, CH_3), 1.22 (t, $^2J_{HH}$ = 7.2 Hz, 12H, $NCH_2C\mathit{H}_3$). $^{13}C\{^1H\}$ NMR (CD_3CN, 298 K): δ 226.5 (CO), 196.3 (C-Au), 138.7, 135.9, 135.1, 128.9, 121.4 (C_{Ar} and CH_{imid}), 52.2 (NCH_2CH_3), 20.3, 17.2 (CH_3), 6.8 (NCH_2CH_3).

Synthesis of $[NEt_4][Fe(CO)_4(AuIPr)]$

$Na_2[Fe(CO)_4]\cdot 2thf$ (0.210 g, 0.580 mmol) and Au(IPr)Cl (0.360 g, 0.580 mmol) were charged in a Schlenk tube under a nitrogen atmosphere and dmso (15 mL) was added. The mixture was stirred for 2 h at room temperature and then, a saturated solution of $[NEt_4]Br$ in H_2O (40 mL) was added up to complete precipitation. The resulting yellow solid was recovered by filtration, washed with H_2O (3 × 15 mL), toluene (3 × 15 mL), and extracted with acetone (15 mL). Crystals of $[NEt_4][Fe(CO)_4(AuIPr)]$ suitable for X-ray crystallography were obtained by slow diffusion of *n*-hexane (35 mL) on the acetone solution (yield 0.287 g, 56 % based on Fe, 56 % based on Au).

$C_{39}H_{56}AuFeN_3O_4$ (883.68): calcd. (%): C 52.98, H 6.39, N 4.76; found: C 53.12, H 6.21, N 4.54. IR (nujol, 293 K) ν_{CO}: 1972(w), 1924(s), 1810(vs) cm^{-1}. IR (dmso, 293 K) ν_{CO}: 1923(s), 1815(vs) cm^{-1}. IR (CH_3CN, 293 K) ν_{CO}: 1926(s), 1820(vs) cm^{-1}. IR (acetone, 293 K) ν_{CO}: 1924(s), 1821(vs) cm^{-1}. ^1H NMR (CD_3CN, 298 K): δ 7.49 (t, $^2J_{HH}$ = 7.4 Hz, 2H, CH_{Ar}), 7.34 (d, $^2J_{HH}$ = 7.4 Hz, 4H, CH_{Ar}), 7.32 (s, 2H, CH_{imid}), 3.19 (q, $^2J_{HH}$ = 7.2 Hz, 8H, NCH_2CH_3), 2.75 (sept, $^2J_{HH}$ = 6.8 Hz, 4H, $CH(CH_3)_2$), 1.39 (d, $^2J_{HH}$ = 6.8 Hz, 12H, $CH(CH_3)_2$), 1.22 (t, $^2J_{HH}$ = 7.2 Hz, 12H, NCH_2CH_3), 1.21 (d, $^2J_{HH}$ = 6.8 Hz, 12H, $CH(CH_3)_2$). $^{13}C\{^1H\}$ NMR (CD_3CN, 298 K): δ 226.4 (CO), 198.3 (C-Au), 145.9, 135.5, 129.6, 123.7, 122.4 (C_{Ar} and CH_{imid}), 52.1 (NCH_2CH_3), 28.5 ($CH(CH_3)_2$), 23.4, 23.0 ($CH(CH_3)_2$), 6.8 (NCH_2CH_3).

Thermal decomposition of $[NEt_4][Fe(CO)_4(AuNHC)]$ (NHC = IMes, IPr) in non-chlorinated solvents

A solution of $[NEt_4][Fe(CO)_4(AuIMes)]$ (0.530 g, 0.663 mmol) in dmso (10 mL) was heated at 130 °C for 3 h and the reaction monitored by IR spectroscopy. Then, a saturated solution of $[NEt_4]Br$ in H_2O (40 mL) was added up to complete precipitation. The resulting solid was recovered by filtration, washed with H_2O (3 × 15 mL), toluene (3 × 15 mL), and extracted with acetone (15 mL). A microcrystalline powder of $[NEt_4]_3[Au_3\{Fe(CO)_4\}_3]$ was obtained after removal of the solvent under reduced pressure (yield 0.134 g, 41 % based on Fe, 41 % based on Au). The compound was identified by comparison of its IR data with those reported in the literature.

Decomposition of $[NEt_4][Fe(CO)_4(AuIPr)]$ to produce $[Au_3\{Fe(CO)_4\}_3]^{3-}$ occurred at 150 °C in dmso. By further increasing the temperature up to 160-170 °C, a complex mixture of decomposition products was formed, among which $[Fe_3S(CO)_9]^{2-}$ was the major species detected by IR spectroscopy.

Synthesis of $Fe(CO)_4(AuIMes)_2$

Au(IMes)Cl (0.176 g, 0.328 mmol) was added as a solid in small portions to a solution of $[NEt_4][Fe(CO)_4(AuIMes)]$ (0.260 g, 0.325 mmol) in acetone (15 mL) and the reaction monitored by IR spectroscopy. The resulting mixture was stirred for 2 h at room temperature and then, the solvent removed under reduced pressure. The residue was washed with H_2O (3 × 20 mL), isopropanol (3 × 20 mL), and extracted with acetone (15 mL). A microcrystalline powder of $Fe(CO)_4(AuIMes)_2$ was obtained after removal of the solvent under reduced pressure (yield 0.213 g, 56 % based on Fe, 56 % based on Au).

Alternatively, $Fe(CO)_4(AuIMes)_2$ may be obtained from the reaction of $Na_2[Fe(CO)_4]\cdot 2thf$ with two equivalents Au(IMes)Cl in thf.

$C_{46}H_{48}Au_2FeN_4O_4$ (1170.67): calcd. (%): C 47.17, H 4.13, N 4.79, Fe 4.78, Au 33.66; found: C 46.89, H 4.34, N 4.98, Fe 5.02, Au 33.35. IR (nujol, 293 K) ν_{CO}: 1980(vs), 1898(sh), 1875(s) cm^{-1}. IR (CH_2Cl_2, 293 K) ν_{CO}: 1979(m), 1894(s) cm^{-1}. IR (acetone, 293 K) ν_{CO}: 1977(m), 1895(s) cm^{-1}. IR (dmf, 293 K) ν_{CO}: 1975(m), 1890(s) cm^{-1}. ^1H NMR (CD_2Cl_2, 298 K): δ 7.04 (s, 4H, CH_{imid}), 6.96 (s, 8H, CH_{Ar}), 2.35 (s, 12H, CH_3), 2.07 (s, 24H, CH_3). $^{13}C\{^1H\}$ NMR (CD_2Cl_2, 298 K): δ 218.2 (CO), 194.5 (C-Au), 138.7, 135.2, 134.7, 128.9 (C_{Ar}), 121.0 (CH_{imid}), 20.8, 17.7 (CH_3).

Synthesis of $Fe(CO)_4(AuIPr)_2$

Au(IPr)Cl (0.204 g, 0.328 mmol) was added as a solid in small portions to a solution of $[NEt_4][Fe(CO)_4(AuIPr)]$ (0.287 g, 0.325 mmol) in acetone (15 mL) and the reaction monitored by IR spectroscopy. The resulting mixture was stirred for 2 h at room temperature and then, the solvent removed *in vacuo*. The residue was washed with H_2O (3 × 20 mL), isopropanol (3 × 20 mL), and extracted with toluene (15 mL). Crystals of $Fe(CO)_4(AuIPr)_2\cdot 1.5$toluene, suitable for X-ray crystallography were obtained by slow diffusion of *n*-pentane (35 mL) on the toluene solution (yield 0.265 g, 61 % based on Fe, 61 % based on Au). Alternatively, $Fe(CO)_4(AuIPr)_2$ may be obtained from the reaction of $Na_2[Fe(CO)_4]\cdot 2thf$ with two equivalents Au(IPr)Cl in thf.

$C_{58}H_{72}Au_2FeN_4O_4$ (1338.99): calcd. (%): C 52.03, H 5.42, N 4.18, Fe 4.17, Au 29.42; found: C 51.89, H 5.64, N 4.03, Fe 4.38, Au 29.19. IR (nujol, 293 K) ν_{CO}: 1974(vs), 1901(sh), 1890(s) cm^{-1}. IR (CH_2Cl_2, 293 K) ν_{CO}: 1974(m), 1884(s) cm^{-1}. ^1H NMR (CD_2Cl_2, 298 K): δ 7.51, 7.33 (br, 12H, CH_{Ar}), 7.16 (s, 4H, CH_{imid}), 2.69 (br, 8H, $CH(CH_3)_2$), 1.30 (br, 48H, $CH(CH_3)_2$). $^{13}C\{^1H\}$ NMR (CD_2Cl_2, 298 K): δ 216.9 (CO), 194.3 (C-Au), 145.7, 134.8, 129.9, 123.8 (C_{Ar}), 122.3 (CH_{imid}), 28.7 ($CH(CH_3)_2$), 24.0 ($CH(CH_3)_2$).

Thermal decomposition of $Fe(CO)_4(AuIPr)_2$

$Fe(CO)_4(AuIPr)_2$ was very stable in solution even after heating at 130-150 °C in dmso. The reactions were periodically monitored by IR spectroscopy and, even after 12-24 hours, the main ν_{CO} bands present in the spectra were those attributable to the starting $Fe(CO)_4(AuIPr)_2$. Then, a saturated solution of $[NEt_4][BF_4]$ in H_2O (40 mL) was added up to complete precipitation. The resulting solid was recovered by filtration, washed with H_2O (3 × 15 mL), toluene (3 × 15 mL), and extracted with solvent of increasing polarity: CH_2Cl_2 (15 mL), thf (15 mL), acetone (15 mL),

CH_3CN (15 mL), and dmso (15 mL). $Fe(CO)_4(AuIPr)_2$ was the main product recovered independently of the experimental conditions. Nonetheless, several attempts of crystallisation were made by layering suitable solvents on the above mentioned solutions. Beside crystals of $Fe(CO)_4(AuIPr)_2$, these attempts resulted in a few crystals of $[Au(IPr)_2][HFe(CO)_4]$, $[NEt_4]_2[Fe_3S(CO)_9]$, and $[Au_{16}S\{Fe(CO)_4\}_4(IPr)_4][BF_4]_n$·solv. These were likely to arise from partial decomposition of $Fe(CO)_4(AuIPr)_2$, that involved also dmso activation and formation of sulphide ions. The crystals of $[Au(IPr)_2][HFe(CO)_4]$, $[NEt_4]_2[Fe_3S(CO)_9]$, and $[Au_{16}S\{Fe(CO)_4\}_4(IPr)_4][BF_4]_n$·solv were separated from the reaction mixtures and analysed by X-ray crystallography, as well as IR spectroscopy ($[NEt_4]_2[Fe_3S(CO)_9]$, and $[Au_{16}S\{Fe(CO)_4\}_4(IPr)_4][BF_4]_n$·solv) and ^1H, ^{19}F and $^{13}C\{^1H\}$ NMR spectroscopy ($[Au_{16}S\{Fe(CO)_4\}_4(IPr)_4][BF_4]_n$·solv).

$[NEt_4]_2[Fe_3S(CO)_9]$. IR (nujol, 293 K) ν_{CO}: 1999(m), 1820(s), 1892(s), 1865(m) cm^{-1}. IR (CH_3CN, 293 K) ν_{CO}: 1988(m), 1932(s), 1904(m), 1873(w) cm^{-1}.

$[Au_{16}S\{Fe(CO)_4\}_4(IPr)_4][BF_4]_n$·solv. IR (nujol, 293 K) ν_{CO}: 1975(s), 1903(m), 1856(w) cm^{-1}. IR (CH_2Cl_2, 293 K) ν_{CO}: 2039(m), 1974(s), 1883(s), 1863(m) cm^{-1}. IR (thf, 293 K) ν_{CO}: 2037(m), 1975(s), 1899(s), 1885(s), 1867(m) cm^{-1}. IR (acetone, 293 K) ν_{CO}: 2037(m), 1973(s), 1885(s), 1869(m) cm^{-1}. ^1H NMR (CD_3COCD_3, 298 K): δ 7.51 (s, 8H, CH_{imid}), 7.43 (t, $^2J_{HH}$ = 7.7 Hz, 8H, CH_{Ar}), 7.26 (d, $^2J_{HH}$ = 7.7 Hz, 16H, CH_{Ar}), 2.67 (sept, $^2J_{HH}$ = 7.4 Hz, 16H, C*H*$(CH_3)_2$), 1.25(d, $^2J_{HH}$ = 7.4 Hz, 48H, CH(C*H*$_3)_2$), 1.17 (d, $^2J_{HH}$ = 7.4 Hz, 48H, CH(C*H*$_3)_2$). $^{13}C\{^1H\}$ NMR (CD_3COCD_3, 298 K): δ 222.3 (CO), 199.2 (C-Au), 150.6, 140.2, 135.0, 128.9, 128.1 (C_{Ar} and CH_{imid}), 33.7 (*C*H$(CH_3)_2$), 28.9, 28.7 (CH(*C*H$_3)_2$). ^{19}F NMR (CD_3COCD_3, 298 K): δ -151.76, -151.81 ($[BF_4]^-$).

Synthesis of $Fe(CO)_4(AuIMes)(AuIPr)$

Au(IMes)Cl (0.176 g, 0.328 mmol) was added as a solid in small portions to a solution of $[NEt_4][Fe(CO)_4(AuIPr)]$ (0.287 g, 0.325 mmol) in acetone (15 mL) and the reaction monitored by IR spectroscopy. The resulting mixture was stirred for 2 h at room temperature and then, the solvent removed under reduced pressure. The residue was washed with H_2O (3 × 20 mL), isopropanol (3 × 20 mL), and extracted with acetone (15 mL). A microcrystalline powder of $Fe(CO)_4(AuIMes)(AuIPr)$ was obtained after removal of the solvent *in vacuo* (yield 0.208 g, 51 % based on Fe, 51 % based on Au).

$C_{52}H_{60}Au_2FeN_4O_4$ (1254.33): calcd. (%): C 49.75, H 4.82, N 4.47; found: C 49.97, H 5.02, N 4.11. IR (acetone, 293 K) ν_{CO}: 1971(s), 1885(vs), 1864(sh) cm^{-1}. ^1H NMR (CD_3COCD_3, 298 K): δ 7.53,

7.38 (s, 4H, CH_{imid}), 7.41 (t, $^2J_{HH}$ = 7.4 Hz, 2H, CH_{Ar}), 7.23 (d, $^2J_{HH}$ = 7.4 Hz, 4H, CH_{Ar}), 6.96 (s, 4H, CH_{Ar}), 2.70 (m, 4H, C*H*$(CH_3)_2$), 2.31 (s, 6H, CH_3), 2.09 (s, 12H, CH_3), 1.25 (d, $^2J_{HH}$ = 6.5 Hz, 12H, CH(C*H*$_3)_2$), 1.17 (d, $^2J_{HH}$ = 6.5 Hz, 12H, CH(C*H*$_3)_2$). $^{13}C\{^1H\}$ NMR (CD_3COCD_3, 298 K): δ 217.8 (CO), 195.1, 193.7 (C-Au), 145.5, 138.2, 135.5, 135.0, 134.6, 129.7, 128.9, 123.6, 122.7, 121.6 (CH_{Ar}+CH_{imid}), 28.5 (*C*H$(CH_3)_2$), 23.6, 23.4 (CH(*C*$H_3)_2$), 20.4, 17.4 (CH_3).

Thermal decomposition of $Fe(CO)_4$(AuIMes)(AuIPr)

A solution of $Fe(CO)_4$(AuIMes)(AuIPr) (0.450 g, 0.359 mmol) in dmso (15 mL) was heated at 130 °C and the reaction monitored by IR spectroscopy. After 3 h, the IR spectrum showed the typical ν_{CO} absorptions of $[Au_3\{Fe(CO)_4\}_3]^{3-}$ and the reaction was stopped without any further work-up.

Synthesis of $Fe(CO)_4$(AuIMes)($AuPPh_3$)·0.5CH_2Cl_2

Au(PPh_3)Cl (0.161 g, 0.326 mmol) was added as a solid in small portions to a solution of [NEt_4][$Fe(CO)_4$(AuIMes)] (0.260 g, 0.325 mmol) in acetone (15 mL) and the reaction monitored by IR spectroscopy. The resulting mixture was stirred for 5 min at room temperature and then, the solvent removed under reduced pressure. The residue was dissolved with CH_2Cl_2 (15 mL), filtered and crystals of $Fe(CO)_4$(AuIMes)($AuPPh_3$)·0.5CH_2Cl_2 suitable for X-ray crystallography were obtained by slow diffusion of *n*-pentane (35 mL) on the CH_2Cl_2 solution (yield 0.171 g, 45 % based on Fe, 45 % based on Au).

$Fe(CO)_4$(AuIMes)($AuPPh_3$) is less stable than $Fe(CO)_4$(AuIPr)($AuPPh_3$), and rapidly decomposes in acetone solution even at room temperature.

$C_{43.5}H_{40}Au_2ClFeN_2O_4P$ (1170.98): calcd. (%): C 44.61, H 3.45, N 2.39; found: C 44.87, H 3.12, N 2.16. IR (nujol, 293 K) ν_{CO}: 1982(s), 1906(sh), 1896(s), 1873(ms) cm^{-1}. IR (acetone, 293 K) ν_{CO}: 1988(ms), 1912(ms), 1886(s) cm^{-1}. IR (CH_2Cl_2, 293 K) ν_{CO}: 1989(ms), 1893(s) cm^{-1}. ^1H NMR (CD_3COCD_3, 298 K): δ 7.77-7.35 (m, 21H, CH_{Ar}+CH_{imid}+Ph), 2.24 (s, 6H, CH_3), 2.04 (s, 12H, CH_3). $^{13}C\{^1H\}$ NMR (CD_3COCD_3, 298 K): δ 218.4 (CO), 193.3 (C-Au), 138.6-121.8 (CH_{Ar}+CH_{imid}+Ph), 20.3, 17.0 (CH_3). $^{13}C\{^1H\}$ NMR (CD_3COCD_3, 298 K): δ 218.4 (CO), 193.3 (C-Au), 138.6, 134.6, 134.0, 133.9, 131.2. 131.1, 129.1, 129.0, 121.8 (CH_{Ar}+CH_{imid}+Ph), 20.3, 17.0 (CH_3). $^{31}P\{^1H\}$ NMR (CD_3COCD_3, 298 K): δ 40.8.

Synthesis of $Fe(CO)_4(AuIPr)(AuPPh_3)$

$Au(PPh_3)Cl$ (0.161 g, 0.326 mmol) was added as a solid in small portions to a solution of $[NEt_4][Fe(CO)_4(AuIPr)]$ (0.287 g, 0.325 mmol) in acetone (15 mL) and the reaction monitored by IR spectroscopy. The resulting mixture was stirred for 2 h at room temperature and then, the solvent removed under reduced pressure. The residue was washed with H_2O (3 × 20 mL), isopropanol (3 × 20 mL), and extracted with CH_2Cl_2 (15 mL). Crystals of $Fe(CO)_4(AuIPr)(AuPPh_3)$ suitable for X-ray crystallography were obtained by slow diffusion of *n*-pentane (35 mL) on the CH_2Cl_2 solution (yield 0.226 g, 57 % based on Fe, 57 % based on Au).

$C_{49}H_{51}Au_2FeN_2O_4P$ (1212.67): calcd. (%): C 48.51, H 4.24, N 2.32; found: C 48.32, H 3.97, N 2.51. IR (nujol, 293 K) ν_{CO}: 1984(s), 1911(s), 1892(s), 1867(s) cm^{-1}. IR (acetone, 293 K) ν_{CO}: 1989(s), 1914(s), 1882(ms) cm^{-1}. IR (CH_2Cl_2, 293 K) ν_{CO}: 1990(s), 1913(s), 1878(ms) cm^{-1}. ^1H NMR (CD_3COCD_3, 298 K): δ 7.74-7.14 (m, 23H, CH_{Ar}+CH_{imid}+Ph), 2.70 (m, 4H, C*H*$(CH_3)_2$), 1.28 (d, $^2J_{HH}$ = 6.8 Hz, 12H, CH(C*H*$_3)_2$), 1.15 (d, $^2J_{HH}$ = 6.8 Hz, 12H, CH(C*H*$_3)_2$). $^{13}C\{^1H\}$ NMR (CD_3COCD_3, 298 K): δ 217.9 (CO), 194.7 (C-Au), 145.5, 134.2, 134.1, 131.1, 129.9, 129.1, 129.0, 123.7, 123.0 (CH_{Ar}+CH_{imid}+Ph), 28.9 (*C*H$(CH_3)_2$), 23.6, 23.5 (CH(*C*H$_3)_2$). $^{31}P\{^1H\}$ NMR (CD_3COCD_3, 298 K): δ 40.8.

Thermal decomposition of $Fe(CO)_4(AuIPr)(AuPPh_3)$

A solution of $Fe(CO)_4(AuIPr)(AuPPh_3)$ (0.450 g, 0.371 mmol) in dmso (15 mL) was heated at 130 °C and the reaction monitored by IR spectroscopy. After 5 h, the IR spectrum showed the typical ν_{CO} absorptions of the starting compound $Fe(CO)_4(AuIPr)(AuPPh_3)$. The temperature was increased up to 150 °C without any clear evidence of decomposition.

Synthesis of $[Au(IMes)_2][Au_3\{Fe(CO)_4\}_2(PPh_3)_2]\cdot 0.67CH_2Cl_2$

A solution of $Fe(CO)_4(AuIMes)(AuPPh_3)$ (0.220 g, 0.188 mmol) in CH_3CN (15 mL) was heated at 80 °C for 3 h and the reaction monitored by IR spectroscopy. Then, a saturated solution of $[NEt_4]Br$ in H_2O (40 mL) was added up to complete precipitation. The resulting solid was recovered by filtration, washed with H_2O (3 × 15 mL), toluene (3 × 15 mL), and extracted with CH_2Cl_2 (15 mL). Crystals of $[Au(IMes)_2][Au_3\{Fe(CO)_4\}_2(PPh_3)_2]\cdot 0.67CH_2Cl_2$ suitable for X-ray crystallography were obtained by slow diffusion of *n*-pentane (35 mL) on the CH_2Cl_2 solution (yield 0.110 g, 51 % based on Fe, 51 % based on Au).

$C_{86.67}H_{79.33}Au_4Cl_{1.33}Fe_2N_4O_8P_2$ (2313.64): calcd. (%): C 44.98, H 3.46, N 2.42; found: C 45.12, H 3.71, N 2.14. IR (nujol, 293 K) ν_{CO}: 1977(w), 1953(s), 1887(s), 1864(sh), 1843(sh) cm^{-1}. IR (CH_3CN, 293 K) ν_{CO}: 1989(w), 1965(m), 1891(s) cm^{-1}. IR (acetone, 293 K) ν_{CO}: 1988(w), 1963(m), 1891(s) cm^{-1}. ^1H NMR (CD_3COCD_3, 298 K): δ7.85−6.98 (m, 42 H, CH_{Ar}+CH_{imid}+Ph), 2.46 (s, 12H, CH_3), 1.76 (s, 24H, CH_3). $^{13}C\{^1H\}$ NMR (CD_3COCD_3, 298 K): δ 220.8 (CO), 185.1 (C-Au), 139.3, 134.6, 134.4, 134.2, 130.6, 129.0, 128.9, 128.8, 123.3 (CH_{Ar}+CH_{imid}+Ph), 20.3, 16.4 ppm (CH_3). $^{31}P\{^1H\}$ NMR (CD_3COCD_3, 298 K): δ 38.5 ppm.

Synthesis of $[Fe_2(CO)_8(AuNHC)]^-$ (NHC = IMes; IPr)

A solution of $[NEt_4][Fe(CO)_4(AuIPr)]$ (0.530 g, 0.600 mmol) in CH_2Cl_2 (20 mL) was heated at 40 °C for 4 h and the reaction monitored by IR spectroscopy. Then, the solvent was removed under reduced pressure and the residue washed with H_2O (3 × 15 mL) and extracted with toluene (10 mL). Crystals of $[NEt_4][Fe_2(CO)_8(AuIPr)]$·1.5toluene suitable for X-ray crystallography were obtained by slow diffusion of *n*-pentane (25 mL) on the toluene solution (yield 0.207 g, 58 % based on Fe, 29 % based on Au).

A few crystals of $[NEt_4][Fe_3(CO)_{10}(CCH_3)]^-$ were isolated as side products of the thermal decomposition of $[NEt_4][Fe(CO)_4(AuIPr)]$ in CH_2Cl_2, and their nature completely unrevealed by means of X-ray crystallography.

$[NEt_4][Fe_2(CO)_8(AuIPr)]$·1.5toluene - $C_{53.5}H_{68}AuFe_2N_3O_8$ (1189.77): calcd. (%): C 59.98, H 5.76, N 3.53; found: C 60.12, H 5.38, N 3.21. IR (nujol, 293 K) ν_{CO}: 2004(w), 1956(s), 1923(ms), 1895(vs), 1880(sh) cm^{-1}. IR (dmso, 293 K) ν_{CO}: 2004(w), 1958(s), 1913(sh), 1900(vs), 1728(ms) cm^{-1}. IR (CH_3CN, 293 K) ν_{CO}: 2006(w), 1960(s), 1903(vs), 1727(ms) cm^{-1}. IR (acetone, 293 K) ν_{CO}: 2004(w), 1958(s), 1912(sh), 1902(vs) cm^{-1}. IR (toluene, 293 K) ν_{CO}: 2005(w), 1963(s), 1900(vs), 1721(m) cm^{-1}. IR (CH_2Cl_2, 293 K) ν_{CO}: 2007(w), 1961(s), 1905(vs), 1715(ms) cm^{-1}. IR (thf, 293 K) ν_{CO}: 2002(w), 1959(s), 1904(vs), 1720(m) cm^{-1}. ^1H NMR (CD_3COCD_3, 298 K): δ 7.50-7.24 (m, 8H, CH_{Ar} +CH_{imid}), 3.44 (q, $^2J_{HH}$ = 6.2 Hz, 8H, NCH_2CH_3), 2.95 (sept, $^2J_{HH}$ = 6.8 Hz, 4H, $CH(CH_3)_2$), 1.36 (d, $^2J_{HH}$ = 6.8 Hz, 12H, $CH(CH_3)_2$), 1.35 (t, $^2J_{HH}$ = 6.2 Hz, 12H, NCH_2CH_3), 1.15 (d, $^2J_{HH}$ = 6.8 Hz, 12H, $CH(CH_3)_2$). $^{13}C\{^1H\}$ NMR (CD_3COCD_3, 298 K): δ 231.5 (CO), 200.4 (C-Au), 145.4, 135.9, 129.4, 123.7, 123.3 (C_{Ar} and CH_{imid}), 51.9 (NCH_2CH_3), 28.2 ($CH(CH_3)_2$), 23.9, 23.3 ($CH(CH_3)_2$), 6.7 (NCH_2CH_3).

The thermal decomposition of $[NEt_4][Fe(CO)_4(AuIMes)]$ under the same experimental conditions described above afforded $[Fe_2(CO)_8(AuIMes)]^-$. IR (CH_2Cl_2, 293 K) ν_{CO}: 2000(w), 1959(s), 1899(vs), 1712(ms) cm^{-1}.

Synthesis of $[NMe_4]_2[Au(IMes)_2][Au_3\{Fe(CO)_4\}_3]$

A solution of $Fe(CO)_4(AuIMes)_2$ (0.450 g, 0.384 mmol) in dmso (15 mL) was heated at 130 °C for 0.5 h and the reaction monitored by IR spectroscopy. Then, a saturated solution of $[NMe_4]Cl$ in H_2O (40 mL) was added up to complete precipitation. The resulting solid was recovered by filtration, washed with H_2O (3 × 15 mL), toluene (3 × 15 mL), and extracted with acetone (15 mL). Crystals of $[NMe_4]_2[Au(IMes)_2][Au_3\{Fe(CO)_4\}_3]$ suitable for X-ray crystallography were obtained by slow diffusion of *n*-hexane (35 mL) on the acetone solution (yield 0.14 g, 52 % based on Fe, 36 % based on Au).

$[NMe_4]_2[Au(IMes)_2][Au_3\{Fe(CO)_4\}_3]\cdot CH_3COCH_3$ was obtained following a similar procedure and employing $[NEt_4]Br$ instead of $[NMe_4]Cl$.

$[NMe_4]_2[Au(IMes)_2][Au_3\{Fe(CO)_4\}_3]$ - $C_{62}H_{72}Au_4Fe_3N_6O_{12}$ (2048.67): calcd. (%): C 36.32, H 3.54, N 4.10; found: C 36.14, H 3.71, N 3.89. IR (nujol, 293 K) ν_{CO}: 1970(m), 1932(s), 1843(s) cm^{-1}. IR (dmso, 293 K) ν_{CO}: 1974(w), 1930(s), 1879(s) cm^{-1}. IR (CH_2Cl_2, 293 K) ν_{CO}: 1975(w), 1929(s), 1877(s) cm^{-1}. IR (CH_3CN, 293 K) ν_{CO}: 1929(s), 1867(s) cm^{-1}. IR (acetone, 293 K) ν_{CO}: 1969(w), 1928(s), 1864(s) cm^{-1}. ^1H NMR (CD_3CN, 298 K): δ 7.25 (s, 4H, CH_{imid}), 6.98 (s, 8H, CH_{Ar}), 3.17 (s, 24H, NMe_4), 2.45 (s, 12H, CH_3), 1.72 (s, 24H, CH_3). $^{13}C\{^1H\}$ NMR (CD_2Cl_2, 298 K): δ 224.4 (CO), 185.3 (C-Au), 139.7, 135.0, 134.6, 129.2 (C_{Ar}), 123.4 (CH_{imid}), 55.6 ($^1J_{CN}$ = 3.9 Hz, NMe_4), 20.6, 16.7 (CH_3).

Synthesis of $[NBu_4][Au_3Fe_2(CO)_8(IMes)_2]\cdot CH_3COCH_3$

A large excess of $[NBu_4][BF_4]$ was added as a solid to a solution of $Fe(CO)_4(AuIMes)_2$ (0.190 g, 0.531 mmol) in dmf (20 mL), and the mixture stirred at 100 °C for 1 h. Then, the orange solution was cooled down to room temperature and H_2O (60 mL) was added until complete precipitation occurred. The solid was recovered by filtration, washed with H_2O (40 mL) and extracted in acetone (10 mL). Needle-like pale yellow crystals of $[NBu_4][Au_3Fe_2(CO)_8(IMes)_2]\cdot CH_3COCH_3$ suitable for X-ray analyses were obtained by slow diffusion of *n*-hexane (30 mL) on the acetone solution (yield 122 g, 25 % based on Fe).

$C_{69}H_{90}Au_3Fe_2N_5O_9$ (1836.06): calcd. (%): C 45.11, H 4.94, N 3.81, Fe 6.09, Au 32.19; found: C 45.41, H 5.12, N 3.62, Fe 6.31, Au 31.85. IR (nujol, 293 K) ν_{CO}: 1948(vs), 1877(sh), 1867(s), 1836(sh), 1712(m) cm^{-1}. IR (acetone, 293 K) ν_{CO}: 1968(sh), 1947(m), 1924(m), 1872(s) cm^{-1}. ^1H NMR (CD_2Cl_2, 298 K): δ 7.12 (s, 8H, CH_{imid}), 6.94 (s, 16H, CH_{Ar}), 3.20 (br, 8H, $NC\mathit{H}_2CH_2CH_2CH_3$), 2.47 (s, 24H, CH_3), 1.74 (s, 48H, CH_3), 1.65 (br, 8H, $NCH_2\mathit{CH}_2CH_2CH_3$), 1.47 (br, 8H, $NCH_2CH_2\mathit{CH}_2CH_3$), 1.01 (br, 12H, $NCH_2CH_2CH_2\mathit{CH}_3$). $^{13}C\{^1H\}$ NMR (CD_2Cl_2, 298 K): δ 220.9 (CO), 185.3 (C-Au), 139.4, 134.6, 134.1, 129.0 (C_{Ar}), 122.8 (CH_{imid}), 58.6 ($NC\mathit{H}_2CH_2CH_2CH_3$), 23.7 ($NCH_2\mathit{C}H_2CH_2CH_3$), 19.6 ($NCH_2CH_2\mathit{C}H_2CH_3$), 20.9, 16.9 ($CH_3$), 13.3 ($NCH_2CH_2CH_2\mathit{C}H_3$).

CHAPTER 3

Synthesis of Na[Fe(CO)$_4$(CuIMes)]

$Na_2[Fe(CO)_4]\cdot 2thf$ (0.320 g, 0.894 mmol) and Cu(IMes)Cl (0.360 g, 0.892 mmol) were charged in a Schlenk tube under a nitrogen atmosphere and dmso (10 mL) was added. The mixture was stirred for 2 h at room temperature and then, the crude product was characterised through IR, ^{1}H and $^{13}C\{^1H\}$ NMR spectroscopies (a few drops of d^6-dmso were added as reference for the NMR characterisation). All attempts to isolate $[Fe(CO)_4(CuIMes)]^-$ in the solid state as $[NEt_4]^+$ salt after addition of a saturated solution of $[NEt_4]Br$ in H_2O failed. Thus, yields were not been determined.

IR (dmso, 293 K) ν_{CO}: 1909(s), 1800(vs) cm^{-1}. ^{1}H NMR (dmso with 5% d^6-dmso, 298 K): δ 7.38 (s,2H, CH_{imid}), 6.97 (s, 4H, CH_{Ar}), (aliphatic protons were hidden by the dmso resonance). $^{13}C\{^1H\}$ NMR (dmso with 5% d^6-dmso, 298 K): δ225.9 (CO), 179.3 (C-Cu), 137.7, 135.8, 134.5, 128.7, 121.9 (C_{Ar} and CH_{imid}), 20.7, 17.4 (CH_3).

Synthesis of [NEt$_4$][Fe(CO)$_4$(CuIPr)]

$Na_2[Fe(CO)_4]\cdot 2thf$ (0.220 g, 0.614 mmol) and Cu(IPr)Cl (0.430 g, 0.882 mmol) were charged in a Schlenk tube under a nitrogen atmosphere and dmso (15 mL) was added. The mixture was stirred for 2 h at room temperature and then, a saturated solution of $[NEt_4]Br$ in H_2O (40 mL) was added up to complete precipitation. The resulting solid was recovered by filtration, washed with H_2O (3 × 15 mL), and extracted with toluene (20 mL). Crystals of $[NEt_4][Fe(CO)_4(CuIPr)]$ suitable for X-ray crystallography were obtained by slow diffusion of *n*-pentane (40 mL) on the toluene solution at -20 °C (yield 0.207 g, 45 % based on Fe, 31 % based on Cu). $[Fe(CO)_4(CuIPr)]^-$ resulted to be rather unstable in solution. Therefore, the NMR characterisation was carried out on the crude reaction mixture in dmso as Na^+ salt after the addition of a few drops of d^6-dmso.

$C_{39}H_{54}CuFeN_3O_4$ (748.24): calcd. (%): C 62.63, H 7.29, N 5.62; found: C 62.89, H 6.94, N 5.39. IR (nujol, 293 K) ν_{CO}: 1913(s), 1801(vs) cm^{-1}. IR (dmso, 293 K) ν_{CO}: 1911(ms), 1800(vs) cm^{-1}. IR (toluene, 293 K) ν_{CO}: 1913(s), 1807(vs) cm^{-1}. ^{1}H NMR (dmso with 5% d^6-dmso, 298 K): δ 7.51, 7.34, 7.23 (br, 8H, CH_{Ar} and CH_{imid}), (the resonance due to $CH(CH_3)_2$ was hidden by the dmso

resonance), 1.17, 1.12 (br, 24H, CH(C*H*$_3$)$_2$). ^{13}C{^{1}H} NMR (dmso with 5% d^6-dmso, 298 K): δ 226.1 (CO), 181.8 (C-Cu), 145.5, 135.9, 129.7, 123.8, 123.4 (C$_{Ar}$ and CH$_{imid}$), 28.6 (*C*H(CH$_3$)$_2$), 24.5, 24.0 (CH(*C*H$_3$)$_2$).

Synthesis of Na[Fe(CO)$_4$(AgIMes)]

Na$_2$[Fe(CO)$_4$]·2thf (0.330 g, 0.922 mmol) and Ag(IMes)Cl (0.550 g, 1.23 mmol) were charged in a Schlenk tube under a nitrogen atmosphere and dmso (10 mL) was added. The mixture was stirred for 2 h at room temperature and then, the crude product was characterised through IR, ^{1}H and ^{13}C{^{1}H} NMR spectroscopies (a few drops of d^6-dmso were added as reference for the NMR characterisation). All attempts to isolate [Fe(CO)$_4$(AgIMes)]$^-$ in the solid state as [NEt$_4$]$^+$ salt after addition of a saturated solution of [NEt$_4$]Br in H$_2$O failed. Thus, yields were not been determined. Among the decomposition products formed during the attempts to isolate [Fe(CO)$_4$(AgIMes)]$^-$, crystals suitable for X-ray crystallography of [NEt$_4$]$_2$[Ag(IMes)$_2$][Ag$_3$Fe$_3$(CO)$_{12}$]·solv,[32] [NEt$_4$]$_2$[HIMes][Ag$_4$Fe$_4$(CO)$_{16}$], [NEt$_4$]$_4$[Ag$_4$Fe$_4$(CO)$_{16}$]·2CH$_3$CN and [NEt$_4$]$_3$[Ag$_5$Fe$_4$(CO)$_{16}$] were obtained.

IR (dmso, 293 K) ν$_{CO}$: 1910(s), 1796(vs) cm^{-1}. ^{1}H NMR (dmso with 5% d^6-dmso, 298 K): δ7.56 (s, 2H, CH$_{imid}$), 7.01 (s, 4H, CH$_{Ar}$), (aliphatic protons were hidden by the dmso resonance). ^{13}C{^{1}H} NMR (dmso with 5% d^6-dmso, 298 K): δ227.0 (CO), (C-Ag too weak to be detected), 138.3, 136.3, 134.8, 129.3, 123.0 (C$_{Ar}$ and CH$_{imid}$), 21.1, 17.8 (CH$_3$).

Synthesis of Na[Fe(CO)$_4$(AgIPr)]

Na$_2$[Fe(CO)$_4$]·2thf (0.336 g, 0.934 mmol) and Ag(IPr)Cl (0.645 g, 1.21 mmol) were charged in a Schlenk tube under a nitrogen atmosphere and dmso (10 mL) was added. The mixture was stirred for 2 h at room temperature and then, the crude product was characterised through IR, ^{1}H and ^{13}C{^{1}H} NMR spectroscopies (a few drops of d^6-dmso were added as reference for the NMR characterisation). All attempts to isolate [Fe(CO)$_4$(AgIPr)]$^-$ in the solid state as [NEt$_4$]$^+$ salt after addition of a saturated solution of [NEt$_4$]Br in H$_2$O failed. Thus, yields were not been determined. Among the decomposition products formed during the attempts to isolate [Fe(CO)$_4$(AgIPr)]$^-$, crystals suitable for X-ray crystallography of [Ag(IPr)$_2$][Fe$_2$(CO)$_8$(AgIPr)]·CH$_2$Cl$_2$,* [NEt$_4$]$_2$[HIPr][Fe$_2$(CO)$_8$(AgIPr)]$_2$[Cl]·2CH$_2$Cl$_2$ and [NEt$_4$]$_4$[Ag$_4$Fe$_4$(CO)$_{16}$] were obtained.

IR (dmso, 293 K) ν$_{CO}$: 1910(s), 1797(vs) cm^{-1}. ^{1}H NMR (dmso with 5% d^6-dmso, 298 K): δ7.69, 7.42, 7.28 (br,8H, CH$_{Ar}$ and CH$_{imid}$), (the resonance due to CH(C*H*$_3$)$_2$ was hidden by the dmso

resonance), 1.22, 1.16 (br, 24H, CH(C*H*$_3$)$_2$). ^{13}C{^{1}H} NMR (dmso with 5% d^6-dmso, 298 K): δ226.8 (CO), 190.0 (br, C-Ag), 145.6, 142.4, 135.8, 129.9, 124.0 (C$_{Ar}$ and CH$_{imid}$), 28.6 (*C*H(CH$_3$)$_2$), 24.3, 24.2 (CH(*C*H$_3$)$_2$).

* [Ag(IPr)$_2$][Fe$_2$(CO)$_8$(AgIPr)]·CH$_2$Cl$_2$: IR (nujol, 293 K) ν$_{CO}$: 1944(s), 1901(ms), 1884(s), 1725(ms) cm^{-1}. IR (CH$_2$Cl$_2$, 293 K) ν$_{CO}$: 1952(s), 1869(s), 1851(ms), 1833(ms) cm^{-1}.

Synthesis of Fe(CO)$_4$(CuIMes)$_2$

Na$_2$[Fe(CO)$_4$]·2thf (0.210 g, 0.587 mmol) and Cu(IMes)Cl (0.469 g, 1.180 mmol) were charged in a Schlenk tube under a nitrogen atmosphere and thf (20 mL) was added. The mixture was stirred for 5 h at room temperature and then filtered off. The solution was layered with *n*-hexane to give yellow crystals of Fe(CO)$_4$(CuIMes)$_2$ (yield 0.22 g, 42 % based on Fe, 41 % based on Cu).

C$_{46}$H$_{48}$Cu$_2$FeN$_4$O$_4$ (903.81): calcd. (%): C 61.19, H 5.36, N 6.21; found: C 60.98, H 5.49, N 6.42. IR (nujol, 293 K) ν$_{CO}$: 1958(s), 1873(m), 1856(s), 1833(m) cm^{-1}. IR (thf, 293 K) ν$_{CO}$: 1950(m), 1872(s), 1850(m) cm^{-1}. IR (acetone, 293 K) ν$_{CO}$: 1950(m), 1859(vs) cm^{-1}. ^{1}H NMR (CD$_3$COCD$_3$, 298 K): δ 7.44 (s, 4H, CH$_{imid}$), 7.04 (s, 8H, CH$_{Ar}$), 2.45 (s, 12H, CH$_3$), 1.74 (s, 24H, CH$_3$). ^{13}C{^{1}H} NMR (CD$_3$COCD$_3$, 298 K): δ217.8 (CO), 177.3 (C-Cu), 139.2, 134.8, 134.5, 129.0, 123.1 (C$_{Ar}$ and CH$_{imid}$), 20.3, 16.3 (CH$_3$).

Synthesis of Fe(CO)$_4$(CuIPr)$_2$·2thf

Na$_2$[Fe(CO)$_4$]·2thf (0.270 g, 0.754 mmol) and Cu(IPr)Cl (0.920 g, 1.89 mmol) were charged in a Schlenk tube under a nitrogen atmosphere and thf (20 mL) was added. The mixture was stirred for 5 h at room temperature and then filtered off. The solution was layered with *n*-hexane to give yellow crystals of Fe(CO)$_4$(CuIPr)$_2$·2thf (yield 0.52 g, 56 % based on Fe, 45 % based on Cu).

C$_{66}$H$_{88}$Cu$_2$FeN$_4$O$_6$ (1216.33): calcd. (%): C 65.21, H 7.30, N 4.61; found: C 64.89, H 7.03, N 4.93. IR (nujol, 293 K) ν$_{CO}$: 1953(s), 1875(m), 1838(s), 1821(vs) cm^{-1}. IR (thf, 293 K) ν$_{CO}$: 1951(s), 1872(s), 1851(vs) cm^{-1}. IR (acetone, 293 K) ν$_{CO}$: 1950(m), 1849(vs) cm^{-1}. IR (CH$_2$Cl$_2$, 293 K) ν$_{CO}$: 1951(s), 1848(vs) cm^{-1}. ^{1}H NMR (CD$_3$COCD$_3$, 298 K): δ7.49 (t, ^{2}J$_{HH}$ = 7.6 Hz, 4H, CH$_{Ar}$), 7.30 (d, ^{2}J$_{HH}$ = 7.4 Hz, 8H, CH$_{Ar}$), 7.12 (s, 4H, CH$_{imid}$),2.67 (br, 8H, C*H*(CH$_3$)$_2$), 1.24 (br, 48H, CH(C*H*$_3$)$_2$). ^{13}C{^{1}H} NMR (CD$_3$COCD$_3$, 298 K): δ215.7 (CO), 181.5 (C-Cu), 145.6, 135.1, 129.8, 123.7, 122.6 (C$_{Ar}$ and CH$_{imid}$), 28.6 (*C*H(CH$_3$)$_2$), 24.1, 23.9 (CH(*C*H$_3$)$_2$).

Synthesis of $Fe(CO)_4(AgIMes)_2$

$Na_2[Fe(CO)_4]\cdot 2thf$ (0.210 g, 0.587 mmol) and Ag(IMes)Cl (0.522 g, 1.180 mmol) were charged in a Schlenk tube under a nitrogen atmosphere and thf (20 mL) was added. The mixture was stirred for 5 h at room temperature and then filtered off. The solution was layered with *n*-hexane to give colourless crystals of $Fe(CO)_4(AgIMes)_2$ (yield 0.21 g, 36 % based on Fe, 36 % based on Ag).

$C_{46}H_{48}Ag_2FeN_4O_4$ (992.47): calcd. (%): C 55.75, H 4.89, N 5.66; found: C 55.92, H 4.74, N 5.48. IR (nujol, 293 K) ν_{CO}: 1958(s), 1874(m), 1860(s), 1841(m) cm^{-1}. IR (CH_2Cl_2, 293 K) ν_{CO}: 1948(m), 1878(s) cm^{-1}. IR (acetone, 293 K) ν_{CO}: 1943(m), 1878(s) cm^{-1}. ^1H NMR (CD_2Cl_2, 298 K): δ 7.70 (s, 4H, CH_{imid}), 7.10 (s, 8H, CH_{Ar}), 2.38 (s, 12H, CH_3), 2.15 (s, 24H, CH_3). $^{13}C\{^1H\}$ NMR (CD_2Cl_2, 298 K): δ 219.3 (CO), 182.6 (C-Ag, $^1J_{C\text{-}Ag}$ = 209 and 180 Hz), 141.7, 134.5, 134.2, 129.8, 129.1 (C_{Ar} and CH_{imid}), 20.9, 17.2 (CH_3).

Synthesis of $Fe(CO)_4(AgIPr)_2$

$Na_2[Fe(CO)_4]\cdot 2thf$ (0.380 g, 1.06 mmol) and Ag(IPr)Cl (1.45 g, 2.73 mmol) were charged in a Schlenk tube under a nitrogen atmosphere and thf (15 mL) was added. The mixture was stirred for 5 h at room temperature and then the solvent was removed under reduced pressure. The residue was washed with H_2O (3 × 20 mL) and extracted with CH_2Cl_2 (10 mL). A microcrystalline powder of $Fe(CO)_4(AgIPr)_2$ was obtained by addition of *n*-pentane (40 mL) to the CH_2Cl_2 solution (yield 0.503 g, 41 % based on Fe, 32 % based on Ag).

$C_{58}H_{72}Ag_2FeN_4O_4$ (1158.30): calcd. (%): C 60.09, H 6.26, N 4.84; found: C 59.86, H 6.42, N 5.01. IR (CH_2Cl_2, 293 K) ν_{CO}: 1951(s), 1870(vs), 1952(sh), 1832(sh) cm^{-1}. ^1H NMR (CD_2Cl_2, 298 K): δ 7.44 (br, 4H, CH_{Ar}), 7.25 (br 8H, CH_{Ar}), 7.14 (s, CH_{imid}), 2.53 (br, 8H, C*H*(CH_3)$_2$), 1.17 (br, 48H, CH(C*H*$_3$)$_2$). $^{13}C\{^1H\}$ NMR (CD_2Cl_2, 298 K): δ 217.6 (CO), 189.2 (C-Ag, $^1J_{C\text{-}Ag}$ = 204 and 182 Hz), 145.6, 135.0, 129.9, 123.8, 122.8 (C_{Ar} and CH_{imid}), 28.6 (*C*H(CH_3)$_2$), 24.2, 23.7 (CH(*C*H$_3$)$_2$).

Synthesis of $[NEt_4]_2[Cu(IMes)_2][Cu_3Fe_3(CO)_{12}]$

A solution of $Fe(CO)_4(CuIMes)_2$ (0.381 g, 0.384 mmol) in dmso (15 mL) was heated at 130 °C for 0.5 h and the reaction monitored by IR spectroscopy. Then, a saturated solution of $[NEt_4]Br$ in H_2O (40 mL) was added up to complete precipitation. The resulting solid was recovered by filtration, washed with H_2O (3 × 15 mL), toluene (3 × 15 mL), and extracted with acetone (15 mL). Crystals of $[NEt_4]_2[Cu(IMes)_2][Cu_3Fe_3(CO)_{12}]$ suitable for X-ray crystallography were obtained by slow

diffusion of *n*-hexane (35 mL) on the acetone solution (yield 0.11 g, 54 % based on Fe, 35 % based on Cu).

$C_{70}H_{88}Cu_4Fe_3N_6O_{12}$ (1627.17): calcd. (%): C 51.72, H 5.46, N 5.17; found: C 51.95, H 5.61, N 4.95. IR (nujol, 293 K) ν_{CO}: 1930(s), 1846(s), 1825(m), 1807(w) cm^{-1}. IR (CH_2Cl_2, 293 K) ν_{CO}: 1927(s), 1845(s) cm^{-1}. IR (CH_3CN, 293 K) ν_{CO}: 1927(s), 1852(s) cm^{-1}. IR (acetone, 293 K) ν_{CO}: 1924(s), 1853(s) cm^{-1}. ^1H NMR (CD_3COCD_3, 298 K): δ 7.46 (s, 4H, CH_{imid}), 7.04 (s, 8H, CH_{Ar}), 3.47 (d, $^2J_{HH}$= 5.5 Hz, 16H, N*C*$H_2$$CH_3$), 2.45 (s, 12H, CH_3), 1.74 (s, 24H, CH_3), 1.37 (t, $^2J_{HH}$ = 5.5 Hz, 24H, NCH_2*C*H_3). $^{13}C\{^1H\}$ NMR (CD_3COCD_3, 298 K): δ 222.8 (CO), 177.4 (C-Cu), 139.3, 134.9, 134.5, 129.0, 123.1 (C_{Ar} and CH_{imid}), 52.2 (N*C*$H_2$$CH_3$), 20.3, 16.4 ($CH_3$), 6.9 ($NCH_2$*C*$H_3$).

Synthesis of $[NEt_4]_2[Ag(IMes)_2][Ag_3Fe_3(CO)_{12}]$·solv

A solution of $Fe(CO)_4(AgIMes)_2$ (0.381 g, 0.384 mmol) in dmso (15 mL) was heated at 130 °C for 0.5 h and the reaction monitored by IR spectroscopy. Then, a saturated solution of $[NEt_4]Br$ in H_2O (40 mL) was added up to complete precipitation. The resulting solid was recovered by filtration, washed with H_2O (3 × 15 mL), toluene (3 × 15 mL), and extracted with acetone (15 mL). Crystals of $[NEt_4]_2[Ag(IMes)_2][Ag_3Fe_3(CO)_{12}]$·solv suitable for X-ray crystallography were obtained by slow diffusion of *n*-hexane (35 mL) on the acetone solution (yield 0.11 g, 46 % based on Fe, 31 % based on Ag). Even though the co-crystallised solvent molecule was not refined in the crystal structure (see below), an acetone molecule was included in the calculation of the yields and elemental analyses, in view of the fact that the crystals of $[NEt_4]_2[Ag(IMes)_2][Ag_3Fe_3(CO)_{12}]$·solv are isomorphous with $[NEt_4]_2[Au(IMes)_2][Au_3Fe_3(CO)_{12}]\cdot CH_3COCH_3$.

$C_{73}H_{94}Ag_4Fe_3N_6O_{13}$ (1858.11): calcd. (%): C 36.32, H 3.54, N 4.10; found: C 36.14, H 3.71, N 3.89. IR (nujol, 293 K) ν_{CO}: 1915(s), 1843(sh), 1808(s), 1789(w) cm^{-1}. IR (dmso, 293 K) ν_{CO}: 1917(s), 1832(s) cm^{-1}. IR (CH_2Cl_2, 293 K) ν_{CO}: 1921(s), 1838(s) cm^{-1}. IR (CH_3CN, 293 K) ν_{CO}: 1920(s), 1842(s) cm^{-1}. IR (acetone, 293 K) ν_{CO}: 1917(s), 1840(s) cm^{-1}. ^1H NMR (CD_3COCD_3, 298 K): δ 7.54 (s, 4H, CH_{imid}), 7.04 (s, 8H, CH_{Ar}), 3.46 (q, $^2J_{HH}$ = 7.0 Hz, 16H, N*C*$H_2$$CH_3$), 2.46 (s, 12H, CH_3), 1.78 (s, 24H, CH_3), 1.39 (t, $^2J_{HH}$ = 7.2 Hz, 12H, NCH_2*C*H_3). $^{13}C\{^1H\}$ NMR (CD_3COCD_3, 298 K): 223.6 (CO), 183.4 (C-Ag, $^1J_{C\text{-}Ag}$ = 196 and 170 Hz), 139.2, 135.2, 134.5, 129.0, 123.3 (C_{Ar} and CH_{imid}), 52.1 (N*C*$H_2$$CH_3$), 20.3, 16.4 ($CH_3$), 6.8 ($NCH_2$*C*$H_3$).

Synthesis of $[NEt_4]_2[Cu(IMes)_2][Ag_3Fe_3(CO)_{12}]\cdot CH_3COCH_3$

$Na_2[Fe(CO)_4]\cdot 2thf$ (0.330 g, 0.920 mmol) and Ag(IMes)Cl (0.550 g, 1.23 mmol) were charged in a Schlenk tube under a nitrogen atmosphere and dmso (10 mL) was added. The mixture was stirred for 2 h at room temperature up to the disappearance of the ν_{CO} peak at 1740 cm^{-1} in the IR spectrum due to $Na_2[Fe(CO)_4]\cdot 2thf$. Then, Cu(IMes)Cl (0.370 g, 0.921 mmol) was added as a solid in small portions. The crude product was precipitated by the slow addition of a saturated solution of $[NEt_4]Br$ in H_2O (40 mL) to the dmso solution. The solid was recovered after filtration, washed with H_2O (3 × 20 mL), and extracted with acetone (10 mL). Crystals of $[NEt_4]_2[Cu(IMes)_2][Ag_3Fe_3(CO)_{12}]\cdot CH_3COCH_3$ suitable for X-ray crystallography were obtained by slow diffusion of *n*-hexane (35 mL) on the acetone solution (yield 0.29 g, 52 % based on Fe, 39 % based on Ag, 17 % based on Cu).

Crystals of $[NEt_2]_2[Cu(IMes)_2][Ag_3Fe_3(CO)_{12}]\cdot CH_3COCH_3$ were obtained following a similar procedure using CH_3CN/*n*-hexane/di-isopropyl-ether for crystallisation instead of acetone/*n*-hexane.

$C_{73}H_{94}Ag_3CuFe_3N_6O_{13}$ (1818.24): calcd. (%): C 48.29, H 5.22, N 4.63; found: C 48.44, H 5.39, N 4.29. IR (nujol, 293 K) ν_{CO}: 1957(w), 1930(s), 1859(m), 1845(m), 1826(s) cm^{-1}. IR (CH_2Cl_2, 293 K) ν_{CO}: 1927(s), 1848(vs) cm^{-1}. IR (CH_3CN, 293 K) ν_{CO}: 1927(s), 1849(vs) cm^{-1}. IR (acetone, 293 K) ν_{CO}: 1923(s), 1849(vs) cm^{-1}.

Synthesis of $[NEt_4]_2[Au(IMes)_2][Ag_3Fe_3(CO)_{12}]\cdot dmf$

$Na_2[Fe(CO)_4]\cdot 2thf$ (0.390 g, 1.09 mmol) and Au(IMes)Cl (0.790 g, 1.47 mmol) were charged in a Schlenk tube under a nitrogen atmosphere and dmso (10 mL) was added. The mixture was stirred for 2 h at room temperature up to the disappearance of the ν_{CO} peak at 1740 cm^{-1} in the IR spectrum due to $Na_2[Fe(CO)_4]\cdot 2thf$. Then, a saturated solution of $[NEt_4]Br$ in H_2O was added up to complete precipitation of the reaction mixture. The solid was recovered by filtration and washed with H_2O (3 × 20 mL) and toluene (3 × 20 mL), and $[NEt_4][Fe(CO)_4(AuIMes)]$ extracted with acetone (20 mL). Then, Ag(IMes)Cl (0.550 g, 1.23 mmol) was added as a solid in small portions to the acetone solution. A solid was formed, recovered by filtration, and dissolved in dmso (10 mL). The resulting solution was heated at 80 °C for 0.5 h, and the crude reaction mixture was precipitated by addition of a saturated solution of $[NEt_4]Br$ in H_2O. The solid was washed with H_2O (3 × 20 mL) and toluene (3 × 20 mL), and extracted with dmf (10 mL). Crystals of $[NEt_4]_2[Au(IMes)_2][Ag_3Fe_3(CO)_{12}]\cdot dmf$ suitable for X-ray crystallography were obtained by slow

diffusion of isopropanol (35 mL) on the dmf solution (yield 0.32 g, 44 % based on Fe, 40 % based on Ag, 11 % based on Au).

$C_{73}H_{94}Ag_3AuFe_3N_7O_{13}$ (1965.67): calcd. (%): C 44.64, H 4.83, N 5.00; found: C 44.35, H 5.07, N 5.21. IR (acetone, 293 K) ν_{CO}: 1922(s), 1850(s) cm^{-1}.

Synthesis of $[Au(IMes)_2]_3[Ag_3Fe_3(CO)_{12}]\cdot$solv

$Na_2[Fe(CO)_4]\cdot 2thf$ (0.390 g, 1.09 mmol) and Au(IMes)Cl (0.850 g, 1.58 mmol) were charged in a Schlenk tube under a nitrogen atmosphere and dmso (10 mL) was added. The mixture was stirred for 2 h at room temperature up to the disappearance of the ν_{CO} peak at 1740 cm^{-1} in the IR spectrum due to $Na_2[Fe(CO)_4]\cdot 2thf$. Then, a saturated solution of $[NEt_4]Br$ in H_2O was added up to complete precipitation of the reaction mixture. The solid was recovered by filtration and washed with H_2O (3 × 20 mL) and toluene (3 × 20 mL), and $[NEt_4][Fe(CO)_4(AuIMes)]$ extracted with acetone (20 mL). Then, Ag(IMes)Cl (0.550 g, 1.23 mmol) was added as a solid in small portions to the acetone solution. A solid was formed, recovered by filtration and dissolved in dmso (10 mL). The resulting solution was heated at 80 °C for 0.5 h, and the crude reaction mixture was precipitated by addition of H_2O. The solid was washed with H_2O (3 × 20 mL) and toluene (3 × 20 mL), and extracted with acetone (15 mL). Crystals of $[Au(IMes)_2]_3[Ag_3Fe_3(CO)_{12}]\cdot$solv suitable for X-ray crystallography were obtained by slow diffusion of *n*-hexane (35 mL) on the acetone solution (yield 0.61 g, 52 % based on Fe, 46 % based on Ag, 36 % based on Au).

$C_{138}H_{144}Ag_3Au_3Fe_3N_{12}O_{12}$ (3244.70): calcd. (%): C 51.10, H 4.48, N 5.19; found: C 51.38, H 4.16, N 4.91. IR (nujol, 293 K) ν_{CO}: 1950(sh), 1917(s), 1843(vs), 1793(sh) cm^{-1}. IR (acetone, 293 K) ν_{CO}: 1922(s), 1848(s) cm^{-1}.

Synthesis of $Fe(CO)_4(CuIPr)_{1.27}(AgIPr)_{0.73}\cdot$1.5toluene

$Na_2[Fe(CO)_4]\cdot 2thf$ (0.336 g, 0.938 mmol) and Ag(IPr)Cl (0.645 g, 1.21 mmol) were charged in a Schlenk tube under a nitrogen atmosphere and dmso (10 mL) was added. The mixture was stirred for 2 h at room temperature up to the disappearance of the ν_{CO} peak at 1740 cm^{-1} in the IR spectrum due to $Na_2[Fe(CO)_4]\cdot 2thf$. Then, Cu(IPr)Cl (0.500 g, 1.03 mmol) was added as a solid in small portions. The crude product was precipitated by the slow addition of H_2O (40 mL) to the dmso solution. The solid was recovered after filtration, washed with H_2O (3 × 20 mL), and extracted with toluene (10 mL). Crystals of $Fe(CO)_4(CuIPr)_{1.27}(AgIPr)_{0.73}\cdot$1.5toluene suitable for X-ray

crystallography were obtained by slow diffusion of *n*-pentane (40 mL) on the toluene solution at -20 °C (yield 0.560 g, 48 % based on Fe, 27 % based on Ag, 56 % based on Cu).

$C_{68.5}H_{84}Ag_{0.73}Cu_{1.27}FeN_4O_4$ (1242.79): calcd. (%): C 66.26, H 6.82, N 4.52; found: C 66.48, H 7.01, N 4.22. IR (nujol, 293 K) ν_{CO}: 1953(s), 1867(s), 1852(s), 1835(s) cm^{-1}. IR (thf, 293 K) ν_{CO}: 1954(s), 1871(m), 1858(vs), 1834(s) cm^{-1}. IR (acetone, 293 K) ν_{CO}: 1952(s), 1853(vs) cm^{-1}. IR (CH_2Cl_2, 293 K) ν_{CO}: 1953(s), 1851(vs), 1833(sh) cm^{-1}. IR (toluene, 293 K) ν_{CO}: 1957(s), 1876(s), 1853(vs), 1832(s) cm^{-1}. IR (CH_3CN, 293 K) ν_{CO}: 1952(s), 1852(vs) cm^{-1}. IR (dmso, 293 K) ν_{CO}: 1947(s), 1848(vs) cm^{-1}. ^1H NMR (CD_2Cl_2, 298 K): δ7.34 (br, 4H, CH_{Ar}), 7.16 (br, 8H, CH_{Ar}), 7.04 (s, 4H, CH_{imid}),2.47 (br, 8H, C*H*(CH_3)$_2$), 1.08 (br, 48H, CH(C*H*$_3$)$_2$). $^{13}C\{^1H\}$ NMR (CD_2Cl_2, 298 K): δ217.6, 216.5, 215.6 (CO)*, 189.2 (C-Ag, $^1J_{C\text{-}Ag}$ = 194 and 167 Hz), 181.5 (C-Cu), 145.6, 135.0, 129.9, 123.8, 122.8 (C_{Ar} and CH_{imid}), 28.5 (*C*H(CH_3)$_2$), 24.2, 23.7 (CH(*C*H$_3$)$_2$).

* The three resonances in the CO region may be assigned to $Fe(CO)_4(AgIPr)_2$, $Fe(CO)_4(CuIPr)(AgIPr)$ and $Fe(CO)_4(CuIPr)_2$, respectively.

Synthesis of $Fe(CO)_4(CuIPr)_{0.64}(AuIPr)_{1.36}$·1.5toluene

$Na_2[Fe(CO)_4]$·2thf (0.310 g, 0.866 mmol) and Cu(IPr)Cl (0.470 g, 0.964 mmol) were charged in a Schlenk tube under a nitrogen atmosphere and dmso (10 mL) was added. The mixture was stirred for 2 h at room temperature up to the disappearance of the ν_{CO} peak at 1740 cm^{-1} in the IR spectrum due to $Na_2[Fe(CO)_4]$·2thf. Then, Au(IPr)Cl (0.620 g, 1.00 mmol) was added as a solid in small portions. The crude product was precipitated by the slow addition of H_2O (40 mL) to the dmso solution. The solid was recovered after filtration, washed with H_2O (3 × 20 mL), and extracted with toluene (10 mL). Crystals of $Fe(CO)_4(CuIPr)_{0.64}(AuIPr)_{1.36}$·1.5toluene suitable for X-ray crystallography were obtained by slow diffusion of *n*-pentane (40 mL) on the toluene solution at -20 °C (yield 0.639 g, 53 % based on Fe, 62 % based on Au, 30% based on Cu).

The same product was also obtained from the 1:1 reaction of $[NEt_4][Fe(CO)_4(AuIPr)]$ and Cu(IPr)Cl in acetone.

$C_{68.5}H_{84}Au_{1.36}Cu_{0.64}FeN_4O_4$ (1391.78): calcd. (%): C 59.11, H 6.09, N 4.03; found: C 59.34, H 5.88, N 4.19. IR (nujol, 293 K) ν_{CO}: 1974(vs), 1963(s), 1890(vs), 1880(vs), 1865(vs), 1848(vs) cm^{-1}. IR (thf, 293 K) ν_{CO}: 1975(ms), 1867(vs) cm^{-1}. IR (acetone, 293 K) ν_{CO}: 1973(ms), 1867(vs) cm^{-1}. IR (CH_2Cl_2, 293 K) ν_{CO}: 1974(ms), 1863(vs) cm^{-1}. IR (toluene, 293 K) ν_{CO}: 1978(s), 1869(vs) cm^{-1}. IR (CH_3CN, 293 K) ν_{CO}: 1971(ms), 1865(vs) cm^{-1}. ^1H NMR (CD_2Cl_2, 298 K): δ7.46 (br, 4H, CH_{Ar}), 7.26 (br, 8H, CH_{Ar}), 7.09 (s, 4H, CH_{imid}),2.60 (br, 8H, C*H*(CH_3)$_2$), 1.19 (br, 48H, CH(C*H*$_3$)$_2$).

$^{13}C\{^{1}H\}$ NMR (CD_2Cl_2, 298 K): δ216.8, 216.1, 215.6 (CO)*, 194.3 (C-Au), 181.2 (C-Cu), 145.6, 134.7, 129.8, 123.7, 122.1 (C_{Ar} and CH_{imid}), 28.6 (*C*H(CH_3)$_2$), 23.8, 23.7 (CH(*C*H_3)$_2$).

* The three resonances in the CO region may be assigned to $Fe(CO)_4(AuIPr)_2$, $Fe(CO)_4(CuIPr)(AuIPr)$ and $Fe(CO)_4(CuIPr)_2$, respectively.

Synthesis of $Fe(CO)_4(AgIPr)_{0.94}(AuIPr)_{1.06}$

$Na_2[Fe(CO)_4]$·2thf (0.336 g, 0.938 mmol) and Ag(IPr)Cl (0.645 g, 1.21 mmol) were charged in a Schlenk tube under a nitrogen atmosphere and dmso (10 mL) was added. The mixture was stirred for 2 h at room temperature up to the disappearance of the ν_{CO} peak at 1740 cm^{-1} in the IR spectrum due to $Na_2[Fe(CO)_4]$·2thf. Then, Au(IPr)Cl (0.620 g, 1.00 mmol) was added as a solid in small portions. The crude product was precipitated by the slow addition of H_2O (40 mL) to the dmso solution. The solid was recovered after filtration, washed with H_2O (3 × 20 mL), and extracted with toluene (10 mL). Crystals of $Fe(CO)_4(AgIPr)_{0.94}(AuIPr)_{1.06}$·1.5toluene suitable for X-ray crystallography were obtained by slow diffusion of *n*-pentane (40 mL) on the toluene solution at -20 °C (yield 0.627 g, 48 % based on Fe, 37 % based on Ag, 45% based on Au).

The same product was also obtained from the 1:1 reaction of $[NEt_4][Fe(CO)_4(AuIPr)]$ and Ag(IPr)Cl in acetone.

$C_{68.5}H_{84}Ag_{0.94}Au_{1.06}FeN_4O_4$ (1393.65): calcd. (%): C 59.06, H 6.08, N 4.02; found: C 59.24, H 5.88, N 3.79. IR (acetone, 293 K) ν_{CO}: 1963(s), 1880(sh), 1869(vs), 1853(vs) cm^{-1}. IR (dmso, 293 K) ν_{CO}: 1960(s), 1863(vs) cm^{-1}. ^{1}H NMR (CD_3COCD_3, 298 K): δ 7.58-7.25 (br, 16H, CH_{Ar} + CH_{imid}), 2.63 (br, 8H, C*H*(CH_3)$_2$), 1.20 (br, 48H, CH(C*H*$_3$)$_2$). $^{13}C\{^{1}H\}$ NMR (CD_3COCD_3, 298 K): δ 220.1, 217.6, 217.1 (CO)*, 194.7 (C-Au), 182.3 (C-Ag, $^{1}J_{C\text{-}Ag}$ = 213 and 195 Hz), 145.7-122.2 (C_{Ar} and CH_{imid}), 28.5 (*C*H(CH_3)$_2$), 24.1-23.3 (CH(*C*H_3)$_2$).

* The three resonances in the CO region may be assigned to $Fe(CO)_4(AgIPr)_2$, $Fe(CO)_4(AgIPr)(AuIPr)$ and $Fe(CO)_4(AuIPr)_2$, respectively.

CHAPTER 4

Synthesis of $[NEt_4]_3[Ag_xCu_{5-x}Fe_4(CO)_{16}]$ from $[NEt_4]_3[Cu_3Fe_3(CO)_{12}]$ and $AgNO_3$

A variable volume (V_{AgNO3}, see list below) of a solution of $AgNO_3$ (0.230 g, 1.36 mmol) in CH_3CN (10 mL) was added dropwise to a solution of $[NEt_4]_3[Cu_3Fe_3(CO)_{12}]$ (0.468 g, 0.432 mmol) in CH_3CN (15 mL). The mixture was stirred for 1 h at room temperature and then, the solvent was removed *in vacuo*. The residue was washed with H_2O (2 × 15 mL) and toluene (2 × 15 mL), and extracted with solvents of increasing polarity (acetone, CH_3CN, dmf). The resulting solutions were analysed by IR spectroscopy and, eventually, layered with an appropriate solvent (acetone/*n*-hexane; CH_3CN/*n*-hexane/di-isopropyl-ether; dmf/isopropanol) in the attempt to obtain crystals suitable for X-ray diffraction. The results were the following:

V_{AgNO3} = 2.55 mL (0.344 mmol).Crystals of $[NEt_4]_3[Ag_{1.02}Cu_{3.98}Fe_4(CO)_{16}]$ were obtained by slow diffusion of isopropanol on the dmf fraction (yield 0.150 g, 31 % based on Ag, 32 % based on Cu).

$C_{40}H_{60}Ag_{1.02}Cu_{3.98}Fe_4N_3O_{16}$ (1425.44): calcd. (%): C 33.71, H 4.24, N 2.95, Fe 15.67, Cu 17.75, Ag 7.72; found: C 33.92, H 4.38, N 2.76, Fe 15.86, Cu 17.59, Ag 7.47. IR (nujol, 293 K) ν_{CO}: 1943(s), 1905(m), 1854(s), 1829(sh) cm^{-1}. IR (acetone, 293 K) ν_{CO}: 1939(s), 1919(sh), 1897(m), 1845(s) cm^{-1}. IR (CH_3CN, 293 K) ν_{CO}: 1943(s), 1922(sh), 1878(m), 1824(sh) cm^{-1}.

V_{AgNO3} = 4.13 mL (0.562 mmol). Crystals of $[NEt_4]_3[Ag_{4.25}Cu_{0.75}Fe_4(CO)_{16}]$ were obtained by slow diffusion of isopropanol on the dmf fraction (yield 0.074 g, 36 % based on Ag, 3 % based on Cu).

$C_{40}H_{60}Ag_{4.25}Cu_{0.75}Fe_4N_3O_{16}$ (1568.63): calcd. (%): C 30.63, H 3.86, N 2.68, Fe 14.24, Cu 3.04, Ag 29.23; found: C 30.41, H 4.04, N 2.39, Fe 13.07, Cu 2.91, Ag 29.44. IR (nujol, 293 K) ν_{CO}: 1943(s), 1897(m), 1867(sh), 1851(s) cm^{-1}. IR (CH_3CN, 293 K) ν_{CO}: 1980(sh), 1965(ms), 1950(s), 1895(sh), 1879(vs), 1835(w) cm^{-1}.

V_{AgNO3} = 6.67 mL (0.907 mmol). Crystals of $[NEt_4]_3[Ag_{4.88}Cu_{0.12}Fe_4(CO)_{16}]$ were obtained by slow diffusion of *n*-hexane and di-isopropyl-ether on the CH_3CN fraction (yield 0.081 g, 27 % based on Ag, 0.5 % based on Cu).

$C_{40}H_{60}Ag_{4.88}Cu_{0.12}Fe_4N_3O_{16}$ (1596.34): calcd. (%): C 30.10, H 3.79, N 2.63, Fe 13.99, Cu 0.48, Ag 32.98; found: C 30.38, H 3.59, N 2.97, Fe 14.12, Cu 0.69, Ag 32.75. IR (nujol, 293 K) ν_{CO}: 1944(s), 1892(m), 1869(sh), 1853(s) cm^{-1}. IR (CH_3CN, 293 K) ν_{CO}: 1947(s), 1882(m) cm^{-1}.

V_{AgNO3} = 7.31 mL (0.994 mmol). Crystals of $[NEt_4]_3[Ag_{4.92}Cu_{0.08}Fe_4(CO)_{16}]$ were obtained by slow diffusion of isopropanol on the dmf fraction (yield 0.095 g, 29 % based on Ag, 0.4 % based on Cu).

$C_{40}H_{60}Ag_{4.92}Cu_{0.08}Fe_4N_3O_{16}$ (1598.11): calcd. (%): C 30.06, H 3.78, N 2.63, Fe 13.98, Cu 0.32, Ag 33.21; found: C 29.86, H 4.05, N 2.32, Fe 13.78, Cu 0.21, Ag 33.02. IR (nujol, 293 K) ν_{CO}: 1947(s), 1891(s) cm^{-1}. IR (dmf, 293 K) ν_{CO}: 1942(s), 1878(s) cm^{-1}.

Synthesis of $[NEt_4]_3[Ag_xCu_{5-x}Fe_4(CO)_{16}]$ from $[NEt_4]_3[Cu_5Fe_4(CO)_{16}]$ and $AgNO_3$

A solution of $AgNO_3$ (0.144 g, 0.850 mmol) in CH_3CN (5 mL) was added dropwise to a solution of $[NEt_4]_3[Cu_5Fe_4(CO)_{16}]$ (0.468 g, 0.340 mmol) in acetone (15 mL). The mixture was stirred for 1 h at room temperature and then, the solvent was removed under reduced pressure. The residue was washed with H_2O (2 × 15 mL) and toluene (2 × 15 mL), and extracted with solvents of increasing polarity (acetone, CH_3CN, dmf). The resulting solutions were analysed by IR spectroscopy and, eventually, layered with an appropriate solvent (acetone/*n*-hexane; CH_3CN/*n*-hexane/di-isopropyl-ether; dmf/isopropanol) in the attempt to obtain crystals suitable for X-ray diffraction.

Crystals of $[NEt_4]_3[Ag_5Fe_4(CO)_{16}]$ were obtained by slow diffusion of *n*-hexane and di-isopropyl-ether on the CH_3CN fraction (yield 0.038 g, 14 % based on Ag).

$C_{40}H_{60}Ag_5Cu_0Fe_4N_3O_{16}$ (1601.66): calcd. (%): C 30.00, H 3.78, N 2.62, Fe 13.95, Ag 33.67; found: C 30.31, H 3.51, N 2.99, C 30.00, H 3.78, N 2.62, Fe 14.12, Ag 33.49. IR (nujol, 293 K) ν_{CO}: 1944(m), 1890(sh), 1867(sh), 1853(s) cm^{-1}. IR (CH_3CN, 293 K) ν_{CO}: 1949(s), 1894(sh), 1878(s), 1833(w) cm^{-1}. IR (dmso, 293 K) ν_{CO}: 1944(s), 1895(sh), 1872(vs), 1833(m) cm^{-1}.

Crystals of $[NEt_4]_3[Ag_{4.81}Cu_{0.20}Fe_4(CO)_{16}]$ were obtained by slow diffusion of isopropanol on the dmf fraction (yield 0.44 g, 16 % based on Ag, 0.3 % based on Cu).

$C_{40}H_{60}Ag_{4.81}Cu_{0.20}Fe_4N_3O_{163}$ (1593.01): calcd. (%): C 30.14, H 3.79, N 2.63, Fe 14.02, Cu 0.80, Ag 32.55; found: C 29.95, H 3.61, N 2.82, Fe 14.25, Cu 0.67, Ag 32.74. IR (dmf, 293 K) ν_{CO}: 1945(vs), 1844(s) cm^{-1}.

Synthesis of $[NEt_4]_3[Ag_{4.37}Cu_{0.63}Fe_4(CO)_{16}]$ from $[NEt_4]_4[Ag_4Fe_4(CO)_{16}]$ and $[Cu(CH_3CN)_4][BF_4]$

$[Cu(CH_3CN)_4][BF_4]$ (0.095 g, 0.306 mmol) was added as a solid in small portions to a solution of $[NEt_4]_4[Ag_4Fe_4(CO)_{16}]$ (0.468 g, 0.289 mmol) in CH_3CN (15 mL). The mixture was stirred for 1 h at room temperature and then, the solvent was removed under reduced pressure. The residue was washed with H_2O (2 × 15 mL) and toluene (2 × 15 mL), and extracted with CH_3CN (15 mL). Crystals of $[NEt_4]_3[Ag_{4.37}Cu_{0.63}Fe_4(CO)_{16}]$ were obtained by slow diffusion of *n*-hexane and di-isopropyl-ether on the CH_3CN fraction (yield 0.121 g, 29 % based on Ag, 16 % based on Cu).

$C_{40}H_{60}Ag_{4.37}Cu_{0.63}Fe_4N_3O_{16}$ (1573.73): calcd. (%): C 30.53, H 3.84, N 2.67, Fe 14.19, Cu 2.54, Ag 29.95; found: C 30.37, H 4.02, N 2.83, Fe 14.02, Cu 2.68, Ag 30.14. IR (CH_3CN, 293 K) ν_{CO}: 1948(s), 1894(sh), 1878(s), 1833(w) cm^{-1}.

Synthesis of $[NEt_4]_3[Ag_{4.90}Cu_{0.10}Fe_4(CO)_{16}]$ from $[NEt_4]_3[Ag_5Fe_4(CO)_{16}]$ and Cu(IMes)Cl

Cu(IMes)Cl (0.354 g, 0.880 mmol) was added as a solid in small portions to a solution of $[NEt_4]_3[Ag_5Fe_4(CO)_{16}]$ (0.468 g, 0.293 mmol) in CH_3CN (15 mL). The mixture was stirred for 1 h at room temperature and then, the solvent was removed under reduced pressure. The residue was washed with H_2O (2 × 15 mL) and toluene (2 × 15 mL), and extracted with CH_3CN (15 mL). Crystals of $[NEt_4]_3[Ag_{4.90}Cu_{0.10}Fe_4(CO)_{16}]$ were obtained by slow diffusion of *n*-hexane and di-isopropyl-ether on the CH_3CN fraction (yield 0.160 g, 34 % based on Ag, 1.1 % based on Cu).

$C_{40}H_{60}Ag_{4.90}Cu_{0.10}Fe_4N_3O_{16}$ (1597.22): calcd. (%): C 30.08, H 3.79, N 2.63, Fe 13.99, Cu 0.40, Ag 33.09; found: C 29.88, H 4.03, N 2.85, Fe 14.15, Cu 0.54, Ag 32.89. IR (CH_3CN, 293 K) ν_{CO}: 1950(s), 1895(sh), 1879(s), 1834(m) cm^{-1}.

Synthesis of $[NEt_4]_3[Ag_xCu_{5-x}Fe_4(CO)_{16}]$ from $[NEt_4]_3[Ag_5Fe_4(CO)_{16}]$ and $[NEt_4]_3[Cu_3Fe_3(CO)_{12}]$

A solution of $[NEt_4]_3[Cu_3Fe_3(CO)_{12}]$ (0.317 g, 0.293 mmol) in CH_3CN (15 mL) was added dropwise to a solution of $[NEt_4]_3[Ag_5Fe_4(CO)_{16}]$ (0.468 g, 0.293 mmol) in CH_3CN (15 mL). The mixture was stirred for 1 h at room temperature and then, the solvent was removed under reduced pressure. The residue was washed with H_2O (2 × 15 mL) and toluene (2 × 15 mL), and extracted with solvents of increasing polarity (acetone, CH_3CN, dmf). The resulting solutions were analysed by IR spectroscopy and, eventually, layered with an appropriate solvent (acetone/*n*-hexane;

CH_3CN/*n*-hexane/di-isopropyl-ether; dmf/isopropanol) in the attempt to obtain crystals suitable for X-ray diffraction.

Crystals of $[NEt_4]_3[Ag_{3.30}Cu_{1.70}Fe_4(CO)_{16}]$ were obtained by slow diffusion of *n*-hexane on the acetone fraction (yield 0.320 g, 47 % based on Ag, 41 % based on Cu).

$C_{40}H_{60}Ag_{3.30}Cu_{1.70}Fe_4N_3O_{16}$ (1526.30): calcd. (%): C 31.48, H 3.96, N 2.75, Fe 14.64, Cu 7.08, Ag 23.32; found: C 31.32, H 4.12, N 2.96, Fe 14.48, Cu 6.87, Ag 23.57. IR (acetone, 293 K) ν_{CO}: 1942(s), 1898(m) cm^{-1}.

Crystals of $[NEt_4]_3[Ag_{3.45}Cu_{1.55}Fe_4(CO)_{16}]$ were obtained by slow diffusion of *n*-hexane and di-isopropyl-ether on the CH_3CN fraction (yield 0.100 g, 15 % based on Ag, 12 % based on Cu).

$C_{40}H_{60}Ag_{3.45}Cu_{1.55}Fe_4N_3O_{16}$ (1532.72): calcd. (%): C 31.34, H 3.95, N 2.74, Fe 14.57, Cu 6.43, Ag 24.28; found: C 31.62, H 3.79, N 2.95, Fe 14.38, Cu 6.29, Ag 24.57. IR (CH_3CN, 293 K) ν_{CO}: 1946(m), 1894(sh), 1847(s) cm^{-1}.

Synthesis of $[Cu(dppe)_2]_3[Ag_{13}Fe_8(CO)_{32}]$ from $[NEt_4]_3[Cu_5Fe_4(CO)_{16}]$ and $Ag(dppe)(NO_3)$

$Ag(dppe)(NO_3)$ (0.482 g, 0.850 mmol) was added as a solid in small portions to a solution of $[NEt_4]_3[Cu_5Fe_4(CO)_{16}]$ (0.468 g, 0.340 mmol) in acetone (15 mL). The mixture was stirred for 1 h at room temperature and then, the solvent was removed under reduced pressure. The residue was dissolved in dmf (10 mL) and further $Ag(dppe)(NO_3)$ (0.482 g, 0.850 mmol) was added as a solid. The mixture was stirred for 1 h at room temperature and then, a saturated solution of $[NEt_4]Br$ in H_2O (40 mL) was added up to complete precipitation of the products. The solid was recovered by filtration, washed with H_2O (2 × 15 mL), toluene (2 × 15 mL), thf (15 mL), acetone (15 mL) and CH_3CN (15 mL), and eventually extracted with dmf (10 mL). Crystals of $[Cu(dppe)_2]_3[Ag_{13}Fe_8(CO)_{32}]$ were obtained by slow diffusion of isopropanol on the dmf solution (yield 0.104 g, 15 % based on Ag, 3.4 % based on Cu).

Whilst repeating this reaction, a few crystals of $Cu_3Br_3(dppe)_3$ were also obtained as side product and mechanically separated from $[Cu(dppe)_2]_3[Ag_{13}Fe_8(CO)_{32}]$.

$C_{188}H_{144}Ag_{13}Cu_3Fe_8O_{32}P_{12}$ (5323.39): calcd. (%): C 42.29, H 2.72, Fe 8.39, Cu 3.58, Ag 26.33; found: C 42.67, H 2.35, Fe 8.53, Cu 3.29, Ag 26.47. IR (nujol, 293 K) ν_{CO}: 1994(s), 1912(m) cm^{-1}. IR (dmf, 293 K) ν_{CO}: 1999(vs), 1916(ms) cm^{-1}.

Synthesis of $[NEt_4]_3[Au_xCu_{5-x}Fe_4(CO)_{16}]$ from $[NEt_4]_3[Cu_3Fe_3(CO)_{12}]$ and $Au(PPh_3)Cl$

A variable amount ($m_{Au(PPh3)Cl}$, see list below) of $Au(PPh_3)Cl$ was added as a solid to a solution of $[NEt_4]_3[Cu_3Fe_3(CO)_{12}]$ (0.468 g, 0.432 mmol) in CH_3CN (15 mL). The mixture was stirred for 1 h at room temperature and then, the solvent was removed under reduced pressure. The residue was washed with H_2O (2 × 15 mL) and toluene (2 × 15 mL), and extracted with solvents of increasing polarity (acetone, CH_3CN, dmf). The resulting solutions were analysed by IR spectroscopy and, eventually, layered with an appropriate solvent (acetone/*n*-hexane; CH_3CN/*n*-hexane/di-isopropyl-ether; dmf/isopropanol) in the attempt to obtain crystals suitable for X-ray diffraction. The results were the following:

$m_{Au(PPh3)Cl}$ = 0.284 g (0.605 mmol). Crystals of $[NEt_4]_3[Au_{1.15}Cu_{3.85}Fe_4(CO)_{16}]$ were obtained by slow diffusion of *n*-hexane on the acetone fraction (yield 0.160 g, 20 % based on Ag, 31 % based on Cu).

$C_{40}H_{60}Au_{1.15}Cu_{3.85}Fe_4N_3O_{16}$ (1534.11): calcd. (%): C 31.33, H 3.94, N 2.74, Fe 14.57, Cu 15.95, Au 14.77; found: C 31.08, H 4.13, N 2.53, Fe 14.29, Cu 16.11, Au 14.89. IR (acetone, 293 K) ν_{CO}: 1946(s), 1884(s), 1831(w) cm^{-1}. IR (dmf, 293 K) ν_{CO}: 1946(s), 1881(s).

$m_{Au(PPh3)Cl}$ = 0.305 g (0.648 mmol). Crystals of $[NEt_4]_3[Au_{1.31}Cu_{3.69}Fe_4(CO)_{16}]$ were obtained by slow diffusion of *n*-hexane on the acetone fraction (yield 0.168 g, 22 % based on Au, 31 % based on Cu).

$C_{40}H_{60}Au_{1.31}Cu_{3.69}Fe_4N_3O_{16}$ (1555.46): calcd. (%): C 30.90, H 3.89, N 2.70, Fe 14.37, Cu 15.08, Au 16.60; found: C 30.77, H 4.04, N 2.56, Fe 14.19, Cu 14.87, Au 16.91. IR (acetone, 293 K) ν_{CO}: 1947(s), 1882(m) cm^{-1}.

Crystals of $[NEt_4]_3[Au_{1.67}Cu_{3.33}Fe_4(CO)_{16}]$ were obtained by slow diffusion of isopropanol on the dmf fraction (yield 0.112 g, 18 % based on Au, 18 % based on Cu).

$C_{40}H_{60}Au_{1.67}Cu_{3.33}Fe_4N_3O_{16}$ (1602.83): calcd. (%): C 29.97, H 3.77, N 2.62, Fe 13.94, Cu 13.20, Au 20.52; found: C 30.14, H 4.02, N 2.36, Fe 13.81, Cu 13.49, Au 20.21. IR (dmf, 293 K) ν_{CO}: 1945(s), 1878(m) cm^{-1}.

$m_{Au(PPh3)Cl}$ = 0.610 g (1.30 mmol). Crystals of $[NEt_4]_3[Au_{2.48}Cu_{2.52}Fe_4(CO)_{16}]$ were obtained by slow diffusion of isopropanol on the dmf fraction (yield 0.130 g, 14 % based on Au, 15 % based on Cu).

$C_{40}H_{60}Au_{2.48}Cu_{2.52}Fe_4N_3O_{16}$ (1710.90): calcd. (%): C 28.08, H 3.53, N 2.46, Fe 13.06, Cu 9.36, Au 28.55; found: C 28.27, H 3.31, N 2.62, Fe 13.21, Cu 9.08, Au 28.27. IR (dmf, 293 K) ν_{CO}: 1951(2), 1887(2) cm^{-1}.

Synthesis of $[NEt_4]_3[Au_xCu_{5-x}Fe_4(CO)_{16}]$ from $[NEt_4]_3[Cu_3Fe_3(CO)_{12}]$ and $Au(Et_2S)Cl$

A variable volume ($V_{Au(Et2S)Cl}$, see list below) of a solution of $Au(Et_2S)Cl$ (0.348 g, 1.08 mmol) in CH_3CN (10 mL) was added dropwise to a solution of $[NEt_4]_3[Cu_3Fe_3(CO)_{12}]$ (0.468 g, 0.432 mmol) in CH_3CN (15 mL). The mixture was stirred for 1 h at room temperature and then, the solvent was removed under reduced pressure. The residue was washed with H_2O (2 × 15 mL) and toluene (2 × 15 mL), and extracted with solvents of increasing polarity (acetone, CH_3CN, dmf). The resulting solutions were analysed by IR spectroscopy and, eventually, layered with an appropriate solvent (acetone/*n*-hexane; CH_3CN/*n*-hexane/di-isopropyl-ether; dmf/isopropanol) in the attempt to obtain crystals suitable for X-ray diffraction. The results were the following:

$V_{Au(Et2S)Cl}$ = 2.80 mL (0.302 mmol). Crystals of $[NEt_4]_3[Au_{2.18}Cu_{2.83}Fe_4(CO)_{16}]$ and $[NEt_4]_3[Au_{2.73}Cu_{2.28}Fe_4(CO)_{16}]$ were obtained by slow diffusion of *n*-hexane and di-isopropyl-ether on the CH_3CN fraction (yield 0.098 g, 47 % based on Au, 11 % based on Cu).

$C_{40}H_{60}Au_{2.73}Cu_{2.28}Fe_4N_3O_{16}$ (1743.59): calcd. (%): C 27.53, H 3.47, N 2.41, Fe 12.80, Cu 8.30, Au 30.82; $C_{40}H_{60}Au_{2.18}Cu_{2.83}Fe_4N_3O_{16}$ (1670.21): calcd. (%): C 28.74, H 3.62, N 2.52, Fe 13.36, Cu 10.76, Au 25.69; found (mixture): C 28.25, H 3.34, N 2.63 Fe 13.05, Cu 9.12, AU 28.55. IR (nujol, 293 K) ν_{CO}: 1948(s), 1911(m), 1864(s) cm^{-1}. IR (acetone, 293 K) ν_{CO}: 1999(w), 1974(m), 1951(vs), 1922(s), 1864(s) cm^{-1}. IR (CH_3CN, 293 K) ν_{CO}: 1950(s), 1915(s), 1864(s) cm^{-1}.

$V_{Au(Et2S)Cl}$ = 7.60 mL (0.821 mmol). Crystals of $[NEt_4]_3[Au_{4.59}Cu_{0.42}Fe_4(CO)_{16}]$ and $[NEt_4]_3[Au_{4.61}Cu_{0.38}Fe_4(CO)_{16}]$ were obtained by slow diffusion of *n*-hexane and di-isopropyl-ether on the CH_3CN fraction (yield 0.104 g, 29 % based on Au, 1.6 % based on Cu).

$C_{40}H_{60}Au_{4.61}Cu_{0.38}Fe_4N_3O_{163}$ (1995.77): calcd. (%): C 24.09, H 3.03, N 2.11, Fe 11.20, Cu 1.21, Au 45.53; $C_{40}H_{60}Au_{4.59}Cu_{0.42}Fe_4N_3O_{163}$ (1991.77): calcd. (%): C 24.11, H 3.03, N 2.11, Fe 11.21, Cu 1.34, Au 45.36; found: C 24.21, H 2.86, N 2.29, Fe 11.34, Cu 1.16, Au 45.61. IR (nujol, 293 K) ν_{CO}: 1954(s), 1869(s) cm^{-1}. IR (acetone, 293 K) ν_{CO}: 1956(s), 1930(ms), 1902(m) cm^{-1}.

Synthesis of $[NEt_4]_3[Au_{1.09}Cu_{3.91}Fe_4(CO)_{16}]$ from $[NEt_4]_3[Cu_5Fe_4(CO)_{16}]$ and $Au(Et_2S)Cl$

A solution of $Au(Et_2S)Cl$ (0.131 g, 0.408 mmol) in acetone (5 mL) was added dropwise to a solution of $[NEt_4]_3[Cu_5Fe_4(CO)_{16}]$ (0.468 g, 0.340 mmol) in acetone (15 mL). The mixture was stirred for 1 h at room temperature and then, the solvent was removed under reduced pressure. The residue was washed with H_2O (2 × 15 mL) and toluene (2 × 15 mL), and extracted with acetone. Crystals of $[NEt_4]_3[Au_{1.09}Cu_{3.91}Fe_4(CO)_{16}]$ were obtained by slow diffusion of *n*-hexane on the acetone fraction (yield 0.32 g, 56 % based on Ag, 48 % based on Cu).

$C_{40}H_{60}Au_{1.09}Cu_{3.91}Fe_4N_3O_{16}$ (1525.44): calcd. (%): C 31.49, H 3.96, N 2.75, Fe 14.64, Cu 16.29, Au 14.07; found: C 31.79, H 4.12, N 2.54, Fe 14.39, Cu 16.47, Au 13.87. IR (acetone, 293 K) ν_{CO}: 1945(s), 1880(m) cm^{-1}.

Synthesis of $[NEt_4]_3[Au_xAg_{5-x}Fe_4(CO)_{16}]$ from $[NEt_4]_4[Ag_4Fe_4(CO)_{16}]$ and $Au(Et_2S)Cl$

A solution of $Au(Et_2S)Cl$ (0.075 g, 0.231mmol) in CH_3CN (4 mL) was added dropwise to a solution of $[NEt_4]_4[Ag_4Fe_4(CO)_{16}]$ (0.468 g, 0.289 mmol) in CH_3CN (15 mL). The mixture was stirred for 1 h at room temperature and then, the solvent was removed under reduced pressure. The residue was washed with H_2O (2 × 15 mL) and toluene (2 × 15 mL), and extracted with solvents of increasing polarity (acetone, CH_3CN, dmf). The resulting solutions were analysed by IR spectroscopy and, eventually, layered with an appropriate solvent (acetone/*n*-hexane; CH_3CN/*n*-hexane/di-isopropyl-ether; dmf/isopropanol) in the attempt to obtain crystals suitable for X-ray diffraction.

Crystals of $[NEt_4]_3[Au_{0.81}Ag_{4.20}Fe_4(CO)_{16}]$ were obtained by slow diffusion of *n*-hexane on the acetone fraction (yield 0.099 g, 21 % based on Au, 21 % based on Ag).

$C_{40}H_{60}Au_{0.81}Ag_{4.20}Fe_4N_3O_{16}$ (1673.38): calcd. (%): C 28.68, H 3.61, N 2.51, Fe 13.34, Ag 27.05, Au 9.53; found: C 29.03, H 3.39, N 2.24, Fe 13.49, Ag 26.85, Au 9.78. IR (acetone, 293 K) ν_{CO}: 1946(vs), 1927(m), 1896(ms), 1874(s), 1835(sh) cm^{-1}.

Crystals of $[NEt_4]_3[Au_{0.64}Ag_{4.36}Fe_4(CO)_{16}]$ were obtained by slow diffusion of *n*-hexane and di-isopropyl-ether on the CH_3CN fraction (yield 0.180 g, 30 % based on Au, 41 % based on Ag).

$C_{40}H_{60}Au_{0.64}Ag_{4.36}Fe_4N_3O_{16}$ (1658.68): calcd. (%): C 28.96, H 3.65, N 2.53, Fe 13.47, Ag 28.35, Au 7.60; found: C 29.31, H 3.39, N 2.22, Fe 13.22, Ag 28.04, Au 7.85. IR (CH_3CN, 293 K) ν_{CO}: 1967(sh), 1950(s), 1930(sh), 1880(s), 1835(sh) cm^{-1}.

CHAPTER 5

Synthesis of $Co(CO)_4$(CuIPr)

$Na[Co(CO)_4]$ (0.410 g, 2.12 mmol) and Cu(IPr)Cl (1.06 g, 2.17 mmol) were charged in a Schlenk tube under a nitrogen atmosphere and thf (15 mL) was added. The mixture was stirred for 20 minutes at room temperature and then, the solvent removed under reduced pressure. The crude product was extracted in toluene (15 mL) and crystals of $Co(CO)_4$(CuIPr) were obtained by slow diffusion of *n*-pentane (30 mL) at -20 °C (yield 1.02 g, 77% based on Co, 76% based on Cu). These crystals displayed the same unit cell reported in the literature.

$C_{31}H_{36}CuCoN_2O_4$ (622.13): calcd. (%): C 59.79, H 5.83, N 4.50; found: C 60.08, H 5.67, N 4.33. IR (nujol, 293 K) ν_{CO}: 2039(mw), 1961(m), 1927(ms) cm^{-1}. IR (toluene, 293 K) ν_{CO}: 2041(s), 1964(s), 1934(s), 1917(sh) cm^{-1}. IR ($CHCl_3$, 293 K) ν_{CO}: 2041(s), 1962(s), 1936(s), 1918(sh) cm^{-1}. IR (CH_2Cl_2, 293 K) ν_{CO}: 2041(s), 1960(s), 1935(s), 1913(sh) cm^{-1}. IR (thf, 293 K) ν_{CO}: 2039(ms), 1961(s), 1935(s), 1915(sh) cm^{-1}. IR (acetone, 293 K) ν_{CO}: 2040(ms), 1961(s), 1937(s), 1913(sh) cm^{-1}. IR (CH_3CN, 293 K) ν_{CO}: 2041(w), 1962(m), 1935(m), 1892(s) cm^{-1}. IR (dmso, 293 K) ν_{CO}: 2039(w), 1957(m), 1934(m), 1889(s) cm^{-1}. ^1H NMR (C_6D_6, 298 K): δ 7.23 (t, $^2J_{HH}$ = 7.5 Hz, 2H, CH_{Ar}), 7.08 (d, $^2J_{HH}$ = 7.5 Hz, 4H, CH_{Ar}), 6.29 (s, 2H, CH_{imid}), 2.59 (sept, $^2J_{HH}$ = 6.3 Hz, 4H, C*H*$(CH_3)_2$), 1.38 (d, $^2J_{HH}$ = 5 Hz, 12H, CH(C*H*$_3)_2$), 1.05 (d, $^2J_{HH}$ = 5 Hz, 12H, CH(C*H*$_3)_2$). $^{13}C\{^1H\}$ NMR (C_6D_6, 298 K): δ 160.3 (C-Cu), 145.4, 134.9, 131.0, 124.5, 122.7 (C_{Ar} and CH_{imid}), 29.0 (*C*H$(CH_3)_2$), 24.5, 24.2 (CH(*C*H$_3)_2$). Note: no peak corresponding to bound CO was located.

Synthesis of $Co(CO)_4$(AgIPr)

$Na[Co(CO)_4]$ (0.200 g, 1.04 mmol) and Ag(IPr)Cl (0.440 g, 1.04 mmol) were charged in a Schlenk tube under a nitrogen atmosphere and thf (15 mL) was added. The mixture was stirred for 60 minutes at room temperature and then, the solvent removed under reduced pressure. The crude product was extracted in toluene (15 mL) and crystals of $Co(CO)_4$(AgIPr) were obtained by slow diffusion of *n*-pentane (30 mL) at -20 °C (yield 0.45 g, 65% based on Co, 65% based on Ag).

$C_{31}H_{36}AgCoN_2O_4$ (667.42): calcd. (%): C 55.85, H 5.45, N 4.20; found: C 55.61, H 5.74, N 4.49. IR (nujol, 293 K) ν_{CO}: 2037(s), 1958(s), 1925(s) cm^{-1}. IR (toluene, 293 K) ν_{CO}: 2040(s), 1962(s), 1933(s) cm^{-1}. IR ($CHCl_3$, 293 K) ν_{CO}: 2040(s), 1959(sh), 1937(s) cm^{-1}. IR (CH_2Cl_2, 293 K) ν_{CO}: 2040(ms), 1958(s), 1935(s) cm^{-1}. IR (thf, 293 K) ν_{CO}: 2039(s), 2024(w), 1958(s), 1935(s) cm^{-1}. IR (acetone, 293 K) ν_{CO}: 2039(s), 1959(s), 1936(s) cm^{-1}. IR (CH_3CN, 293 K) ν_{CO}: 2041(m), 1959(s), 1934(s), 1893(mw) cm^{-1}. IR (dmso, 293 K) ν_{CO}: 2038(m), 1955(s), 1935(s), 1890(m) cm^{-1}. ^1H NMR (CD_2Cl_2, 298 K): δ 7.67 (s, 2H, CH_{imid}), 7.49 (t, $^2J_{HH}$ = 7.8 Hz, 2H, CH_{Ar}), 7.36 (d, $^2J_{HH}$ = 7.8 Hz, 4H, CH_{Ar}), 2.65 (sept, $^2J_{HH}$ = 6.8 Hz, 4H, C*H*(CH_3)$_2$), 1.39 (d, $^2J_{HH}$ = 6.8 Hz, 12H, CH(C*H*$_3$)$_2$), 1.31 (d, $^2J_{HH}$ = 6.8 Hz, 12H, CH(C*H*$_3$)$_2$). $^{13}C\{^1H\}$ NMR (CD_2Cl_2, 298 K): δ 205.8 (br, CO), 185.3 (C-Ag, $^1J_{C\text{-}Ag}$ = 234 and 202 Hz), 144.8, 134.2, 129.5, 123.2, 123.1 (C_{Ar} and CH_{imid}), 27.9 (*C*H(CH_3)$_2$), 23.1, 22.4 (CH(*C*H$_3$)$_2$).

Synthesis of $Co(CO)_4$(AuIPr)

Na[$Co(CO)_4$] (0.190 g, 0.984 mmol) and Au(IPr)Cl (0.610 g, 0.984 mmol) were charged in a Schlenk tube under a nitrogen atmosphere and thf (15 mL) was added. The mixture was stirred for 30 minutes at room temperature and then, the solvent removed under reduced pressure. The crude product was extracted in toluene (15 mL) and crystals of $Co(CO)_4$(AuIPr) were obtained by slow diffusion of *n*-pentane (30 mL) at -20 °C (yield 0.58 g, 78% based on Co, 78% based on Au).

$C_{31}H_{36}AuCoN_2O_4$ (756.51): calcd. (%): C 49.20, H 4.80, N 3.70; found: C 49.36, H 4.52, N 3.94. IR (nujol, 293 K) ν_{CO}: 2044(s), 1969(s), 1939(s) cm^{-1}. IR (toluene, 293 K) ν_{CO}: 2048(s), 1973(s), 1949(s) cm^{-1}. IR ($CHCl_3$, 293 K) ν_{CO}: 2047(s), 1970(sh), 1952(s) cm^{-1}. IR (CH_2Cl_2, 293 K) ν_{CO}: 2047(s), 1968(s), 1951(s) cm^{-1}. IR (acetone, 293 K) ν_{CO}: 2046(s), 1969(s), 1952(s) cm^{-1}. IR (CH_3CN, 293 K) ν_{CO}: 2048(s), 1971(s), 1950(s) cm^{-1}. IR (dmso, 293 K) ν_{CO}: 2045(s), 1964(s), 1949(s), 1892(m) cm^{-1}. ^1H NMR (CD_2Cl_2, 298 K): δ 7.53 (t, $^2J_{HH}$ = 7.8 Hz, 2H, CH_{Ar}), 7.34 (d, $^2J_{HH}$ = 7.8 Hz, 4H, CH_{Ar}), 7.27 (s, 2H, CH_{imid}), 2.63 (sept, $^2J_{HH}$ = 6.8 Hz, 4H, C*H*(CH_3)$_2$), 1.35 (d, $^2J_{HH}$ = 6.8 Hz, 12H, CH(C*H*$_3$)$_2$), 1.25 (d, $^2J_{HH}$ = 6.8 Hz, 12H, CH(C*H*$_3$)$_2$). $^{13}C\{^1H\}$ NMR (CD_2Cl_2, 298 K): δ 207.6 (br, CO), 187.2 (C-Au), 145.7, 134.1, 130.4, 124.0, 122.8 (C_{Ar} and CH_{imid}), 28.8 (*C*H(CH_3)$_2$), 23.9, 23.7 (CH(*C*H$_3$)$_2$).

Synthesis of [Co(CO)$_4$(AuIMes)]

Na[Co(CO)$_4$] (0.190 g, 0.984 mmol) and Au(IMes)Cl (0.530 g, 0.988 mmol) were charged in a Schlenk tube under a nitrogen atmosphere and thf (15 mL) was added. The mixture was stirred for 30 minutes at room temperature and then, the solvent removed under reduced pressure. The crude product was extracted in toluene (15 mL) and a microcrystalline powder of Co(CO)$_4$(AuIPr) was obtained by slow addition of *n*-pentane (30 mL) (yield 0.49 g, 74% based on Co, 74% based on Au).

$C_{25}H_{24}AuCoN_2O_4$ (672.07): calcd. (%): C 44.64, H 3.60, N 4.17; found: C 44.25, H 3.91, N 3.87.
IR (thf, 293 K) ν_{CO}: 2044(s), 2023(w), 1967(s), 1947(s) cm^{-1}.

Synthesis of [Cu(IMes)$_2$][Cu{Co(CO)$_4$}$_2$]

Na[Co(CO)$_4$] (0.410 g, 2.12 mmol) and Cu(IMes)Cl (0.880 g, 2.18 mmol) were charged in a Schlenk tube under a nitrogen atmosphere and thf (15 mL) was added. The mixture was stirred for 20 minutes at room temperature and then, the solvent removed under reduced pressure. The crude product was extracted in toluene (15 mL) and crystals of [Cu(IMes)$_2$][Cu{Co(CO)$_4$}$_2$] were obtained by slow diffusion of *n*-pentane (30 mL) at -20 °C (yield 0.59 g, 52% based on Co, 50% based on Cu). The crystals obtained are a polymorph (Space Group *C*2/*c*) of the previously reported structure (Space Group *P*2$_1$/*n*).

$C_{50}H_{48}Cu_2Co_2N_4O_8$ (1077.86): calcd. (%): C 55.76, H 4.50, N 5.21; found: C 55.35, H 4.84, N 5.04.
IR (thf, 293 K) ν_{CO}: 2039(w), 2022(m), 1950(s), 1936(s), 1885(s) cm^{-1}. ^{1}H NMR (C_6D_6, 298 K): δ6.74 (s, 4H, CH_{Ar}), 5.96 (s, 2H, CH_{imid}), 2.07 (s,6H, *CH$_3$*), 1.96 (s,12H, *CH$_3$*). $^{13}C\{^1H\}$ NMR (C_6D_6, 298 K): δ 178.8 (C-Cu), 139.6, 135.1, 134.5, 129.5, 121.4, (C_{Ar} and CH_{imid}), 17.3, 16.8 (*C*H$_3$). Note: no peak corresponding to bound CO was located. Note: During the several attempts to crystallise [Cu(IMes)$_2$][Cu{Co(CO)$_4$}$_2$], also a few crystals of [Cu(IMes)$_2$][Co(CO)$_4$] were obtained.

Synthesis of [Ag(IMes)$_2$][Ag{Co(CO)$_4$}$_2$]

Na[Co(CO)$_4$] (0.200 g, 1.04 mmol) and Ag(IMes)Cl (0.370 g, 1.04 mmol) were charged in a Schlenk tube under a nitrogen atmosphere and thf (15 mL) was added. The mixture was stirred for 60 minutes at room temperature and then, the solvent removed under reduced pressure. The crude product was extracted in toluene (15 mL) and crystals of [Ag(IMes)$_2$][Ag{Co(CO)$_4$}$_2$] were

obtained by slow diffusion of *n*-pentane (30 mL) at -20 °C (yield 0.31 g, 51% based on Co, 51% based on Ag).

$C_{50}H_{48}Ag_2Co_2N_4O_8$ (1166.52): calcd. (%): C 51.55, H 4.16, N 4.81; found: C 51.89, H 3.89, N 4.52. IR (nujol, 293 K) ν_{CO}: 2022(s), 1934(s) cm^{-1}. IR (toluene, 293 K) ν_{CO}: 2040(m), 2025(m), 1959(s), 1935(s) cm^{-1}. IR ($CHCl_3$, 293 K) ν_{CO}: 2039(mw), 2025(w), 1956(sh), 1937(s) cm^{-1}. IR (CH_2Cl_2, 293 K) ν_{CO}: 2038(w), 2026(m), 1937(s) cm^{-1}. IR (thf, 293 K) ν_{CO}: 2038(w), 2025(m), 1939(s), 1887(w) cm^{-1}. IR (acetone, 293 K) ν_{CO}: 2038(w), 2027(m), 1944(s), 1940(s), 1892(w) cm^{-1}. IR (CH_3CN, 293 K) ν_{CO}: 2039(sh), 2028(sh), 1940(m), 1895(w) cm^{-1}. IR (dmso, 293 K) ν_{CO}: 2038(sh), 2027(m), 1937(s), 1890(ms) cm^{-1}. ^1H NMR (CD_3COCD_3, 298 K): δ 7.53 (s, 4H, CH_{imid}), 7.04 (s, 8H, CH_{Ar}), 2.46 (s, 12H, CH_3), 1.78 (s, 24H, CH_3). $^{13}C\{^1H\}$ NMR (CD_2Cl_2, 298 K): δ 206.0 (br, CO), 182.5 (C-Ag, $^1J_{C\text{-}Ag}$ = 207 and 180 Hz), 139.2, 135.2, 134.5, 129.1, 123.3 (C_{Ar} and CH_{imid}), 20.3, 16.5 (CH_3).

Synthesis of $[HIPr]_2[Ag_2\{Co(CO)_4\}_4]$

$Co(CO)_4(AgIPr)$ (0.350 g, 0.524 mmol) and $Co_2(CO)_8$ (0.180 g, 0.527 mmol) were charged in a Schlenk tube under a nitrogen atmosphere and thf (15 mL) was added. The mixture was heated at refluxing temperature for 300 minutes and then, the solvent removed under reduced pressure. The crude product was washed with H_2O (20 mL), toluene (15 mL) and extracted in CH_2Cl_2 (15 mL). Slow diffusion of *n*-pentane (30 mL) at -20 °C afforded a few crystals of $[HIPr]_2[Ag_2\{Co(CO)_4\}_4]$ whereas the majority of product recovered was unreacted $Co(CO)_4(AgIPr)$. Because of this, yields were not calculated and $[HIPr]_2[Ag_2\{Co(CO)_4\}_4]$ was only characterised by SC-XRD.

Synthesis of $[Co_4(CO)_8(\mu\text{-}\eta^7\text{-IMes})]$

$[Cu(IMes)_2][Cu\{Co(CO)_4\}_2]$ (0.828 g, 0.768 mmol) and $Co_2(CO)_8$ (0.450 g, 1.32 mmol) were charged in a Schlenk tube under a nitrogen atmosphere and thf (15 mL) was added. The mixture was heated at refluxing temperature for 300 minutes and then, the solvent removed under reduced pressure. The crude product was washed with H_2O (20 mL), toluene (15 mL) and extracted with toluene (15 mL). Slow diffusion of *n*-pentane (30 mL) at -20 °C afforded a few crystals of $[Co_4(CO)_8(\mu\text{-}\eta^7\text{-IMes})]\cdot 0.5$toluene whereas the majority of product recovered was unreacted $[Cu(IMes)_2][Cu\{Co(CO)_4\}_2]$. Because of this, yields were not calculated and $[HIPr]_2[Ag_2\{Co(CO)_4\}_4]$ was only characterised by SC-XRD.

CHAPTER 6

Synthesis of $[NEt_4]_2[Pt_6(CO)_{10}(dppm)]\cdot CH_3CN$

dppm (0.310 g, 0.806 mmol) was added as a solid to a solution of $[NEt_4]_2[Pt_6(CO)_{12}]$ (0.700 g, 0.396 mmol) in CH_3CN (15 mL). The resulting mixture was stirred at room temperature for 2 h and then, the solvent removed *in vacuo*. The residue was washed with toluene (20 mL), and extracted with CH_3CN (20 mL). Crystals of $[NEt_4]_2[Pt_6(CO)_{10}(dppm)]\cdot CH_3CN$ suitable for X-ray analyses were obtained by layering *n*-hexane (4 mL) and di-isopropyl-ether (30 mL) on the CH_3CN solution (yield 0.550 g, 65 % based on Pt).

$C_{53}H_{63}N_3O_{10}P_2Pt_6$ (2134.54): calcd. C 29.82, H 2.97, N 1.97; found: C 30.05, H 3.11, N 1.74. IR (nujol, 293 K) ν_{CO}: 2000(s), 1980(s), 1949(s), 1778(m), 1756(m), 1750(m) cm^{-1}. IR (CH_3CN, 293 K) ν_{CO}: 2006(s), 1980(vs), 1780(s), 1770(s) cm^{-1}. $^{31}P\{^1H\}$ NMR (CD_3CN, 298 K) δ (ppm): 51.0 ($^1J_{PtP}$ = 4960 Hz (1Pt), $^2J_{PtP}$ = 602 Hz (2Pt) and 15 Hz (1Pt), $^2J_{PP}$ = 88 Hz).

Synthesis of $[NEt_4]_2[Pt_9(CO)_{16}(dppm)]$

A solution of $[NEt_4]_2[Pt_{12}(CO)_{20}(dppm)_2]$ (0.823 g, 0.198 mmol) in CH_3CN (15 mL) was added to a solution of $[NEt_4]_2[Pt_6(CO)_{12}]$ (0.350 g, 0.198 mmol) in CH_3CN (15 mL). The resulting mixture was stirred at room temperature for 2 h and then, the solvent removed *in vacuo*. The residue was washed with toluene (20 mL), and extracted with CH_3CN (20 mL). The resulting CH_3CN solution was employed for the IR and $^{31}P\{^1H\}$ NMR analyses.

IR (CH_3CN, 293 K) ν_{CO}: 2018(vs), 1828(s) cm^{-1}. $^{31}P\{^1H\}$ NMR (CD_3CN, 298 K) δ (ppm): 47.3 ($^1J_{PtP}$ = 4941 Hz (1Pt), $^2J_{PtP}$ = 562 Hz (2Pt), $^2J_{PP}$ = 85 Hz), 39.0 ($^1J_{PtP}$ = 5047 Hz (1Pt), $^2J_{PtP}$ = 697 Hz (2Pt), $^2J_{PP}$ = 85 Hz).

Synthesis of $[NEt_4]_2[Pt_{12}(CO)_{20}(dppm)_2]\cdot 2CH_3CN\cdot 2dmf$

A solution of $HBF_4\cdot Et_2O$ (80 μL, 0.588 mmol) was added dropwise to a solution of $[NEt_4]_2[Pt_6(CO)_{10}(dppm)]\cdot CH_3CN$ (0.550 g, 0.258 mmol) in dmf (15 mL). The reaction was monitored by IR and the final product was precipitated by the addition of a saturated solution of $[NEt_4]Br$ in H_2O (40 mL). After filtration, the solid was washed with H_2O (40 mL), dried under

reduced pressure and extracted with dmf (10 mL). Crystals of $[NEt_4]_2[Pt_{12}(CO)_{20}(dppm)_2]\cdot 2CH_3CN\cdot 2dmf$ suitable for X-ray analyses were obtained by layering isopropanol (30 mL) on the dmf solution diluted with some CH_3CN (5 mL) (yield 0.319 g, 59 % based on Pt).

Crystals of $[NEt_4]_2[Pt_{12}(CO)_{20}(dppm)_2]\cdot 4dmf$ can be obtained by following an analogous procedure, without the final addition of CH_3CN.

$C_{96}H_{104}N_6O_{22}P_4Pt_{12}$ (4158.81): calcd. C 27.73, H 2.52, N 2.02; found: C 27.51, H 2.89, N 1.91. IR (nujol, 293 K) ν_{CO}: 2013(vs), 1856(m), 1819(s), 1810(s) cm^{-1}. IR (CH_3CN, 293 K) ν_{CO}: 2020(vs), 1851(m), 1829(s), 1808(m) cm^{-1}. $^{31}P\{^1H\}$ NMR (dmf-d7, 298 K) δ (ppm): 46.2 ($^1J_{PtP}$ = 4962 Hz (1Pt), $^2J_{PtP}$ = 546 Hz (2Pt), $^2J_{PP}$ = 83 Hz), 38.7 ($^1J_{PtP}$ = 5144 Hz (1Pt), $^2J_{PtP}$ = 626 Hz (2Pt), $^2J_{PP}$ = 83 Hz).

Synthesis of $[NEt_4]_2[Pt_{18}(CO)_{30}(dppm)_3]$

A solution of $HBF_4\cdot Et_2O$ (20 μL, 0.147 mmol) was added dropwise to a solution of $[NEt_4]_2[Pt_{12}(CO)_{20}(dppm)_2]\cdot 4dmf$ (0.258 g, 0.061 mmol) in dmf (10 mL). The reaction was monitored by IR and the final product was precipitated by the addition of a saturated solution of $[NEt_4]Br$ in H_2O (40 mL). After filtration, the solid was washed with H_2O (40 mL), dried under reduced pressure and extracted with dmf (10 mL). The resulting dmf solution was employed for the IR and $^{31}P\{^1H\}$ NMR analyses. All attempts to crystallise $[NEt_4]_2[Pt_{18}(CO)_{30}(dppm)_3]$ failed, affording crystals of $[NEt_4]_2[Pt_{12}(CO)_{20}(dppm)_2]$, instead.

IR (dmf, 293 K) ν_{CO}: 2032(vs), 1871(m), 1856(s), 1843(m), 1821(m) cm^{-1}. $^{31}P\{^1H\}$ NMR (dmf-d^7, 298 K) δ (ppm): 46.1 ($^1J_{PtP}$ = 5105 Hz (1Pt), $^2J_{PtP}$ = 548 Hz (2Pt) and 15 Hz (1Pt), $^2J_{PP}$ = 70 Hz), 43.8 ($^1J_{PtP}$ = 4952 Hz (1Pt), $^2J_{PtP}$ = 540 Hz (2Pt), $^2J_{PP}$ = 78 Hz), 36.2 ($^1J_{PtP}$ = 5095 Hz (1Pt), $^2J_{PtP}$ = 601 Hz (2Pt), $^2J_{PP}$ = 78 Hz).

Synthesis of $[NEt_4]_2[Pt_6(CO)_{10}(P\text{^}P)]$

P^P (0.319 g, 0.806 mmol) was added as a solid to a solution of $[NEt_4]_2[Pt_6(CO)_{12}]$ (0.700 g, 0.396 mmol) in CH_3CN (15 mL). The resulting mixture was stirred at room temperature for 2 h and then, the solvent removed *in vacuo*. The residue was washed with toluene (20 mL), and extracted with CH_3CN (20 mL). An amorphous powder of $[NEt_4]_2[Pt_6(CO)_{10}(P\text{^}P)]$ was obtained after removing CH_3CN under reduced pressure from the filtrated (yield 0.517 g, 62 % based on Pt).

$C_{52}H_{62}N_2O_{10}P_2Pt_6$ (2107.47): calcd. C 29.64, H 2.97, N 1.33; found: C 29.38, H 3.12, N 1.14. IR (CH_3CN, 293 K) ν_{CO}: 2006(s), 1979(vs), 1774(s) cm^{-1}. $^{31}P\{^1H\}$ NMR (CD_3CN, 298 K) δ (ppm): 62.2 ($^1J_{PtP}$ = 5059 Hz (1Pt), $^2J_{PtP}$ = 453 Hz (2Pt) and 17 Hz (1Pt), $^2J_{PP}$ = 120 Hz).

Synthesis of $[NEt_4]_2[Pt_6(CO)_{10}(dppf)]\cdot 2CH_3CN$

dppf (0.695 g, 0.806 mmol) was added as a solid to a solution of $[NEt_4]_2[Pt_6(CO)_{12}]$ (0.700 g, 0.396 mmol) in CH_3CN (15 mL). The resulting mixture was stirred at room temperature for 2 h and then, the solvent removed *in vacuo*. The residue was washed with toluene (20 mL), and extracted with CH_3CN (20 mL). Crystals of $[NEt_4]_2[Pt_6(CO)_{10}(dppf)]\cdot 2CH_3CN$ suitable for X-ray analyses were obtained by layering *n*-hexane (4 mL) and di-isopropyl-ether (30 mL) on the CH_3CN solution (yield 0.558 g, 60 % based on Pt).

$C_{64}H_{74}FeN_4O_{10}P_2Pt_6$ (2347.60): calcd. C 32.74, H 3.18, N 2.39; found: C 32.92, H 2.89, N 2.51. IR (CH_3CN, 293 K) ν_{CO}: 2005(sh), 1993(vs), 1802(sh), 1782(s) cm^{-1}. $^{31}P\{^1H\}$ NMR (CD_3CN, 298 K) δ (ppm): 49.3 ($^1J_{PtP}$ = 5247 Hz (1Pt), $^2J_{PtP}$ = 543 Hz (2Pt).

Synthesis of $Pt(dppb)_2$

dppb (0.511 g, 1.200 mmol) was added as a solid to a solution of $[NEt_4]_2[Pt_6(CO)_{12}]$ (0.700 g, 0.396 mmol) in CH_3CN (15 mL). The resulting mixture was stirred at room temperature for 4 h affording a microcrystalline solid, which was recovered by filtration. The solid was extracted with CH_2Cl_2 (10 mL). Crystals of $Pt(dppb)_2$ suitable for X-ray analyses were obtained by layering *n*-hexane (25 mL) on the CH_2Cl_2 solution (yield 0.489 g, 20 % based on Pt).

$C_{56}H_{56}P_4Pt$ (1047.97): calcd. C 64.17, H 5.39; found: C 64.44, H 5.61. $^{31}P\{^1H\}$ NMR (CD_2Cl_2, 298 K) δ (ppm): 0.5 ($^1J_{PtP}$ = 3750 Hz).

Synthesis of $Pt_2(CO)_2(dppa)_3\cdot 0.5CH_3CN$

dppa (0.473 g, 1.200 mmol) was added as a solid to a solution of $[NEt_4]_2[Pt_6(CO)_{12}]$ (0.700 g, 0.396 mmol) in CH_3CN (15 mL). The resulting mixture was stirred at room temperature for 4 h affording a microcrystalline solid, which was recovered by filtration. The solid was extracted with CH_2Cl_2 (10 mL). Crystals of $Pt_2(CO)_2(dppa)_3\cdot 0.5CH_3CN$ suitable for X-ray analyses were obtained by layering *n*-hexane (2 mL) and di-isopropyl-ether (30 mL) on the crude CH_3CN solution before any work-up (yield 0.392 g, 20 % based on Pt).

$C_{81}H_{61.5}N_{0.5}O_2P_6Pt_2$ (1649.80): calcd. C 58.97, H 3.76, N 0.42; found: C 59.19, H 3.51, N 0.62. IR (nujol, 293 K) ν_{CO}: 1928(vs) cm^{-1}. IR (CH_2Cl_2, 293 K) ν_{CO}: 1930(vs) cm^{-1}. IR (toluene, 293 K) ν_{CO}: 1935(vs) cm^{-1}. $^{31}P\{^1H\}$ NMR (CD_2Cl_2, 298 K) δ (ppm): -19.9 ($^1J_{PtP}$ = 3391 Hz).

Synthesis of $Pt_8(CO)_6(PPh_2)_2(C{\equiv}CPPh_2)_2(dppa)_2{\cdot}2thf$

dppa (0.473 g, 1.200 mmol) was added as a solid to a solution of $[NEt_4]_2[Pt_9(CO)_{18}]$ (0.895 g, 0.396 mmol) in thf (15 mL). The resulting mixture was stirred at room temperature for 4 h and layered with *n*-hexane (15 mL). After slow diffusion of the solvent, a few crystals of $Pt_8(CO)_6(PPh_2)_2(C{\equiv}CPPh_2)_2(dppa)_2{\cdot}2thf$ suitable for X-ray analyses were obtained (yield 0.077 g, 5 % based on Pt). These crystals are completely not soluble in any organic solvent.

$C_{118}H_{96}O_8P_8Pt_8$ (3450.42): calcd. C 41.07, H 2.80; found: C 41.31, H 2.68. IR (nujol, 293 K) ν_{CO}: 2023(vs), 2008(ms) cm^{-1}.

Stepwise reaction of $[Pt_6(CO)_{12}]^{2-}$ with PTA

Solid PTA was added in small portions (22.2 mg each time, 0.141mmol) to a CH_3CN (20 mL) solution of $[NEt_4]_2[Pt_6(CO)_{12}]$ (0.250 g, 0.142mmol). The solution was stirred at room temperature under nitrogen after each addition for 30 min and, then the reaction was monitored by FT-IR spectroscopy in the same solvent. The different spectra recorded are summarised below. The nature of the cation does not affect the outcome of the reactions. The PTA-derivatives of $[Pt_6(CO)_{12}]^{2-}$ are air sensitive which hampered $^{31}P\{^1H\}$ NMR spectroscopy and ESI-MS studies.

Starting material: $[Pt_6(CO)_{12}]^{2-}$ (orange solution). IR (CH_3CN, 293 K) ν_{CO}: 2000(s), 1800(m) cm^{-1}.

After one equivalent of PTA: $[Pt_6(CO)_{11}(PTA)]^{2-}$ (orange solution). IR (CH_3CN, 293 K) ν_{CO}: 1992(s), 1779(m) cm^{-1}.

After two equivalents of PTA: $[Pt_6(CO)_{10}(PTA)_2]^{2-}$ (orange solution). IR (CH_3CN, 293 K) ν_{CO}: 1976(s), 1759(m) cm^{-1}.

Stepwise reaction of $[Pt_9(CO)_{18}]^{2-}$ with PTA

Solid PTA was added in small portions (15.6 mg each time, 0.0994 mmol) to a CH_3CN (20 mL) solution of $[NEt_4]_2[Pt_9(CO)_{18}]$ (0.250 g, 0.0992 mmol). The solution was stirred at room temperature under nitrogen after each addition for 30 min and, then the reaction was monitored by

FT-IR spectroscopy in the same solvent. The different spectra recorded are summarised below. The nature of the cation does not affect the outcome of the reactions.

Starting material: $[Pt_9(CO)_{18}]^{2-}$ (red solution). IR (CH_3CN, 293 K) ν_{CO}: 2030(s), 1840(m) cm^{-1}.

After one equivalent of PTA: $[Pt_9(CO)_{17}(PTA)]^{2-}$ (red solution). IR (CH_3CN, 293 K) ν_{CO}: 2025(s), 1831(m) cm^{-1}. $^{31}P\{^1H\}$ NMR (CH_3CN/CD_3CN, 298 K) δ (ppm): -47.7 ($^1J_{PtP}$ = 4550 Hz, $^2J_{PtP}$ = 430 Hz). ESI-MS (CH_3CN): ES- *m/z* (relative intensity in parentheses): 1130(*53*), 1194(*100*), 1260(*26*), 1571(*12*), 1635(*27*), 1700(*16*) attributable to $[Pt_9(CO)_{18}]^{2-}$, $[Pt_9(CO)_{17}(PTA)]^{2-}$, $[Pt_9(CO)_{16}(PTA)_2]^{2-}$, $[Pt_{12}(CO)_{23}(PTA)]^{2-}$, $[Pt_{12}(CO)_{22}(PTA)_2]^{2-}$, $[Pt_{12}(CO)_{21}(PTA)_4]^{2-}$.

After two equivalents of PTA: $[Pt_9(CO)_{16}(PTA)_2]^{2-}$ (red solution). IR (CH_3CN, 293 K) ν_{CO}: 2014(s), 1826(m) cm^{-1}.$^{31}P\{^1H\}$ NMR (CH_3CN/CD_3CN, 298 K) δ (ppm): -43.1 ($^1J_{PtP}$ = 4534 Hz, $^2J_{PtP}$ = 504 Hz).

After three equivalents of PTA: $[Pt_9(CO)_{15}(PTA)_3]^{2-}$ (red solution). IR (CH_3CN, 293 K) ν_{CO}: 2008(s), 1817(m) cm^{-1}.$^{31}P\{^1H\}$ NMR (CH_3CN/CD_3CN, 298 K) δ (ppm): -37.8 (2P, $^1J_{PtP}$ = 4558Hz, $^2J_{PtP}$ = 514 Hz), -38.7 (1P, $^1J_{PtP}$ = 4634 Hz, $^2J_{PtP}$ = 508 Hz).

Stepwise reaction of $[Pt_{12}(CO)_{24}]^{2-}$ with PTA

Solid PTA was added in small portions (10.4 mg each time, 0.0662 mmol) to a CH_3CN (20 mL) solution of $[NEt_4]_2[Pt_{12}(CO)_{24}]$ (0.250 g, 0.0660 mmol). The solution was stirred at room temperature under nitrogen after each addition for 30 min and, then the reaction was monitored by FT-IR spectroscopy in the same solvent. The different spectra recorded are summarised below. The nature of the cation does not affect the outcome of the reactions.

Starting material: $[Pt_{12}(CO)_{24}]^{2-}$ (green solution). IR (CH_3CN, 293 K) ν_{CO}: 2047(s), 1865(m) cm^{-1}.

After one equivalent of PTA: $[Pt_{12}(CO)_{23}(PTA)]^{2-}$ (green solution). IR (CH_3CN, 293 K) ν_{CO}: 2040(s), 1854(m) cm^{-1}.

After two equivalents of PTA: $[Pt_{12}(CO)_{22}(PTA)_2]^{2-}$ (green solution). IR (CH_3CN, 293 K) ν_{CO}: 2035(s), 1844(m) cm^{-1}. $^{31}P\{^1H\}$ NMR (CH_3CN/CD_3CN, 298 K) δ (ppm): -49.0 (br, $^1J_{PtP}$ = 4550 Hz, $^2J_{PtP}$ = 468 Hz). The resonances are very broad also at low temperature (down to 203 K in CH_3CH_2CN). ESI-MS (CH_3CN): ES- *m/z* (relative intensity in parentheses): 1506(*34*), 1571(*100*), 1636(*32*), 1700(*10*), 1883(*5*), 1950(*20*), 2012(*40*), 2077(*42*), 2145(*6*) attributable to $[Pt_{12}(CO)_{24}]^{2-}$, $[Pt_{12}(CO)_{23}(PTA)]^{2-}$, $[Pt_{12}(CO)_{22}(PTA)_2]^{2-}$, $[Pt_{12}(CO)_{21}(PTA)_3]^{2-}$, $[Pt_{15}(CO)_{30}]^{2-}$, $[Pt_{15}(CO)_{29}(PTA)]^{2-}$, $[Pt_{15}(CO)_{28}(PTA)_2]^{2-}$, $[Pt_{15}(CO)_{27}(PTA)_3]^{2-}$, $[Pt_{15}(CO)_{26}(PTA)_4]^{2-}$.

After three equivalents of PTA: $[Pt_{12}(CO)_{21}(PTA)_3]^{2-}$ (green solution). IR (CH_3CN, 293 K) ν_{CO}: 2022(s), 1829(m) cm^{-1}.

After four equivalents of PTA: a mixture of $[Pt_{12}(CO)_{20}(PTA)_4]^{2-}$ and $[Pt_9(CO)_{15}(PTA)_3]^{2-}$ is present in solution as evidenced by IR spectroscopy and the change of the colour of the solution from the typical green colour of the $[Pt_{12}(CO)_{24-x}(PTA)_x]^{2-}$ (x = 0-4) clusters to the red colour of $[Pt_9(CO)_{18-x}(PTA)_x]^{2-}$ (x = 0-3). A more selective synthesis of $[Pt_{12}(CO)_{20}(PTA)_4]^{2-}$ consists in the oxidation of $[Pt_9(CO)_{15}(PTA)_3]^{2-}$.

Synthesis of $[NEt_4]_2[Pt_{12}(CO)_{20}(PTA)_4]\cdot 1.5CH_3COCH_3$

Solid PTA (46.8 mg, 0.299 mmol) was added to a CH_3CN (20 mL) solution of $[NEt_4]_2[Pt_9(CO)_{18}]$ (0.250 g, 0.0992 mmol). The resulting red solution was stirred at room temperature under nitrogen for 2 h. IR monitoring at this stage showed the presence in solution of $[Pt_9(CO)_{15}(PTA)_3]^{2-}$. Air was introduced in the reaction vessel for a few minutes resulting in the change of the colour of the solution from red to green. Hence, air was removed under reduced pressure and the nitrogen atmosphere restored. The reaction mixture was filtered, and the filtrate layered with *n*-hexane (3 mL) and di-isopropyl-ether (35 mL), affording crystals of $[NEt_4]_2[Pt_{12}(CO)_{20}(PTA)_4]\cdot 1.5CH_3COCH_3$ (yield 0.174 g, 60 % based on Pt).

$C_{64.5}H_{97}N_{14}O_{21.5}P_4Pt_{12}$ (3877.52): calcd. C 19.98, H 2.52, N 5.06; found: C 20.11, H 2.87, N 4.88. IR (nujol, 293 K) ν_{CO}: 1992(s), 1811(m) cm^{-1}. IR (CH_3CN, 293 K) ν_{CO}: 2014(s), 1830(m) cm^{-1}. $^{31}P\{^1H\}$ NMR (CD_3COCD_3, 298 K) δ (ppm): -42.6 ($^1J_{PtP}$ = 4571 Hz, $^2J_{PtP}$ = 502 Hz), -43.8 ($^1J_{PtP}$ = 4588 Hz, $^2J_{PtP}$ = 511 Hz). ESI-MS (CH_3CN): ES- *m/z* (relative intensity in parentheses): 1259(*10*), 1323(*40*), 1701(*19*), 1765(*100*), 1830(*30*) attributable to $[Pt_9(CO)_{16}(PTA)_2]^{2-}$, $[Pt_9(CO)_{15}(PTA)_3]^{2-}$, $[Pt_{12}(CO)_{21}(PTA)_3]^{2-}$, $[Pt_{12}(CO)_{20}(PTA)_4]^{2-}$, $[Pt_{12}(CO)_{19}(PTA)_5]^{2-}$.

Stepwise reaction of $[Pt_{15}(CO)_{30}]^{2-}$ with PTA

Solid PTA was added in small portions (9.80 mg each time, 0.0624 mmol) to a CH_3CN (20 mL) solution of $[NEt_4]_2[Pt_{15}(CO)_{30}]$ (0.250 g, 0.0621 mmol). The solution was stirred at room temperature under nitrogen after each addition for 30 min and, then the reaction was monitored by FT-IR spectroscopy in the same solvent. The different spectra recorded are summarised below. The nature of the cation does not affect the outcome of the reactions. The outcome of these reactions is not very clear since the purported $[Pt_{15}(CO)_{30-x}(PTA)_x]^{2-}$ (x = 0-5) clusters are expected to show ν_{CO}

bands in the IR spectra very similar to $[Pt_{12}(CO)_{24-x}(PTA)_x]^{2-}$ (x = 0-4). Moreover, both $[Pt_{12}(CO)_{24-x}(PTA)_x]^{2-}$ (x = 0-4) and $[Pt_{15}(CO)_{30-x}(PTA)_x]^{2-}$ (x = 0-5) are green in solution.

Starting material: $[Pt_{15}(CO)_{30}]^{2-}$ (green solution). IR (CH_3CN, 293 K) ν_{CO}: 2054(s), 1873(m) cm^{-1}.

After one equivalent of PTA (green solution). IR (CH_3CN, 293 K) ν_{CO}: 2048(s), 1862(m) cm^{-1}.

After two equivalents of PTA (green solution). IR (CH_3CN, 293 K) ν_{CO}: 2042(s), 1852(m) cm^{-1}.

After three equivalents of PTA (green solution). IR (CH_3CN, 293 K) ν_{CO}: 2035(s), 1843(m) cm^{-1}.

After four equivalents of PTA (green solution). IR (CH_3CN, 293 K) ν_{CO}: 2024(s), 1836(m) cm^{-1}.

After five equivalents of PTA (green solution). IR (CH_3CN, 293 K) ν_{CO}: 2015(s), 1828(m) cm^{-1}.

Synthesis of $[NMe_3(CH_2Ph)]_2[Pt_{15}(CO)_{25}(PTA)_5]\cdot CH_3COCH_3$.

Solid PTA (44.1 mg, 0.281 mmol) was added to a CH_3COCH_3 (20 mL) solution of $[NMe_3(CH_2Ph)]_2[Pt_{12}(CO)_{24}]$ (0.250 g, 0.0653 mmol). The resulting solution was stirred at room temperature under nitrogen for 2 h. The solution at this stage displayed a black colour typical of a mixture of $[Pt_9(CO)_{15}(PTA)_3]^{2-}$ (red) and $[Pt_{12}(CO)_{20}(PTA)_4]^{2-}$ (green), as also indicated by IR spectroscopy. Air was introduced in the reaction vessel for a few minutes resulting in the change of the colour of the solution from black to green; IR monitoring showed the typical ν_{CO} bands of $[Pt_{15}(CO)_{55}(PTA)_5]^{2-}$. Hence, air was removed under reduced pressure and the nitrogen atmosphere restored. The reaction mixture was filtered, and the filtrate layered with *n*-hexane (40 mL), affording crystals of $[NMe_3(CH_2Ph)]_2[Pt_{15}(CO)_{25}(PTA)_5]\cdot CH_3COCH_3$ (yield 0.136 g, 54 % based on Pt).

$C_{78}H_{98}N_{17}O_{26}P_5Pt_{15}$ (4770.93): calcd. C 20.32, H 2.14, N 5.16; found: C 19.94, H 2.33, N 5.07. IR (nujol, 293 K) ν_{CO}: 1991, 1828 cm^{-1}. IR (CH_3CN, 293 K) ν_{CO}: 2015(s), 1834(m) cm^{-1}. IR (CH_3COCH_3, 293 K) ν_{CO}:2014, 1834 cm^{-1}. $^{31}P\{^1H\}$ NMR (CD_3COCD_3, 298 K) δ (ppm): -46.2 (2P, $^1J_{PtP}$ = 4560 Hz, $^2J_{PtP}$ = 480 Hz), -47.1 (2P, $^1J_{PtP}$ = 4544 Hz, $^2J_{PtP}$ = 540 Hz), -54.1 1P, ($^1J_{PtP}$ = 4694 Hz, $^2J_{PtP}$ = 470 Hz).

Synthesis of $[NEt_4]_2[Pt_9(CO)_{18}]\cdot py$

Crystals of $[NEt_4]_2[Pt_9(CO)_{18}]\cdot py$ suitable for X-ray crystallography were obtained by slow diffusion of isopropanol (40 mL) on a solution of $[NEt_4]_2[Pt_9(CO)_{18}]$ (0.997 g, 0.396 mmol) in pyridine (15 mL) (yield 0.80 g, 78% based on Pt).

$C_{39}H_{45}N_3O_{18}Pt_9$ (2599.59): calcd. C 18.01, H 1.75, N 1.62; found: C18.36, H 1.98, N 1.21. IR (pyridine, 293 K) ν_{CO}: 2031(vs), 1839(m) cm^{-1}. IR (nujol mull, 293 K) ν (CO): 2016(vs), 1811(m) cm^{-1}.

Synthesis of $[NEt_4]_2[Pt_{12}(CO)_{22}(PPh_2py)_2]$

Solid PPh_2py (0.206 g, 0.782 mmol) was added in small portions to an acetone (20 mL) solution of $[NEt_4]_2[Pt_{12}(CO)_{24}]$ (1.28 g, 0.391 mmol). The solution was stirred at room temperature under nitrogen for 30 minutes. Then, the solvent was removed *in vacuo*, the solid washed with water (40 mL) and toluene (40 mL) and extracted in acetone (20 mL). Crystals of $[NEt_4]_2[Pt_{12}(CO)_{22}(PPh_2py)_2]$ suitable for X-ray analyses were obtained by slow diffusion of *n*-hexane (40 mL) on the acetone solution (yield 0.95g, 68% based on Pt).

$C_{72}H_{68}N_4O_{22}P_2Pt_{12}$ (3744.32): calcd. C 23.09, H 1.83, N 1.50; found: C 23.33, H 2.05, N 1.21. IR (acetone, 293 K) ν_{CO}: 2024(vs), 1847(m) cm^{-1}. IR (nujol mull, 293 K) ν_{CO}: 2030(vs), 1825(m) cm^{-1}.

Synthesis of $Pt_5(XylNC)_{10}\cdot 2$toluene

Solid XylNC (0.610 g, 4.65 mmol) was added in small portions to a CH_3CN (20 mL) solution of $[NEt_4]_2[Pt_6(CO)_{12}]$ (0.64 g, 0.362 mmol). The solution was stirred at room temperature under nitrogen for 30 minutes. Then, the solvent was removed *in vacuo*, the solid washed with water (40 mL) and extracted in toluene (15 mL). Crystals of $Pt_5(XylNC)_{10}\cdot 2$toluene suitable for X-ray analyses were obtained by slow diffusion of *n*-pentane (30 mL) on the toluene solution at -20 °C (yield 0.55g, 51% based on Pt).

$C_{104}H_{106}N_{10}Pt_5$ (2471.43): calcd. C 50.53, H 4.33, N 5.67; found: C 50.22, H 4.54, N 5.19. IR (toluene, 293 K) ν_{CN}: 2117(vs), 1663(m) cm^{-1}. IR (nujol mull, 293 K) ν_{CN}: 2111(vs), 2080(sh), 1651(s) cm^{-1}.

Synthesis of $Pt_9(XylNC)_{13}(CO)\cdot$solv

Solid XylNC (0.400 g, 3.05 mmol) was added in small portions to an acetone (20 mL) solution of $[NEt_4]_2[Pt_{15}(CO)_{30}]$ (0.890 g, 0.221 mmol). The solution was stirred at room temperature under nitrogen for 30 minutes. Then, the solvent was removed *in vacuo*, the solid washed with water (40 mL) and extracted in toluene (15 mL). Crystals of $Pt_9(XylNC)_{13}(CO)\cdot$solv suitable for X-ray

analyses were obtained by slow diffusion of *n*-pentane (30 mL) on the toluene solution at -20 °C (yield 0.21 g, 16% based on Pt).

$C_{118}H_{117}N_{13}OPt_9$ (3489.05): calcd. C 40.61, H 3.38, N 5.22; found: C 40.89, H 2.97, N 4.88. IR (toluene, 293 K) ν_{CN}: 2112(vs), 1774(m) cm^{-1}. IR (nujol mull, 293 K) ν_{CN}: 2096(vs), 1770(m), 1667(s) cm^{-1}.

Synthesis and characterisation of $[PPh_4]_4[Pt_{27}(CO)_{31}]$

A solution of $[PPh_4]_2[Pt_{15}(CO)_{30}]$ (0.70 g, 0.158 mmol) in thf (20 mL) was heated at 65 °C under H_2 atmosphere for 8 hours. Then, the solvent was removed under reduced pressure and the residue washed with H_2O (3 × 15 mL), isopropanol (3 × 15 mL), toluene (3 × 15 mL), thf (3 × 15 mL) and extracted in acetone (20 mL). Crystals of $[PPh_4]_4[Pt_{27}(CO)_{31}]$ suitable for X-ray diffraction have been obtained by slow diffusion of isopropanol on the acetone solution.

IR (nujol, 293 K) ν_{CO}: 2003(vs), 1953(sh), 1849(m), 1803(s), 1770(ms), 1747(ms). IR (CH_3CN, 293 K) ν_{CO}: 2021(vs), 1844(w), 1815(m), 1779(w) cm^{-1}. IR (acetone, 293 K) ν_{CO}: 2018(vs), 1816(m) cm^{-1}. IR (CH_2Cl_2, 293 K) ν_{CO}: 2019(vs), 1811(m).

Synthesis of $[PPh_4]_2[Pt_{12}(CO)_{10}(SnCl)_2(SnCl_2)_4\{Cl_2Sn(\mu\text{-}OH)SnCl_2\}_2]$

$HBF_4{\cdot}Et_2O$ (500 μl, 3.67 mmol) was added in small portions over a period of 2 h to a solution of $[PPh_4]_4[Pt_6(CO)_6(SnCl_2)_2(SnCl_3)_4]$ (0.910 g, 0.282 mmol) in CH_3CN (30 mL). After the addition of the first 300 μl of $HBF_4{\cdot}Et_2O$ the solution turned from green to brown and the unique ν_{CO} band moved from 2038 to 2046 cm^{-1}; this further moved to 2056 cm^{-1} after the addition of other 200 μl of $HBF_4{\cdot}Et_2O$. The solvent was, then, removed *in vacuo* and the residue dissolved in CH_2Cl_2 (20 mL), where it displayed a single ν_{CO} band at 2066 cm^{-1}. Crystals of $[PPh_4]_2[Pt_{12}(CO)_{10}(SnCl)_2(SnCl_2)_4\{Cl_2Sn(\mu\text{-}OH)SnCl_2\}_2]$ suitable for X-ray analyses were obtained from slow diffusion of *n*-hexane (40 mL) on the CH_2Cl_2 solution (yield 0.386 g, 53 % based on Pt). Yield is given as the amount of crystals effectively isolated. Some of $[PPh_4]_2[Pt_{12}(CO)_{10}(SnCl)_2(SnCl_2)_4\{Cl_2Sn(\mu\text{-}OH)SnCl_2\}_2]$ remained in the CH_2Cl_2/*n*-hexane after diffusion. Moreover, some side products not soluble in CH_2Cl_2 remained during the work-up. Among them, it was possible to identify the starting material $[Pt_6(CO)_6(SnCl_2)_2(SnCl_3)_4]^{4-}$, that was soluble in CH_3CN and identified by IR spectroscopy.

$C_{58}H_{42}Cl_{18}O_{12}P_2Pt_{12}Sn_{10}$ (5158.94): calcd. C 13.49, H 0.82, Sn 23.24, Pt 45.34; found: C 13.81, H 1.12, Sn 23.04, Pt 45.62. IR (nujol, 293 K) ν_{CO}: 2067(s) cm^{-1}. IR (CH_2Cl_2, 293 K) ν_{CO}: 2069(s) cm^{-1}.

Samples of $[PPh_4]_2[Pt_{12}(^{13}CO)_{10}(SnCl)_2(SnCl_2)_4\{Cl_2Sn(\mu\text{-}OH)SnCl_2\}_2]$ can be prepared starting from $[PPh_4]_4[Pt_6(^{12}CO)_8(SnCl_2)(SnCl_3)_4]$ and following the same procedure as above. $[PPh_4]_2[Pt_{12}(^{13}CO)_{10}(SnCl)_2(SnCl_2)_4\{Cl_2Sn(\mu\text{-}OH)SnCl_2\}_2]$ displays $\nu(^{13}CO)$ in CH_2Cl_2 at 2019(s) cm^{-1}.

^1H NMR (CD_2Cl_2, 298 K) δ (ppm): 7.64-7.96 (m, 40H, *Ph*), 6.93 (br, 2H, OH).

$^{13}C\{^1H\}$ NMR (CD_2Cl_2, 298 K) δ (ppm) ^{13}CO enriched sample (only the CO region is given): 185.0 (br), 190.2 (br).$^{13}C\{^1H\}$ NMR (CD_2Cl_2, 243 K) δ (ppm): 185.2 (br), 190.5 (br).$^{13}C\{^1H\}$ NMR (CD_2Cl_2, 213 K) δ (ppm): 185.5 (br), 190.7 (br).

Synthesis of $[PPh_4]_2[Pt_7(CO)_6(SnBr_2)_4\{Br_2Sn(\mu\text{-}OH)SnBr_2\}\{Br_2Sn(\mu\text{-}Br)SnBr_2\}]$

$HBF_4{\cdot}Et_2O$ (500 μl, 3.67 mmol) was added in small portions over a period of 2 h to a solution of $[PPh_4]_4[Pt_6(CO)_6(SnCl_2)_2(SnCl_3)_4]$ (1.04 g, 0.282 mmol) in CH_3CN (30 mL). The solvent was, then, removed *in vacuo* and the residue dissolved in CH_2Cl_2 (20 mL). Orange-red crystals of $[PPh_4]_2[Pt_7(CO)_6(SnBr_2)_4\{Br_2Sn(\mu\text{-}OH)SnBr_2\}\{Br_2Sn(\mu\text{-}Br)SnBr_2\}]$ suitable for X-ray analyses were obtained from slow diffusion of *n*-hexane (40 mL) on the CH_2Cl_2 solution (yield 0.515 g, 47% based on Pt). The formation of these orange-red crystals was accompanied by a few yellow crystals of $[PPh_4][Pt(CO)(Br)(SnBr_3)_2]$ and $[PPh_4]_2[Pt_2(CO)_2(Br)_4(SnBr_2)]$. Crystals of $[PPh_4][Pt(CO)(Br)(SnBr_3)_2]$ and $[PPh_4]_2[Pt_2(CO)_2(Br)_4(SnBr_2)]$ were mechanically separated from $[PPh_4]_2[Pt_7(CO)_6(SnBr_2)_4\{Br_2Sn(\mu\text{-}OH)SnBr_2\}\{Br_2Sn(\mu\text{-}Br)SnBr_2\}]$ and their structures determined by means of single crystal X-ray diffraction. Since only a few crystals of $[PPh_4][Pt(CO)(Br)(SnBr_3)_2]$ and $[PPh_4]_2[Pt_2(CO)_2(Br)_4(SnBr_2)]$ were obtained, yields were not registered.

$[PPh_4]_2[Pt_7(CO)_6(SnBr_2)_4\{Br_2Sn(\mu\text{-}OH)SnBr_2\}\{Br_2Sn(\mu\text{-}Br)SnBr_2\}]$. $C_{54}H_{41}Br_{17}O_7P_2Pt_7Sn_8$ (4537.43): calcd. C 14.30, H 0.91, Sn 21.18, Pt 30.13; found: C 14.58, H 1.14, Sn 20.94, Pt 29.95. IR (nujol, 293 Kν_{CO}: 2060(s) cm^{-1}. IR (CH_2Cl_2, 293 K) ν_{CO}: 2064(s) cm^{-1}.

^1H NMR (CD_2Cl_2, 298 K) δ (ppm): 7.64-7.96 (m, 40H, *Ph*), 3.14 (br, 1H, OH).

$[PPh_4][Pt(CO)(Br)(SnBr_3)_2]$. IR (nujol, 293 K) ν(CO): 2088(s) cm^{-1}.

CHAPTER 7

Synthesis of $[NBu_4]_6[Ni_{22-x}Pd_{20+x}(CO)_{48}]\cdot 4CH_3COCH_3$ (x = 0.62)

A solution of $Pd(Et_2S)_2Cl_2$ (0.293 g, 0.821 mmol) in CH_2Cl_2 (12 mL) was added in small portions to a solution of $[NBu_4]_2[Ni_6(CO)_{12}]$ (1.257 g, 1.072 mmol) in CH_2Cl_2 (30 mL) over a period of 6 h. The resulting mixture was stirred at room temperature for 24 h and then, the solvent removed *in vacuo*. The residue was washed with H_2O (3 × 20 mL), toluene (3 × 20 mL), CH_2Cl_2 (20 mL), thf (20 mL), and extracted with acetone (20 mL). Crystals of $[NBu_4]_6[Ni_{22-x}Pd_{20+x}(CO)_{48}]\cdot 4CH_3COCH_3$ (x = 0.63) suitable for X-ray analyses were obtained by layering *n*-hexane (40 mL) on the acetone solution (yield 0.136 g, 53 % based on Pd, 7 % based on Ni).

$C_{156}H_{240}N_6Ni_{21.38}O_{52}Pd_{20.62}$ (6481.20): calcd. C 28.91, H 3.73, N 1.30, Ni 19.35, Pd 33.87; found: C 29.10, H 3.92, N 1.04, Ni 19.54, Pd 33.68. IR (nujol, 293 K) ν_{CO}: 1985(vs), 1830(s), 1750(br) cm^{-1}. IR (CH_2Cl_2, 293 K) ν_{CO}: 2004(vs), 1877(s) cm^{-1}. IR (acetone, 293 K) ν_{CO}: 1999(vs), 1882(s), 1863(sh) cm^{-1}. IR (CH_3CN, 293 K) ν_{CO}: 1999(vs), 1873(s), 1856(s) cm^{-1}. IR (dmso, 293 K) ν_{CO}: 1995(vs), 1867(s) cm^{-1}.

Synthesis of $[NEt_4]_6[Ni_{29-x}Pd_{6+x}(CO)_{42}]\cdot 3CH_3CN\cdot$solv (x = 0.09)

A solution of $Pd(Et_2S)_2Cl_2$ (0.330 g, 0.927 mmol) in CH_3CN (20 mL) was added in small portions to a solution of $[NEt_4]_2[Ni_6(CO)_{12}]$ (1.320 g, 1.390 mmol) in CH_3CN (30 mL) over a period of 6 h. The resulting mixture was stirred at room temperature for 24 h and then, the solvent removed *in vacuo*. The residue was washed with H_2O (3 × 20 mL), toluene (3 × 20 mL), thf (20 mL), acetone (20 mL), and extracted with CH_3CN (20 mL). Crystals of $[NEt_4]_6[Ni_{29-x}Pd_{6+x}(CO)_{42}]\cdot CH_3CN\cdot$solv suitable for X-ray analyses were obtained by layering *n*-hexane (3 mL) and di-isopropyl-ether (40 mL) on the CH_3CN solution (yield 0.412 g, 61 % based on Pd, 32% based on Ni).

$C_{95}H_{129}N_9Ni_{28.91}O_{42}Pd_{6.09}$ (4414.11): calcd. C 25.85, H 2.95, N 2.86, Ni 38.44, Pd 14.68; found: C 26.03, H 3.12, N 3.04, Ni 38.75, Pd 14.39. IR (nujol, 293 K) ν_{CO}: 2000(vs), 1854(s), 1744(br) cm^{-1}. IR (CH_3CN, 293 K) ν_{CO}: 1995(vs), 1873(s), 1854(sh) cm^{-1}. IR (dmf, 293 K) ν_{CO}: 1988(vs), 1873(s), 1851(sh) cm^{-1}.

Synthesis of $[NEt_4]_6[Ni_{29+x}Pd_{6-x}(CO)_{42}]\cdot 3CH_3CN\cdot$solv (x = 0.27)

A solution of $Pd(Et_2S)_2Cl_2$ (0.330 g, 0.927 mmol) in CH_3CN (20 mL) was added in small portions to a solution of $[NEt_4]_2[Ni_6(CO)_{12}]$ (1.380 g, 1.453 mmol) in CH_3CN (30 mL) over a period of 6 h. The resulting mixture was stirred at room temperature for 24 h and then, the solvent removed *in vacuo*. The residue was washed with H_2O (3 × 20 mL), toluene (3 × 20 mL), thf (20 mL), acetone (20 mL), and extracted with CH_3CN (20 mL). Crystals of $[NEt_4]_6[Ni_{29+x}Pd_{6-x}(CO)_{42}]\cdot CH_3CN\cdot$solv suitable for X-ray analyses were obtained by layering *n*-hexane (3 mL) and di-isopropyl-ether (40 mL) on the CH_3CN solution (yield 0.385 g, 54 % based on Pd, 29% based on Ni).

$C_{95}H_{129}N_9Ni_{29.27}O_{42}Pd_{5.73}$ (4409.19): calcd. C 25.88, H 2.95, N 2.86, Ni 38.96, Pd 13.83; found: C 25.99, H 2.78, N 3.01, Ni 38.81, Pd 14.21. IR (nujol, 293 K) ν_{CO}: 2005(vs), 1835(s), 1744(br) cm^{-1}. IR (CH_3CN, 293 K) ν_{CO}: 1999(vs), 1873(s), 1849(sh) cm^{-1}.

$[NMe_4]_2[NMe_3CH_2Ph]_4[Ni_{36-x}Pd_{5+x}(CO)_{46}]\cdot 3CH_3CN\cdot$solv (x = 0.41)

$[Pd(CH_3CN)_4][BF_4]_2$ (0.920 g, 2.07 mmol) was added as a solid in small portions to a solution of $[NMe_3CH_2Ph]_2[Ni_6(CO)_{12}]$ (2.50 g, 2.53 mmol) in thf (80 mL) over a period of 6 h. The resulting mixture was stirred at room temperature for 24 h and then, the solvent removed *in vacuo*. The residue was washed with H_2O (3 × 20 mL), and extracted with acetone (20 mL). A saturated solution of $[NMe_4]Cl$ in H_2O (50 mL) was added up to complete precipitation of the compound. The solid was recovered by filtration, washed with H_2O (3 × 20 mL), toluene (3 × 20 mL), thf (15 mL), and extracted with CH_3CN (20 mL). Crystals of $[NMe_4]_2[NMe_3CH_2Ph]_4[Ni_{36-x}Pd_{5+x}(CO)_{46}]\cdot 3CH_3CN\cdot$solv (x = 0.41) suitable for X-ray analyses were obtained by layering *n*-hexane (2 mL) and di-isopropyl-ether (40 mL) on the CH_3CN solution (yield 0.76 g, 37% based on Ni, 41% based on Pd).

$C_{100}H_{97}N_9Ni_{35.58}O_{46}Pd_{5.41}$(4826.21): calcd. C 25.03, H 2.04, N 2.63, Ni 43.00, Pd 11.95; found: C 25.34, H 2.29, N 2.31, Ni 43.28, Pd 12.15. IR (CH_3CN, 293 K) ν_{CO}: 2005(vs), 1858(s) cm^{-1}.

Synthesis of $[NBu_4]_6[Ni_{37-x}Pd_{7+x}(CO)_{48}]\cdot 6CH_3CN$ (x = 0.69)

$[Pd(CH_3CN)_4][BF_4]_2$ (1.25 g, 2.81 mmol) was added as a solid in small portions to a solution of $[NBu_4]_2[Ni_6(CO)_{12}]$ (3.50 g, 2.99 mmol) in thf (30 mL) over a period of 6 h. The resulting mixture was stirred at room temperature for 24 h and then, the solvent removed *in vacuo*. The residue was washed with H_2O (3 × 15 mL), toluene (3 × 15 mL), thf (20 mL), and extracted with CH_3CN (20 mL). Crystals of $[NBu_4]_6[Ni_{37-x}Pd_{7+x}(CO)_{48}]\cdot 6CH_3CN$ (x = 0.69) suitable for X-ray analyses were

obtained by layering *n*-hexane (2 mL) and di-isopropyl-ether (40 mL) on the CH_3CN solution (yield 0.89 g, 30% based on Ni, 41% based on Pd).

$C_{156}H_{234}N_{12}Ni_{36.31}O_{48}Pd_{7.69}$ (5995.51): calcd. C 31.40, H 3.96, N 2.82, Ni 35.29, Pd 13.66; found: C 31.16, H 4.12, N 2.65, Ni 3498, Pd 13.89. IR (CH_3CN, 293 K) ν_{CO}: 1983(vs), 1838(s) cm^{-1}.

Synthesis of $[NBu_4]_5[HNi_{37-x}Pd_{7+x}(CO)_{48}]\cdot 2CH_3COCH_3\cdot$solv (x = 0.53)

$[Pd(CH_3CN)_4][BF_4]_2$ (0.426 g, 0.959 mmol) was added as a solid in small portions to a solution of $[NBu_4]_2[Ni_6(CO)_{12}]$ (1.17 g, 0.998 mmol) in thf (30 mL) over a period of 6 h. The resulting mixture was stirred at room temperature for 24 h and then, the solvent removed *in vacuo*. The residue was washed with H_2O (3 × 15 mL), toluene (3 × 15 mL), thf (20 mL), and extracted with acetone (20 mL). Crystals of $[NBu_4]_5[HNi_{37-x}Pd_{7+x}(CO)_{48}]\cdot 2CH_3COCH_3\cdot$solv (x = 0.53) suitable for X-ray analyses were obtained by layering *n*-hexane (40 mL) on the acetone solution (yield 0.38 g, 41% based on Ni, 53% based on Pd).

$C_{134}H_{192}N_5Ni_{36.47}O_{50}Pd_{7.53}$ (5615.50): calcd. C 28.81, H 3.47, N 1.25, Ni 37.85, Pd 14.29; found: C 28.64, H 3.26, N 1.51, Ni 37.98, Pd 14.02. IR (nujol, 293 K) ν_{CO}: 2004(vs), 1972(sh), 1873(s), 1854(sh) cm^{-1}. IR (acetone, 293 K) ν_{CO}: 2013(vs), 1875(s) cm^{-1}. IR (CH_3CN, 293 K) ν_{CO}: 2006(vs), 1867(s) cm^{-1}.

Synthesis of $[NBu_4]_2[Pt_{6-x}Ni_x(CO)_{12}]$ (x = 1.25)

A solution of $[NBu_4]_2[Pt_9(CO)_{18}]$ (1.00 g, 0.365 mmol) in thf (30 mL) was added dropwise to a solution of $[NBu_4]_2[Ni_6(CO)_{12}]$ (0.43 g, 0.365 mmol) in thf (20 mL). The mixture was stirred for 2 h at room temperature and then, the solvent was removed under reduced pressure. The residue was washed with H_2O (3 × 15 mL) and toluene (3 × 15 mL), and extracted with thf (50 mL). Crystals of $[NBu_4]_2[Pt_{4.75}Ni_{1.25}(CO)_{12}]$ suitable for X-ray crystallography were obtained by slow diffusion of *n*-hexane (150 mL) on the thf solution (yield 0.77 g, 61% based on Pt, 24% based on Ni).

$C_{44}H_{72}N_2Ni_{1.25}O_{12}Pt_{4.75}$ (1820.41): calcd. C 29.03, H 3.99, N 1.54, Ni 3.98, Pt 50.91; found: C 29.34, H 4.15, N 1.31, Ni 4.21, Pt 50.68. IR (nujol, 293 K) ν_{CO}: 1997(vs), 1980(s), 1818(m)1779(vs) cm^{-1}. IR (CH_3CN, 293 K) ν_{CO}: 2005(vs), 1797(m) cm^{-1}.

Synthesis of $[NBu_4]_4[Pt_{6-x}Ni_x(CO)_{12}][Cl_{1.77}Br_{0.23}]$ (x = 2.53)

A solution of $PdCl_2(Et_2S)_2$ (0.161 g, 4.42 mmol) in thf was added dropwise to a solution of $[NBu_4]_2[Ni_6(CO)_{12}]$ (1.00 g, 6.31 mmol) in thf (30 mL). The mixture was stirred for 24 h at room temperature and then, the solvent was removed *in vacuum*. The residue was washed with H_2O (3 × 15 mL) and toluene (3 × 15 mL), and extracted with thf (20 mL). Crystals of $[NBu_4]_4[Pt_{6-x}Ni_x(CO)_{12}][Cl_{1.77}Br_{0.23}]$ (x = 2.53) suitable for X-ray crystallography were obtained by slow diffusion of *n*-hexane (80 mL) on the thf solution. The presence of some Br^- ions in the crystals is due to contamination of the starting $[NBu_4]_2[Ni_6(CO)_{12}]$ salt with some $[NBu_4]Br$.

$C_{76}H_{144}Br_{0.23}Cl_{1.77}N_4Ni_{2.53}O_{12}Pt_{3.48}$ (2213.03): calcd. C 41.26, H 6.57, N 2.53, Ni 6.63, Pt 30.70; found: C 41.08, H 6.74, N 2.69, Ni 6.38, Pt 30.56. IR (thf, 293 K) ν_{CO}: 1995(vs), 1797(m) cm^{-1}. IR (CH_3CN, 293 K) ν_{CO}: 1997(vs), 1796(m) cm^{-1}.

Synthesis of $[NBu_4]_2[Pt_{6-x}Ni_x(CO)_{12}]$ (x = 3.24, 4.15, 4.16)

A solution of $[NBu_4]_2[Ni_6(CO)_{12}]$ (0.70 g, 0.60 mmol) in thf (30 mL) was added dropwise to a solution of $[NBu_4]_2[Pt_6(CO)_{12}]$ (0.95 g, 0.48 mmol) in thf (20 mL). The mixture was stirred for 2 h at room temperature and then, the solvent was removed under reduced pressure. The residue was washed with H_2O (3 × 15 mL) and toluene (3 × 15 mL), and extracted with CH_2Cl_2 (35 mL). A mixture of crystals of $[NBu_4]_2[Pt_{2.76}Ni_{3.24}(CO)_{12}]$, $[NBu_4]_2[Pt_{1.85}Ni_{4.15}(CO)_{12}]$ and $[NBu_4]_2[Pt_{1.84}Ni_{4.16}(CO)_{12}]$ suitable for X-ray crystallography were obtained by slow diffusion of *n*-hexane (100 mL) on the CH_2Cl_2 solution (yield 0.88 g, 45% based on Pt, 64% based on Ni).
$C_{44}H_{72}N_2Ni_{3.24}O_{12}Pt_{2.76}$ (1550.38): calcd. C 34.15, H 4.69, N 1.81, Ni 12.14, Pt 34.80; $C_{44}H_{72}N_2Ni_{4.15}O_{12}Pt_{1.85}$ (1425.59): calcd. C 37.14, H 5.10, N 1.97, Ni 16.91, Pt 25.37; $C_{44}H_{72}N_2Ni_{4.16}O_{12}Pt_{1.84}$ (1424.23): calcd. C 37.17, H 5.11, N 1.97, Ni 16.97, Pt 25.26; found: C 36.85, H 4.89, N 1.96, Ni 15.86, Pt 28.34. IR (nujol, 293 K) ν_{CO}: 2025(vw), 1966(vs), 1811(m) 1783(s) cm^{-1}. IR (CH_2Cl_2, 293 K) ν_{CO}: 1996(vs), 1793(m) cm^{-1}. IR (thf, 293 K) ν_{CO}: 1992(vs), 1798(m) cm^{-1}. IR (acetone, 293 K) ν_{CO}: 1989(vs), 1801(m) cm^{-1}. IR (CH_3CN, 293 K) ν_{CO}: 1995(vs), 1798(m) cm^{-1}. IR (dmso, 293 K) ν_{CO}: 1990(vs), 1797(m) cm^{-1}.

Synthesis of $[NBu_4]_2[Pt_{6-x}Ni_x(CO)_{12}]$ (x = 4.41)

A solution of $[NBu_4]_2[Ni_6(CO)_{12}]$ (0.49 g, 0.42 mmol) in thf (15 mL) was added dropwise to a solution of $[NBu_4]_2[Pt_6(CO)_{12}]$ (0.48 g, 0.24 mmol) in thf (20 mL). The mixture was stirred for 2 h at room temperature and then, the solvent was removed under reduced pressure. The residue was

dissolved with CH_3CN (15 mL) and stirred at room temperature for 8 days. After then, the solvent was removed *in vacuo*. The solid residue washed with H_2O (3 × 15 mL) and toluene (3 × 15 mL), and extracted with thf (20 mL). Crystals of $[NBu_4]_2[Pt_{1.59}Ni_{4.41}(CO)_{12}]$ suitable for X-ray crystallography were obtained by slow diffusion of *n*-hexane (80 mL) on the thf solution (yield 0.36 g, 33% based on Pt, 45% based on Ni).

$C_{44}H_{72}N_2Ni_{4.41}O_{12}Pt_{1.59}$ (1390.14): calcd. C 38.10, H 5.24, N 2.02, Ni 18.43, Pt 22.37; found: C 38.31, H 5.02, N 1.84, Ni 18.65, Pt 22.09. IR (CH_2Cl_2, 293 K) ν_{CO}: 1989(vs), 1788(m) cm^{-1}.

Synthesis of $[NBu_4]_2[Pt_{6-x}Ni_x(CO)_{12}]$ (x = 5.78, 5.90)

A solution of $[NBu_4]_2[Ni_6(CO)_{12}]$ (1.27 g, 1.08 mmol) in thf (20 mL) was added dropwise to a solution of $[NBu_4]_2[Pt_6(CO)_{12}]$ (0.43 g, 0.216 mmol) in thf (10 mL). The mixture was stirred for 2 h at room temperature and then, the solvent was removed *in vacuo*. The residue was dissolved with CH_3CN and the solution heated at refluxing temperature for 1 h. The solvent was removed under reduced pressure, the solid residue washed with H_2O (3 × 15 mL) and toluene (3 × 15 mL), and extracted with thf (20 mL) and acetone (20 mL). Crystals of $[NBu_4]_2[Pt_{0.22}Ni_{5.78}(CO)_{12}]$, and $[NBu_4]_2[Pt_{0.10}Ni_{5.90}(CO)_{12}]$ suitable for X-ray crystallography were obtained by slow diffusion of *n*-hexane (100 mL) on the thf solution and *n*-hexane/di-isopropyl-ether (100 mL) on the CH_3CN solution, respectively.

Synthesis of $[NEt_4]_4[Pt_{12-x}Ni_x(CO)_{21}]$ (x = 2.91)

A solution of $[NEt_4]_2[Ni_6(CO)_{12}]$ (0.45 g, 0.47 mmol) in acetone (30 mL) was added dropwise to a solution of $[NEt_4]_2[Pt_9(CO)_{18}]$ (1.00 g, 0.40 mmol) in acetone (20 mL). The mixture was stirred for 2 h at room temperature and then, the solvent was removed under reduced pressure. The residue was washed with H_2O (3 × 15 mL) and toluene (3 × 15 mL), and extracted with acetone (35 mL). Crystals of $[NEt_4]_4[Pt_{9.09}Ni_{2.91}(CO)_{21}]$ suitable for X-ray crystallography were obtained by slow diffusion of *n*-hexane (100 mL) on the acetone solution.

IR (acetone, 293 K) ν_{CO}: 1998(vs), 1802(s) cm^{-1}. IR (CH_3CN, 293 K) ν_{CO}: 1984(vs), 1797(s) cm^{-1}. IR (dmso, 293 K) ν_{CO}: 1978(vs), 1796(s) cm^{-1}.

Synthesis of $[NBu_4]_4[Pt_{12-x}Ni_x(CO)_{21}]$ (x = 5.82)

A solution of $[NBu_4]_2[Ni_6(CO)_{12}]$ (0.49 g, 0.42 mmol) in thf (15 mL) was added dropwise to a solution of $[NBu_4]_2[Pt_6(CO)_{12}]$ (0.48 g, 0.24 mmol) in thf (20 mL). The mixture was stirred for 2 h at room temperature and then, the solvent was removed under reduced pressure. The residue was dissolved with CH_3CN (15 mL) and stirred at room temperature for 8 days. After then, the solvent was removed *in vacuo*. The solid residue was washed with H_2O (3 × 15 mL) and toluene (3 × 15 mL), and extracted with thf (20 mL) and acetone (20 mL). Crystals of $[NBu_4]_4[Pt_{6.18}Ni_{5.82}(CO)_{21}]$ suitable for X-ray crystallography were obtained by slow diffusion of *n*-hexane (80 mL) on the acetone solution.

IR (nujol, 293 K) ν_{CO}: 1979 (vs), 1790 (vs), 1712(m) cm^{-1}. IR (thf, 293 K) ν_{CO}: 1983 (vs), 1814 (m) cm^{-1}. IR (acetone, 293 K) ν_{CO}: 1983(vs), 1818(m) cm^{-1}. IR (CH_3CN, 293 K) ν_{CO}: 1989(vs), 1821(m) cm^{-1}. IR (dmso, 293 K) ν_{CO}: 1984(vs), 1815(m) cm^{-1}.

Synthesis of $[NMe_4]_4[Pt_{12-x}Ni_x(CO)_{21}]\cdot CH_3CN$ (x = 6.29)

A solution of $[NMe_4]_2[Ni_6(CO)_{12}]$ (0.56 g, 0.669 mmol) in thf (20 mL) was added dropwise to a solution of $[NMe_4]_2[Pt_6(CO)_{12}]$ (0.55 g, 0.335 mmol) in thf (30 mL). The mixture was stirred for 2 h at room temperature and then, the solvent was removed *in vacuo*. The residue was dissolved in CH_3CN and the resulting solution was treated with $HBF_4{\cdot}Et_2O$. The oxidation was stopped when the ν_{CO} bands shifted from 1984(vs), 1792(m) to 2006(vs), 1829(m) cm^{-1}. The solvent was removed under reduced pressure, the solid residue washed with H_2O (3 × 15 mL), toluene (3 × 15 mL) and extracted with CH_3CN (20 mL). After the first attempt of crystallisation of the product by slow diffusion *n*-hexane/di-isopropyl-ether on the CH_3CN solution, the solvent was removed *in vacuo* and the solid residue was extracted again in CH_3CN (20 mL). Crystals of $[NMe_4]_4[Pt_{5.71}Ni_{6.29}(CO)_{21}]$ suitable for X-ray crystallography were obtained by slow diffusion of *n*-hexane/di-isopropyl-ether (80 mL) on the CH_3CN solution.

IR (CH_3CN, 293 K) ν_{CO}: 1993(vs), 1836(m) cm^{-1}.

Synthesis of $[NEt_4]_4[Pt_{12-x}Ni_x(CO)_{21}]\cdot CH_3CN$ (x = 6.41)

dppe (0.264 g, 0.663 mmol) was added as a solid to a solution of $[NEt_4]_2[Pt_3Ni_3(CO)_{12}]$ (0.90 g, 0.663 mmol) in CH_3CN (30 mL). The mixture was stirred for 2 h at room temperature and then, the solvent was removed under reduced pressure. The residue was washed with H_2O (3 × 15 mL),

toluene (3 × 15 mL), thf (3 × 15 mL) and extracted with acetone (20 mL) and CH_3CN (20 mL). Crystals of $[NEt_4]_4[Pt_{5.59}Ni_{6.41}(CO)_{21}]$ suitable for X-ray crystallography were obtained by slow diffusion of *n*-hexane/di-isopropyl-ether (60 mL) on the CH_3CN solution.

IR (nujol, 293 K) ν_{CO}: 1993(sh), 1972(sh), 1954(vs), 1779(s) 1754(s), 1732(m) cm^{-1}.

Synthesis of $[NBu_4]_4[Pt_{19-x}Ni_x(CO)_{22}]$ (x = 2.27)

A solution of $[NBu_4]_2[Ni_6(CO)_{12}]$ (0.35 g, 0.30 mmol) in thf (30 mL) was added dropwise to a solution of $[NBu_4]_2[Pt_{12}(CO)_{24}]$ (1.05 g, 0.30 mmol) in thf (20 mL). The mixture was stirred for 2 h at room temperature and then, the solvent was removed under reduced pressure. The residue was washed with H_2O (3 × 15 mL) and toluene (3 × 15 mL), and extracted with CH_2Cl_2 (20 mL). After the first attempt of crystallisation of the product by slow diffusion of *n*-hexane on the CH_2Cl_2 solution, the solvent was removed *in vacuo* and the solid residue was extracted in acetone (20 mL). Crystals of $[NBu_4]_4[Pt_{16.73}Ni_{2.27}(CO)_{22}]\cdot CH_3COCH_3$ suitable for X-ray crystallography were obtained by slow diffusion of *n*-hexane (60 mL) on the acetone solution.

IR (nujol, 293 K) ν_{CO}: 2010(s), 1815(sh), 1773(m) cm^{-1}. IR (CH_3CN, 293 K) ν_{CO}: 2001(vs), 1989(sh), 1926(w), 1797(s) cm^{-1}.

Synthesis of $[NBu_4]_4[Pt_{19-x}Ni_x(CO)_{22}]$ (x = 3.23)

A solution of $[NBu_4]_2[Ni_6(CO)_{12}]$ (0.71 g, 0.60 mmol) in thf (30 mL) was added dropwise to a solution of $[NBu_4]_2[Pt_6(CO)_{12}]$ (0.50 g, 0.25 mmol) in thf (20 mL). The mixture was stirred for 2 h at room temperature and then, the solvent was removed under reduced pressure. The residue was dissolved in dmso (15 mL) and heated at 130 °C for 11 h. After then, the resulting solution was stirred at room temperature for 3 days. A saturated solution of $[NEt_4]Br$ in H_2O (40 mL) was added up to complete precipitation. The resulting solid was recovered by filtration, washed with H_2O (3 × 15 mL), toluene (3 × 15 mL), thf (3 x 15 mL) and extracted with acetone (20 mL). After two attempts of crystallisation of the product by slow diffusion of *n*-hexane on the acetone solution, the solvent was removed *in vacuo* and the solid residue was extracted in CH_3CN (20 mL). Crystals of $[NBu_4]_4[Pt_{19-x}Ni_x(CO)_{22}]\cdot 2CH_3CN$ suitable for X-ray crystallography were obtained by slow diffusion of *n*-hexane/di-isopropyl-ether (60 mL) on the CH_3CN solution.

IR (nujol, 293 K) ν_{CO}: 1990(s), 1960(sh), 1798(sh), 1770(m), 1750(m) cm^{-1}.

References

1 L. Mond, C. Langer and F. Quincke, *J. Chem. Soc., Trans.*, 1890, **57**, 749–753.

2 F. A. Cotton, *Q. Rev. Chem. Soc.*, 1966, **20**, 389–401.

3 S. Zacchini, *Eur. J. Inorg. Chem.*, 2011, **2011**, 4125–4145.

4 N. T. Tran, D. R. Powell and L. F. Dahl, *Angew. Chem. Int. Ed*, 2000, **112**, 4287.

5 G. Longoni and P. Chini, *J. Am. Chem. Soc.*, 1976, **98**, 7225–7231.

6 S. Kawi and B. C. Gates, *Clusters and Colloids-from Theory to Applications*, VCH Publishers, Weinheim, Germany, 1994.

7 E. Charalambous, L. H. Gade, B. F. G. Johnson, J. Lewis, M. McPartlin and H. R. Powell, *J. Chem. Soc. Chem. Commun.*, 1990, 688.

8 A. J. Amoroso, L. H. Gade, B. F. G. Johnson, J. Lewis, P. R. Raithby and W.-T. Wong, *Angew. Chemie Int. Ed. English*, 1991, **30**, 107–109.

9 P. Chini, *J. ORGANOMET. CHEM*, 1980, **200**, 37–61.

10 P. Chini and V. G. Albano, *J. Organomet. Chem.*, 1968, **15**, 433–440.

11 K. J. Bradd, B. T. Heaton, J. A. Iggo, C. Jacob, J. T. Sampanthar and S. Zacchini, *Dalt. Trans.*, 2008, 685–690.

12 F. Calderoni, F. Demartin, F. Fabrizi de Biani, C. Femoni, M. C. Iapalucci, G. Longoni and P. Zanello, *Eur. J. Inorg. Chem.*, 1999, **1999**, 663–671.

13 B. K. Teo and H. Zhang, *Coord. Chem. Rev.*, 1995, **143**, 611–636.

14 P. P. Edwards and M. J. Sienko, *Int. Rev. Phys. Chem.*, 1983, **3**, 83–137.

15 D. Bonincontro, A. Lolli, A. Storione, A. Gasparotto, B. Berti, S. Zacchini, N. Dimitratos and S. Albonetti, *Appl. Catal. A Gen.*, 2019, **588**, 117279–117289.

16 W. A. Herrmann, *Angew. Chemie Int. Ed.*, 2002, **41**, 1290.

17 B. Najafabadi Khalili and J. Corrigan, *Chem. Commun.*, 2015, **51**, 665–667.

18 J. A. Cabeza and P. García-Álvarez, *Chem. Soc. Rev.*, 2011, **40**, 5389–5405.

19 E. Huyee, E. A. Keiter and R. L. Keiter, *Chimica Inorganica*, Padova, 2nd edn., 1999.

20 S. Sculfort and P. Braunstein, *Chem. Soc. Rev.*, 2011, **40**, 2741–2760.

21 P. Croizat, S. Sculfort, R. Welter and P. Braunstein, *Organometallics*, 2016, **35**, 3949–3958.

22 I. Ciabatti, C. Femoni, M. C. Iapalucci, S. Ruggieri and S. Zacchini, *Coord. Chem. Rev.*, 2018, **355**, 27–38.

23 M. Bortoluzzi, I. Ciabatti, C. Cesari, C. Femoni, M. C. Iapalucci and S. Zacchini, *Eur. J. Inorg. Chem.*, 2017, **2017**, 3135–3143.

24 I. Ciabatti, C. Femoni, M. Hayatifar, M. C. Iapalucci, A. Ienco, G. Longoni, G. Manca and S. Zacchini, *Inorg. Chem.*, 2014, **53**, 9761–9770.

25 M. Bortoluzzi, C. Cesari, I. Ciabatti, C. Femoni, M. Hayatifar, M. C. Iapalucci, R. Mazzoni and S. Zacchini, *J. Clust. Sci.*, 2017, **28**, 703–723.

26 B. Berti, M. Bortoluzzi, C. Cesari, C. Femoni, M. C. Iapalucci, R. Mazzoni, F. Vacca and S. Zacchini, *Eur. J. Inorg. Chem.*, 2019, **2019**, 3084–3093.

27 C. E. Coffey, J. Lewis and R. S. Nyholm, *J. Chem. Soc.*, 1964, 1741–1749.

28 V. G. Albano, M. Monari, M. C. Iapalucci and G. Longoni, *Inorg. Chim. Acta*, 1993, **213**, 183–190.

29 O. Rossell, M. Seco and P. G. Jones, *Inorg. Chem.*, 1990, **29**, 348–350.

30 H. Clavier and S. P. Nolan, *Chem. Commun.*, 2010, **46**, 841.

31 B. Berti, M. Bortoluzzi, C. Cesari, C. Femoni, M. C. Iapalucci, R. Mazzoni, F. Vacca and S. Zacchini, *Inorg. Chem.*, 2020, **59**, 2228–2240.

32 B. Berti, M. Bortoluzzi, C. Cesari, C. Femoni, M. C. Iapalucci, R. Mazzoni, F. Vacca and S. Zacchini, *Inorg. Chem.*, 2019, **58**, 2911–2915.

33 R. Bianchi, G. Gervasio and D. Marabello, *Inorg. Chem.*, 2000, **39**, 2360–2366.

34 A. Kotsinaris, G. Kyriacou and C. Lambrou, *J. Appl. Electrochem.*, 1998, **28**, 613–616.

35 M. Lourdichi and R. Mathieu, *Organometallics*, 1986, **5**, 2067–2071.

36 P. Brun, G. M. Dawkins, M. Green, R. M. Mills, J.-Y. Salaün, F. G. A. Stone and P. Woodward, *J. Chem. Soc., Chem. Commun.*, 1981, 966–968.

37 K. K. Chakrahari, R. P. B. Silalahi, J.-H. Liao, S. Kahlal, Y.-C. Liu, J.-F. Lee, M.-H. Chiang, J.-Y. Saillard and C. W. Liu, *Chem. Sci.*, 2018, **9**, 6785–6795.

38 V. G. Albano, F. Calderoni, M. C. Iapalucci, G. Longoni, M. Monari and P. Zanello, *J. Clust. Sci.*, 1995, **6**, 107–123.

39 B. Berti, M. Bortoluzzi, C. Cesari, C. Femoni, M. C. Iapalucci, R. Mazzoni and S. Zacchini, *Eur. J. Inorg. Chem.*, 2020, **2020**, 2191–2202.

40 P. Braunstein, J. Rosé, A. Dedieu, Y. Dusausoy, J.-P. Mangeot, A. Tiripicchio and M. Tiripicchio-Camellini, *J. Chem. Soc., Dalt. Trans.*, 1986, 225–234.

41 V. G. Albano, F. Azzaroni, M. C. Iapalucci, G. Longoni, M. Monari, S. Mulley, D. M. Proserpio and A. Sironi, *Inorg. Chem.*, 1994, **33**, 5320–5328.

42 V. G. Albano, F. Calderoni, M. C. Iapalucci, G. Longoni and M. Monari, *J. Chem. Soc. Chem. Commun.*, 1995, 433.

43 A. Iturmendi, M. Iglesias, J. Munarriz, V. Polo, V. Passarelli, J. J. Pérez-Torrente and L. A. Oro, *Green Chem.*, 2018, **20**, 4875–4879.

44 A. Fürstner, M. Alcarazo, R. Goddard and C. W. Lehmann, *Angew. Chemie Int. Ed.*, 2008, **47**, 3210–3214.

45 D. A. Imbrich, W. Frey, S. Naumann and M. R. Buchmeiser, *Chem. Commun.*, 2016, **52**, 6099–6102.

46 B. Berti, M. Bortoluzzi, C. Cesari, C. Femoni, M. C. Iapalucci, L. Soleri and S. Zacchini, *Inorg. Chem.*, 2020, **59**, 15936–15952.

47 V. G. Albano, L. Grossi, G. Longoni, M. Monari, S. Mulley and A. Sironi, *J. Am. Chem. Soc.*, 1992, **114**, 5708–5713.

48 D. Collini, C. Femoni, M. C. Iapalucci and G. Longoni, *Comptes Rendus Chim.*, 2005, **8**, 1645–1654.

49 C. Femoni, M. C. Iapalucci, G. Longoni, C. Tiozzo and S. Zacchini, *Angew. Chemie Int. Ed.*, 2008, **47**, 6666–6669.

50 N. N. Grennwood and A. Earnshaw, *Chemistry of the Elements*, Oxford, 2nd edn., 1998.

51 P. Chini, S. Martinengo and G. Longoni, *Gazz. Chim. Ital.*, 1975, 105.

52 R. Usón, A. Laguna, M. Laguna, P. G. Jones and G. M. Sheldrick, *J. Chem. Soc., Dalt. Trans.*, 1981, 366–370.

53 S. Banerjee, M. K. Karunananda, S. Bagherzadeh, U. Jayarathne, S. R. Parmelee, G. W. Waldhart and N. P. Mankad, *Inorg. Chem.*, 2014, **53**, 11307–11315.

54 T. L. Blundell and H. M. Powell, *J. Chem. Soc. A*, 1971, 1685–1690.

55 J. A. Cabeza, I. del Río, J. M. Fernández-Colinas, E. Pérez-Carreño, M. G. Sánchez-Vega and D. Vázquez-García, *Organometallics*, 2009, **28**, 1832–1837.

56 G. Whittell and I. Manners, *Angew. Chemie Int. Ed.*, 2011, **50**, 10288–10289.

57 G. Booth and J. Chatt, *J. Chem. Soc. A Inorganic, Phys. Theor.*, 1969, 2131.

58 S. M. J. C. Calabrese, L. F. Dahl, P. Chini, G. Longoni, *J. Am. Chem. Soc.*, 1972, **96**, 2614–2616.

59 G. Longoni and P. Chini, *J. Am. Chem. Soc.*, 1976, **98**, 7225–7231.

60 C. Femoni, F. Kaswalder, M. C. Iapalucci, G. Longoni, M. Mehlstäubl and S. Zacchini, *Chem. Commun.*, 2005, 5769.

61 B. Berti, C. Femoni, M. C. Iapalucci, S. Ruggieri and S. Zacchini, *Eur. J. Inorg. Chem.*, 2018, 2018, 3285–3296.

62 L. Bengtsson-Kloo, C. M. Iapalucci, G. Longoni and S. Ulvenlund, *Inorg. Chem.*, 1998, **37**, 4335–4343.

63 C. Femoni, F. Kaswalder, M. C. Iapalucci, G. Longoni, M. Mehlstäubl, S. Zacchini and A. Ceriotti, *Angew. Chemie Int. Ed.*, 2006, **45**, 2060–2062.

64 C. Femoni, F. Kaswalder, M. C. Iapalucci, G. Longoni and S. Zacchini, *Eur. J. Inorg. Chem.*, 2007, **2007**, 1483–1486.

65 C. Femoni, M. C. Iapalucci, G. Longoni, T. Lovato, S. Stagni and S. Zacchini, *Inorg. Chem.*, 2010, **49**, 5992–6004.

66 G. Schmid, 1994.

67 P. R. Braunstein, P.; Oro, L. A.; Raithby, 1999.

68 C. Cesari, I. Ciabatti, C. Femoni, M. C. Iapalucci, F. Mancini and S. Zacchini, *Inorg. Chem.*, 2017, **56**, 1655–1668.

69 B. Berti, C. Cesari, F. Conte, I. Ciabatti, C. Femoni, M. C. Iapalucci, F. Vacca and S. Zacchini, *Inorg. Chem.*, 2018, **57**, 7578–7590.

70 C. Cesari, I. Ciabatti, C. Femoni, M. C. Iapalucci, F. Mancini and S. Zacchini, *Inorg. Chem.*, 2017, **56**, 1655–1668.

71 I. Ciabatti, C. Femoni, M. C. Iapalucci, G. Longoni, T. Lovato and S. Zacchini, *Inorg. Chem.*, 2013, **52**, 4384–4395.

72 L. K. Batchelor, B. Berti, C. Cesari, I. Ciabatti, P. J. Dyson, C. Femoni, M. C. Iapalucci, M. Mor, S. Ruggieri and S. Zacchini, *Dalt. Trans.*, 2018, **47**, 4467–4477.

73 B. Berti, M. Bortoluzzi, A. Ceriotti, C. Cesari, C. Femoni, M. Carmela Iapalucci and S. Zacchini, *Inorg. Chim. Acta*, 2020, **512**, 119904.

74 J. B. Ballif, P. Braunstein, A. D. Burrows, R. D. Adams and W. Wuz, *J. Clust. Sci.*, 1994, **5**, 443–466.

75 L. R. J.-P. Barbier, R. Bender, P. Braunstein, J. Fischer, *J. Chem. Res*, 1978, 2913.

76 Z. Béni, R. Ros, A. Tassan, R. Scopelliti and R. Roulet, *Inorg. Chim. Acta*, 2005, **358**, 497–503.

77 M. Kawano, J. W. Bacon, C. F. Campana, B. E. Winger, J. D. Dudek, S. A. Sirchio, S. L. Scruggs, U. Geiser and L. F. Dahl, *Inorg. Chem.*, 2001, **40**, 2565.

78 E. Cattabriga, I. Ciabatti, C. Femoni, T. Funaioli, M. C. Iapalucci and S. Zacchini, *Inorg. Chem.*, 2016, **55**, 6068–6079.

79 B. Berti, M. Bortoluzzi, C. Cesari, C. Femoni, M. C. Iapalucci and S. Zacchini, *Inorg. Chim. Acta*, 2020, **503**, 119432–119432.

80 G. R. Desiraju, *Acc. Chem. Res.*, 2002, **35**, 565–573.

81 G. R. Desiraju, *Chem. Commun.*, 2005, 2995.

82 S. Aime, M. R. Chierotti, R. Gobetto, A. Russo and M. J. Stchedroff, *Inorg. Chim. Acta*, 2003, **351**, 251–255.

83 C. Femoni, M. C. Iapalucci, G. Longoni, S. Zacchini and E. Zazzaroni, *Dalt. Trans.*, 2007, 2644–2651.

84 N. W. Alcock and J. H. Nelson, *J. Chem. Soc. Dalt. Trans.*, 1982, 2415.

85 J. H. Nelson, W. L. Wilson, L. W. Cary, N. W. Alcock, H. J. Clase, G. S. Jas, L. Ramsey-Tassin and J. W. Kenney, *Inorg. Chem.*, 1996, **35**, 883–892.

86 W. Hieber, W. Beck and G. Zeitler, *Angew. Chemie*, 1961, **73**, 364–368.

87 N. T. Tran, M. Kawano, D. R. Powell and L. F. Dahl, *J. Chem. Soc. Dalt. Trans.*, 2000, 4138–4144.

88 C. Femoni, M. C. Iapalucci, G. Longoni, H. Svensson and J. Woloska, *Angew. Chemie Int. Ed.*, 2000, **39**, 1635–1637.

89 B. Berti, C. Cesari, C. Femoni, T. Funaioli, M. C. Iapalucci and S. Zacchini, *Dalt. Trans.*, 2020, **49**, 5513–5522.

90 C. Femoni, M. C. Iapalucci, G. Longoni, P. H. Svensson, P. Zanello and F. Fabrizi de Biani, *Chem. - A Eur. J.*, 2004, **10**, 2318–2326.

91 B. Cordero, V. Gómez, A. E. Platero-Prats, M. Revés, J. Echeverría, E. Cremades, F. Barragán and S. Alvarez, *Dalt. Trans.*, 2008, 2832.

92 F. Fabrizi de Biani, C. Femoni, M. C. Iapalucci, G. Longoni, P. Zanello and A. Ceriotti, *Inorg. Chem.*, 1999, **38**, 3721–3724.

93 P. M. and P. Z. F. Demartin, F. Fabrizi de Biani, C. Femoni, M. C. Iapalucci, G. Longoni, *J. Clust. Sci.*, 2001, **12**, 61–74.

94 D. Collini, F. Fabrizi De Biani, D. S. Dolzhnikov, C. Femoni, M. C. Iapalucci, G. Longoni, C. Tiozzo, S. Zacchini and P. Zanello, *Inorg. Chem.*, 2011, **50**, 2790–2798.

95 C. Femoni, M. C. Iapalucci, G. Longoni and P. H. Svensson, *Chem. Commun.*, 2001, 1776–1777.

96 G. Doyle, K. A. Eriksen and D. Van Engen, *J. Am. Chem. Soc.*, 1986, **108**, 445–451.

97 C. Femoni, F. Kaswalder, M. C. Iapalucci, G. Longoni, M. Mehlstäubl and S. Zacchini, *Chem. Commun.*, 2005, 5769–5771.

98 G. Longoni, P. Chini and A. Cavalieri, *Inorg. Chem.*, 1976, **15**, 3025–3029.